Unione Europea

Ministero dell'Istruzione,
dell'Università e della Ricerca

TESI DI DOTTORATO

Integrated methodologies for qualitative and quantitative characterization of historical pigments

Tutor:
Prof.ssa Maria Brai

Co-Tutor:
Prof. S.O. Troja

Dottoranda:
Dott.ssa Dorotea Fontana

Coordinatore:
Prof. Bernardo Spagnolo

SSD: FIS/07

Università degli Studi di Palermo
Dipartimento di Fisica e Chimica

Corso di DOTTORATO DI RICERCA INTERNAZIONALE
in FISICA APPLICATA - XXIV Ciclo

"Light is a thing that cannot be reproduced,

but must be represented by something else – by color"

Paul Cezanne

Table of Contents

Integrated methodologies for qualitative and quantitative characterization of historical pigments

Introduction

In order to guarantee the safeguard of Cultural Heritage it is necessary to have a complete scientifical and technological knowledge of the artworks, preparatory at any valorisation, conservation and/or restoration program.

This kind of knowledge must be acquired through the study of the structural and chemical-physic characteristics of the materials that compose the artwork; the valorisation of the degradation processes; the integration of different material used in the different restoration phases with the original ones.

In the Cultural Heritage field, the study of the pigments covers a crucial role, both for historical-artistic and diagnostic reasons and for deepening knowledge of the degradation phenomena.

Starting from these assumptions, the research activities conducted under this thesis, had as main objective to investigate the possibility of increasing the deductible information from non-destructive and non-invasive investigations for the study of pictorial materials, validating technical and analysis protocols based on a comparative study of the data returned by complementary methods of investigation.

In this context, the need of integrated scientific approaches among the analytical techniques nowadays available reflects the fact that an artwork is to be considered such as a complex physical system able to react with the external inputs according to its own constituent materials and the chemical-physical features of the environment.

Unfortunately, the complexity and the diversity of artistic materials and environmental conditions, that control the dynamics of degradation processes, make difficult to establish universally valid analytical protocols. The characteristics of cultural heritage, thus requiring a multidisciplinary and integrated approach at all levels of intervention, from the diagnostics, the preservation and restoration to the valorisation and the fruition.

The correlation between diagnostic and fruition, less obvious than that one increasingly accepted between scientific research and restoration, it is today more and stronger. This is because the modern analysis techniques allow to observe the works of art from new points of view, to know the intrinsic nature of matter, imperceptible to the naked eye, to see details contributing to the vision of the artwork as a whole, bearing witness to the artistic and technical knowledge of the author.

Then, a focused diagnostic investigation permits to identify the materials chosen by the artist, obtaining information about the client, on the basis of the preciousness and rarity of matter, on the executive

techniques, or even on dating, as well as assess the state of conservation, rebuilding the history of the work of art from the realization to the present day.

In the case of the investigations on pictorial works or painted works of art, in addition to a purely archaeometric value, the characterization of the pictorial materials and the decay products of an artwork is of fundamental importance in the case of restoration, prior to which is necessary to establish the compatibility between the materials present and those to be employed during cleaning, consolidation and protection procedures of artistic surfaces. In fact, in accordance with the minimum disrupt of the delicate system work of art, the two moments, cognitive and conservative coincide. So, often, the restoration represents the only opportunity for a deepening knowledge of artwork from all points of view.

To meet the requirements of minimal interaction with the surfaces of historic and artistic value, the non-invasive diagnostic tests have the enormous advantage of respecting the integrity of the cultural heritage surfaces and, consequently, of increasing the number of measurement points by improving statistical result. In this way the analysis can be performed in a greater number of points or areas of the work and, more importantly, repeated several times over time, thus to guarantee the monitoring of possible compositional, structural and chromatic variations both during the restoration within the desirable scheduled maintenance that should concern all the works of art and their environmental contexts.

On the basis of the before considerations, this thesis present the research methodology used for the study of materials through the analysis carried out on samples of pictorial layer reproduced in laboratory according to the typical mixtures realized by the ancient artists.

Starting from that assumption, 4 pigments per each hue were chosen, and in particular: cinnabar, sinopia, hematite and carmine for red; lead-tin yellow, ochre, raw Sienna and French ochre for yellow; lapis lazuli, artificial ultramarine, indigo and azurite for blue; bone white, zinc white, titanium white and chalk white for white. Each pigment was characterized by means of XRF, Raman and Spectrophotometric measurements, and then binary mixtures were realized, mixing cinnabar, lead-tin yellow, lapis lazuli and chalk white to reproduce different colours and shade realized by ancient artists.

The thesis is then focus to obtain information related to the characterization and identification of the single component present in the mixture and also to the quantitative information on the two pigments mixed.

The integrated approach, here used, consists in the employ of the chemical-physical characterization techniques and the analytical methods for the management of the data.

Particular attention has been devoted to the presentation of three characterization techniques more spread in Cultural Heritage field and here used:

- a techniques of elemental analysis, X-ray fluorescence (XRF), widely described in Chapter 2,
- a technique of compositional analysis, Raman Spectroscopy, whose potential are discussed in Chapter 3,
- Spectrophotometric diagnostic techniques that allow to perform analysis of the optical behaviour of the surfaces with portable instruments for *in situ* acquisitions and rapid execution times, presented in Chapter 4.

The comparison of the considered spectroscopic techniques was particularly useful in the study of our samples for the complementarities of the results provided in both elementary and compositional information, allowing to obtain a more precise characterization.

In the study of materials of historical and artistic interest, in fact, the physic-chemical characterization and evaluation of their conservation status may be accompanied and supplemented by the analysis of the physic-optical properties of surfaces. Applying colorimetric and spectrophotometric analysis is possible to have information of the colorimetric behaviour of the surface analyzed and to study the chromatic variation due to degradation and/or restoration processes.

To verify the advantages of the integrated use of these diagnostic techniques historical pigments have been studied, selected after an accurate literature search (reported in Chapter 5), both in terms of the historicity and compatibility with other pigments. The analysis, discussed in Chapter 6, reports the elemental, compositional and colorimetric characterization of pure and mixed samples, in order to identify the fingerprint of each pure pigment and to verify the presence of these also in the binary mixtures.

Final aim of the work is to collect quantitative information on each pigment that compose the mixtures, and to obtain calibration curves to be used on unknown mixtures and to trace the quantity of each pigments present in the mixtures.

Chapter 1
Diagnostic methods for Cultural Heritage

The characterization methodologies applied on Cultural Heritage are, actually, the main scientifically analysis carried out on historical-artistic samples to obtain information related to origin of materials, realization techniques, manufactures, artistes, etc.
In this chapter the integrated methodologies for the characterization of cultural heritage are presented, focusing the attention on the information that can be obtained during a diagnostic analysis of the historical-artistic surfaces.
The attention will be based on the characterization of polychrome surface, focusing the attention on the historical pigments used by the ancient artists, on the techniques applied to realize a painting (or polychrome surface) and on state of art of the application of non-invasive diagnostic methods.

1.1 Historical pigments: their use in the past

The pigments are substances present in the form of fine powder, which to be used needs to be dispersed in a transparent homogeneous medium (said binder) that allows it to be spread on any substrate and give it colour [1]. The pigment does not form chemical bonds with the binder, is insoluble in it, so then the final product is not a solution but a paste more or less dense, homogeneous and easily to spread. The pigment spread through the binder acquires characteristics of opacity, thus becoming opaque to the preparatory layer. The hiding power of the paint film mainly depends on three factors: the degree of grinding of the pigment (the finer the powder is the greater the light scattering), its refractive index with respect to the medium, and the shade of its colour.
The first pigments of history were inorganic, mainly of vegetable or mineral origin [2-4], among the latter include the so-called "earths" (so named for the origin resulting from the grinding of the rocks naturally present in certain territories from which the pigment often took the name). In general the chemical constituents of such pigments are oxides, carbonates, sulphides, sulphates, etc., of various metals, and have crystalline structure. Subsequently, over the centuries, especially in conjunction with the industrial revolution, a long series of organic and synthesis pigments were introduced, i.e. a base of carbon and hydrogen, made in order to continuously improve the colour palette available by the artist.

Currently, the synthesis pigments are the most used in painting, both because cheaper than natural ones, and because more stable to chemical and biological alterations.

Over the centuries, needs of economic as well as artistic nature have meant that the ancient artists were usually to realise their works not only using pure pigments, but also mixing them together in different proportions [5-6]. This greatly expanded the palette of colours available, and helped to create shades and special effects that can still admire today in many works. Being able to identify the individual components of these mixtures is important for further study about the painting techniques used by an artist or from the school to which he belonged, or to identify any false or same following retouches.

The positive results obtained in recent years in the identification of pigments on a variety of substrates by using a variety of non-invasive methodologies, such as X-ray fluorescence (XRF), Raman spectroscopy and Colorimetry, in this thesis we will try just to test the potential of these techniques in the analysis of painting mixtures, testing the ability of different instrumental apparatus to characterize the individual components.

1.1.1 Painting mixtures

As mentioned above, the ancient artists usually mixed different pigments in different proportions to obtain different hues and shades. Here are described two types of mixtures typically created by the ancient artists realized respectively mixing white in order to obtain different Tints (level of saturation) and mixing two different hues of the three primary colours, to obtain the secondary ones.

1.1.1.1 Mixtures with white

Before starting to talk about the mixtures realized with white pigments, here are described the terms used to define the colours.

Defining the colour are often used different terms such as *hue*, *tint*, *tone* and *shade* and each of these has a very specific meaning. For a painter, knowing the difference between them all is important when communicating concepts in your painting.

Hue is a term that seems more complicated than it is. A hue is just a colour. More specifically, a hue is any colour on the *colour wheel* (Fig. 1.1). There are three primary colours, red, blue and yellow; combining any two of those will give one of the secondary colours. A third set of colours, the tertiary colours, fills in the six gaps between the primary and secondary: colours– red-orange, blue-green, red-violet and so on.

Figure 1.1 – Basic colour wheel.

Colours on exact opposites of the colour wheel are known as *complementary colours*. Mixing a colour with its complement will give a muddy brown.

It is possible to notice that black and white are not colours on the colour wheel, and thus are not hues. So where do they fit in when it comes to mixing colours?

Tones, *Shades* and *Tints* are variations of the hues found on the basic colour wheel when white, black or both are mixed in, respectively.

Every individual colour on the basic colour wheel can be altered in three ways by Tinting, Shading or Toning. And that's before we even think about mixing two colours together.

Tones are created when both black and white (which is grey) are added to a hue. Any colour that is *"greyed down"* is considered a Tone. Depending on the proportions of black, white and the original hue used, tones can be darker or lighter than the original hue, and will also appear less saturated or intense than the original hue.

Shades are created when only black is added to a hue. This results in a rich, often more intense and darker colour. Because of the overpowering nature of many black pigments, adding black to a hue is a tricky and sometimes frustrating exercise when mixing paint. Many blacks will change the character of a hue even in small amounts, so they should be used sparingly. Alternatively, a hue can often be made darker by adding another dark hue rather than black.

Lightening the twelve basic colours to create *Tints*. Basically it is simply any colour with white added. This will lighten and desaturate the hue, making it less intense. That means that it is possible to go from

an extremely pale, nearly white to a barely tinted pure hue. Artists often add a tiny touch of white to a pure pigment to give the colour some body. So for example a bright Red can quickly become a bright Pink.

Is that kind of chromatic sensation that is considered in that work to obtain information about the amount of pigments used to create the mixtures?

1.1.1.2 Itten Theory

Before going into the description and implementation of the test object of analysis, are defined in the system what are the subtractive primary and secondary colours. To do this will be exploited to the Theory of Chromatic Circle (or Chromatic Wheel) by Johannes Itten in his book *Kunst der Farbe* [7].

Johannes Itten (Suedernlinden, 1888 - Zurich, 1967) was a painter, designer and Swiss writer who was part of the Bauhaus school, remembered as an artist and theorist of colour.

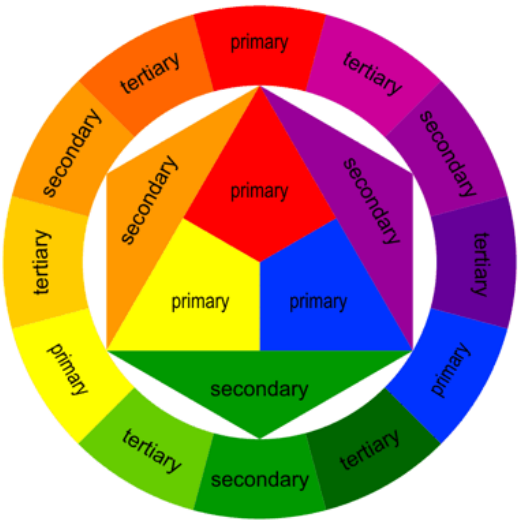

Figure 1.2 – Itten's colour wheel.

According to his theory, the colour wheel is used to determine, for each colour, which is the result of mixing with another colour, and find the complementary of each. All colours can be achieved by mixing the *three primary colours* yellow, red and blue, in different percentages and in addition they cannot be played from a mixture of others. Primary colours mixed in equal proportions; two by two we get the *secondary colours*: orange, green, purple. Then combining with a secondary one of the primary from which it is composed are obtained *tertiary*, etc. [8].

Twelve colours can be obtained so that, in the schematic called *"colour wheel"* proposed by J. Itten (Figure 1.2), occupy fixed positions and follow each other in the order of the spectrum.

Figure 1.2 represents the chromatic disc into twelve parts, in it the three primary colours are placed within an equilateral triangle in which the yellow is up, the blue at the left and the red at the right.
In the circle which is inscribed the triangle a hexagon is developed, obtaining other three triangles in which the compounds obtained by the union of the primary colours are placed, two by two, obtaining the following secondary colour:

YELLOW + RED = ORANGE

RED + BLUE = PURPLE

YELLOW + BLUE = GREEN

The ring created around the inscription circle of the triangle, is divided into twelve equal sectors, in which are placed the primary and secondary colours alternated (a sector every two) by tertiary.
The latter result from the combination of a primary with a secondary such as:

YELLOW + ORANGE = ORANGE-YELLOWISH

RED + ORANGE = ORANGE-REDDISH

RED + PURPLE = PURPLE-REDDISH

BLUE + PURPLE = PURPLE-BLUISH

GREEN + BLUE = BLUE-GREENISH

YELLOW + GREEN = GREEN - YELLOWISH

In this way are obtained 12 equal parts in which the colours follow one another like the spectrum. The colours are equidistant from each other and the opposites are complementary. Each of these colours and its complementary when mixed together give rise to a gray-black.
J.Itten states that: *"The complementary form a singular pair. As opposed, support one another, juxtaposed reach the highest degree of brightness, mixed vanish - like fire and water - in the gray"*.
From the physical point of view (additive synthesis) are called complementary two coloured lights whose mixture gives a white light. Once isolated a colour of the spectrum, the combination of the remaining provides the complementary. The sum of the residual colours is always complementary to the colour excluded from it.
The choice of historical pigments to analyze and characterize in this paper, was carried out according to the theory proposed by Itten and based on their historical authenticity used in the major works of art of history until the Modern age [8,9].

1.1.2 The technique

The pictorial samples analyzed in this work are mixtures of pigments spread on cardboard canvas using the technique of casein tempera [10].

In the modern age usage of term, tempera painting employs a medium that may be freely diluted with water but upon drying becomes sufficient insoluble to allow over painting with more tempera or with oil and varnish medium [11]. Tempera paintings are best executed on rigid panels coated with absorbent glue gesso. Tempera paintings are characterized by a brilliant, luminous crispness that is never exactly duplicated by the use of oil or other mediums. Although their materials are applied in many distinct variations of techniques, tempera paintings may usually be identified as such without much doubt.

The dried paint film does not become yellow or darken with age as faulty oil painting may do, because the medium itself in no yellowing compared with oil, and there is considerably less excess of binder in the finished painting. The bulk of the liquid (water) evaporates completely from the film. Many of the conditions that cause extensive cracking and other failures in oil painting are not present in tempera. Tempera mediums are not foolproof; if improperly formulated or applied, they may be subject to as many defects as oil mediums. As a general rule, the tempera techniques' are not well suited to casual or spontaneous styles and for the most part require serious consideration and a familiarity gained through intelligent understanding of their principles. Tempera paintings of extreme age are usually covered with a characteristic all over crackle of small size, which ordinarily has no effect on the adhesion of the paint.

Tempera vehicles owe their distinctive characteristics to the fact that they are emulsions. An emulsion is a stable mixture o fan aqueous liquid with an oily, fatty, waxy, or resinous substance. Tempera emulsions dry to form transparent films; their milky appearance when wet is caused by the refraction and dispersion of light from the countless tiny globules of oil.

The principal early types of tempera emulsion were: egg yolk, emulsions of egg and oil, gum tempera, wax emulsions and casein tempera.

1.1.3 The medium

Casein has been used since the earliest recorded beginnings of art [10]. Casein is a phosphoprotein contained in the milk of mammals, and in order to be used must be extracted from milk, washed, dried, and finally made to react with the alkali, with which it forms the so-called caseinates; among them the most common is the ammonium caseinate, used precisely as paint binder.

Fresh white curd, the casein of good skim milk, is a crumbly soft substance which, if ground on a plate with the addition of about one-fifth its volume of slave lime, becomes liquid. In that forms it can easily be emulsified, like egg, and it can then be thinned with water.
The casein should be prepared fresh each day, which can be done in two or three minutes. Casein must be diluted very strongly with about three to five parts of water or even more; it sets quickly and well and becomes exceedingly hard an luminous.
For easel painting one had better use technically pure casein, insoluble in water but soluble in ammonia. This casein is a coarse powder made of artificially dried and ground curd. The powder should be fresh and dry and must not smell as if putrefied; otherwise the emulsion will spoil quickly.
The casein solution looks turbid and white like paste. Under no circumstances must casein be allowed to boil. If the water used is very hard, white sediment forms at the bottom, carbonate of lime, which is harmless and removable. The ammonium carbonate should be very fresh, and, if so, will show a high degree of effervescence.
Ammonia casein is easily kept undiluted in a clean, well-corked bottle. Water may be added immediately before use. The adhesive power here also is very great, although note equal to that of lime casein. It very quickly becomes insoluble in water, so that a tempering with formalin, as with albuminous bodies such as glue, is unnecessary.
Casein tempera has enormous adhesive power, and many painters for this reason prefer it to egg emulsion.

1.2 Diagnostic methods

Until a few decades ago, the study of works of art was done essentially through the historical-artistic approaches, i.e., through the help of historical, bibliographic and archive researches.
They, however useful to clarify the historical context in which the cultural object has been achieved, do not provide useful and accurate information for the knowledge of object's material, its state of degradation and the causes which produced it, that are all essential information to get a proper knowledge of the work [12].
For that reason now is considered indispensable combine with the historical-artistic analysis on Cultural Heritage also the use of scientific methods, which can provide a complete knowledge about materials and techniques used in a particular territory and in certain periods of time (characterization), this in turn

allows to date the artefact (dating) and to ascertain possible counterfeits in case of anachronisms in material or type (authentication).

All this information are of fundamental importance because they represent a preliminary study to subsequent conservation and, if necessary, restoration projects of work of art itself; restoration that must be as compatible and coherent as possible with the original materials.

In the context of scientific methods particularly important have the spectroscopic techniques, namely those regarding the effects light-matter interaction. In this thesis particular attention will deal to X-ray fluorescence (XRF), Raman spectroscopy and Spectrophotometric analysis for the elemental, compositional and colorimetric characterization of the object understudy, respectively.

1.2.1 The effectiveness of the diagnostic methods

The diagnostic techniques applied to Cultural Heritage are usually divided into two major types [9]:

- invasive methods, which require the sampling of a sample, i.e. the removal of minimum quantities of material of the artwork, to be analyzed;
- non-invasive methods, which do not consider the sampling and can thus be performed directly on artwork (*in situ*), interacting with the surfaces through various forms of light-matter interactions.

Which in turn, invasive diagnostic methods can be divided into destructive, if they involve the physical destruction or modification of the sample, and not destructive, if they allow the study of the nature and structure of the sample without this being altered or modified.

When solution of a specific problem, that needs to be investigated, raises the possibility of choosing between the various techniques of investigation, the current trend is to give as much space as possible to the non-invasive techniques.

However, it should point out that among the techniques that require sampling are used only those those are subject to certain conditions:

- sampling should not in any way cause damage the work of art, and consequently the sample taken must be as small as possible;
- the microscopic sample must be representative of the whole material analyzed, so they are not taken into account samples of uncertain origin.

Further criteria that are taken into consideration using a particular diagnostic technique are:

- high specificity;

- high spatial resolution;
- immunity to interference.

Based on the above criteria, are listed in table 1.1 the main analysis techniques with their advantages and disadvantages.

Technique	Information	Specificity	Spatial resolution	Immunity to interference
SEM	Poor, elemental	Good	Excellent	Good
XRF	Good, elemental	Excellent	Good	Good
XRD	Good, elemental	Discrete	Poor	Poor
PIXE/PIGE	Good, elemental	Good	Poor	Good
Raman	Excellent, molecular	Excellent	Excellent	Good
IR	Good, molecular	Good	Discrete	Poor
UV/Vis	Poor, molecular	Good	Discrete	Discrete
Optical Microscopy	Poor, elemental and molecular	Good	Good	Good
Colorimetry	Excellent, optical	Good	Good	Excellent

Table 1.1 - Advantages and disadvantages of the main techniques available for the analysis of work of art.

As we see in the table, there is no a perfect technique under all points of view. For example, although the infrared spectroscopy has a high specificity, it has a poor spatial resolution and a high level of interference. Spectroscopy UV/visible instead has a discrete spatial resolution but the spectra in general consist of a few wide bands that do not lend themselves to an unambiguous identification. However of all the methods listed, there are some that have the best features for the study of works of art, and these are: XRF, Raman spectroscopy and Colorimetry. In fact, they have high specificity, high sensitivity, high spatial resolution and are non-destructive (both applied in situ and in laboratory). The techniques provides information on elemental composition and degradation materials for XRF, on the molecular composition, the bonds, the chemical environment, the phases and the crystal structure of the sample examined for Raman spectroscopy and on surface reflectance, colour and chromatic variation for Colorimetry. Therefore are all suitable for characterization studies of pigments and dyes on extensive media [13-22].

Due to their characteristics, these techniques are used successfully to provenance studies, authentication [23] and identification of the degradation products of numerous materials.

It is possible therefore to conclude that, among elemental, molecular and optical techniques currently available for analysis on Cultural Heritage, XRF, Raman spectroscopy and Spectrophotometry are the most powerful and reliable for in situ characterizations.

1.2.2 Integration of diagnostic methodologies for Cultural Heritage

There are so many techniques that allow to obtain useful data for the study of work of art, in particular in our case for a painting, and the choice of a particular methodology is motivated by the issue concerning the object under consideration and in particular the question that is necessary to solve. In any case, any diagnostic program relating to a painting, or in general, to polychrome art-work, isn't solvable without an accurate characterization of the pigments used for the drafts; so the pigments become the absolute protagonists of the integrated multiple methodologies applications. Through the identification of pigments used is possible, for example, to date a painting in an indirect way, to formulate hypotheses about the author for artworks not attributed as well as to guide interventions for cleaning and restoration or conservation programs. Is difficult to achieve these objectives through a methodology that involves a single technique but, in most cases, is the integrated application of multiple techniques that allow to obtain results that enable to find the answers.

From this point of view is set the aim of the research presented in this occasion that involved the characterization of historical pigments, pure and mixed, selected by a wide chrometeca and analyzed by various analytical techniques such as X-Ray Fluorescence (XRF), Raman Spectroscopy and Colorimetry.

The results obtained are discussed in order to highlight the strengths and limitations of each techniques used for the characterization of pigments used for a polychrome surface, and also for the evaluation of quantitative information on binary mixtures realized to have information on the amount (%) of each pigment that compose the mixtures.

The information and the limits of each integrated methodologies used in that research activity are reported and discussed in the next section.

1.3 State of art

The characterization of the materials constituting a work of art is the main issue for obtaining fundamental information necessary to plan an appropriate conservation procedure in the field of Cultural Heritage (CH). The knowledge of the chemical composition of the works of art indeed offers an insight on the realization techniques used by the artists, on the presence of forgeries and retouches,

on the degradation processes affecting the CH and on the compatibility of the materials to be used for the conservation. In this context, the identification and chemical characterization of pigments also play a relevant role, in order to answer technical and historical questions and to track the original appearance of the works of art [24].

The pigments have always been part of the colour palette of the artists, thanks to their high colouring power, availability, stability and persistence over time [25]. The different historical epochs have seen the introduction of new pigments either in their pure form or in special mixtures so expanding the palette of the available colours. The study of the pigment features has been topic of many papers focused on pigment identification, characterization and dating [26-28].

Nevertheless, if the qualitative analysis is now widely established and widespread, there are still open questions concerning the quantitative analysis especially when complex matrices are investigated. This is the case of pictorial mixtures, where the pigments can be inhomogeneously distributed and mixed with variable concentrations. Due to different nature of materials and also of different degradation process, during the years was born the necessity to use the qualitative and quantitative information obtained by characterization techniques for plan correct restoration and conservation programmes of polychrome surfaces.

The knowledge of the exact amount of different constituents of the paint and the technique used is important for a careful program of conservation of polychrome works. Moreover, the identification and chemical characterisation of pigments is useful to acquire or deepen information about the artist; this information can also be useful for authentication purposes because of the availability of these pigments has been changing through the centuries and so the identification of one pigment respect to another one can be used as a *terminus post quem* or *ante quem* the artwork was realized.

Starting from that point of view, XRF, Raman, and colorimetric measurements were carried out to characterize the pigments used to prepare binary mixtures.

In particular, chemical characterization by X-ray fluorescence (XRF) technique has been very important in the study of works of art, such as icons, frescoes, sculptures, ceramics, murals, porcelain, paper and other materials [29]. The need for reliable chemical and physical techniques allowing non-destructive and *in situ* investigations is increasing [30-32]. These features are guaranteed by the portable XRF spectrometers, widely used in the CH field [33-39].

When XRF is applied for the characterization of pictorial mixtures, some problems can be occur; in these samples, the absorption of X-rays through different constituent elements will result in a modification of the detected intensity due to the mixture density, and to the shielding effect due to the heavier component. In the last year, few works are be devote to the study of this kind of effect to obtain

quantitative analysis from XRF spectra of pigment mixture [40], obtaining good results, but a problem remains: the proper characterization of the samples analyzed.

To overcome this problem, the uses of spectroscopic techniques that provide complementary information allow characterizing unequivocally the samples analyzed.

Raman spectroscopy is one of the most useful methodologies used for this purpose, thanks to its main property to characterize the chemical composition of artworks. Many scientific works confirmed the validity of its use as *in situ* non invasive methodology: ceramics [41, 42], gems and precious stones [43], metals [44], manuscript [45], a frescos [46], mural paintings [47, 48]. However, its use is limited to qualitative information, for the identification of the pigments used, and gives no information on the colorimetric characteristics and chromatic variation caused by degradation effects of material, important for the proper monitoring of the conservation status. In fact, the medium used to realize the painting layer, generally organic, causes a very high fluorescence that can cover the weak Raman signal from the pigment not allowing to recognize the material fingerprint and also making uncertain a quantitative analysis.

So in contact spectrophotometric analysis (Colorimetry), made with portable spectrophotometers, are coupled with elemental and composition characterization, in order to quantify chromatic variations and put them in relation with the possible environmental causes that have determined, and non-invasive techniques providing high repeatability of measurement over time. This technique is widely used for restoration and conservation programs to obtain chromatic information on the palette used by the artist [49-52] and, in some cases, to recognize the pigments on the basis of first derivative curve of Spectral Reflectance Factor (SRF%) [53-55].

The aim of this work, after a complete characterization of pure pigments selected by means of XRF, Raman and Spectrophotometric analysis, is to obtain quantitative information on the specimens of painting layer realized, in order to track the quantity of each pigments used to prepare the laboratory mixtures, and to extract calibration curves to the aim of evaluating the pigment concentration in unknown mixtures.

Bibliography

[1] Matteini, M., Moles, A. "La Chimica nel Restauro. I Materiali dell'Arte Pittorica", Nardini ed. (2004).

[2] Feller, R.L. "Artists Pigments: a Handbook of their History and Characteristics" Vol. 1, National Gallery of Art, Washington, D.C. (1986).

[3] Roy, A. "Artists Pigments: a Handbook of their History and Characteristics" Vol. 2, National Gallery of Art, Washington, D.C. (1993).

[4] West Fitzhugh, E. "Artists Pigments: a Handbook of their History and Characteristics" Vol. 3, National Gallery of Art, Washington, D.C. (1997).

[5] Cennini, C. "Il Libro dell'Arte o Trattato della Pittura", Le Monnier (1859).

[6] Vasari, G. "Le Vite de' più eccellenti pittori, scultori e architetti", Ed. Giuntina e Torrentiniana (1568).

[7] Itten J., 2007, *L'arte del colore*, Ed. Il Saggiatore, (pp. 159).

[8] Küppers H., 2005, *Il grande atlante dei colori*, Ed. DuMont, (pp. 165).

[9] Raffrenato F., "*Potenzialità della Spettroscopia Raman per la caratterizzazione delle miscela pittoriche"*, graduation thesis Master degree on Science and Technologies applied on Conservation and Restoratio of Cultural Heritage*, Università degli Studi di Catania*, A.A. 2007/2008.

[10] Doerner, M. "The materials of the artist and their use in painting", ISBN 0-15-657716-X.

[11] Mayer, R. "The Artist's Handbook of materials and techniques", Viking, NYC (USA), 1991, ISBN 0-670- 83701-6.

[12] Cavallaro, A. *"La Spettroscopia Raman nella Caratterizzazione dei Pigmenti Pittorici e delle Ceramiche"*, Graduation thesys (2004).

[13] Rosi, F., Miliani, C., Borgia, I., Brunetti, B., Sgamellotti, A. "Identification of Nineteenth Century Blue and Green pigments by In Situ X-Ray Fluorescence and Micro-Raman Spectroscopy", J. Raman Spectrosc. 35 (2004), 610-615.

[14] Ricci, C., Borgia, I., Brunetti, B.G., Miliani, C., Sgamellotti, A., Seccaroni, C., Passalacqua, P. "The Perugino's Palette: Integration of an Extended In Situ XRF Study by Raman Spectroscopy", J. Raman Spectrosc. 35 (2004), 616-621.

[15] Mazzeo, R., Baraldi, P., Lujàn, R., Fagnano, C., "Characterization of Mural Painting Pigments from the Thubchen Lakhang Temple in Lo Manthang, Nepal", J. Raman Spectrosc. 35 (2004), 678-685.

[16] Bersani, D., Lottici, P.P., Antonioli, G., Campani, E., Casoli, A., Violante, C. "Pigments and Binders in the Wall Paintings of Santa Mari a della Steccata in Parma (Italy): the Ultimate Technique of Parmigianino", J. Raman Spectrosc. 35 (2004), 694-703.

[17] Ambers, J. "Raman Analysis of Pigments from the Egyptian Old Kingdom", J. Raman Spectrosc. 35 (2004), 768-773.

[18] Centeno, S.A., Mahon, D., Wypyski, M.T. "Examination of a Spanish Medieval Processional Crucifix Substantially Reworked in the 20th Century", J. Raman Spectrosc. 35 (2004), 774-780.

[19] Hayez, V., Denoël, S., Genadry, Z., Gilbert, B. "Identification of Pigments on a 16 th Century Persian Manuscript by Micro-Raman Spectroscopy", J. Raman Spectrosc. 35 (2004), 781-785.

[20] Edwards, H.G.M., Jorge Villar, S.E., Eremin, K.A. "Raman Spectroscopic Analysis of Pigments from Dynastic Egyptian Funerary Artefacts", J. Raman Spectrosc. 35 (2004), 786-795.

[21] Clark, R.H.J. "Raman Microscopy in the Identification of Pigments on Manuscripts and Other Artwork". Scientific Examination of Art: Modern Techniques in Conservation and Analysis (2005), 162-185.

[22] Clark, R.H.J., Gibbs, P.J. "Raman Microscopy of a 13th-Century Illuminated Text", Analytical Chemistry News & Features (1998), 99-104.

[23] Reiche, I., Pages-Camagna, S., Lambacher, L. "In Situ Raman Spectroscopic Investigation of the Adorning Gemstones on the Reliquary Heinrich's Cross from the Treasury of Basel Cathedral", J. Raman Spectrosc. 35 (2004), 719-725.

[24] Lewis, P.A. "Colorants: organic and inorganic pigments, in Azimuth, in: K. Nassau (Ed.), in: Color for Science, Art and technology, 1", Elsevier, Amsterdam, 1998,pp. 283–312.

[25] Klockenkämper, R., von Bohlen, A., Moens, L. "Analysis of pigments and inks on oil paintings and historical manuscripts using total reflection X-ray fluorescence spectrometry", X-Ray Spectrom 29 (2000) 119–129.

[26] Bruni, S., Cariati, F., Casadio, F., Toniolo, L. "Spectrochimical characterization by micro–FTIR spectroscopy of blue pigments in different polychrome works of art", Vibr. Spectro. 20 (1999) 1525.

[27] Clark, R.J.H. "Pigment identification by spectroscopic means: an art/science interface", C. R. Chem. 5 (2002) 7–20.

[28] Sawczak, M., Kaminska, A., Rabczuk, G., Ferretti, M., Jendrzejewski, R., Sliwinski, G. "Complementary use of the Raman and XRF techniques for non-destructive analysis of historical paint layers", Appl. Surf. Sci. 255 (2009) 5542–5545.

[29] Trentelman, K., Bouchard, M., Ganio, M., Namowicz, C., Schmidt Patterson, C., Walton, M. "The examination of works of art using in situ XRF line and area scans", X-Ray Spectrom. 39 (2010) 159–166.

[30] Alberghina, M.F., Barraco, R., Brai, M., Casaletto, M.P., Ingo, G.M., Marrale, M., Policarpo, D., Schillaci, T., Tranchina, L. "Degradation study of XVIII century graffiti on the walls of Chiaramonte Palace (Palermo, Italy)", Appl. Phys. A 100 (2010) 953–963.

[31] Brai, M., Casaletto, M.P., Gennaro, G., Marrale, M., Schillaci, T., Tranchina, L. "Degradation of stone materials in the archaeological context of the Greek–Roman Theatre in Taormina (Sicily, Italy)", Appl. Phys. A 100 (2010) 945–951.

[32] Vandenabeele, P., Garcia-Moreno, R., Mathis, F., Leterme, K., Van Eslande, E., Hocquet, F.P., Rakkaa, S., Laboury, D., Moens, L., Strivay, D., Hartwing, M. "Multidisciplinary investigation of the tomb of Menna (TT69), Theban Necropolis, Egypt", Spectrochim. Acta Part A 73 (2009) 546–552.

[33] Glinsman, L.D. "The practical application of air-path X-ray fluorescence spectrometry in the analysis of museum objects", Rev. Conserv. 6 (2005) 3–17.

[34] Colombo, C., Bracci, S., Conti, C., Greco, M., Realini, M. "Non-invasive approach in the study of polychrome terracotta sculptures: employment of the portable XRF to investigate complex stratigraphy", X-Ray Spectrom. 40 (2011) 273–279.

[35] Kriznar, A., Munoz, V., de la Paz, F., Respaldiza, M.A., Vega, M. "Portable XRF study of pigments applied in Juan Hispalense's 15th century panel painting", X-Ray Spectrom. 40 (2011) 96–100.

[36] Pessanha, S., Guilherme, A., Carvalho, M.L. "Comparison of matrix effects on portable and stationary XRF spectrometers for cultural heritage samples", Appl. Phys. A 97 (2009) 497–505.

[37] Ruvalcaba Sil, J.L., Ramírez Miranda, D., Aguilar Melo, V., Picazo, F. "SANDRA: a portable XRF system for the study of Mexican cultural heritage", X-Ray Spectrom. 39 (2010) 338–345.

[38] Migliori, A., Bonanni, P., Carraresi, L., Grassi, N., Mandò, P.A. "A novel portable XRF spectrometer with range of detection extended to low-Z elements", X-Ray Spectrom. 40 (2011) 107–112.

[39] Alberghina, M.F., Barraco, R., Brai, M., Schillaci, T., Tranchina, L. "Comparison of LIBS and XRF measurements on bronze alloys for monitoring plasma effects", Spectrochim. Acta B 66 (2011) 129–137.

[40] Fontana, D., Alberghina, M.F., Barraco, R., Basile, S., Tranchina, L., Brai, M., Gueli, A., Troja S. O. "Historical pigments characterisation by quantitative X-ray fluorescence", Journal of Cultural Heritage (2013), http://dx.doi.org/10.1016/j.culher.2013.07.001.

[41] Ayora-Canada, M.J., Domínguez-Arranz A., Dominguez-Vidal, A. "Raman Microspectroscopic study of Iberian pottery from the La Vispesa archaeological site", Spain. J. Raman Spectrosc.43 (2012) 317–322.

[42] Ying San Liou, Yi Chang Liu and Hsing Yi Huang, "Micro-Raman spectroscopic study of cord-marked pottery decorated with red coatings from Taiwan, ca 2600–1700 B.C.", J. Raman Spectrosc. 42 (2011) 1062–1068.

[43] Reiche, I., Pages-Camagna S., Lambacher, L. "In situ Raman spectroscopic investigations of the adorning gemstones on the reliquary Heinrich's Cross from the treasury of Basel Cathedral", J. Raman Spectrosc. 35 (2004) 719–725.

[44] Bertolotti, G., Bersani, D., Lottici, P.P., Alesiani, M., Malcherek, T., Schluter, J. "Micro-Raman study of copper hydroxychlorides and other corrosion products of bronze samples mimicking archaeological coins", Anal Bioanal Chem 402 (2012) 1451–1457.

[45] Muralha, V.S.F., Burgio, L., Clark, R.J.H. "Raman spectroscopy analysis of pigments on 16–17th c. Persian manuscripts", Spectrochimica Acta Part A 92 (2012) 21– 28.

[46] Castriota, M., Meduri, E., Barone, T., De Santo G., Cazzanelli, E. "Micro-Raman investigations on the fresco 'Trapasso della Vergine' in the Church of S. Giovanni Battista of Paterno Calabro in southern Italy", J. Raman Spectrosc. 39 (2008) 284–288.

[47] Clark, R.J.H., Hark, R.R., Salvadò, N., Butí, S., Pradell, T. "Spectroscopy study of mural paintings from the Pyrenean Church of Saint Eulàlia of Unha", J. Raman Spectrosc. 41 (2010) 1128–1134.

[48] Apollonia, L., Vaudan, D., Chatel, V., Aceto, M., Mirti, P. "Combined use of FORS, XRF and Raman spectroscopy in the study of mural paintings in the Aosta Valley (Italy)", Anal Bioanal Chem 395 (2009) 2005–2013.

[49] Hahn, O., Oltrogge, D., Bevers, H. "Coloured Prints Of The 16th Century: Non-Destructive Analyses On Coloured Engravings From Albrecht Dürer And Contemporary Artists", Archaeometry 46, 2 (2004) 273–282.

[50] Berns, R.S., Byrns, S., Casadio, F., Fiedler, I., Gallagher, C., Imai, F.H., Newman, A., Taplin, L.A. "Rejuvenating the color palette of Georges Seurat's *A Sunday on La Grande Jatte - 1884*: a simulation", COLOR research and application, Volume 31, Number 4, August 2006, 279-293.

[51] Acquaviva, S., D'Anna, E., De Giorgi, M.L., Della Patria, A., Pezzati, L. "Optical characterization of pigments by reflectance spectroscopy in support of UV laser cleaning treatments", Appl. Phys. A 92, (2008) 223–227.

[52] Gil, M., Green, R., Carvalho, M.L., Seruya, A., Queralt, I., Candeias, A.E., Mirão, J. "Rediscovering the palette of Alentejo (Southern Portugal) earth pigments: provenance establishment and characterization by LA-ICP-MS and spectra-colorimetric analysis", Appl Phys A (2009) 96: 997–1007.

[53] Bacci, M., Casini, A., Cucci, C., Picollo, M., Radicati, B., Vervat, M. "Non-invasive spectroscopic measurements on the Il ritratto della figliastra by Giovanni Fattori: identification of pigments and colourimetric analysis", Journal of Cultural Heritage 4 (2003) 329–336.

[54] Fernandez Rodriguez, J.M., Fernandez Fernandez, J.A. "Application of the Second Derivative of the Kubelka–Munk Function to the Semiquantitative Analysis of Roman Paintings", COLOR research and application, Volume 30, Number 6, December 2005, 448-456.

[55] Dupuis, G., Menu, M. "Quantitative characterisation of pigment mixtures used in art by fibre-optics diffuse-reflectance spectroscopy", Appl. Phys. A 83 (2006) 469–474.

Chapter 2
X-ray fluorescence analysis

This chapter is devoted to the X-Ray Fluorescence (XRF), non-invasive technique particularly used in the Cultural Heritage field.
This technique, through the study of the X fluorescence radiation, allows to determine the major and trace elements constituents the sample. Such radiation is emitted by the atoms after excitation generated by irradiating the sample with X-rays or high-energy gamma
This investigation methodology is widely used in analytical chemistry, biology, medicine, physics, metallurgy and, especially in recent decades, it is widely used in the study of cultural heritage through the development of portable systems for *in situ* investigations.
Here a historical overview and a part concerning the physical phenomena involved in the generation, transmission and detection of X-rays within the matter are exposed. Particular attention is also paid to the description of the instrumental apparatus used for XRF analyses, portable ED-XRF spectrometer available at *Laboratorio di Tecniche Fisiche per lo Studio e la Caratterizzazione dei Beni Culturali – UniNetLab – Dipartimento di Fisica e Chimica – Università degli studi di Palermo.*

2.1 X-ray fluorescence: historical overview

The history of X-ray fluorescence dates back to the accidental discovery of X-rays by the German physicist Wilhelm Conrad Roentgen [1]. He discovered X-rays[1] on November 8, 1895 at the Physics Institute of Julius-Maximilian's University of Würzburg, Germany. While studying cathode rays using a low pressure gas-filled discharge tube, a so called Hittorf-Crookes tube. Near the tube he noticed a weak visible photoluminescence which was emitted by a Barium Platinum-Cyanide fluorescent screen whenever the cathode-ray tube was turned on. Röntgen recognized that this visible fluorescence was

[1] X-rays can be classified as short wavelength electromagnetic radiation, generated in nature by slowing electrons in the outer field of an atomic nucleus or by changing the bound states of electrons involving transitions between the inner electronic shells of an atom. Generally the wavelength of this type of electromagnetic radiation is lower than 10 nm. In case of XRF analysis, typically radiation is used with an energy between 1 keV and 100 keV which corresponds to a wavelength of approximately 1 nm down to 0:01 nm.

caused by "*eine neue Art von Strahlen*" originating from the Hittorf-Crookes tube. Due to its unknown character, he called the radiation X-rays [2].

Shortly after the discovery it became clear that X-rays could be used to look into the structure of a living human body and the interior of optically non-transparent materials. In 1901 Wilhelm C. Röntgen received the first Nobel Prize in physics for his work.

The discovery of X-rays led to some other important breakthroughs. Barkla studied the nature of X-rays with respect to the atomic structure by observing the secondary X-rays radiated from the target sample. During his experiments he discovered the polarization of X-rays (1906), the gaps in atomic absorption (1909), and the distinction between continuous and characteristic X-rays, consisting of several series of X-rays referred to as K, L, and M ...series (1911). Building on Barkla's work, von Laue investigated the wave properties of X-rays. He demonstrated X-ray diffraction from a single crystal, which was composed of a 3D-structure with a regularly repeating pattern (1912). Attracted by the experiments of von Laue, Bragg observed X-ray diffraction patterns from single crystals of NaCl and KCl to be the regular patterns of an isometric system showing differences in the X-ray intensity when comparing Sodium and Potassium. The experiments of von Laue and Bragg formed the starting point of crystal structure analysis using X-rays.

In 1913, H.G.J. Mosley made possible the X-rays use in the analytical chemistry, by showing the relationship between atomic number (Z) and the reciprocal of the wavelength ($1/\lambda$) for each spectral series of emission lines for each element. So Mosley constructed the early X-ray spectrometer with a cold cathode tube where the air within the tube provided the electrons and the analyte which served as the tube target. Unfortunately, in his instrumental apparatus nearly 99% of the energy was lost as heat due to the use of electron for creating X-rays. In the same year, the Bragg brothers built their first x-ray analytical device based around a pinhole and slit collimator. Like Mosley's instrument, the Braggs ran into difficulty in maintaining efficiency [3, 4].

The intuition of replacing electrons with x-ray photons to excite secondary x-ray radiation resulting in the generation of x-ray spectra was of Coster and Nishina (1925).

Within a decade, XRF became an important method of analysis for elements with atomic numbers greater than twenty-two. Although the earliest commercial XRF devices used simple air path conditions, machines were soon developed utilizing helium or vacuum paths, permitting the detection of lighter elements.

From 1960's several improvements were made on XRF devices such as:

- chromium or rhodium target x-ray tubes to excite longer wavelengths. This development was quickly followed by that of multichannel spectrometers for the simultaneous measurement of many elements.
- lithium drifted silicon detector (Si(Li)) was created, providing very high resolution and X-ray photon separation without the use of an analyzing crystal.
- a new procedure known as total reflection x-ray fluorescence (TRXRF) was developed by Schwenke, where a Si(Li) detector is positioned almost on top of a thin film of sample. The primary radiation enters the sample at an angle that is only slightly smaller than the critical angle for reflection. This significantly lowers the background scattering and fluorescence, permitting the detection of concentrations of only a few tenths of a ppb and for that reason it is used extensively for trace analysis.

2.2 X-ray production

The most widespread apparatus for producing X rays consists in a vacuum tube called Coolidge tube. Containing two electrodes: one heated emits electrons (cathode), and an anode, supporting a piece of metal called target. When a high voltage is applied across the two electrodes, the electrons stream toward the target (usually made of metal with high meting point) and strike it at high speed, producing X rays. When the electrons strike the target, X rays are produced by two processes:

- one process takes place when the electrons are slowed down and deflected by the atoms of the target; the kinetic energy of the electrons is converted directly into X-ray radiation, called *bremsstrahlung*. The higher the voltage of the tube, the greater the kinetic energy of the electrons that strike the target, and the shorter the minimum wavelength of the X rays that can be produced.
- The other process involves the electrons of the target's atoms. In a schematic vision, the electrons can be considered arranged around the nucleus of the atom in a number of shells one within the other. When a high-speed electron from the cathode strikes an atom of the target, it sometimes ejects an electron from one of the inner shells. That one is immediately replaced by an electron from an outer (higher-energy) shell. The energy lost by the "electronic rearrangement" is given off as an X ray.

2.2.1 Characteristic X-Rays

As said before, when an atom is disrupted from its normal configuration by some excitation process, it may exist in an excited state only for time of nanosecond order, because it tend to return to its lower energetically configuration [5].

The energy emitted in the transition from the excited to the ground state takes the form of a *characteristic X-ray photon* (Fig 2.1) whose energy is given by the energy difference between the initial and final states:

- if the vacancy is created in the K shell of an atom, then a characteristic K X-ray is liberated when that vacancy is subsequently filled.
- Differences between a and b lines are related to the shell involved: transition L-K shells create Ka lines; transition M-K shells create Kb line.
- Vacancies created in outer shells by the filling of a K shell vacancy are subsequently filled with the emission of L-, M-, series characteristic X-rays.

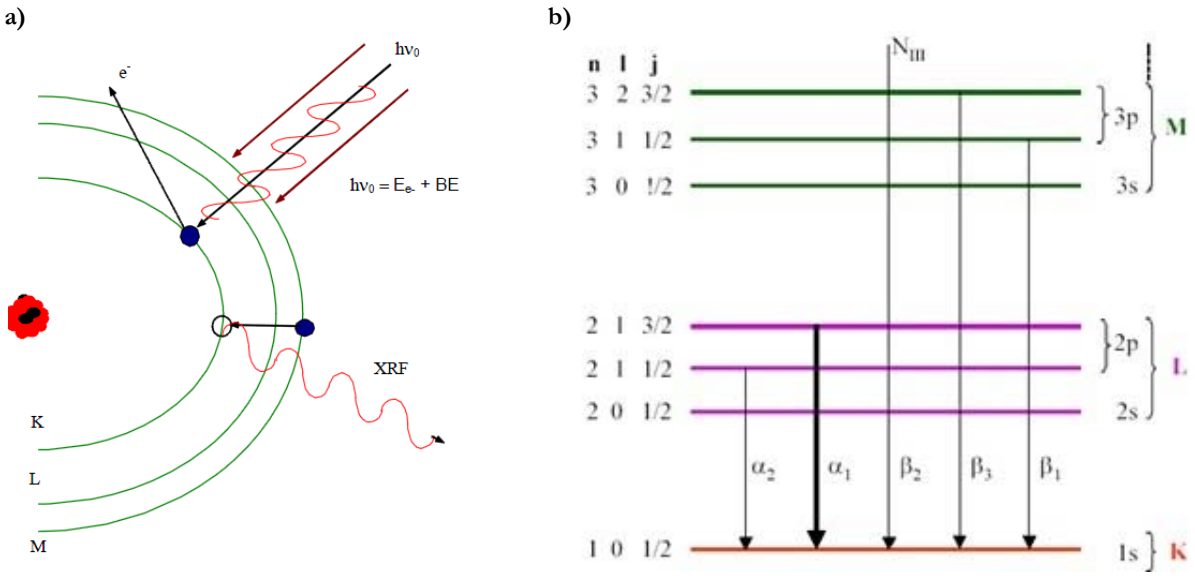

Figure 2.1 - (a) Schema of x-ray fluorescence physical process, and **(b)** transition between electronic levels related to the XRF process, permitted by selection rules.

Because their energy is greatest, the K-series X-rays are generally of most practical significance. Their energy increases regularly with atomic number of the element and is, for example, about 1 keV for sodium with Z = 11, 10 keV for gallium with Z = 31, and 100 keV for radium with Z = 88. Because the energy of the characteristic X-ray is unique to each individual element, they are often used in the elemental analysis of unknown samples. A large number of different physical processes can lead to the population of excited atomic states from which characteristic X-rays originate. In general, the relative

yields of the K, L, and subsequent series will depend on the excitation method, but the energy of the characteristic photons is fixed by the basic atomic binding energies.

2.2.2 Bremsstrahlung

As said before, when an energetic electron beam is deflected by the atoms of a (high Z) material, X-rays in a broad wavelength band are emitted. This radiation is called *Bremsstrahlung* as it is released during the sudden deceleration of the primary electrons, as a result of their interaction with the electrons of the lattice atoms in the target [6]. At each collision, the electrons are decelerated and part of the kinetic energy lost is emitted as X-ray photons and also characteristic X-ray lines of the target materials are produced. The continuum is characterized by a minimal wavelength given by eq. (2.1)

$$\lambda_{\mathrm{min}}\ (\mathrm{nm}) \ = \ 1.24/\mathrm{E}_{\mathrm{max}}\ (\mathrm{keV}) \ = \ 1.24/V\ (\mathrm{kV}) \tag{2.1}$$

where $\mathrm{E}_{\mathrm{max}}$ is the maximum energy of the electrons and V the potential used to accelerate them. In Fig. 2.2 are shown *bremsstrahlung* spectra emitted by X-ray tubes operated at different accelerating potentials.

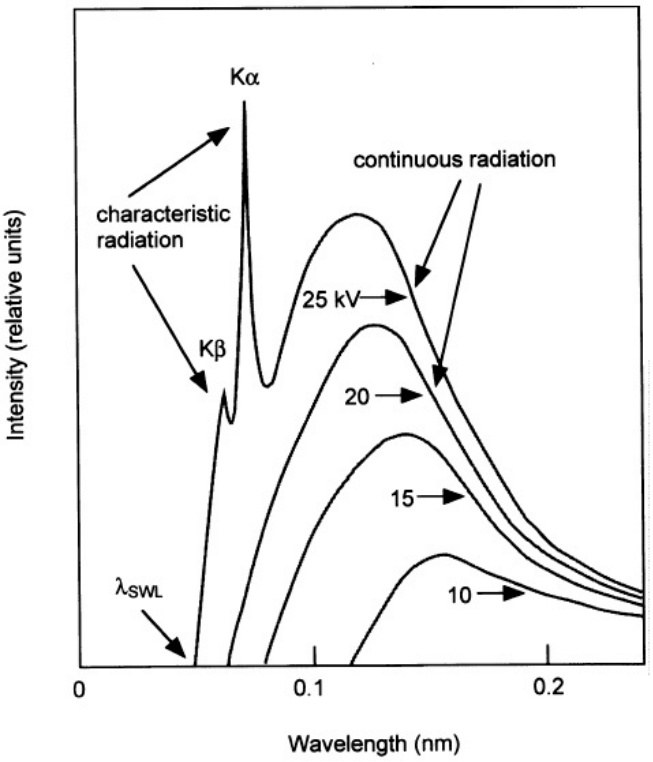

Figure 2.2 - Excitation spectra emitted by a Mo X-ray tube operated at various accelerating voltages. The excitation spectrum consists of a *bremsstrahlung* continuum upon which the characteristic lines of the anode material are superimposed (http://www.stanford.edu/group/glam/xlab/MatSci162_172/LectureNotes/01_Properties%20&%20Safety.pdf).

2.3 Interaction of X-rays with matter

The energies of X-ray photons are of the same order of magnitude as the binding levels of inner- shell electrons (K, L, and M … levels) and therefore can be used to excite and/or probe these atomic levels. The wavelength λ of an X-ray photon is inversely related to its energy E according to eq. (2.1), where 1 eV is the kinetic energy of an electron that has been accelerated over a voltage difference of 1 V ($1eV = 1.602 \cdot 10^{-19} J$). When X-ray beam passes through matter, some photons will be absorbed inside the material or scattered away from the original path, as illustrated in Fig. 3.3. The intensity I_0 of an X-ray beam passing through a layer of thickness d and density ρ is reduced to intensity I according to the Lambert-Beer law:

$$I = I_0 e^{-\mu\rho d} \tag{2.2}$$

The intensity of photons beam is reduced but their energy is generally unchanged. The term μ is called the *mass absorption coefficient* and has the dimension cm^2/g. The product $\mu_L = \mu_\rho$ is called the *linear absorption coefficient* and is expressed in cm^{-1}. $\mu(E)$ is sometimes also called the total cross-section for X-ray absorption at energy E.

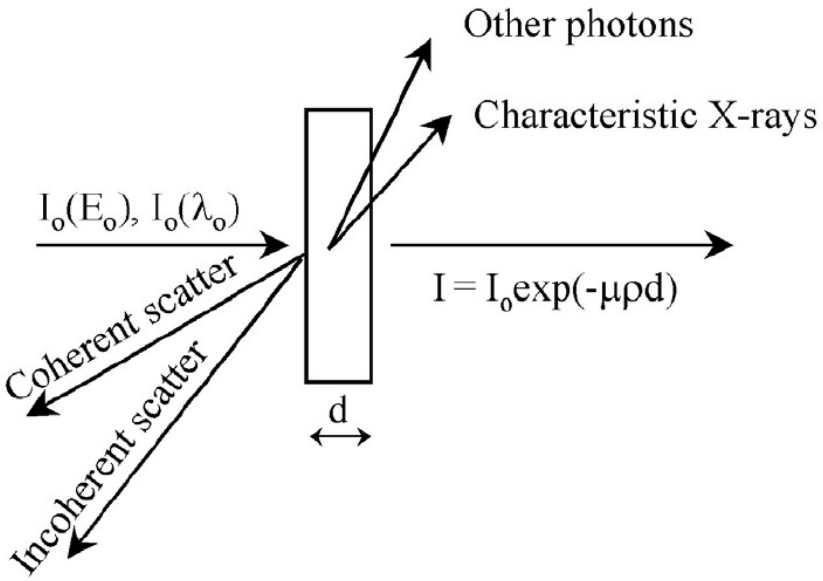

Figure 2.3 - Interaction of X-ray photons with matter [6].

For a pure material, the mass absorption coefficient is directly related to the total atomic absorption cross section σ_α (cm^2/atom) by the following equation:

$$\mu = \frac{N_A}{A}\sigma_\alpha \tag{2.3}$$

where N_A is Avogadro's number and A is the atomic weight. For a compound material, the absorption coefficient is obtained from the sum of the absorption cross section of the constituent atoms by:

$$\mu = \frac{N_A}{MW}\sum_i x_i\,\sigma_{ai} \tag{2.4}$$

Where the molecular weight of a compound containing x_i atoms of type i is given by $MW = \sum_i x_i A_i$. Fig. 2.4 shows a plot of the energy dependence of the mass absorption coefficient of several chemical elements in the X-ray energy range between 10-30,000 eV. The absorption edge discontinuities are clearly visible. A given material will attenuate high energy (i.e. hard) X-rays less than low energy (soft) X-rays.

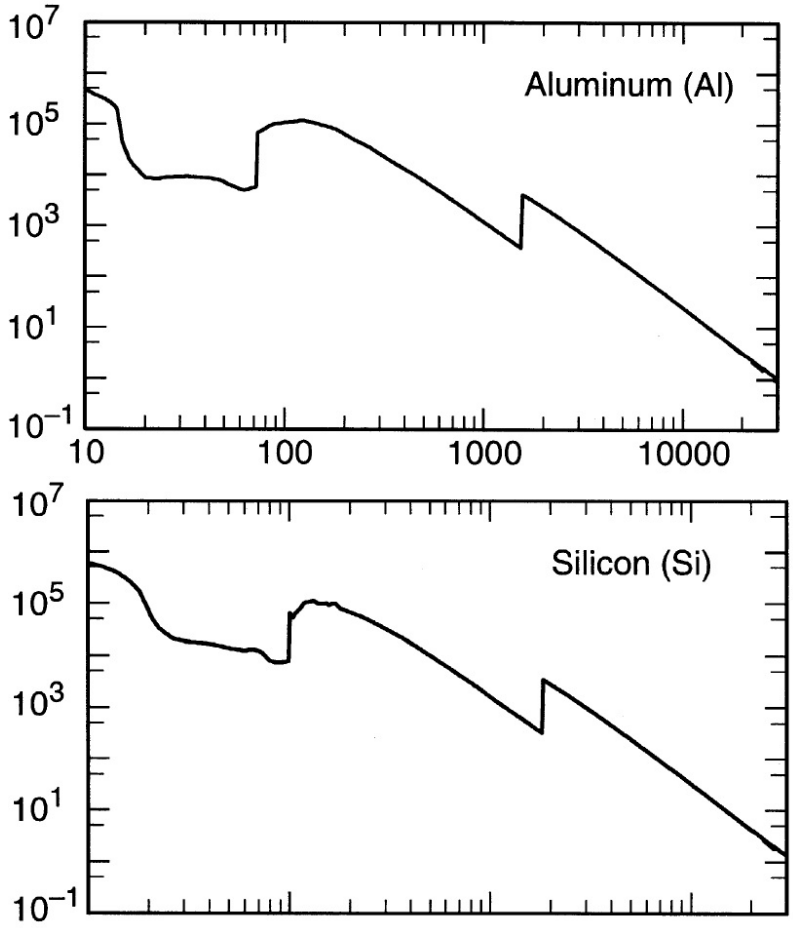

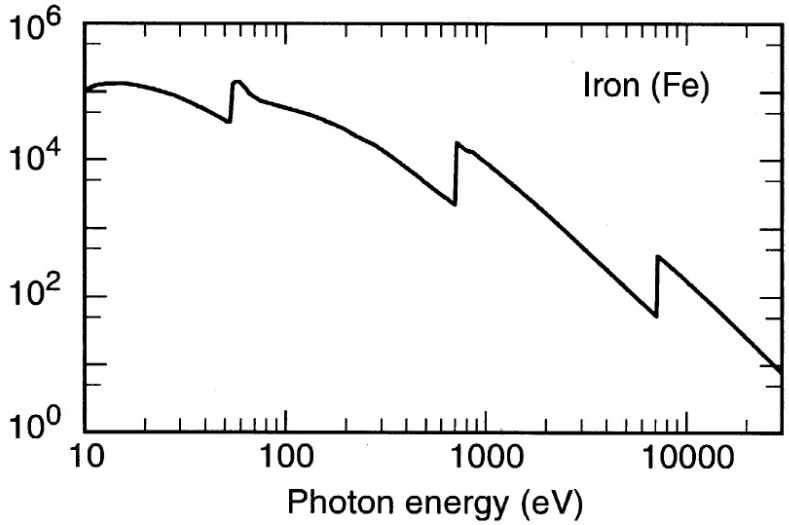

Figure 2.4 - Energy dependence of the mass absorption coefficient μ of 3 different elements [7].

The mass absorption coefficient μ plays a very important role in quantitative XRF analysis. Both the exciting primary radiation and the fluorescence radiation are attenuated in the sample. To relate the observed fluorescence intensity to the concentration, this attenuation must be taken into account.
As illustrated in Fig. 2.4, the absorption of radiation in matter is the cumulative effect of several types of photon-matter interaction processes. Accordingly, in the X-ray range the mass attenuation coefficient μ_i of element i can be express as:

$$\mu_i = \tau_i + \sigma_i \tag{2.5}$$

where τ_i is the cross-section for photo-electric ionization and σ_i the cross-section for scattering interactions. All cross-sections are energy (or wavelength) dependent is more or less proportional to $Z^4\lambda^3$.

2.3.1 Photoelectric Effect

In the photoelectric absorption process, a photon is completely absorbed by the atom and an electron of inner shell is ejected.
The X photon beams undergoes an exponential attenuation whose intensity is equal to:

$$I/I_0 = e^{(-\mu x)} \tag{2.6}$$

where I is the number of photons transmitted at a distance x respect to the number of incident photons I_0 and μ is the linear attenuation coefficient expressed in cm^{-1}.

The X photon interacts with the inner levels and is totally absorbed. Part of the photon is used to overcome the binding energy of the electron and the rest is transferred in the form of kinetic energy. Following this interaction a photoelectron is emitted from one of these levels.

The photoelectric process is the predominant mode of interaction for X-rays of relatively low energy.

The is not an equation valid for all the ranges of E_γ and Z for each atom, but a rough approximation is:

$$\tau \cong \text{constant} \times \frac{Z^n}{E_\gamma^{3,5}} \tag{2.7}$$

where the exponent n varies between 4 and 5 over the X-ray energy region of interest. This severe dependence of the photoelectric absorption probability on the atomic number of the absorber is a primary reason for the preponderance of high-Z materials (such as lead) in X-ray shields.

In the energy region, discontinuities in the curve or "absorption edges" appear at x-ray energies that correspond to the binding energies of electrons in the various shells of the absorber atom. The edge lying highest in energy therefore corresponds to the binding energy of the K-shell electron.

For X-radiation of sufficient energy most of the photoelectrons are emitted from the inner orbital levels (more bound to the nucleus), as well as the shells K or L. The photoelectron is emitted with energy equal to:

$$E = h\nu_0 - E_b \tag{2.8}$$

where $h\nu_0$ is the energy of the incident photon and E_b is the binding energy of the photoelectron in its original electronic level.

After the interaction, the electron, that has absorbed the energy of x-ray photon, is ejected and a vacancy has been created in one of the inner shells [1]. The atom (an ion now) is left in a highly excited state and it will almost immediately return to a more stable electron configuration by emitting an Auger electron (non-radiative process) or a characteristic X-ray photon (radiative process). The latter process is called *X-ray fluorescence* (Fig. 2.5).

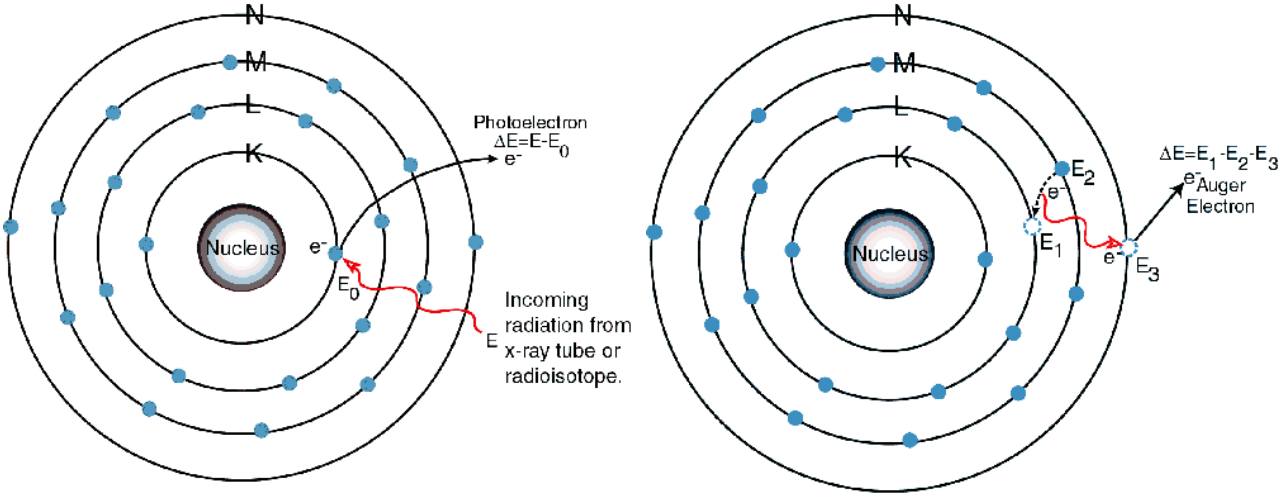

Figure 2.5 - Photoelectric ionization can be followed by either radiative relaxation, causing the emission of characteristic fluorescent X-rays or non-radiative relaxation, involving the emission of Auger electrons [8].

The probability of a core hole in the *K* or *L* shells to be filled by a radiative process, in competition with non-radiative process, represent the *fluorescence yield* (Fig. 2.6).

For light elements (Z < 20), predominantly Auger electrons are produced during the relaxation upon K-shell ionisation ($\omega_K < 0.2$) while the medium to heavy elements are preferentially relaxing in a radiative manner ($0.2 < \omega_K < 1.0$).

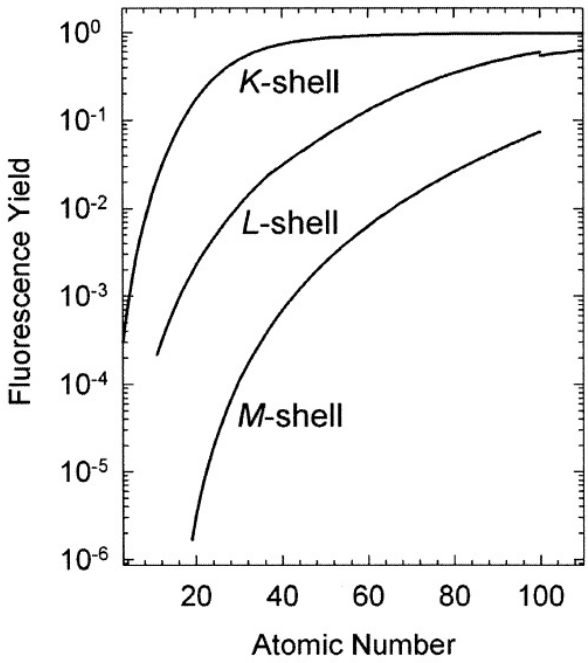

Figure 2.6 – Fluorescence yields for *K*, *L* and *M* shells for $3 \leq Z \leq 110$. The plotted curves for the L and M shells represent average subshell effective yields [7].

Photoelectric absorption can only occur if the energy of the photon E is equal or higher than the binding energy ϕ of the electron. Since photo-electric absorption can occur at each of the excitable energy levels of the atom, the total photo electric cross section τ_i is the sum of sub-shell-specific contributions:

$$\tau_i = \tau_{i,K} + \tau_{i,L} + \tau_{i,M} + \cdots = \tau_{i,K} + \left(\tau_{i,L1} + \tau_{i,L2} + \tau_{i,L3}\right) + \left(\tau_{i,M1} + \cdots + \tau_{i,M5}\right) + \cdots \quad (2.9)$$

As the energy of the X-ray photon decreases, the cross section increases, i.e., more vacancies are created.

The graph of a photo-electric cross-section present abrupt decrease in the cross-section because X-rays with lower energy can no longer eject electrons from the K- shell

However, these photons continue to interact with the more weakly bound electrons in the L and M-shells. The discontinuities in the photo-electric cross-section are called absorption edges. The ratio of the cross section just above and just below the absorption edge is called the jump ratio, r. An element can therefore be determined with high sensitivity by means of XRF when the exciting radiation has its maximum intensity at energy just above the K- edge of that element.

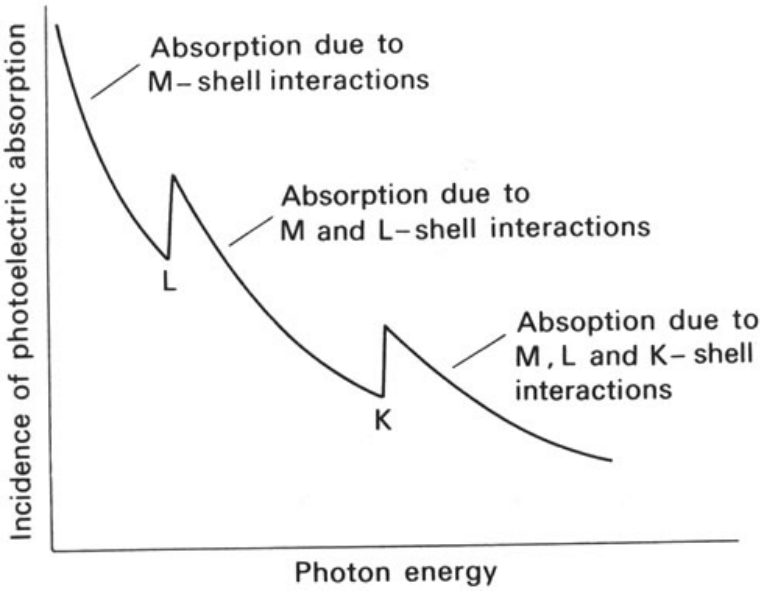

Figure 2.7 - Energy dependence of the x-ray photoelectric absorption cross section.

2.3.2 Scattering

When the interaction between radiation and matter causes only a change of direction to the photons, that process is called scattering [1]. The scattering process can be divided in two groups:

- If the energy of the photon is the same before and after scattering, the process is called elastic or Rayleigh scattering. Elastic scattering takes place between photons and bound electrons and forms the basis of X-ray diffraction.
- If the photon loses some of its energy, the process is called inelastic or Compton scattering.

Compton scattering is an example of inelastic scattering, because the wavelength of the scattered light is different from the incident radiation. Still, the origin of the effect can be considered as an elastic collision between a photon and an electron.

Accordingly, the total cross section for scattering σ_i can be written as the sum of two components:

$$\sigma_i = \sigma_{R,i} + \sigma_{C,i} \tag{2.10}$$

where $\sigma_{R,i}$ and $\sigma_{C,i}$ respectively denote the cross sections for Rayleigh and Compton scatter of element i.

Compton scattering occurs when X-ray photons interact with electron of the outer shell (weakly bound electrons) (Fig. 2.8).

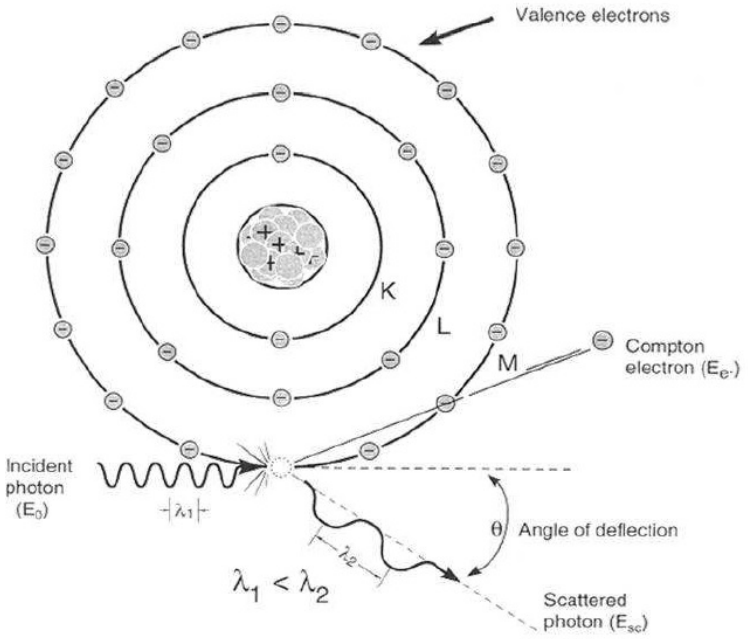

Figure 2.8 - Compton scattering (λ_1, wavelength incident beam; λ_2, wavelength scattered beam; θ scattering angle) [9].

In this process, the incoming x-ray photon is deflected through an angle θ with respect to its original direction ($\lambda_1 < \lambda_2$). The photon transfers a portion of its energy to the electron, which is then known as a recoil electron (Compton electron). The expression that relates the energy transfer and the scattering

angle for any given interaction can simply be derived by writing simultaneous equations for the conservation of energy and momentum.

After inelastic scattering over an angle , a photon, with initial energy , will have a lower energy given by the Compton equation:

$$E' = \frac{E}{1 + \frac{E}{m_0 c^2}(1 - \cos\theta)} \tag{2.11}$$

where is the mass energy of the electron (0.511 MeV). For small scattering angles , very little energy is transferred. Some of the original energy is always retained by the incident photon. The angular distribution of scattered rays is predicted by the *Klein-Nishina formula* for the differential scattering cross section $d\sigma/d\Omega$. The *Klein–Nishina formula* gives the differential cross section of photons scattered from a single free electron in lowest order of quantum electrodynamics. At low frequencies this is referred to as Thomson scattering; at higher frequencies (e.g., x-rays such in our case) this is referred to as Compton scattering.

$$\frac{d\sigma}{d\Omega} = Zr_0^2 \left(\frac{1}{1 + \alpha(1 - \cos\theta)}\right)^{\alpha} + \left(\frac{1 + \cos^2\theta}{2}\right) + \left(1 + \frac{\alpha^2(1 - \cos\theta)^2}{(1 + \cos^2\theta)[1 + \alpha(1 - \cos\theta)]}\right) \tag{2.12}$$

where $\alpha = h\nu/m_0c^2$ and r_0 is the classical electron radius. Figure 2.9 shows this by illustrating the strong tendency for forward scattering at high values of the gamma-ray energy.

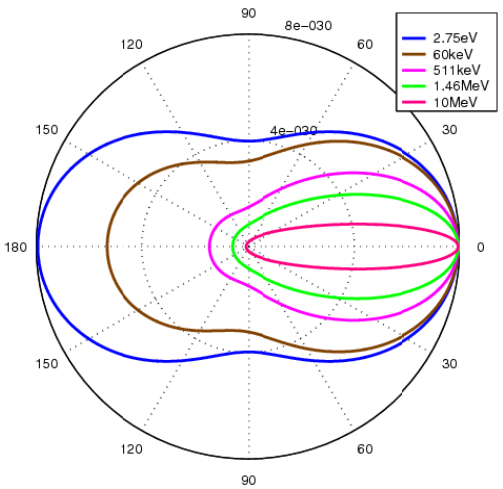

Figure 2.9 - Klein–Nishina distribution of scattering-angle cross sections over a range of commonly encountered energies [http://en.wikipedia.org/wiki/Klein%E2%80%93Nishina_formula].

2.3.3 Selection rules, characteristic lines and X-ray spectra

Characteristic X-ray photons arise from the ejection of an inner orbital electron from an excited atom, and subsequent transition of atomic orbital electrons from states of high to low energy. Each chemical element present in the sample will generate a series of characteristic lines constituting a polychromatic beam of characteristic and scattered radiation coming from the specimen.

To namely the transition that occur form one shell to another can be expressed by two different nomenclatures: IUPAC and Siegbahn name. The IUPAC name is given by the name of the shell that are involved in the transition, i.e., the X-ray line arising from a vacancy in the K-shell filled by an electron originally belonging to the L_3-shell is the K-L_3 transition. However, this transition is more commonly referred to as the $K_{\alpha 1} - \text{line}$in the Siegbahn nomenclature; similarly, fluorescent X-rays resulting from L_3 -M_5 transitions are better known as $L_{\alpha 1} - \text{photons}$.

Table 2.1 lists a number of observed X-ray lines and their corresponding IUPAC Siegbahn names.

Series	IUPAC name	Siegbahn name	Relative Intensity
K-lines	K-L_3	$K_{\alpha 1}$	100
	K-L_2	$K_{\alpha 2}$	~50
	K-M_3	$K_{\beta 1}$	~17
	K-M_2	$K_{\beta 3}$	~8
L_3-lines	L_3-M_5	$L_{\alpha 1}$	100
	L_3-M_4	$L_{\alpha 2}$	~10
	L_3-$N_{5,4}$	$L_{\beta 2}$	~25
	L_3-M_1	L_{ℓ}	~5
	M_3-N_1	$L_{\beta 6}$	~1
L_2-lines	L_2-M_4	$L_{\beta 1}$	100
	L_2-N_4	$L_{\gamma 1}$	~20
	L_2-M_1	L_{η}	~3
	L_2-O_1	$L_{\gamma 6}$	~3
L_1-lines	L_1-M_3	$L_{\beta 3}$	100
	L_1-M_2	$L_{\beta 4}$	~70
	L_1-N_3	$L_{\gamma 3}$	~30
	L_1-N_2	$L_{\gamma 2}$	~30
M-lines	M_5-N_7	$M_{\alpha 1}$	
	M_5-N_6	$M_{\alpha 2}$	
	M_5-N_6	M_{β}	

Table 2.1 - Principal X-ray transition identify by IUPAC and Siegbahn nomenclature. Here also reported their approximate intensities relative to the major line in each subshell [1,2].

As said before, Moseley first established the relationship between the wavelength λ of a characteristic X-ray photon and the atomic number Z of the excited element (1913); this law establish a relation between x-ray wavelength (λ) and Z :

$$\frac{1}{\lambda} = K \cdot (Z - \sigma^2) \tag{2.13}$$

Each unique atom has a number of available electrons that can take part in the transfer and, since millions of atoms are typically involved in the excitation of a given specimen, all possible de-excitation routes are taken. These de- excitation ways occur following a simple set of selection rules that account for the majority of the observed wavelengths.

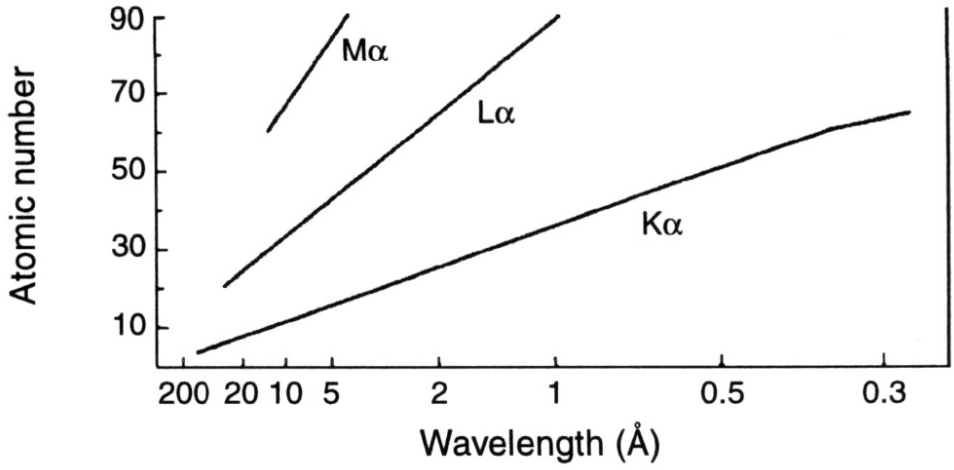

Figure 2.10 - Variation of characteristic line wavelengths with atomic number [1,2].

Each electron in an atom can be defined by four quantum numbers. The first of these quantum numbers is the principal quantum number n, which can take all integral values. When n is equal to 1, the level is referred to as the K level; when n is 2, the L level, and so on.

The four quantum numbers for selection rules are here listed and explained:

- ℓ is the angular quantum number and this can take all values from $(n - 1)$ to zero;
- m is the magnetic quantum number and can take values from $+\ell$ to $-\ell$;
- s is the spin quantum number with a value of ±½;
- the total momentum J of an electron is given by the vector sum of $\ell + s$. Since no two electrons within a given atom can have the same set of quantum numbers, a series of levels or shells can be constructed.

Table 3.2 lists the atomic structures of the first three principal shells.

- The first shell, the $K-shell$, has a maximum of two electrons and these are both in the $1s$ level (orbital). Since the value of J must be positive in this instance the only allowed value is +½

  $\rightarrow J = +{}^{1}/_{2}$

- In the second shell, the $L\ shell$, there are eight electrons: two in the $2s$ level and six in the $2p$ levels.

  In this instance J has a value of ½ for the $1s$ level and 3/2 or ½ for the $2p$ level, thus giving a total of three possible L transition levels.

  - $J = {}^{1}/_{2}$ for $1s$ level

  $\rightarrow J = {}^{3}/_{2}\ or\ {}^{1}/_{2}$ for $2p$ level

  These levels are referred to as L_1, L_2 and L_3 respectively.

- In the M level, there are a maximum of 18 electrons: 2 in the $3s$ level, 8 in the $3p$ level and 10 in the $3d$ level.

  Again, with the values of 3/2 or ½ for J in the $3p$ level and 5/2 and 3/2 in the $3d$ level, a total of five M transition levels are possible (M_1 to M_5).

  $\rightarrow J = {}^{3}/_{2}\ or\ {}^{1}/_{2}$ for $3p$ level

  $\rightarrow J = {}^{5}/_{2}\ or\ {}^{3}/_{2}$ for $3d$ level

- Similar rules can be used to build up additional levels: N, O, etc.

Shell (number of electrons)	n	ℓ	m	s	Orbitals	J
K (2)	1	0	0	±½	1s	½
L (8)	2	0	0	±½	2s	½
	2	1	1	±½	2p	½, 3/2
	2	1	0	±½	2p	½, 3/2
	2	1	-1	±½	2p	½, 3/2
M (18)	3	0	0	±½	3s	½
	3	1	1	±½	3p	½, 3/2
	3	1	0	±½	3p	½, 3/2
	3	1	-1	±½	3p	½, 3/2
	3	2	2	±½	3d	3/2, 5/2
	3	2	1	±½	3d	3/2, 5/2
	3	2	0	±½	3d	3/2, 5/2
	3	2	-1	±½	3d	3/2, 5/2
	3	2	-2	±½	3d	3/2, 5/2

Table 2.2 - Atomic structures of the first three principal shells [1,2].

To obtain the production of x-ray lines, all the quantum number have to change. The selection rules s require that the principal quantum number must change by at least one ($\Delta n \geq 1$), the angular quantum number must change by only one ($\Delta \ell = \pm 1$), and the J quantum number must change by zero or one ($\Delta J = 0, \pm 1$).

Application of the selection rules indicates that in, for example, the K series, only $L_2 \rightarrow K$ and $L_3 \rightarrow K$ transitions are allowed for a change in the principal quantum number of one. There are equivalent pairs of transitions for $n = 2$, $n = 3$, $n = 4$, etc. Figure 2.11 shows the lines that are observed in the K series.

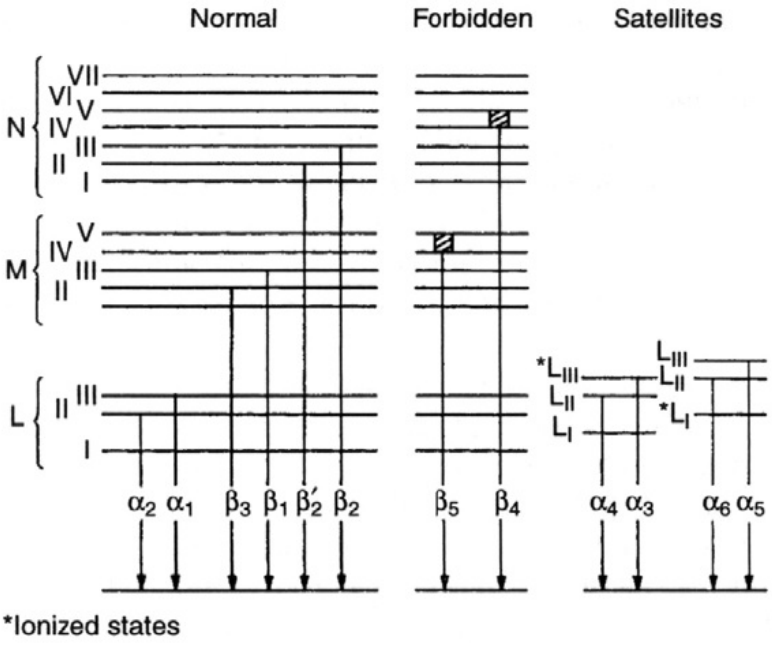

Figure 2.11 - Observed lines in the K-series [1,2].

In a typical XRF spectrum, the normal lines are represented; however certain lines may also occur in X-ray spectra that, at first sight, do not abide to the basic selection rules. These lines are called forbidden lines; they arise from outer orbital levels where there is no sharp energy distinction between orbital. A third type is satellite lines arising from dual ionizations. Following the ejection of the initial electron in the photoelectric process, a short, but finite, period of time elapses before the vacancy is filled.

Since they are relatively weak, neither forbidden transitions nor satellite lines have great analytical significance; however, they may cause some confusion in the qualitative interpretation of spectra and may sometimes be misinterpreted as being analytical lines of trace elements.

By way illustrative, Figure 2.12 shows an example of XRF spectrum acquired on a brownish patina on a lead alloy.

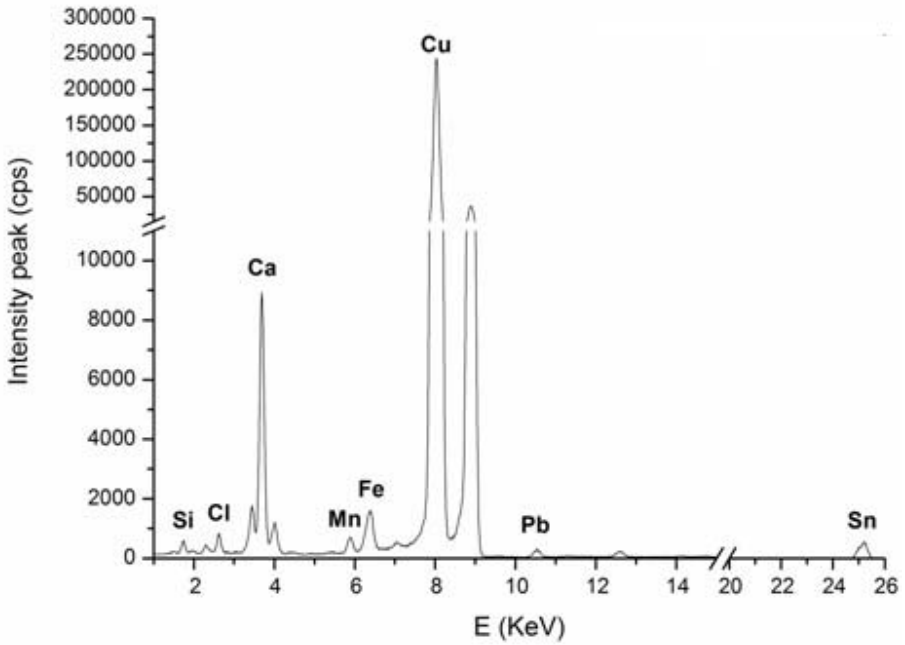

Figure 2.12 – XRF spectra of a brownish patina of a lead alloy.

2.4 Principles of X-Ray Fluorescence

While the roots of the method go back to the early part of this century, where electron excitation systems were employed, it is only during the last 30 years or so that the technique has gained major significance as a routine means of elemental analysis.

The most striking feature of XRF analysis is that this technique allows the qualitative and quantitative analysis of almost all the elements (Be–U) in an unknown sample. The analysis is in principle non-destructive, has high precision and accuracy, has simultaneous multielement capacity, requires only a short irradiation time so that a high sample throughput is possible; on- line analysis is also possible and the running costs are low. The technique is extremely versatile for applications in many fields of science, research and quality control, has low detection limits, and a large dynamic range of concentrations covering up to 9 orders of magnitude.

The working principle of XRF analysis is the measurement of wavelength or energy and intensity of the characteristic X-ray photons emitted from the sample [10,11]. This allows the identification of the elements present in the analyte and the determination of their mass or concentration. All the

information for the analysis is stored in the measured spectrum, which is a line spectrum with all characteristic lines superimposed above a certain fluctuating background.

Other interaction processes, mainly the elastic and inelastic scattering of the primary radiation on sample and substrate, induce the background (Fig. 2.13).

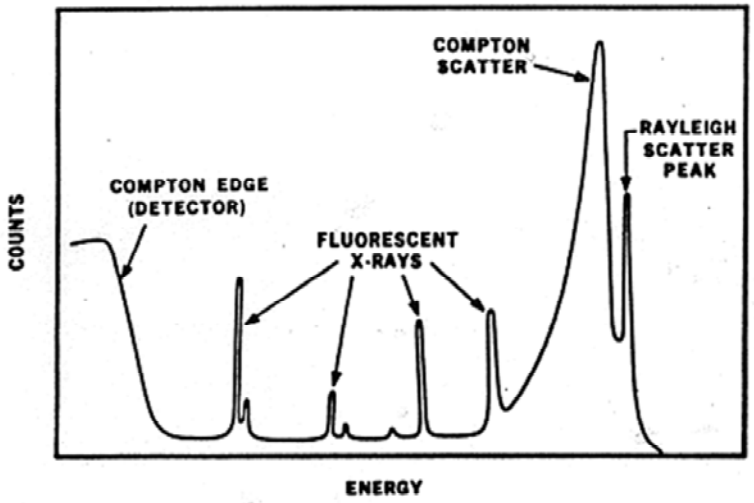

Figure 2.13 – XRF spectrum with the elastic and inelastic scattering effect (http://www.chimica.unipd.it/nicola.tiso/pubblica/_private/Dispense/XRF%20Bertoncello%20STBC11.pdf)

The absorption effects of the primary radiation and the fluorescence radiation created in the analyte result in a shallow layer a few tenths of a millimetre deep that provides information on its composition. This requires a perfectly homogeneous sample which often occurs naturally but must sometimes be produced by acid dissolution into liquids or by grinding and the preparation of pressed pellets. In both examples the feature of non-destructiveness is lost.

Most ideally thin films or small amounts of microcrystalline structure on any substrate are the ideal analyte where also the quantification process is simple because there is linearity between fluorescence intensity and concentration. In thick samples corrections for absorption and enhancement effects are necessary.

Measurement of the spectrum of the emitted characteristic fluorescence radiation is performed using wavelength dispersive (WD) and energy dispersive (ED) spectrometers. In wavelength dispersive X-ray fluorescence analysis (WDXRF), the result is an intensity spectrum of the characteristic lines versus wavelength measured with a Bragg single crystal as dispersion medium while counting the photons with a Geiger-Müller, a proportional or scintillation counter. In energy dispersive X-ray fluorescence analysis (EDXRF), a solid-state detector is used to count the photons, simultaneously sorting them according to energy and storing the result in a multichannel memory. The result is X-ray energy vs. intensity

spectrum. The range of detectable elements ranges from Be ($Z = 4$) for the light elements and goes up to U ($Z = 92$) on the high atomic number Z side. The concentrations that can be determined with standard spectrometers of WD or ED type lie are situated in a wide dynamic range: from the percent to the μg/g level. In terms of mass the nanogram range is reached with spectrometers having the standard excitation geometry.

By introducing special excitation geometries, optimized sources and detectors, the picogram and even femtogram range of absolute analyte detection capacity can be reached; in terms of concentrations, the same improvement factor can be attained, i.e. from the μg/g towards the pg/g level under the best conditions.

In principle, XRF analysis is a multielement analytical technique and in particular, the simultaneous determination of all the detectable elements present in the sample is inherently possible with EDXRF. In WDXRF both the sequential and the simultaneous detection modes are possible.

The physical size of an XRF spectrometer ranges from handheld, battery-operated field units to high-power laboratory units with compact tabletop units and larger ones requiring several cubic meters of space including a 10–20 kW electrical power supply and efficient cooling units with high pressure water and a heat sink.

2.5 X-ray fluorescence experimental apparatus

A typical instrumental portable apparatus for XRF [12-15] analysis is composed of four main functional units (Fig. 2.14):

a) an excitation source,

b) a positioning system and pointing spectrometer;

c) a detector;

d) a chain spectrometric which allows the counting of detected photons and the subsequent analysis of the spectrum.

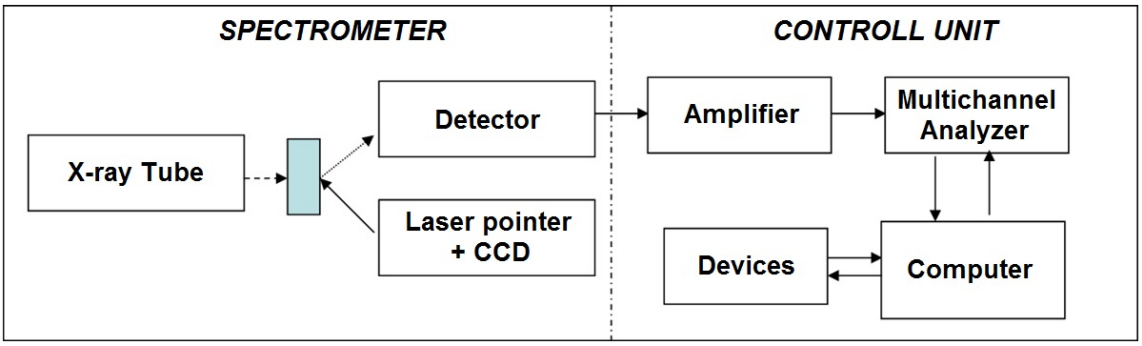

Figure 2.14 - Block diagram of an instrumental apparatus for X-ray fluorescence analysis.

2.5.1 X-ray tube

The source can be a radio isotope that emits photons of appropriate energy, or a small X-ray tube powered with a voltage sufficient to induce the fluorescence X in the elements constituting the sample of interest. Currently there is a tendency to favour the second solution because there are commercially tubes of very small dimensions, the beam produced can be made much collimated in order to irradiate a small area of the surface examined; the intensity and the spectrum of the excitation beam can be suitably modified, thus optimizing system performance spectrometer.

In X-ray tube electrons are generated and accelerated to high speeds and then bombarded a target usually composed of a pure metal (e.g. W, Mo, Cr, or Rh). Upon reaching the target the electrons either interact and ionize the target, creating characteristic x-rays, or are decelerated upon nearing the nuclei, creating a Bremsstrahlung continuum. Figure 2.15 illustrates the production of the X-ray beam.

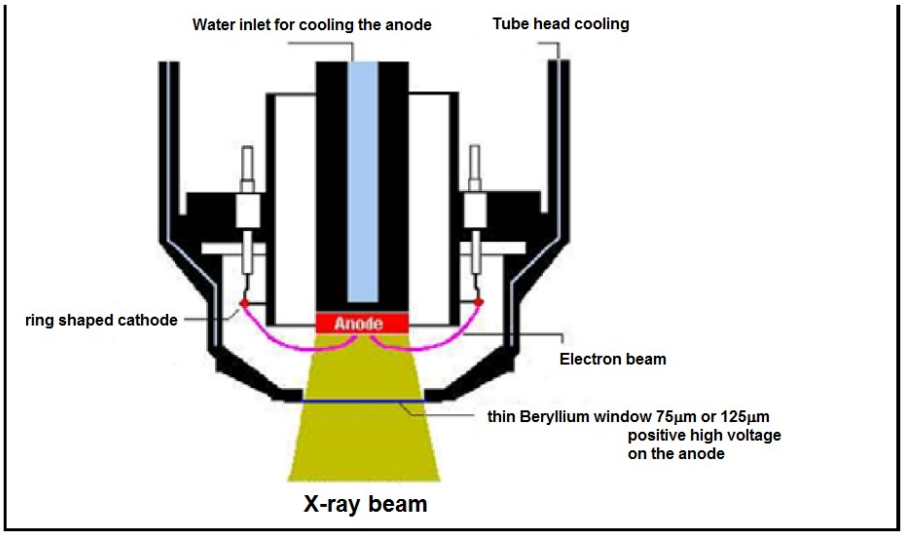

Figure 2.15 – Diagram of an end window x-ray tube [16].

Some characteristics of portable X-ray tubes are reported in Table 2.3. Technological developments relating to the miniaturization of X-ray tubes and to the materials which constitute the anode, have made possible the realization of ED-XRF spectrometers specifically dedicated to different applications, making this technique extremely versatile and optimized from time to time to respond to a large amount of issues that characterizes the analytical needs in the field of archaeometry and conservation science [12].

Identifiable Elements	**Anode Characteristics**			
	Material	***Voltage (kV)***	***Current (mA)***	***Characteristic peak***
P, S, Cl	Ca (line K)	8 - 10	0.1 - 1	3.7 keV + BS
P, S, Cl	Pd (line L)	3 - 5	0.1 - 1	2.8 keV + BS
Cl, K, Ca	Ti (line K)	10	0.1 - 1	4.5 keV + BS
K ÷ Y (line K); Cd ÷ U (line L)	Mo (line K)	30	0.1 - 1	17.5 keV + BS
K ÷ Sn (line K); Cd ÷ U (line L)	Pd (line L)	35	0.1 - 1	21.1 keV + BS
K ÷ Y (line K) ; Tb ÷ U (line L)	W	35	0.1 - 1	BS
Zn ÷ Ba (line K); Tb ÷ U (line L)	W	50	0.1 - 1	BS

Table2.3 - Characteristics of portable X-ray tubes divided for elements analyzed in the archaeometric field [10]. For each anode is indicated below the constituent material, the maximum voltage (kV), current (mA), the rows and the radiation characteristics of Bremsstralhung (BS).

A filter can be placed between the tube and the sample to remove undesirable background radiation below a certain voltage. The level of radiation filtered out is dependent on the filter element composition and its thickness.

2.5.2 Collimator

Collimators are usually circular or a slit and restrict the size or shape of the source beam for exciting small areas. Collimator sizes range from 12microns to several mm. Figure 2.16 illustrates the general function of a collimator.

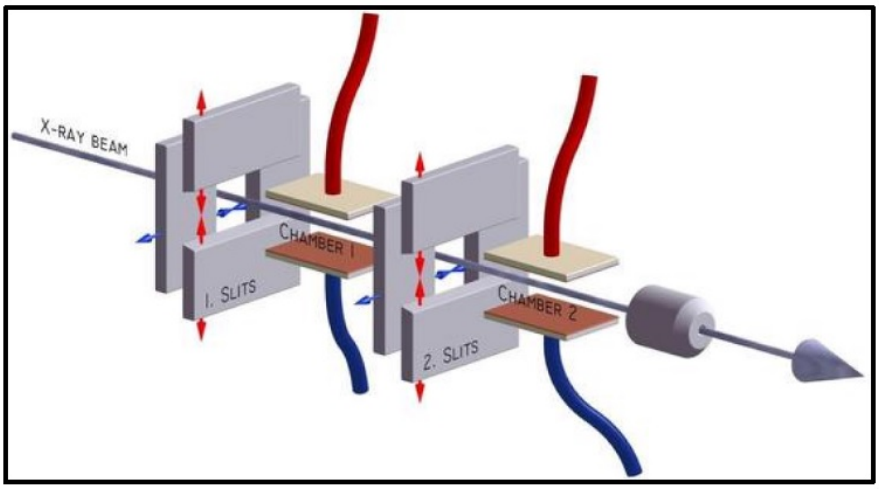

Figure 2.16 - X-ray passing through a collimator [16].

2.5.3 Detector

Regarding the detectors there are many choice possibilities that enable the realization of measurement systems capable to work in the whole interval of energies relative to the characteristic emissions of the elements (from a few keV to energies above 100 keV).

In recent years, a big advantage is determined by the availability of thermoelectrically cooled detectors (called non-cryogenic), which allow a drastic reduction in weight and size and facilitate the development of systems for the analysis of elements with low atomic number.

The main characteristics of the detectors to be used in X-rays spectrometry are:

a) high energy resolution,

b) high quantum efficiency,

c) ability to achieve high counting accrued.

Last few decades have seen the development of high-resolution semiconductor detectors, such as Si-PIN, Si-drift (SSD), CdTe and $Cd_{(1\sim x)}$ Zn_xTe (CZT), characterized by an energy resolution comparable to that of semiconductor detectors cooled with liquid nitrogen. To analyze the secondary X-rays emitted from the sample, after stimulation, normally two types of detectors are used, those cooled with liquid nitrogen, and those with thermoelectric cooling.

The classic cryogenic detectors, such as silicon drift Lithium [Si(Li)] and high purity Germanium (HPGe) have satisfactory energy resolution, typically of the order of 140 eV (FWHM) determined for the Kα line of Manganese (5.9 keV). The main drawback of such detectors derives from the necessity to cooling systems with liquid nitrogen, which are certainly not suitable for a portable instrumentation.

Subsequently were introduced silicon diodes (Si-PIN) cooled simply by a Peltier cell. The compactness of such systems makes possible the construction of measurement apparatuses suitable for in situ analysis. Unfortunately, however, their energy resolution, of the order of 180 - 200 eV (FWHM) at 5.9 keV, is most often insufficient for the archaeometric purposes, especially for the identification of the light elements. Characterized by a thickness of about 300 μm, in fact, are used up to 30 keV, beyond which the efficiency decreases due to the reduced thickness.

In addition to the Si-PIN detectors are available Mercury iodide (HgI_2) and Zinc Cadmium telluride detectors (CZT), these cooled by a Peltier cell.

The detectors HgI_2, the first to be built, have a energy resolution of about 180 - 200 eV at 5.9 keV and an efficiency of about 100% over the whole range of X-rays; CZT detectors have a thickness of 2 mm, an efficiency of about 100% over the entire range of X-rays and energy resolution of 300 eV, 700 eV and 1500 eV respectively at 5.9 keV, 59.6 keV and 122 keV.

All the advantages of the two types of detectors just described are present simultaneously in the silicon drift detectors (SDD) [17-21]. The configuration of the readout electronics and the small size of the anode drastically reduce the capacity of the anode and consequently the electronic noise. The SDD detectors allow to obtain good energy resolution even at ambient temperatures or with the use of a simple Peltier cell (150 eV FWHM at 5.9 keV). Following the development of the SDD, were implemented prototypes of portable measuring apparatus, consisting of compact housings including either the chip that the cooling system, which allowed the implementation of systems for portable XRF archaeometric analysis.

In figure 2.17 is shown the comparison between the efficiency of a detector Si (Li) (thickness of 3 mm) and that of two detectors thermoelectric cooling: a) detector SSD or Si-PIN (thickness of 300 μm), b) CZT detector (thickness of 1.5 mm).

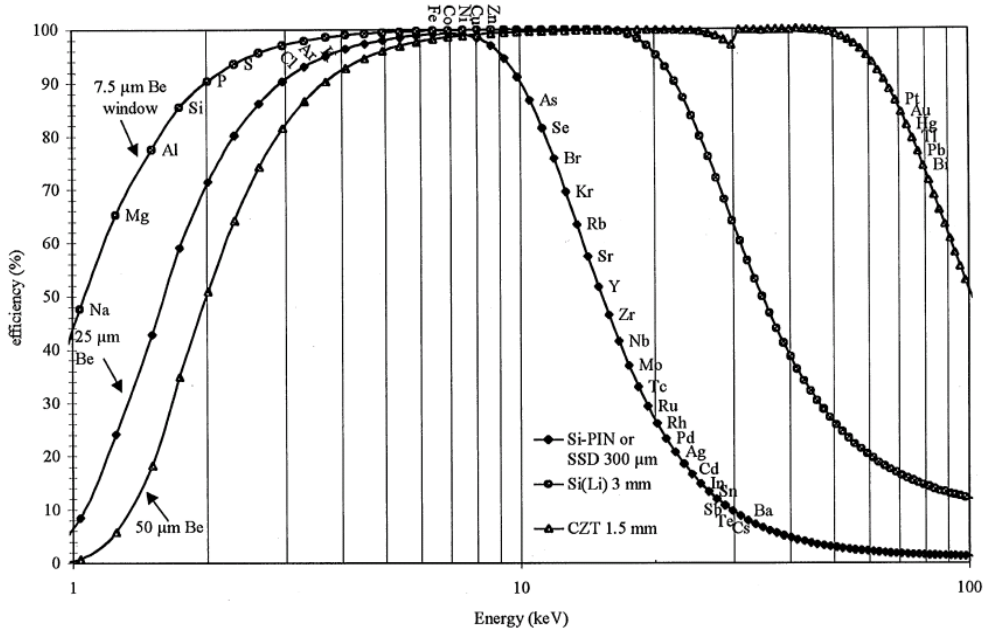

Figure 2.17 - Efficiency (%) calculated for a detector Si (Li) detector SSD or Si-PIN and CZT detector with different windows of beryllium, respectively of 7.5 µm, 25 µm and 50 µm [12].

Instead the figure 2.18 shows the comparison between the resolution of a detector Si (Li), a Si-PIN and an SSD. In the same figure, shows the difference in energy between the lines Kα of the elements (from sodium to cadmium) or lines Lα and Lβ (from tin to lead) and those of adjacent elements with atomic number.

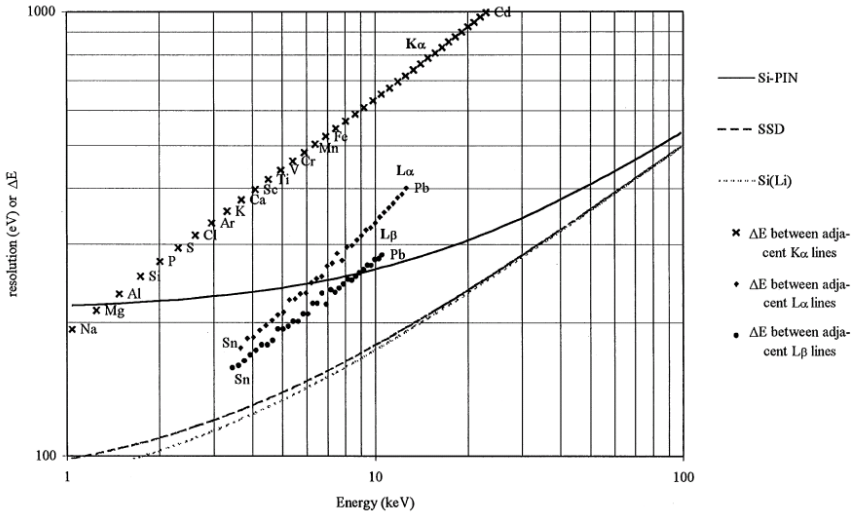

Figure 2.18 - Energy resolution (eV) of a detector Si (Li), a Si-PIN and an SSD and energy differences (ΔE) calculated between the elements and those with atomic number next to it [12].

The energy resolution of a thermoelectrically cooled detector is sufficient to discriminate the lines Kα of the different elements, except for the light elements for which a resolution of 250 eV at 5.9 keV can cause a substantial overlap of the peaks. In table 2.4 provides an overview of the characteristics of semiconductor detectors used for X-ray spectroscopy so far mentioned.

Table 2.4 – Comparison between the performance of different X-ray detectors [10]: Si (Li) - an area of 10 mm^2; HPGe - area of 30 mm^2 ; Si-PIN - area of 7 mm^2; HgI_2 - an area of 5 mm^2; SSD - an area of 3.5 mm^2

	S (Li)	**HPGe**	**Si-PIN**	**HgI_2**	**SDD**
Resolution (FWHM @ 5.9 KeV)	140	150	180	200	155
Useful energy range (keV)	1-50*	1-120	2-25	2-120	2-25
Efficiency %**	0.8	2.5	0.55	0.4	0.3
Signal creation (□ s)	6-12	6	12	12	2
Cooling system	N_2 liquid	N_2 liquid	*Peltier*	*Peltier*	*Peltier*

* Depends on the detector thickness.
** Value calculated at 1 cm distance from the source.

In general there exist two type of XRF techniques: WD-XRF (Wave Dispersive - XRF) and ED-XRF. The WD-XRF technique allows to reveal elements with low atomic number, such as beryllium (Z = 2), unlike the ED-XRF technique reveals elements with higher Z, but allow to perform simultaneously and in short time the analysis of all the elements present in the sample. However in the last decade, thanks to the use of detectors with higher detection efficiency, of new materials in the detector windows and to the possibility to flush an inert gas such as helium between the sample and the detector window, the systems ED-XRF allow now reveal elements with Z>11.

Contrary to WD-XRF, which separates in all the wavelength components the radiation emitted by the sample through an analyzer crystal in which all the different X energy lines coming from the sample are diffracted in different directions, the ED-XRF spectrometry reveals the energy of the X characteristics lines, differentiating in the spectral lines and allowing in this way the recognition of the elements present in a sample.

2.5.4 The ArtTAX 400 (Bruker AXS)

The instrumentation for X-ray fluorescence analyses, available at *Laboratorio di Tecniche Fisiche per lo Studio e la Caratterizzazione dei Beni Culturali – UniNetLab – Dipartimento di Fisica e Chimica – Università degli studi di Palermo,* consists of a portable spectrometer ArtTAX 400 (Bruker AXS), which allows energy dispersive analysis - ED-XRF (Energy Dispersive - XRF) [22].

The ARTAX is the first commercially available, portable micro-XRF spectrometer designed to meet the requirements for a spectroscopic analysis of unique and valuable objects on site, i.e. in archeometry and art history. The system performs a simultaneous multi element analysis in the element range from Na(11) to U(92) and reaches a spatial resolution of down to 30 μm.

The main components ARTAX system in terms of functionality are: the X-ray tube system, collimators, filters, detector and signal processing hardware and software; as schematised in the Figure 2.14. The ARTAX employs a Silicon based detector.

The ARTAX can use a variety of changeable filters, tube voltage and current settings making them uniquely capable of being configured to maximize their sensitivity to specific elements of interest.

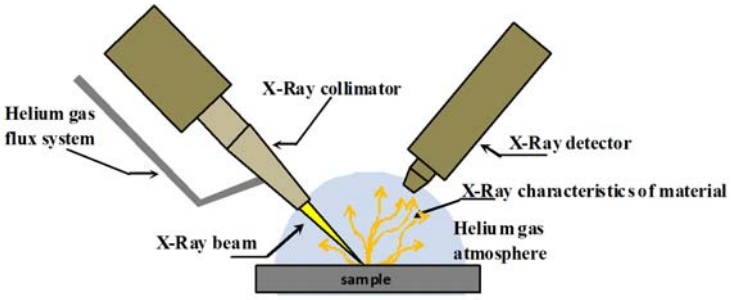

a)

b)

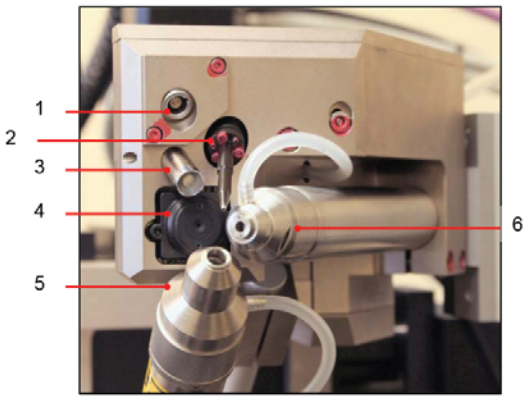

Figure 2.19 - a) ArtTAX 400 XRF spectrometer (Bruker AXS), b) Detail of the head of measurement: **1.** Collision sensor **2.** Laser pointer for positioning of the measuring point **3.** LED for illumination of the sample **4.** CCD camera **5.** Optical emission of the X-ray beam of excitation and helium flow; **6.** Collecting optics of X-ray fluorescence and helium flow.

- Figure 2.19 shows the r Artax 400 (Bruker AXS) and all the components are described below: SSD detection system with energy resolution lower than 145 eV to 5.9 keV, whose characteristics and advantages compared to other detection systems in the solid state are fully described below (Section 2.5.3.4);

- X-ray tube, with a maximum voltage of 50 kV and a maximum current of 1500 μA, with Molybdenum anode, equipped with a system of micro collimators different diameter that optimize the spatial resolution of the analysis. Table 2.5 suggests some filter types, available in ArtAX 400, for certain applications. Note that the unit allow the user to fabricate any filter or secondary target they think is best for their application.

Filter	Thickness	kV range	Elements
No filter	N/A	4-50	All, Na-Ca
Cellulose	Single sheet	5-10	Si-Ti
Thin aluminum	25-75 μm	8-12	S-V
Thick aluminum	75-200 μm	10-20	Ca-Cu
Thin anode element	25-75 μm	25-40	Ca-Mo
Thick anode element	100-150 μm	40-50	Cu-Mo
Copper	200-500 μm	50	>Fe

Table 2.5 – Available filters that can be used with the ARTAX units [16].

- laser pointing system and CCD camera for the measuring geometry control and the photographic documentation of the analyzed points;
- a manual positioning system to handling the measuring head along the three directions XYZ;
- a PC for remote control of the system and the management of the measurement set up and the acquisition of the XRF spectrum of the sample point under consideration;
- system for the helium purge between sample and detector which can detect even the light elements: thanks to the presence of He, which has a Z considerably lower than that of the nitrogen present in the air, the characteristic X-rays emitted from the sample are not reduced to photoelectric absorption caused by air molecules.

As said before, the ARTAX system presents a SSD detection system. The silicon drift detector (SDD) is a device characterized by a very low capacity of the electrode charge collection. This feature, together with integration on the chip of the first stage of pre-amplification electronics, provides excellent energy resolution at high rates count at temperatures close to the ambient one, obtained with a simple thermoelectric cooling. Initially designed in the '80s at the Politecnico di Milano for measures in the field of high energy physics, the SDD detectors have also found a place in other fields of application. In particular, the SDD detector optimized for X spectroscopy measurements - proposed in the early 2000s by the group of Politecnico di Milano and realized in collaboration with the Max-Planck Institut Halbleiterlabor of Monaco - has gradually replaced the detectors until now traditionally used to X

fluorescence measurements, thanks to the excellent performance and extremely compact. The manufacturing technology of these devices is in very rapid development and they are implemented continuously with new configurations and geometries. The undoubted advantages compared to Si(Li) are represented by the excellent resolutions obtainable (typically 140eV - 150eV to the Kα line of Mn to -10°C, but with the latest devices values are reached even below 130eV), but also by the very short time formation constants and the elimination of the cooling system with liquid nitrogen. This latter aspect is reflected in an extreme compactness which, together with the ability to support high rates of counting (up to more than 105 counts per second), offers the possibility of obtain a very wide solid angle covered by the detector.

In this way the measurement time can be significantly limited, or can be obtained a higher counting statistics. The larger solid angle covered can be used to work at a lower value of beam current while maintaining sufficient counting statistics: this can have great importance, especially for applications in the cultural heritage field, in which it is often necessary to limit the current to not damage to the specimen.

Bibliography

[1] Koen, H.A, Janssens, R.E., Van Grieken, "Non-destructive Microanalysis of Cultural Heritage Materials", (Eds.), Elsevier, Amsterdam, The Netherlands, 2004 - 800 p. - ISBN 0-444-50738-8.

[2] Gauglitz, G., Vo-Dinh, T. "The Handbook of Spectroscopy", (Eds.), Wiley-VCH, 2003 - 1000 pp, ISBN 3-527-29782-0.

[3] Bertin, E., "Principles and Practice of X-Ray Spectrometric Analysis", Plenum Press: New York, 1970, p 1-2, 114-115.

[4] Jenkins, R., "X-Ray Fluorescence Spectrometry", John Wiley and Sons: New York, 1988, p 51-53, 78-83, 87.

[5] Knoll, G.F, "Radiation Detection and Measurement – 3rd ed.", John Wiley & Sons, Inc., 2000 – pp 816, ISBN 0-471-07338-5.

[6] Janssen, K., "Modern Methods for Analysing Archaeological and Historical Glass, Volume I", John Wiley & Sons, 2013, ISBN:9780470516140.

[7] X-Ray data booklet, Lawrence Berkeley National Laboratory, Third edition, September 2009.

[8] Amptek, "X-ray Fluorescence Spectroscopy", URL http://www.amptek.com.

[9] De Wolfe, R., "Implementation, Analytical Characterization and Application of a Novel Portable XRF/XRD Instrument", Course Master Chemistry, Ghent University 2011-2012.

[10] Janssens, K., Vittiglio, G., Deraedt, I., Aerts, A., Vekemans, B., Vincze, L., Wei, F., Deryck, I., Schalm, O., Adams, F., Rindby, A., Knochel, A., Simionovici, A., Snigirev, A. "Use of Microscopic XRF for Non-destructive Analysis in Art and Archaeometry", X-Ray Spectrom. 29 (2000) 73–91.

[11] Potts, P.J., Ellis, A.T., Holmes, M., Kregsamer, P., Streli, C., West M., Wobrauschek, P. "X-ray Fuorescence spectrometry", J. Anal. At. Spectrom., 2000, 15, 1417±1442.

[12] Cesareo, R., Gigante, G.E., Castellano, A. "Thermoelectrically cooled semiconductor detectors for non-destructive analysis of works of art by means of energy dispersive X-ray fluorescence", Nucl. Instr. and Methods in Physics Research A 428 (1999) 171-181.

[13] Cesareo, R., Castellano, A., Marabelli, M., Buccolieri, G., Quarta, S., Santopadre, P., Ieole, M., Ridolfi, S., Gigante, G.E. "*Optimization* of portable systems for energy dispersive X ray

fluorescence analysis of paintings", In situ applications of X ray fluorescence techniques, IAEA, Vienna, (2005) 151-164.

[14] Longoni, A., Fiorini, C., Leutenegger, P., Sciuti, S., Fronterotta, G., Struder, L., Lechner, P. "A portable XRF spectrometer for non destructive analyses in archeometry", Nuclear Instruments and Methods in Physics Research A 409 (1998) 407-409.

[15] Cesareo, R., Gigante, G.E., Canegallo, P., Castellano, A., Iwanczyk, J.S., Dabrowski, A. "Applications of non-cryogenic portable EDXRF systems in archeometry", Nuclear Instruments and Methods in Physics Research A 380 (1996) 440-445.

[16] Draft Bruker Xrf Spectroscopy user guide: spectral interpretation and sources of interference

[17] Grassi, N. "Rivelatori a deriva di silicio per spettroscopia X: studio del possibile utilizzo in misure PIXE con fascio esterno", Tesi di Laurea, A.A. 2001- 2002, Università degli Studi Di Firenze.

[18] Gatti, E., Rehak, P. "Review of semiconductor drift detectors", Nuclear Instruments and Methods in Physics Research A 541 (2005) 47–60.

[19] Lechner, P., Eckbauer, S., Hartmann, R., Krisch, S., Hauff, D., Richter, R., Soltau, H., Struder, L., Fiorini, C., Gatti, E., Longoni, A., Sampietro, M. "Silicon drift detectors for high resolution room temperature X-ray spectroscopy", Nucl. Instr. and Meth. in Phys. Research A 377 (1996) 346-351.

[20] Leutenegger, P., Longoni, A., Fiorini, C., Struder, L., Kemmer, J., Lechner, P., Sciuti, S., Cesareo, R. "Works of art investigation with silicon drift detectors", Nuclear Instruments and Methods in Physics Research A 439 (2000) 458-470.

[21] Fiorini, C., Longoni, A., Hartmann, R., Lechner, P., Struder, L. "Silicon drift detectors with On –Chip Electronics for X-ray spectroscopy", Journal of X-ray science and technology 7 (1997) 117-129.

[22] Bronk, H., Röhrs, S., Bjeoumikhov, A., Langhoff, N., Schmalz, J., Wedell, R., Gorny, H.E., Herold, A., Waldschläger, U. "ArtTAX – a new mobile spectrometer for energy-dispersive micro X-ray fluorescence spectrometry on art and archaeological objects", Fresenius J Anal Chem 371 (2001) 307–316.

Chapter 3
Raman Spectroscopy

Since the end of the '80s, in response to technical progress, began to appear reviews in scientific journals related to the possible applications of Raman spectroscopy (RS) [1-5]. A review specifically dedicated to diagnostic research on paint pigments appeared as early as 1992 [6] and this was followed by many others [7-9].

The instrumental apparatus for RS becoming more affordable, both economically and as users. In other words, while the RS until a few years ago was the prerogative of the most sophisticated laboratories, today, academic institutions are increasingly working in contact with cultural operators.

In this chapter are described the analysis technique and the basic physical principles of RS. Finally, are also discussed the instrumental characteristics of the spectrometer used, available at PH3DRA Laboratories (Physics for Dating Diagnostics Dosimetry Research and Application – *Dipartimento di Fisica e Astronomia,Università di Catania*) used for the measurements acquisition given in the following chapters dedicated to experimental results obtained in the course of research activity related to this thesis.

3.1 Light-Matter interaction

A atom can be emit (create) or absorb (annihilate) photon by undergoing downward or upward transitions between its energy levels, conserving energy in the process. Three forms of interaction are possible: spontaneous emission, absorption and stimulated emission [10].

To explain the processes described above, is useful to consider the energy levels E_1 and E_2 of a atom placed in an optical resonator of volume V that can sustain a number of electromagnetic modes and the interaction between the atom and the photons of a prescribed radiation mode of frequency $v \approx v_0$, where $hv_0 = E_2 - E_1$, since photons of this energy match the atomic energy-level difference. In the case of a spontaneous emission the atom is initially in the upper energy level and it may drop spontaneously to the lower energy level and release its energy in the form of a photon (Fig. 3.1).

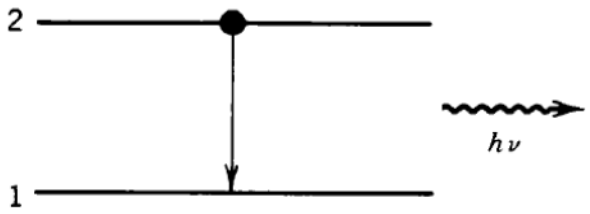

Figure 3.1 - Spontaneous emission of a photon into the mode of frequency v by an atomic transition from energy level 2 to energy level 1. The photon energy $hv \approx E_2 - E_1$ [10].

In this case the transition is independent of the number of photons that may already be in the mode. The probability density (per second), or rate, of this spontaneous transition depends on v in a way that characterizes the atomic transition.

$$p_{sp} = \frac{c}{V}\sigma(v) \tag{3.1}$$

In a cavity of volume V, the probability density (per second), or rate, of this spontaneous transition depends on v in a way that characterizes the atomic transition.

The function $\sigma(\mathrm{v})$ is a narrow function of v centred about the atomic resonance frequency v_0.

The term "probability density" signifies that the probability of an emission taking place in an incremental time interval between t and $\mathrm{t} + \Delta\mathrm{t}$ is simply $p_{sp}\Delta t$. Because it is a probability density, p_{sp} can be greater than 1 (s^{-1}), although of course $p_{sp}\Delta t$ must always be smaller than 1. Thus, if there are a large number N of such atoms, a fraction of approximately $\Delta N = (p_{sp}\Delta t)N$ atoms will undergo the transition within the time interval Δt. We can therefore write $\frac{dN}{dt} = p_{sp}N$, so that the number of atoms $N(t) = N(0)\exp(-p_{sp}t)$ decays exponentially with time constant $1/p_{sp}$ (Fig. 3.2.).

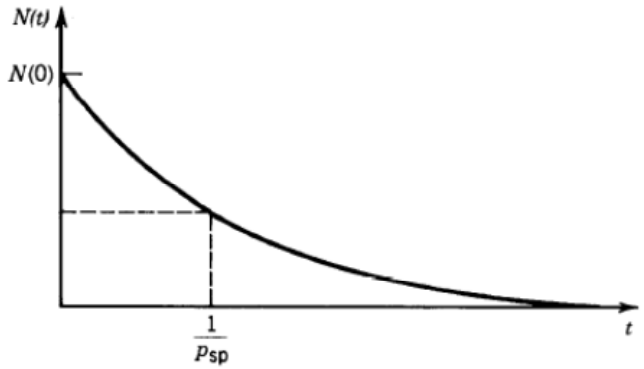

Figure 3.2 - Spontaneous emission into a single mode causes the number of excited atoms to decrease exponentially with time constant $1/p_{sp}$ [10].

In the absorption process the atom is initially in the lower energy level and the radiation mode contains a photon, the photon may be absorbed, thereby raising the atom to the upper energy level (Fig. 3.3).

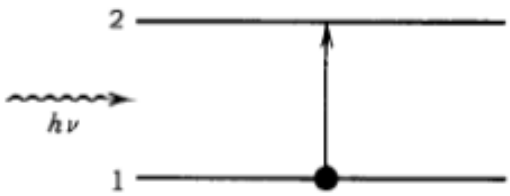

Figure 3.3 - Absorption of a photon hv leads to an upward transition of the atom from energy level 1 to energy level 2 [10].

The probability density for the absorption of a photon from a given mode of frequency v in a cavity of volume V is governed by the same law that governs spontaneous emission into that mode,

$$p_{ab} = \frac{c}{V}\sigma(v) \tag{3.2}$$

However, if there are n photons in the mode, the probability density that the atom absorbs one photon is n times greater,

$$P_{ab} = n\frac{c}{V}\sigma(v) \tag{3.3}$$

In the case of stimulated process the atom may be stimulated to emit another photon into the same mode (Fig. 3.4). The probability density p_{st} that this process occurs in a cavity of volume V is governed by the same transition cross section,

$$p_{st} = \frac{c}{V}\sigma(v) \tag{3.4}$$

As in the case of absorption, if the mode originally carries n photons, the probability density that the atom is stimulated to emit an additional photon is

$$P_{st} = n\frac{c}{V}\sigma(v) \tag{3.5}$$

After the emission, the radiation mode carries $n + 1$ photons. Since $P_{st} = P_{ab}$, is useful use the notation W_i for the probability density of both stimulated emission and absorption.

The total probability density of the atom emitting a photon into the mode is $p_{sp} + P_{st} = (n + 1)\left(\frac{c}{V}\right)\sigma(v)$.

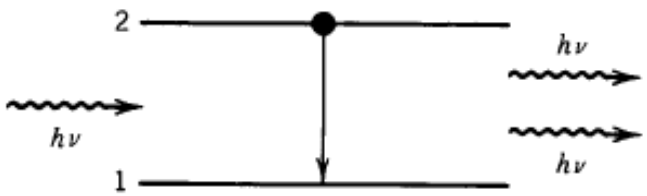

Figure 3.4 - Stimulated emission is a process whereby a photon hv stimulates the atom to emit a clone photon as it undergoes a downward transition [10].

The probability process described above are regulated by transition cross section

$$S = \int_0^\infty \sigma(v)dv \tag{3.6}$$

which has unit of cm^2-Hz, is called the transition strength or oscillator strength, and represent the strength of the interaction. Its shape governs the relative magnitude of the interaction with photons of different frequencies. The shape (profile) of $\sigma(v)$ is readily separated from its overall strength by defining a normalized function with units of Hz-1 and unity area, $g(v) = \sigma(v)/S$, know as the lineshape function, so that $\int_0^\infty g(v)dv = 1$. The transition cross section can therefore be written in terms of its strength and its profile as

$$\sigma(v) = Sg(v) \tag{3.7}$$

The lineshape function $g(v)$ is centred about the frequency where $\sigma(v)$ is largest and drops sharply for v different from v_0. Transitions are therefore most likely for photons of frequency $v \approx v_0$. The width of the function $g(v)$ is know as the transition linewitdth. The linewidth Δv is defined as the full width of the function $g(v)$ at half its maximum value (FWHM). In general, the width of the function $g(v)$ is inversely proportional to its central value (since its area is unity),

$$\Delta v \propto \frac{1}{g(v_0)} \tag{3.8}$$

It is also useful to define the peak transition cross section, which occurs at the resonance frequency, $\sigma_0 = \sigma(v_0)$. The function $\sigma(v)$ is therefore characterized by its height σ_0, width Δv, area S, and profile $g(v)$, as Fig. 3.5.

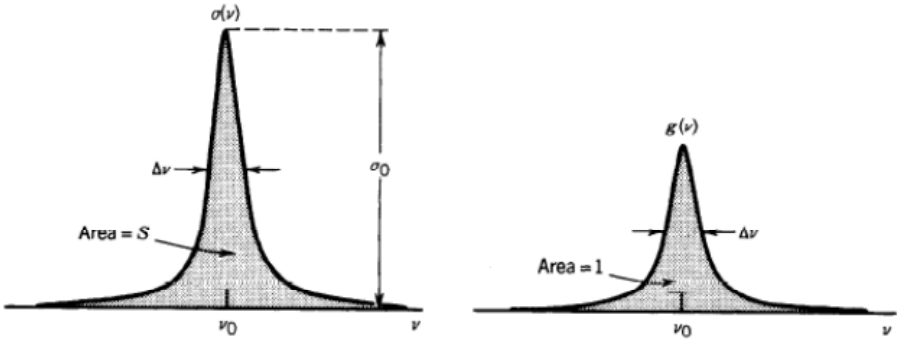

Figure 3.5 - The transition cross section $\sigma(\nu)$ and the lineshape function $g(\nu)$ [10].

3.2 Scattering processes

When monochromatic radiation of frequency ω_1 is incident on systems, most of it is transmitted without change but, in addition, some scattering of the radiation occurs [11].

In both the classical and quantum mechanical treatments, the origin of scattered radiation is considered to be the oscillating electric and magnetic multipole moments induced in a molecule by the electromagnetic fields of the incident light waves. Normally, the most significant multipole source is the oscillating electric dipole. The intensity I, radiated by an oscillating electric dipole induced in a molecule by the electric field of the incident radiation of frequency ω_1, is given by:

$$I = k'_\omega \omega_s^4 p_0^2 \, sin^2 \, \theta \tag{3.9}$$

where θ is the angle created by the incident radiation with the axis of the dipole, and

$$k'_\omega = \frac{1}{32\pi^2 \varepsilon_0 c_0^3} \tag{3.10}$$

and p_0 is the amplitude of the induced electric dipole with frequency ω_s which is generally but not necessarily different from ω_1. Here, and in much of the subsequent theoretical treatments it is convenient to use the frequency ω. However in some situations it is used the wavenumber $\tilde{\nu}$ in accord with normal practice. So, introducing the relation

$$\omega_s = 2\pi c_0 \tilde{\nu}_s \tag{3.11}$$

the eq. (3.9) can be written as:

$$I = k'_{\tilde{\nu}} \tilde{\nu}_s^4 p_0^2 \, sin^2 \, \theta \tag{3.12}$$

where

$$k'_{\tilde{\nu}} = \frac{\pi^2 c_0}{2\varepsilon_0} \tag{3.13}$$

Now, if the frequency content of the scattered radiation is analysed, it is possible to observe that are present not only the frequency ω_1 associated with the incident radiation but also, in general, pairs of new frequencies of the type $\omega_1 \pm \omega_M$. In molecular systems, the frequencies ω_M are related to the transitions between rotational, vibrational and electronic levels. The scattered radiation usually has polarization characteristics different from those of the incident radiation:.

- the scattering without change of frequency is the Rayleigh scattering,
- that with change of frequency is called Raman scattering. In the spectrum of the scattered radiation, the new frequencies are termed Raman lines, or bands,. Raman bands at frequencies less than the incident frequency (i.e. of the type $\boldsymbol{\omega_1 - \omega_M}$) are referred to as Stokes bands, and those at frequencies greater than the incident frequency (i.e. of the type $\boldsymbol{\omega_1 + \omega_M}$) as anti-Stokes bands.

3.2.1 Phenomenological model

This model is based on the photon description of electromagnetic radiation. It must be considered that before the interaction of the radiation with the system there are n_1 photons each of energy

$$E = \hbar\omega_1 \tag{3.14}$$

where ω_1 is the frequency of the incident monochromatic radiation, and the molecule has energy E_1.
The interaction of the radiation with a molecule leads to annihilation of one photon of energy $\hbar\omega_1$, creation of a new photon of energy

$$E_f = \hbar\omega_s \tag{3.15}$$

and the transition of the molecule to a state with energy E_f.
The radiation now consists of:

- $\boldsymbol{(n_1 - 1)}$ photons of energy $\boldsymbol{\hbar\omega_1}$

- one photon of energy $\hbar\boldsymbol{\omega_s}$.

In the overall process, energy must be conserved so the final level of energy can be expressed by

$$E_{fi} = \hbar(\omega_1 - \omega_s) \text{ or } \omega_s = \omega_1 - \omega_{fi} \tag{3.16}$$

However, as already said, the energy $\hbar\omega_1$ does not correspond to any electronic transition energy and the photon of energy $\hbar\omega_1$ is not absorbed in the strict spectroscopic sense. The role of the incident radiation is rather to perturb the molecule and open the possibility of spectroscopic transitions other than direct absorption.

For classification purposes in the applications of the energy transfer model it is convenient to introduce the total number of incident photons annihilated ($\boldsymbol{N}$), . and the overall number of photons involved in a single scattering process $\boldsymbol{N+1}$, that is the number of photons annihilated and created.

The scattering process under consideration (elastic or inelastic) involves two photons, one incident and one scattered, so that $\boldsymbol{N+1=2}$:

- it describes Rayleigh scattering (elastic) when $\boldsymbol{f = i}$ and $\boldsymbol{\omega_s = \omega_1}$
- and Raman scattering (inelastic) when $\boldsymbol{f \neq i}$.
- For Raman scattering if $\boldsymbol{E_f > E_i}$, then $\boldsymbol{\omega_s = \omega_1 - \omega_M}$ and we have Stokes Raman scattering;
- if $\boldsymbol{E_f < E_i}$, then $\boldsymbol{\omega_s = \omega_1 + \omega_M}$ and we have anti-Stokes Raman scattering.

The Rayleigh and Raman scattering processes are summarized in Fig 3.6.

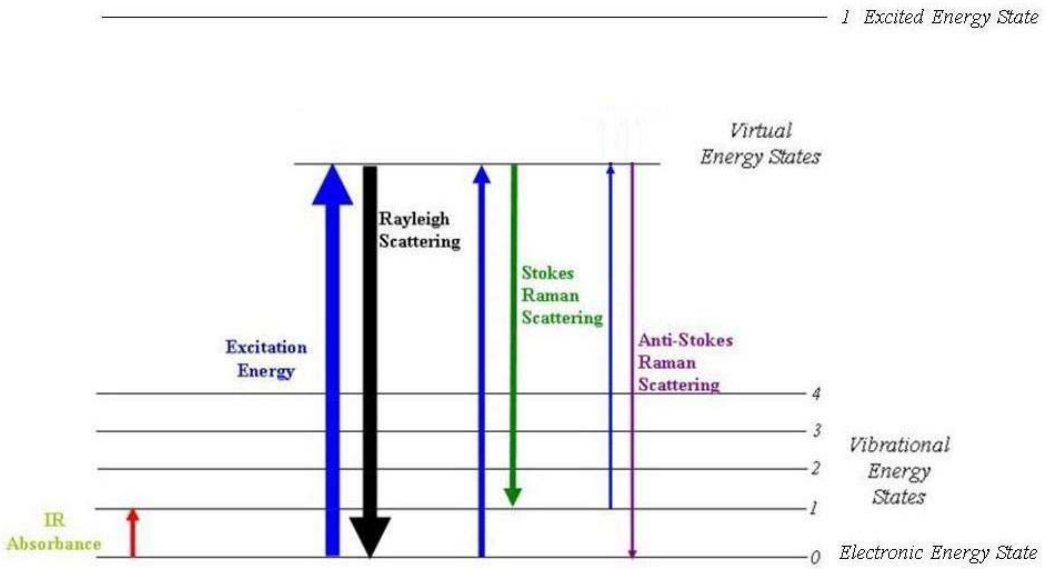

Figure 3.6 - Rayleigh and Raman process.

In the energy level diagram an arrow pointing upwards indicates photon annihilation and an arrow pointing downwards indicates photon creation. Unbroken horizontal lines denote discrete quantum states of the molecule. In a real absorption process energy is conserved and the resulting state of the system is a discrete state. In the Raman process, absorption without energy conservation is called virtual absorption and the resulting state is described as a virtual state. At this early stage in the development, the energy level say nothing about the mechanisms of the photon–molecule interactions or the probability of their occurrence.

Raman scattering is inherently incoherent and as a result the intensity of scattering from a material system of N non-interacting molecules is simply N times that from one molecule and is independent of the bulk structure of the material system.

In contrast, Rayleigh scattering from a material system depends on the nature and structure of the system as well as the concentration of the scattering species The intensity of Rayleigh and Raman scattering is directly proportional to the irradiance of the incident radiation and so such scattering can be described as a linear process [11].

3.3 Rayleigh and Raman scattering: classical theory

The approach to the theory of Rayleigh and Raman scattering can be classical or quantum mechanics; in this paragraph here reported the approach in which both the electromagnetic radiation and the material system are treated classically. Although the classical theory cannot deal with all aspects of Rayleigh and Raman scattering, it does provide useful information on different aspect of scattering such as the frequency dependence and also some aspects of the selection rules [12,13].

3.3.1 First-order induced electric dipole

To study the Raman scattering phenomena, consider a molecule subject to an incident radiation and consider this radiation as a monochromatic radiation [12]. The objective is to calculate for a molecule the frequency-dependent linear induced electric dipole vectors $p^{(1)}$, using the relationship

$$\boldsymbol{p^{(1)} = \alpha \cdot E} \tag{3.17}$$

where E is the electric field vector of the incident, monochromatic radiation of frequency ω_1, and $\boldsymbol{\alpha}$ is the polarizability tensor of the molecule. The polarizability tensor will be a function of the molecular

vibrational frequencies. The scattering system shall be consider one molecule which is free to vibrate, but does not rotate: the molecule is space-fixed in its equilibrium configuration, but the nuclei may vibrate about their equilibrium positions. The molecule may oscillate around its centre, Q, and the inter-nuclear distance Q_k can be written as:

$$Q_k = Q_{k0} cos(\omega_k t + \delta_k) \tag{3.18}$$

where Q_{k0} is the normal coordinate amplitude and δ_k a phase factor. The variation of the polarizability with vibrations of the molecule can be expressed by expanding each component $\alpha_{\rho\sigma}$ of the polarizability tensor $\boldsymbol{\alpha}$ in a Taylor series, as follows:

$$\alpha_{\rho\sigma} = (\alpha_{\rho\sigma})_0 + \sum_k \left(\frac{\partial \alpha_{\rho\sigma}}{\partial Q_k}\right)_0 Q_k + \frac{1}{2}\sum_{k,l}\left(\frac{\partial^2 \alpha_{\rho\sigma}}{\partial Q_k \partial Q_l}\right)_0 Q_k Q_{l\ldots} \tag{3.19}$$

where $(\alpha_{\rho\sigma})_0$ is the value of $\alpha_{\rho\sigma}$ at the equilibrium configuration. The subscript '0' on the derivatives indicates that these are to be taken at the equilibrium configuration. It is possible to make the electrical harmonic approximation and so neglect the terms which involve powers of Q higher than the first orderNow it is possible to write eq. (3.19) as follow

$$(\alpha_{\rho\sigma})_k = (\alpha_{\rho\sigma})_0 + (\alpha'_{\rho\sigma})_k Q_k \tag{3.20}$$

where

$$(\alpha'_{\rho\sigma})_k = \left(\frac{\partial \alpha_{\rho\sigma}}{\partial Q_k}\right)_0 \tag{3.21}$$

The $(\alpha'_{\rho\sigma})_k$ are components of a new tensor $\boldsymbol{\alpha}'_k$ which can call a derived polarizability tensor. As eq. (3.20) is valid for all tensor components it is possible to write

$$\boldsymbol{\alpha}_k = \boldsymbol{\alpha}_0 + \boldsymbol{\alpha}'_k Q_k \tag{3.22}$$

where $\boldsymbol{\alpha}_k$ is a tensor with components $(\alpha_{\rho\sigma})_k$. Combining eq. (1.10) with eq. (1.13) we obtain the time dependence of the polarizability tensor:

$$\boldsymbol{\alpha}_k = \boldsymbol{\alpha}_0 + \boldsymbol{\alpha}'_k Q_{k0} cos(\omega_k t + \delta_k) \tag{3.23}$$

Introducing into eq. (3.17) the frequency dependence of E given by:

$$\boldsymbol{E} = \boldsymbol{E}_0 cos\omega_1 t \tag{3.24}$$

and of $\boldsymbol{\alpha}_k$ given by eq. (3.23), obtain:

$$\boldsymbol{p}^{(1)} = \boldsymbol{\alpha}_0 \boldsymbol{E}_0 cos\omega_1 t + \boldsymbol{\alpha}'_k \boldsymbol{E}_0 Q_{k0} cos(\omega_k t + \delta_k) cos\omega_1 t \tag{3.25}$$

Using the trigonometric identity

$$cosAcosB = \frac{1}{2}\{cos(A+B) + cos(A-B)\} \tag{3.26}$$

the second term in eq. (1.17) may be rewritten and then the expression for $\boldsymbol{p}^{(1)}$ became

$$\boldsymbol{p}^{(1)} = \boldsymbol{p}^{(1)}(\omega_1) + \boldsymbol{p}^{(1)}(\omega_1 - \omega_k) + \boldsymbol{p}^{(1)}(\omega_1 + \omega_k) \tag{3.27}$$

Here, the Rayleigh line is represented by

$$\boldsymbol{p}^{(1)}(\omega_1) = \boldsymbol{p}_0^{Ray} cos\omega_1 t \tag{3.28}$$

$$\text{with } \boldsymbol{p}_0^{Ray} = \boldsymbol{\alpha}^{Ray} \cdot \boldsymbol{E}_0 \tag{3.29}$$

$$\text{and } \boldsymbol{\alpha}^{Ray} = \boldsymbol{\alpha}_0 \tag{3.30}$$

Indeed Raman bands are represented by

$$\boldsymbol{p}^{(1)}(\omega_1 \pm \omega_k) = \boldsymbol{p}_{k0}^{Ram} cos(\omega_1 \pm \omega_k \pm \delta_k)t \tag{3.31}$$

$$\text{with } \boldsymbol{p}_{k0}^{Ram} = \boldsymbol{\alpha}_k^{Ram} \cdot \boldsymbol{E}_0 \tag{3.32}$$

$$\text{And } \boldsymbol{\alpha}_k^{Ram} = \frac{1}{2}\boldsymbol{\alpha}'_k Q_k \tag{3.33}$$

3.3.2 $\boldsymbol{\alpha^{Ray}}$ and $\boldsymbol{\alpha_k^{Ram}}$ scattering conditions

The necessary condition for Rayleigh scattering is that $\boldsymbol{\alpha}^{Ray}$ be non-zero. As all molecules are polarisable, the classical equilibrium polarizability tensor $\boldsymbol{\alpha}_0$ will always have some non-zero components and so $\boldsymbol{\alpha}^{Ray}$ is always non-zero. Thus all molecules exhibit Rayleigh scattering [11].

The corresponding necessary condition for Raman scattering associated with a molecular frequency ω_k is that a Raman α_k^{Ram} be non-zero. This requires that at least one of the components $\left(\alpha'_{\rho\sigma}\right)_k$ of the derived polarizability tensor $\boldsymbol{\alpha}'_k$ is non-zero. As said before, in the eq. (3.21) the $\left(\alpha'_{\rho\sigma}\right)_k$ factor is the derivative of the $\rho\sigma$ component of the polarizability tensor with respect to the normal coordinate of vibration Q_k, taken at the equilibrium position. Thus, the condition for Raman activity is that, for at

least one component of the polarizability tensor, a plot of that component against the normal coordinate must have a non-gradient at the equilibrium position.

3.3.3 Selection rules for fundamental vibrations

The study of molecular vibration can be deal with starting from classical model that consider the nuclei such as simple material points with mass m. Inter-nuclear forces that hold together the molecule are considered similar to those performed by springs without mass which, when disturbed, they tend to re-establish the distances and angles of the equilibrium condition. The selection rules in their classical form, although appearing deceptively simple in concept, become progressively more difficult to apply as the complexity of the molecule increases. In dealing with these specific cases it will be instructive to consider the infrared activity as well as the Raman activity so that comparisons can be made. According to classical theory, the condition for vibrational infrared activity is that at least one of the dipole moment component derivatives with respect to the normal coordinate Q_k, taken at the equilibrium position, should be non-zero. This means that, for at least one of the components of the dipole moment vector, a plot of that component against the normal coordinate must have a non-zero gradient at the equilibrium position.

3.3.3.1 Diatomic molecules

First, consider a homonuclear diatomic molecule A_2 which has just one mode of vibration. Such a molecule has no permanent dipole moment in the equilibrium position because of the symmetry of the electron distribution. This symmetry does not change with small changes in the internuclear separation, and so the dipole remains zero during a vibration and hence the derivative is zero. Clearly the molecule has a non-zero polarizability, and that may be represent by a ellipsoid; however, considering a σ bond, the polarizability will be the same in all directions at right angles to the bond, and the polarizability tensor is then defined by just two components:

- $\boldsymbol{\alpha}_{\parallel}$, the polarizability along the bond,
- $\boldsymbol{\alpha}_{\perp}$, the polarizability at right angles to the bond. For a given internuclear separation the mean polarizability $\boldsymbol{\alpha}$ is then given by $\frac{\mathbf{1}}{\mathbf{3}}(\boldsymbol{\alpha}_{\parallel} + \mathbf{2}\boldsymbol{\alpha}_{\perp})$ and the anisotropy $\boldsymbol{\gamma}$ by $(\boldsymbol{\alpha}_{\parallel} - \boldsymbol{\alpha}_{\perp})$.

How During the vibration of the A_2 molecule these polarizability components change but is not so easy to calculate how much amount that changing.

In such molecules, it is reasonably to expect $\left(\frac{\partial \alpha_{\parallel}}{\partial Q}\right)_0$ and $\left(\frac{\partial \gamma}{\partial Q}\right)_0$ to be non-zero and of different magnitudes and hence $\left(\frac{\partial \alpha}{\partial Q}\right)_0$ and $\left(\frac{\partial \gamma}{\partial Q}\right)_0$ to be non-zero. Thus, the vibrations of A_2 diatomic molecules will be Raman active.

Consider now the case of a heteronuclear diatomic molecule AB which has also just one mode of vibration. The consideration given above for polarizability changes in A_2 molecules can be expected to apply to AB molecules, and thus the vibration will be Raman active. Indeed the molecule AB will necessarily have a permanent dipole moment because there will be an asymmetry in its electron distribution. The variation of the dipole moment component along the bond direction with inter-nuclear distance can be represented as shown in Fig. 3.7.

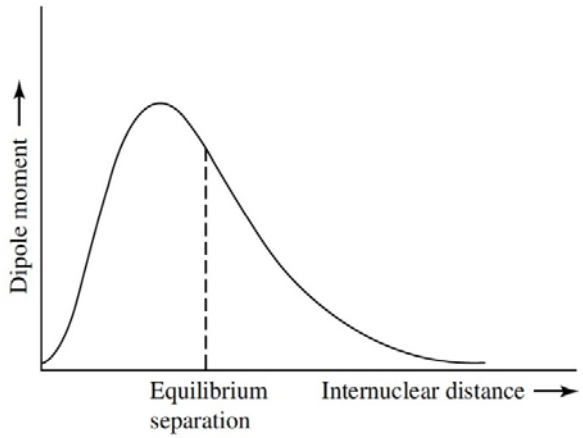

Figure 3.7 - Variation of dipole moment with internuclear distance in a diatomic molecule AB (here the dipole moment derivative at the equilibrium separation is negative) [12].

The components of the dipole at right angles to the bond direction are, of course, always zero; the maximum dipole moment must occur at an internuclear distance different from the equilibrium distance, so that the derivative at the equilibrium position is non-zero. This is the case for all heteronuclear diatomic molecules and thus the vibration in AB molecules will be Raman active.

3.3.3.2 Polyatomic molecules

Consider now a polyatomic molecule composed by N atoms. The total number of coordinates, necessary to specify the position of this N atoms, is 3N; of that coordinates 3 are used to describe the translational motion. In the non-linear molecules we need also another 3 coordinates to specify the space molecule orientation, indeed in the linear molecule we need only 2 coordinates.

So the number of vibrational coordinates are:

- Non-linear polyatomic molecule → 3N (total) – 3 (translational) – 3 (orientation) = 3N-6
- Linear polyatomic molecule → 3N (total) – 3 (translational) – 2 (orientation) = 3N-5.

The 3N-6 number of coordinates of a non-linear molecule con be described by 3N-6 vibrational motion. In each vibrational motion all the atoms in the molecule vibrate with the same frequency and pass through the equilibrium positions simultaneously. The related vibration of single atoms can be differs in amplitude and direction but the centre does not move and the molecule don't rotate.

In polyatomic molecules the total dipole moment can be considered made up of contributions from individual bond dipoles, and then consider each heteronuclear bond as having a non-zero bond dipole derivative at the equilibrium position and combine such derivatives vectorially to determine Raman activities in particular modes of vibration.

Similarly, the total molecular polarizability can be regarded as made up of contributions from individual bond polarizabilities, and assume that these bond polarizabilities show the same qualitative behaviour as in A_2. However, in polyatomic molecules the forms of the vibrations are relatively complicated and involve, for example, the stretching and compression of more than one bond. The Raman activity of such a vibration depends on the components of the overall derived polarizability tensor which is formed by tensor addition of individual derived bond polarizability tensors, taking into account the relative phases of the motions in each bond.

In nature there are different polyatomic molecules; starting to talk about very simple model: linear symmetric molecule ABA. Such a molecule has four modes of vibration: a symmetric stretching mode Q_1 , an antisymmetric stretching mode Q_2, and two bending modes Q_{3a} and Q_{3b}. This ABA molecule has no permanent dipole because of the symmetry of the electron distribution: the symmetric stretching mode Q_1 there are simultaneously stretching and compression of the A–B bonds, however, for this kind of vibration the non-zero bond polarizability derivatives in the two A–B bonds are additive and the vibration is Raman active.

This evidence can be expressed by the following equations that are refered to the ellipsoid axes of the molecular polarizability: $\left(\frac{\partial \alpha_{xx}}{\partial Q_1}\right)_0 = \left(\frac{\partial \alpha_{yy}}{\partial Q_1}\right)_0$ and $\left(\frac{\partial \alpha_{zz}}{\partial Q_1}\right)_0$ are non-zero; also $\left(\frac{\partial \alpha_{xy}}{\partial Q_1}\right)_0 = \left(\frac{\partial \alpha_{yz}}{\partial Q_1}\right)_0 = \left(\frac{\partial \alpha_{zx}}{\partial Q_1}\right)_0 = 0$.

The situation is quite different for the antisymmetric stretching mode Q_2, in which one the A–B bonds are stretched and compressed not at the same moments. Indeed, for that kind of stretching, the bond polarizability derivatives cancel each other and for the molecular polarizability derivatives is obtained

$\left(\frac{\partial\alpha_{xx}}{\partial Q_2}\right)_0 = \left(\frac{\partial\alpha_{yy}}{\partial Q_2}\right)_0 = \left(\frac{\partial\alpha_{zz}}{\partial Q_2}\right)_0 = \left(\frac{\partial\alpha_{xy}}{\partial Q_1}\right)_0 = \left(\frac{\partial\alpha_{yz}}{\partial Q_2}\right)_0 = \left(\frac{\partial\alpha_{zx}}{\partial Q_2}\right)_0 = 0$ and so $\left(\frac{\partial a}{\partial Q_2}\right)_0$ and $\left(\frac{\partial\gamma}{\partial Q_2}\right)_0$ are both zero. Thus, the Q_2 mode is Raman inactive.

For the degenerate bending modes Q_{3a} and Q_{3b}, all six molecular polarizability derivatives are zero for both modes. Thus, $\left(\frac{\partial a}{\partial Q_{3a}}\right)_0 = \left(\frac{\partial a}{\partial Q_{3b}}\right)_0 = \left(\frac{\partial\gamma}{\partial Q_{3a}}\right)_0 = \left(\frac{\partial\gamma}{\partial Q_{3b}}\right)_0 = 0$ and both modes are Raman inactive.

Finally, consider the case of a non-linear ABA molecule. Such a molecule has three modes of vibration: Q_1, a symmetric stretching mode; Q_2, a symmetric bending mode; and Q_3, an antisymmetric stretching mode.

The vibration models can be defined as: (a) Q_1 is Raman active with $\left(\frac{\partial\alpha_{xx}}{\partial Q_1}\right)_0$, $\left(\frac{\partial\alpha_{yy}}{\partial Q_1}\right)_0$ and $\left(\frac{\partial\alpha_{zz}}{\partial Q_1}\right)_0$ non-zero, and $\left(\frac{\partial\alpha_{xy}}{\partial Q_1}\right)_0 = \left(\frac{\partial\alpha_{yz}}{\partial Q_2}\right)_0 = \left(\frac{\partial\alpha_{zx}}{\partial Q_2}\right)_0 = 0$ so that both $\left(\frac{\partial a}{\partial Q_1}\right)_0$ and $\left(\frac{\partial\gamma}{\partial Q_1}\right)_0$ are non-zero; (b) Q_2 is also Raman active with the same dipole and polarizability components non-zero; (c) Q_3 is also Raman active. This activity arises because the space-fixed z and y axes no longer remain axes of the polarizability ellipsoid during the whole of the vibration.

Thus, although α_{yz} is zero, in the equilibrium configuration $\left(\frac{\partial\alpha_{yz}}{\partial Q_3}\right)_0$ is non-zero. This is the only non-zero component of the derived polarizability for this mode, and hence $\left(\frac{\partial a}{\partial Q_{3a}}\right)_0 = 0$, although $\left(\frac{\partial\gamma}{\partial Q_3}\right)_0$ is non-zero.

In molecules containing many atoms many of the vibrational frequencies are very close in value so that bands overlie each other and a relatively simple spectrum results. In some molecules, especially those of high symmetry, some vibrations may be both infrared and Raman inactive; however, such modes may be active in light-scattering spectra of non-linear origin, as for example in hyper-Raman spectra.

3.3.4 Coherence properties of Rayleigh and Raman scattering

The classical treatment given earlier is based on a single scattering molecule which, although free to vibrate, is space-fixed in its equilibrium configuration. However in any experimental study scattering will be observed from a relatively large number of molecules and their orientations will not necessarily be fixed. For such an assembly of molecules there is an important difference between Rayleigh and Raman scattering.: Rayleigh scattering is in phase with the incident radiation, whereas Raman scattering has an arbitrary phase relation to the incident radiation. This is because the phase of Raman scattering depends on the phase of the molecular vibration and this to a very good approximation varies arbitrarily from molecule to molecule; so the molecules act as independent sources of radiation.

The situation is different for Rayleigh scattering because interference between the scattering from different molecules is possible and so the structural arrangement of the scattering molecules will play a role.

With the coherence properties of Rayleigh and Raman scattering previously discussed it is possible to proceed from the simple case of one space-fixed molecule to an assembly of freely rotating molecules and calculate the intensity and polarization properties of the scattered radiation as a function of the illumination–observation geometry.

3.3.5 Raman spectra

Raman spectra are normally presented in terms of wavenumber shift $\Delta\tilde{\upsilon}$ that, for a given Raman band is define as $\Delta\tilde{\nu} = \tilde{\nu}_1 + \tilde{\nu}'$ that represent the difference between the absolute peak wavenumber ($\tilde{\nu}_1$) and the exciting radiation wavenumber $\tilde{\nu}_1$.

With this definition $\Delta\tilde{\upsilon}$ is positive for Stokes Raman scattering ($\tilde{\nu}' = \tilde{\nu}_1 - \tilde{\nu}_M$) and negative for anti-Stokes Raman scattering ($\tilde{\nu}' = \tilde{\nu}_1 + \tilde{\nu}_M$). The characteristic molecular property, the wavenumber $\tilde{\nu}_M$ is given by $|\Delta\tilde{\upsilon}|$; for Stokes Raman scattering $\Delta\tilde{\upsilon} = \tilde{\nu}_M$.

For Stokes Raman scattering $\tilde{\nu}_M$ can be used as an equivalent alternative to $\Delta\tilde{\nu}$. It has been recommended by IUPAC that Raman spectra should be plotted with the abscissa linear in the wavenumber shift $\Delta\tilde{\upsilon}$ (unit: cm^{-1}) increasing to the left, and the ordinate linear and proportional to the intensity.

As an example a theorical Raman spectrum is reported in Fig. 3.8, which show the recommended conventions. The use of a quotient of a physical quantity and a unit, that is quantity calculus, in the labelling of the wavenumber axis should be noted.

This practice means that the values of the quantities are presented as pure numbers. Quantity calculus should also be used for the intensity axis when the intensity has a specific unit; otherwise, the ordinate axis should be labelled 'intensity' with an arrow indicating that the intensity increases upwards.

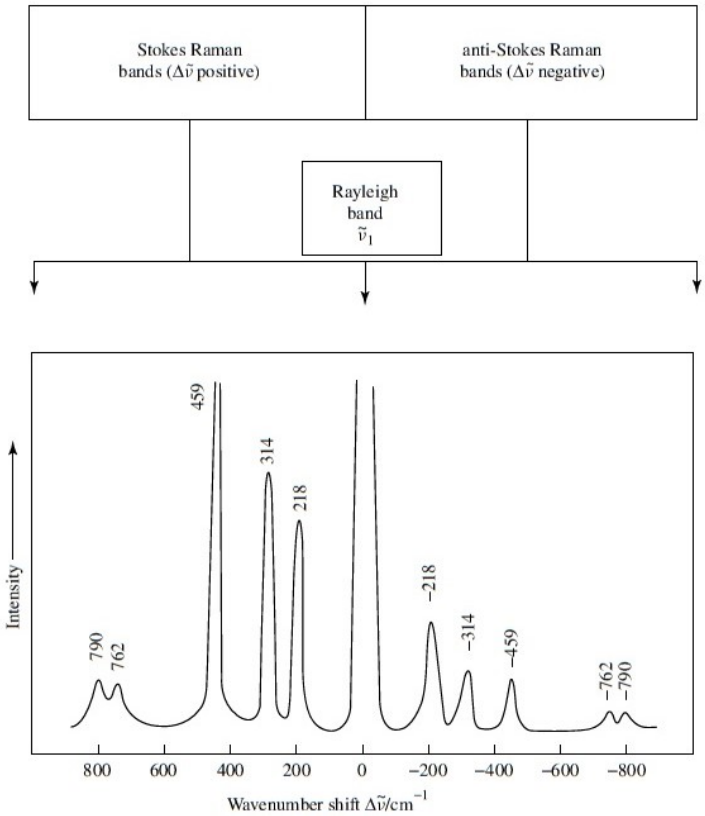

Figure 3.8 - Rayleigh and Raman spectra of carbon tetrachloride (liquid) presented according to IUPAC recommendations. Note that normally only Stokes Raman bands are studied. It is then acceptable to label the abscissa as wavenumber/cm^{-1} [12].

3.3.6 Limitations of the classical theory

The classical theory gives the correct frequency dependence for Rayleigh scattering and vibrational Raman scattering. However, it has many limitations:

- it cannot be applied to molecular rotations beacuse classical theory does not ascribe specific discrete rotational frequencies to molecules.
- the result for the vibrational Raman scattering tensor given by eq. (1.25) $\boldsymbol{\alpha_k^{Ram} = \frac{1}{2}\alpha'_k Q_k}$ is only partly correct. When quantum mechanics is used for the treatment of molecular vibrations, the classical amplitude $\boldsymbol{Q_k}$ is replaced by a quantum mechanical amplitude.
- classical theory explain only the formation of different Raman bands, don't give any explanation on Stokes and Anti-Stokes different intensity.

3.4 Full quantum mechanical treatment of Rayleigh and Raman scattering

In this chapter there is show how quantum mechanics, on the basis of certain assumptions, enables to obtain expressions for the first-order induced transition electric dipole moment $\left(\boldsymbol{p}^{(1)}\right)_{fi}$ and hence the transition polarizability $(\alpha)_{\mathrm{fi}}$ for Rayleigh and Raman scattering.

The treatment is based on time-dependent perturbation theory [14]. As said in the previous paragraph, the general formula for $(\alpha)_{\mathrm{fi}}$ obtained by classical treatment is not particularly tractable and it is necessary to introduce a number of simplifications to obtain more useful expressions for $(\alpha)_{\mathrm{fi}}$. The formulae obtained with quantum-mechanic treatments are then used to valuate particular types of Raman scattering, namely rotational, vibrational and electronic Raman scattering, under normal and resonance conditions.

3.4.1 Unperturbed time-dependent wave function

Now start with the unperturbed time-dependent wave function for the molecule:

$$\Psi_r^{(0)} = \psi_r exp - it(\omega_r - i\Gamma_r) \tag{3.34}$$

Where Γ_r is related to the half-width half-height or the transition line and the lifetime of the state $\tau \propto \frac{1}{2\Gamma_r}$ and $\omega_r = \frac{E_r}{\hbar}$.

The perturbed wave function can be expressed as:

$$\Psi_r' = \Psi_r^{(0)} + \Psi_r^{(1)} + \cdots \tag{3.35}$$

From this it is possible to define the electric dipole transition moment for the transition $f \leftarrow i$ when the system is perturbed:

$$(p)_{fi} = \langle \Psi_f' | \hat{p} | \Psi_i' \rangle \tag{3.36}$$

Placing eq. (3.35) into eqn. (3.36) the equation became:

$$(p)_{fi} = \left(p^{(0)}\right)_{fi} + \left(p^{(1)}\right)_{fi} + \ldots. \tag{3.37}$$

where

$$\left(p^{(0)}\right)_{fi} = \langle \Psi_f^{(0)} | \hat{p} | \Psi_i^{(0)} \rangle \tag{3.38}$$

$$\left(p^{(1)}\right)_{fi} = \langle \Psi_f^{(1)} | \hat{p} | \Psi_i^{(0)} \rangle + \langle \Psi_f^{(0)} | \hat{p} | \Psi_i^{(1)} \rangle \tag{3.39}$$

It is the first term that gives rise to both Rayleigh and Raman scattering. Using first order time-dependent perturbation theory, the wave function can be written as:

$$\Psi_i^{(1)} = \sum_r a_{ir}\, \Psi_r^{(0)} \; and \; \Psi_f^{(1)} = \sum_r a_{fr}\, \Psi_r^{(0)} \tag{3.40}$$

Placing this into eq. (3.39):

$$\left(\tilde{p}^{(1)}\right)_{fi} = \sum_r a^*_{fr} \langle \Psi_r^{(0)} | \hat{p} | \Psi_i^{(0)} \rangle + \sum_r a_{ir} \langle \Psi_f^{(0)} | \hat{p} | \Psi_r^{(0)} \rangle \tag{3.41}$$

Where the tilde above the p is a reminder that this term is in general complex. The coefficients present in the previous equation are then given by the perturbation Hamiltonian generated by the incoming photon:

$$a_{ir} = -\frac{i}{\hbar} \int_0^t \langle \Psi_r^{(0)} | H_p | \Psi_i^{(0)} \rangle \, dt' \tag{3.42}$$

$$a^*_{fr} = \frac{i}{\hbar} \int_0^t \langle \Psi_f^{(0)} | H_p | \Psi_r^{(0)} \rangle \, dt' \tag{3.43}$$

$$H_p = -\hat{p}_\sigma E_\sigma \tag{3.44}$$

$$E_\sigma = \tilde{E}_{\sigma 0} exp(-it\omega_0) + \tilde{E}^*_{\sigma 0} exp(it\omega_0) \tag{3.45}$$

Place now the eq. (3.34) in these equations. Since the lifetime of the initial and final states are taken to be infinite $\Gamma_i = \Gamma_f = 0$.

$$\begin{aligned} \left(\tilde{p}^{(1)}\right)_{fi} = & \frac{i}{\hbar} \sum_{r \neq f,i} \left[\frac{\langle \psi_f^{(0)} | \hat{p}_\sigma | \psi_r^{(0)} \rangle \langle \psi_r^{(0)} | \hat{p}_\rho | \psi_i^{(0)} \rangle}{\omega_{rf} - \omega_0 - i\Gamma_r} + \frac{\langle \psi_f^{(0)} | \hat{p}_\rho | \psi_r^{(0)} \rangle \langle \psi_r^{(0)} | \hat{p}_\sigma | \psi_i^{(0)} \rangle}{\omega_{ri} + \omega_0 + i\Gamma_r} \right] \tilde{E}^*_{\sigma 0} exp\left[it\left(\omega_0 + \omega_{fi}\right) \right] \\ & + \frac{i}{\hbar} \sum_{r \neq f,i} \left[\frac{\langle \psi_f^{(0)} | \hat{p}_\sigma | \psi_r^{(0)} \rangle \langle \psi_r^{(0)} | \hat{p}_\rho | \psi_i^{(0)} \rangle}{\omega_{rf} + \omega_0 + i\Gamma_r} + \frac{\langle \psi_f^{(0)} | \hat{p}_\rho | \psi_r^{(0)} \rangle \langle \psi_r^{(0)} | \hat{p}_\sigma | \psi_i^{(0)} \rangle}{\omega_{ri} - \omega_0 - i\Gamma_r} \right] \tilde{E}_{\sigma 0} exp\left[-it\left(\omega_0 - \omega_{fi}\right) \right] \end{aligned} \tag{3.46}$$

where

$$\omega_{rf} = \omega_r - \omega_f \tag{3.47}$$

The radiation dipole that is associated with this complex transition moment is:

$$\left(p^{(1)}\right)_{fi} = \left(\tilde{p}^{(1)}\right)_{fi} + \left(\tilde{p}^{(1)}\right)^{*}_{fi} \tag{3.48}$$

Here are two frequency dependencies in the transition moment, $(\omega_0 - \omega_{fi})$ and $(\omega_0 + \omega_{fi})$:

- the $(\boldsymbol{\omega_0 - \omega_{fi}})$ term will only be associated with real radiation if $(\boldsymbol{\omega_0 - \omega_{fi}}) > 0$. This is always true if initial state is lower then or equal to the final state. If the final state is lower then as long as the photon has has an energy larger then the energy gap between the initial and final state this will be true. This term take care of both Rayleigh and Raman scattering.
- the $(\boldsymbol{\omega_0 + \omega_{fi}})$ term will only be associated with real radiation if $(\boldsymbol{\omega_0 + \omega_{fi}}) > 0$.

From this it is possible to define a general transition polarizability tensor:

$$\left(\alpha_{\rho\sigma}\right)_{fi} = \frac{i}{\hbar}\sum_{r\neq f,i}\left[\frac{\langle\psi_f^{(0)}|\hat{p}_\sigma|\psi_r^{(0)}\rangle\langle\psi_r^{(0)}|\hat{p}_\rho|\psi_i^{(0)}\rangle}{\omega_{rf}+\omega_0+i\Gamma_r} + \frac{\langle\psi_f^{(0)}|\hat{p}_\rho|\psi_r^{(0)}\rangle\langle\psi_r^{(0)}|\hat{p}_\sigma|\psi_i^{(0)}\rangle}{\omega_{ri}-\omega_0-i\Gamma_r}\right] \tag{3.49}$$

In general this term is complex, but by choosing ω_0 carefully it can become real; after that step it is possible to treat this term as the polarizability tensor from the classical analysis.

Equation (3.39) can be written in terms of an operator:

$$\left(\alpha_{\rho\sigma}\right)_{fi} = \langle\psi_f^{(0)}|\hat{\alpha}_{\rho\sigma}|\psi_i^{(0)}\rangle \tag{3.50}$$

$$\hat{\alpha}_{\rho\sigma} = \frac{i}{\hbar}\sum_{r\neq f,i}\left[\frac{\hat{p}_\sigma|\psi_r^{(0)}\rangle\langle\psi_r^{(0)}|\hat{p}_\rho}{\omega_{rf}+\omega_0+i\Gamma_r} + \frac{\hat{p}_\rho|\psi_r^{(0)}\rangle\langle\psi_r^{(0)}|\hat{p}_\sigma}{\omega_{rf}-\omega_0-i\Gamma_r}\right] \tag{3.51}$$

In order to make this operator easer to deal with, starting to make a series of approximations:

1) adiabatic approximation:

$$|\psi_j\rangle = |e^j\rangle|v^j\rangle|R^j\rangle \tag{3.52}$$

$$\omega_j = \omega_{e^j} + \omega_{v^j} + \omega_{R^j} \tag{3.53}$$

That is the total wavefunction is separable into three parts: electronic, vibrational, and rotational.

2) The last assumption that is made is that the ground state of the molecule is non-degenerate.

After all of this what we are left with is:

$$(\alpha_{\rho\sigma})_{v^f R^f, v^i R^i} = \langle R^f|\langle v^f|\hat{\alpha}_{\rho\sigma}(Q)|v^i\rangle|R^i\rangle \tag{3.54}$$

$$\hat{\alpha}_{\rho\sigma}(Q) = \frac{1}{\hbar}\sum_{r\neq f,i}\left[\frac{\langle e^g|\hat{P}_\sigma|e^r\rangle\langle e^r|\hat{P}_\rho|e^g\rangle}{\omega_{e^re^g}+\omega_0} + \frac{\langle e^g|\hat{P}_\rho|e^r\rangle\langle e^r|\hat{P}_\sigma|e^g\rangle}{\omega_{e^re^g}-\omega_0}\right] \tag{3.55}$$

Dividing the rotational and vibrational parts of the tensor, the equation 3.56 is obtained:

$$\left(\alpha_{\rho\sigma}\right)_{v^fR^f,v^iR^i} = \langle R^f|l_{\rho\rho'}l_{\sigma\sigma'}|R^i\rangle\langle v^f|\hat{\alpha}_{\rho'\sigma'}(Q)|v^i\rangle \tag{3.56}$$

where $l_{\rho\rho'}l_{\sigma\sigma'}$ are directional cosines used in the transformation.

3.4.2 Vibrational transitions in molecules

If there is no any rotational transitions, such as in the case of solid molecules, then the first term in eq. (3.57) will become one and now it is possible to proceed in the same manner as the classical analysis and expand $\hat{\alpha}_{\rho\sigma}$ as a Taylor series; so the eq. (3.57) became:

$$\left(\alpha_{\rho\sigma}\right)_{v^f,v^i} = \left(\hat{\alpha}_{\rho\sigma}\right)_0\langle v^f|v^i\rangle + \frac{1}{2}\sum_k\left(\frac{\partial\hat{\alpha}_{\rho\sigma}}{\partial Q_k}\right)_0\langle v^f|Q_k|v^i\rangle \tag{3.58}$$

Doing an harmonic oscillator approximation, the vibrational wavefunctions can be written as:

$$\phi_{v^j} = \prod_k \phi^k_{v^j}(Q_k) \tag{3.59}$$

That is the product of harmonic oscillators, one for each normal mode of vibration with quantum number υ^j_k . Placing this into eq. (3.58):

$$\left(\alpha_{\rho\sigma}\right)_{v^f,v^i} = \left(\hat{\alpha}_{\rho\sigma}\right)_0\prod_k\langle\phi^k_{v^f}|\phi^k_{v^i}\rangle + \frac{1}{2}\sum_k\left(\frac{\partial\hat{\alpha}_{\rho\sigma}}{\partial Q_k}\right)_0\prod_k\langle\phi^k_{v^f}|Q_k|\phi^k_{v^i}\rangle \tag{3.60}$$

It is possible to find now what transitions are allowed by looking at the properties of the harmonic oscillator wavefunctions:

$$\langle\phi^k_{v^f}|\phi^k_{v^i}\rangle = \begin{cases}0 & for\ \ v^f_k \neq v^f_k\\ 1 & for\ \ v^f_k = v^f_k\end{cases} \tag{3.61}$$

$$\langle \phi_{v^f}^k | Q_k | \phi_{v^i}^k \rangle = \begin{cases} \sqrt{v_k^i + 1 b_{vk}} & for \quad v_k^f = v_k^i + 1 \\ \sqrt{v_k^i b_{vk}} & for \quad v_k^f = v_k^i - 1 \\ 0 & otherwise \end{cases} \tag{3.62}$$

where

$$b_{vk} = \sqrt{\frac{\hbar}{2\omega_k}} \tag{3.63}$$

In order to have, in the eq. (3.60), the two to be non-zero some conditions have to be satisfied:

1) The first term is non-zero only if none of the vibrational quantum numbers change and if $\hat{\boldsymbol{\alpha}}_{\boldsymbol{\rho\sigma}}$ is non-zero. Since not all the components of the equilibrium polarizability tensor can be zero there will always be Rayleigh scattering.
2) The second term is non-zero if all the terms in the product are non-zero. This means that for the $\mathbf{k^{th}}$ mode $\mathbf{v_k^f = v_k^i \pm 1}$ and $\mathbf{v_j^f = v_j^i}$ for $\mathbf{j = k}$. A transition of this type gives rise to the Stokes and anti-Stokes lines. In addition to this $\left(\frac{\partial \hat{\alpha}_{\rho\sigma}}{\partial Q_k}\right)_0$ must also be non-zero.

For spectroscopy it is more convenient to use the wavenumber, $\tilde{\nu}$, instead of frequency,ω for spectra. Now with the selection rules for vibrational transitions calculated it is straightforward to find the wavenumber shifts useful for the Raman effect: a negative wavenumber shift $(\tilde{\nu}_0 - |\Delta\tilde{\nu}|)$ will give the Stokes line and a positive wavenumber shift $(\tilde{\nu}_0 + |\Delta\tilde{\nu}|)$ will give anti-Stokes lines.
The energy levels of a harmonic oscillator is given by:

$$G_{(\upsilon)} = \frac{E_\upsilon}{hc} = \left(\upsilon + \frac{1}{2}\right)\tilde{\nu} \tag{3.64}$$

These energy levels are evenly spaced so the selection rule $\Delta\upsilon = \pm 1$ will lead to Raman lines with a wavenumber shift equal to $\tilde{\nu}_k$, for all allowed transitions (see Fig. 3.9).

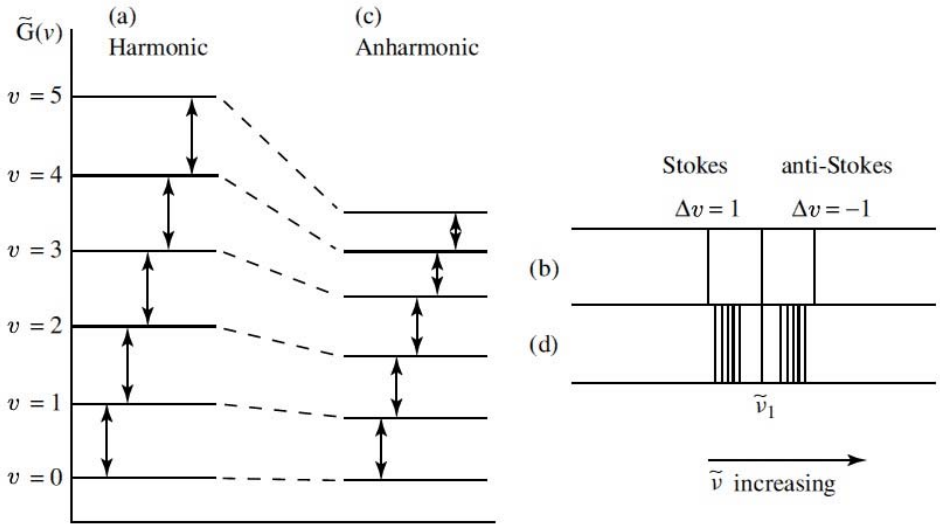

Figure 3.9 - Vibrational states **(a)** and Raman spectra **(b)** for a harmonic oscillator. Vibrational states **(c)** and Raman spectra **(d)** for an anharmonic oscillator [14].

For most molecule the vibrational modes are anharmonic. In this case the energy levels look like:

$$G_{(\upsilon)} = \left(\upsilon + \frac{1}{2}\right)\tilde{\nu}_e - \left(\upsilon + \frac{1}{2}\right)^2 \tilde{\nu}_e x_e \tag{3.65}$$

Where $\tilde{\nu}_e$ is the harmonic wavenumber and $x_e \ll 1$. Now the wavenumber shift for selection rules $\Delta\upsilon = 1$ is:

$$|\Delta\tilde{\nu}| = \tilde{\nu}_e - 2(\upsilon + 1)\tilde{\nu}_e x_e \tag{3.66}$$

Now the wavenumber shift is dependent on the vibrational quantum number meaning the spectra lines will be spread out as depicted in Fig.3.9(d).

3.5 Raman experimental apparatus

Essentially a Raman apparatus is composed by 5 components:

1) Source
2) Spectrometer
3) Sampling system
4) Detector

5) Controller PC

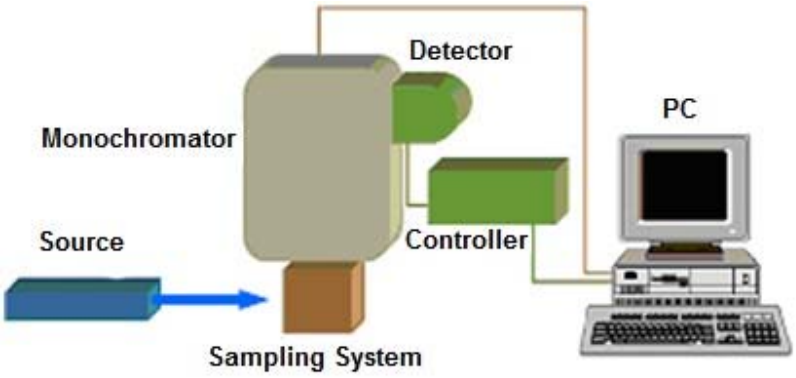

Figure 3.10 – schema for a experimental raman apparatus

3.5.1 Sources

To distinguish the Raman peaks it is necessary that the source used is monochromatic, in order to have only one Rayleigh line, from which the Raman lines can be well distinguished. Most common laser used in raman spectroscopy are show in fig 3.11; they are wavelength than go from violet (488nm) to infrared (1064nm).

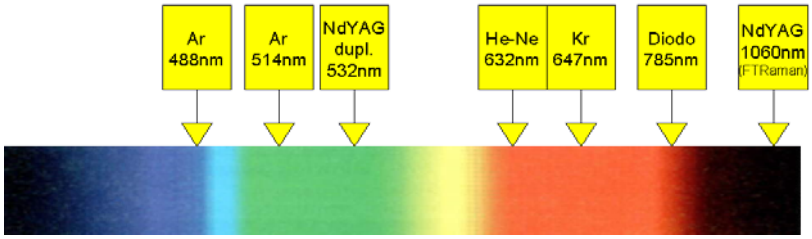

Figure 3.11 – lasers wavelenght used for Raman Spectroscopy

Although the Raman shift is independent of excitation wavelength (λ), that rule is not valid for the bands intensity. Figure 3.12 show an example of a spectrum obtained at different λ, together with a graph with a best-fit line that shows the dependence of the intensity of Raman lines I_R by ν_p (frequency of the light source):

$$I_R = f\left(\nu_p - \Delta\nu\right)^4$$

where $\Delta\nu$ is Raman shift.

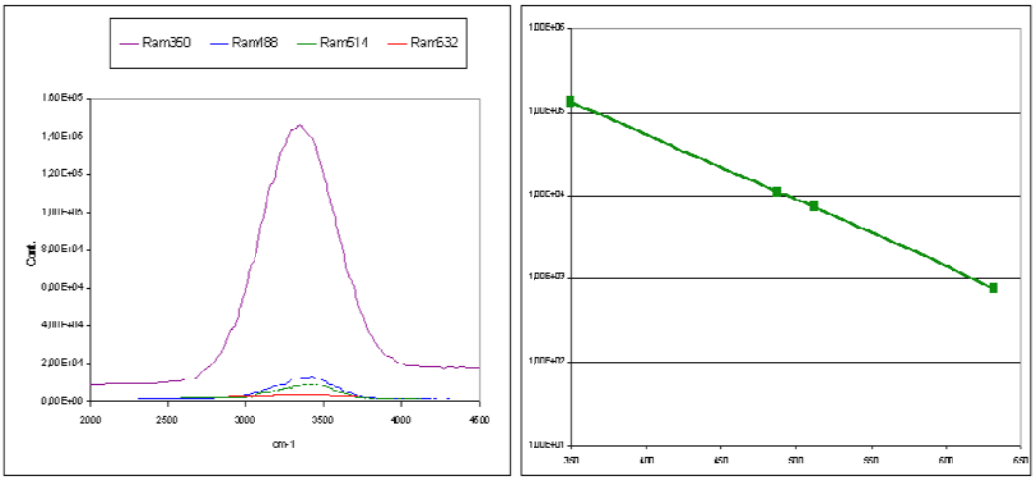

Figure 3.12 –Raman spectra obtained with different excitation wavelength (left) and graph with best-fit straight line

It is possible to note that although grows with increasing excitation wavelength, fluorescence also increases, up to completely cover the weak Raman signal. It is therefore necessary choose suitably the laser wavelength best suited for each type of sample. If the sample is a weak Raman emitter, it is better to use a far infrared laser (1060 nm) that stimulate very little fluorescence; in this way the Raman lines, although weak, can often be distinguished.

Using the spectrometer, as well as disperse the spectrum into its various components, it is possible to separate the intense Rayleigh scattering from the Raman signals.

3.5.2 Sampling system

Essentially there are three types of sampling, macro, micro and remote. The macro allows to analyze macroscopic samples, micro-sampling foresees the use of an optical microscope, while the remote system uses a sampling head to perform micro measurements but in different environments, thanks to the use of optical fibers.

The experimental measurements carried out for this thesis were made using a micro sampling system, namely MicroRaman.

3.5.3 PH3DRA experimental apparatus

In the schema below, the experimental apparatus used in this work is presented.

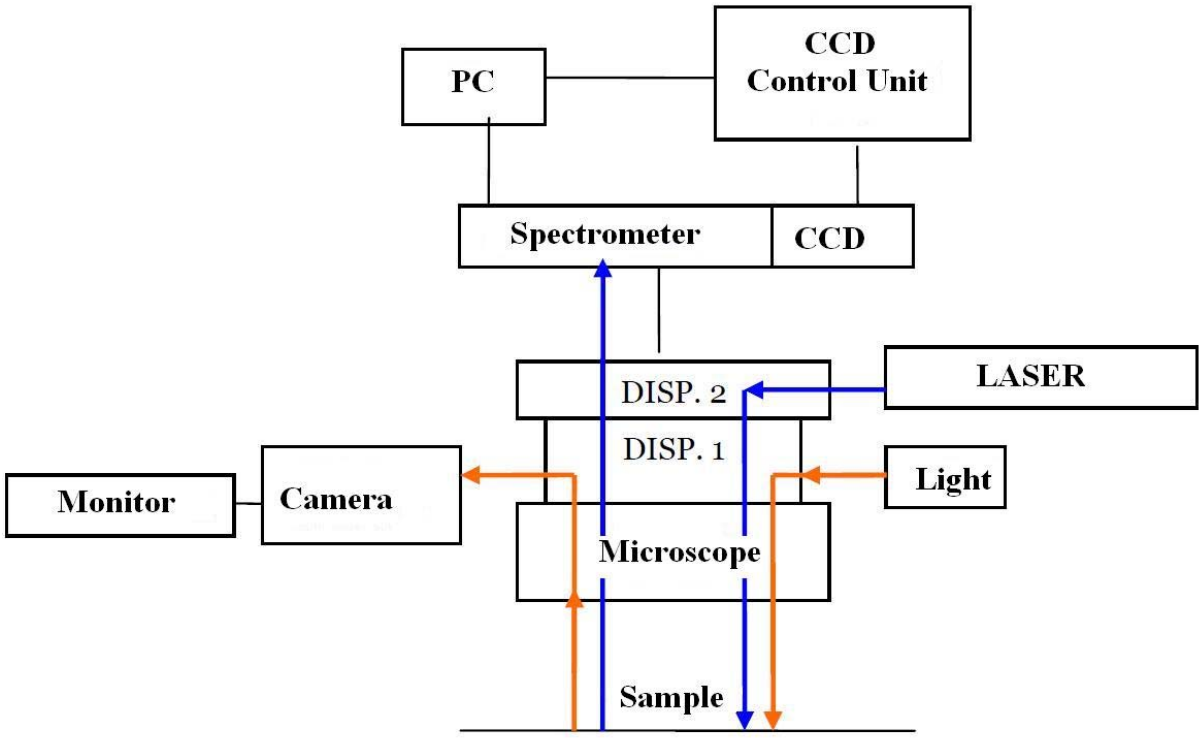

Figure 3.13 – experimental Raman apparatus used at PH3DRA laboratories.

Here presented all the components.

3.5.3.1 Optical Centring, focalization and observation

The laser light coming from the source arrive to the first device (DISP.2), where are located the interference filter, after a collimator and two mirrors that redirect the laser on a second filter (Notch filter), that in this phase is used as a mirror and reflect the laser on a diaphragm. From the diaphragm the laser goes inside another device (DISP.1) and finally arrive to the microscope.

The apparatus presents an Olimpus BX40 microscope with 4 different objective:

10× / 0.25

50× / 0.50

50× / 0.75

100× / 0.90

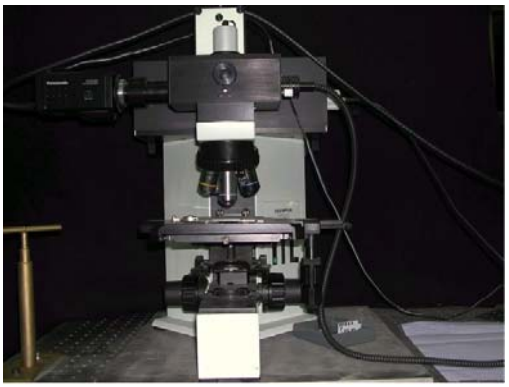

Figure 3.14 – Olimpus BX40 microscope.

The lighting of the sample, necessary for its centering and focusing, is provided by a light source of variable intensity (white source).
This light is transmitted through an optical fiber to a device of mirrors [DISP1], entering inside of the microscope tube, and from that comes on the sample, through some lens.
The light emitted by the sample walk through the inverse path to the DISP1 from which arrive to the camera that use an ½ inch CCD. The imagine acquired is transferred to a monitor. It is possible now the sample focusing.

3.5.3.2 Notch filter

One of the fundamental component of an experimental Raman apparatus is the Notch filter. It is a filter able to separate the Raman signal from the Rayleigh ones, that come from the sample [15]. This is necessary because the Rayleigh signal, 10^6-10^{12} times more intense than Raman, can cover completely the weak Stokes and/or Anti-Stokes peaks. The filter reflect the light with the same frequency of the laser used, stopping it, and indeed let it pass all the other frequency. This means that each laser has a specific Notch filter, centred on the emission wavelength.
The Notch guarantee an excellent transmission at high frequency and blocks the transmission of light with frequency of 785nm (in particular in the range 776-794nm).
After the laser light diffusion from the sample, the beam is collected by the microscope objective and walk through the inverse path inside the microscope. The beam goes in DISP.1, and it is reflected by different mirrors; after walk through the DISP.2, and through the diaphragm arrive to the Notch, that in this phase is a filter, scattering Rayleigh component. A series of mirrors and an optical fiber sent the beam to the spectrometer.

3.5.3.5 The Spectrometer

The spectrometer is a device that allow to separate the spectrum in its different component using diffraction gratings. A diffraction grating is a collection of reflecting (or transmitting) elements separated by a distance comparable to the wavelength of light under study. It may be thought of as a collection of diffracting elements, such as a pattern of transparent slits in an opaque screen, or a collection of reflecting grooves on a substrate. A reflection grating consists of a grating superimposed on a reflective surface, whereas a transmission grating consists of a grating superimposed on a transparent surface. An electromagnetic wave incident on a grating will, upon diffraction, have its electric field amplitude, or phase, or both, modified in a predictable manner.

When monochromatic light is incident on a grating surface, it is diffracted into discrete directions. We can picture each grating groove as being a very small, slit-shaped source of diffracted light. The light diffracted by each groove combines to form a diffracted wavefront. The usefulness of a grating depends on the fact that there exists a unique set of discrete angles along which, for a given spacing d between grooves, the diffracted light from each facet is in phase with the light diffracted from any other facet, so they combine constructively.

By convention, angles of incidence and diffraction are measured from the grating normal to the beam. For either reflection or transmission gratings, the algebraic signs of two angles differ if they are measured from opposite sides of the grating normal. Other sign conventions exist, so care must be taken in calculations to ensure that results are self consistent.

These relationships are expressed by the grating equation:

$$m\lambda = d(\sin\alpha + \sin\beta)$$

which governs the angles of diffraction from a grating of groove spacing d. Here m is the diffraction order (or spectral order), which is an integer. For a particular wavelength λ, all values of m for which $|\mathrm{m}\lambda/\mathrm{d}| < 2$ correspond to physically realizable diffraction orders.

Figure 3.15 show a general schema of a diffraction grating.

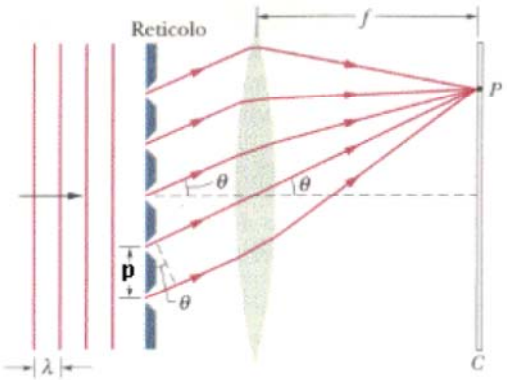

Figure 3.15 – plane wave diffraction by a diffraction grating.

That one is composed by a system with N slits, parallel, equidistant, with the same width.

The path difference between waves from adjacent slits is equal to $\mathrm{psen}\,\theta$. If this difference is equals to wavelength (or to a multiple of it), all the waves coming from all the slits will be in phase in P, and it will be possible to observe a bright line. The condition to have the maximum in the interference pattern at the angle θ is:

$$\mathrm{p}\sin\theta = \mathrm{m}\lambda$$

with $\mathrm{m} = 0, 1, 2, 3, \ldots$ that is the maximum order number.

If now the incident radiation contains different wavelengths, for each of them the maximum of m order will be at a specific angle, while at $\theta = 0$ will see all the wavelengths corresponding to $\mathrm{m} = 0$ (maximum of zero-order). If the source contains different wavelengths will be observed so many maximum for each order. In particular, we observe that the components with higher wavelength will be scattered at higher θ angles. In this way the grating splits the incident light into its components at different wavelengths, thus allowing to analyze them separately.

In the spectrometer used in this work is produced by Jobin-Yvon; the spectrometer TRIAX 320 is constituted by two interchangeable diffraction gratings, each of which can rotate around an axis passing through the plane of the grating itself and parallel to it.

The beam coming from the optical fibre is first collected by a collimating mirror that reflects it on the grating. Here is split into various wavelengths and directed to a focusing mirror that reflects it towards the slit exit, the opening of which represents a compromise between resolution and signal intensity (to large openings corresponds a signal intense, but at the same time a lower spectral resolution). From here then passes to the adapter which is interfaced to the multichannel CCD for detection.

All moving parts of the TRIAX 320, ie the slits, the grating's Turret, the shutter and the stepper-motor

which moves the grating in order to select the desired wavelength, are controlled remotely via a PC through the RS-232 or IEEE-488.

The density of the grating changes the resolution and the width of the spectrum.

The grating should therefore be chosen in order to have the best resolution and sensitivity in the range of wavelengths of interest. Currently the turret allocates 2 gratings, one from 600, the other from 1800 g/mm.

One of the main features of a diffraction grating is the resolving power R:

$$R = \frac{\lambda}{\lambda_2 - \lambda_1} = \frac{\lambda}{\Delta\lambda}$$

where λ_2 and λ_1 are two wavelengths so close as to be just barely resolvable according to the Rayleigh criterion through the grating used. Apparatus used, for the grating of 1800 g/mm the resolution certified is equal to 0065 nm, while for the grating of 600 g/mm the resolution certified is equal to 0.175 nm.

3.5.3.4 The Detector

Once the spectrometer has broken up the Raman radiation in its various components, they are dispatched to a tool that reveals the photons for each wavelength of the range of the Raman shift. This tool can be essentially of two types: single or multi channel.

The multichannel detectors are also known as CCD (charge coupled devices), and they base their operation on an electronic device that uses the optical characteristics of semiconductors.

A CCD detector consists essentially of an array of photodiodes or pixels in silicon. When the shutter is opened, each pixel that is hit by a photon produces a charge for the photoelectric effect. The charges of adjacent pixels are collected separately through a grid of electrodes. When after a time T of acquisition, said integration time, the shutter is closed, the control unit of the CCD manages the voltage of each electrode so as to convey the charge collected from each single pixel in a reading register, one pixel at a time , with an assigned order, row by row or column by column, until the end of the array.

The main characteristics of a CCD detector are the following:

1) Quantum Efficiency: the ratio between the number of photoelectrons produced and those actually incident on the detector per second and per single pixel. It is usually expressed as a percentage and indicates the theoretical sensitivity of a CCD.

   Measuring the quantum efficiency for each value of the wavelength in which the spectrum of

the incident light is divided, it is possible to construct the curve of spectral sensitivity of each sensor;

2) Pixel well capacity: this represents the maximum value of photoelectrons that a CCD can accumulate in a single pixel;
3) Linearity: in the CCD detectors linearity is typically better than 0.01%. This means that the number of electrons generated in a pixel is directly proportional to the amount of incident light;
4) Dark Current: represents a certain percentage of electrons that the detector produces spontaneously, and which causes statistical fluctuations of the output signal;
5) Readout Noise: is the noise introduced by the electronics associated with the detector.

The detector used in this work is the CCD Symphony by Horiba Jobin-Yvon [16].

The control system of the temperature of the detector Symphony controls and regulates the temperature of the detector through the cooling circuit and the thermostatic circuit.

The thermal stability of the CCD is provided by the control unit: once reached thermal equilibrium the control unit makes sure that the temperature of the CCD does not have drifts above 0.1°C compared to the established value.

The CCD 4000, in order to provide the best performance and avoid the dark current and provide a high signal to noise ratio, working at a temperature of -70°C (203K) through cooling system "super" thermoelectric (STE), enabling long integration times.

The detection head employs a particular multi-stage Peltier system thermally coupled with the CCD, placed inside a chamber under high vacuum, and the heat is conducted out of the surface of the array as the current through the Peltier cell.

The CCD detector (CCD Detector Head) is assembled on the appropriate output port of the spectrometer.

As previously mentioned, a CCD detector consists essentially of an array of silicon photodiodes. The signal from the CCD is then processed, amplified and converted to digital by the electronics of the CCD control unit and from this arrives to the memory of the PC.

3.5.3.5 CCD 4000 detector controller

The control unit of the CCD Symphony provides the coordination of all the functions of the analysis system, including the distribution of the current, temperature regulation, control of reading data and digitization of pixels information. The coordination between the various functions of the analysis system is also supplied by the Symphony control unit that provides the current, manages the

temperature regulation, the digital control of the reading and the transfer to the memory of the signal; also regulates the signals I/O for the CCD detector (Figure 3.16).

The control unit has a modular architecture and highly technological addressed pulling down of the background noise and rapid acquisition of spectra, to provide the best results in few time. The communication between the control unit and the remote computer is done through the ethernet 10/100, which provides 100% of data integrity; also the control platform provides flexibility in the selection and during storage of the operating parameters of the detector and for the definition of the scanning. For integration of the Symphony control system and of the detector, the application software LabSpec for spectroscopy is present, which allows a wide capture mode spectra, providing full control of the experimental conditions.

Figure 3.16 – Triax 320 spectrometer with CCD 4000

Bibliography

[1] AA.VV. Br.25 (1989) 589-621.

[2] Gerrard, D.L. "Raman Spectroscopy" Anal. Chem. 66 (1994) 547R-557R.

[3] Huong, P.V. "New possibilities of Raman micro-spectroscopy" Vibrational Spectroscopy 11 (1996) 17-28.

[4] Lawson, E.E., Barry, B.W., Williams, A.C. "Biomedical Applications of Spectroscopy" J. Raman Spectrosc. 28 (1997) 111-117.

[5] Lyin, L.A., Keating, C.K., Fox, A.P., Baker, B.E., He, L., Nicewarner, S.R., Mulvaney, S.P., Natan, M.J. "Raman Spectroscopy" Anal. Chem. 70 (1998) 341R-361R.

[6] Best, S.P., Clark, R.J.H., Withnall, R. "Non-destructive pigment analysis of artefacts by Raman spectroscopy" Endeavour 16 (1992) 66-73.

[7] Clark, R.J.H. " Raman microscopy: sensitive probe of pigments on manuscripts, paintings and other artefacts" J. Mol. Struct. 480-481 (1999) 15-20.

[8] Clark, R.J.H. "Pigment identification by spectroscopic means: an arts/science interface" C. R. Chimie 5 (2002) 7-20.

[9] Vandenabeele, P. "Raman spectroscopy in art and archaeology" J. Raman Spectrosc. 35 (2004) 607-609.

[10] Bahaa E. A. Saleh, Malvin Carl Teich, "Fundamentals of Photonics", John Wiley & Sons, Inc., 1991, pp 982, ISBNs: 0-471-83965-5 (Hardback); 0-471-2-1374-8 (Electronic).

[11] Robinson, W.R., Frame, E.S, Frame II, G.M. "Undergraduate Instrumental Analysis, 6th Edition", CRC Press (2004).

[12] Derek A. Long, "The Raman Effect: A Unified Treatment of the Theory of Raman Scattering by Molecules", John Wiley & Sons Ltd, 2002, pp.611, ISBNs: 0-471-49028-8 (Hardback); 0-470-84576-7 (Electronic).

[13] Crisp, M.D. "Raman Effect in Semiclassical Theory", Coherence and Quantum Optics, 1973, pp 309-317.

[14] Krawczyk, C. "The Raman Effect".

[15] Kaiser Optical System, Inc., catalogo, www.kosi.com

[16] HORIBA Jobin-Yvon Optical Spectroscopy Division, "Symphony 1024 x 128 Thermoelectric Front Illuminated CCD Detector", catalogo, www.jobinyvon.com

Chapter 4
Spectrophotometric analysis

Surface colour measurement is important for a very wide range of applications including industrial paint, printing, photography, textiles, plastics and also on Cultural Heritage field to obtain information on the absolute colour values of samples analysed (painting, buildings, paper,...). For demanding colour measurement, a spectral approach is definitely needed.

Ultimately colour is a sensation produced in the human brain when a light flux interacts with matter.....but.....what happens when light meets matter? There is always an interaction: light is scattered at a wall's surface, reflected off a surface of water, partially absorbed and partially reflected by a green leaf, refracted when it enters glass, and excites chemical processes in retinal rods and cones. The details depend on the structure of the matter and on the wavelength of the light. Additional phenomena are refraction, diffraction, fluorescence and transparency. How it is possible that light passes almost completely unimpeded through a structure like the cornea or through water molecules?

Due to its wave properties, even the diffraction of light is manifest within the eye: the smaller the pupil is, the larger the smallest image of a point source of light at the retina will be. A few of the more important processes are showed in Fig. 4.1.

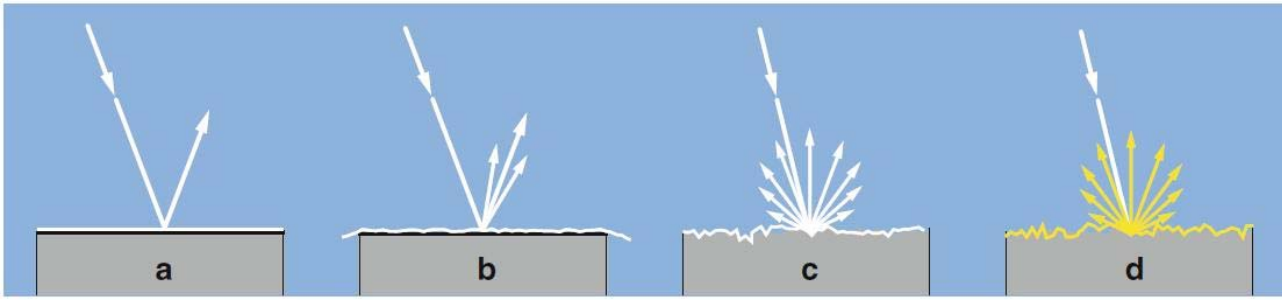

Figure 4.1 - Some of the interactions of white light with surfaces. **(a)** Specular reflection at a smooth surface. **(b)** Reflection from paper with a slightly rough surface. **(c)** Diffuse reflection from a whitewashed wall; no absorption. **(d)** Diffuse reflection with absorption of the shorter wavelengths at a painted yellow wall [1].

In this chapter, after a description of effects of light-matter interaction will be dealt the colour specification based on European norms given by the CIE (*Commission Internationale de l'Eclairage*), focusing the attention on the three main "characters" of chromatic sensation: object, illuminator, and detector.

4.1 Physical processes

When light encounters a surface or passes through a medium, inevitable interaction occurs between the light and the electrons of the atoms and molecules of the material. The basic principle is always the same with visible, ultraviolet, or infrared light. As already explained in the previous chapter, the basic process of the interaction of light with matter can be described more precisely by means of quantum theory. Now starting to talk about all the process that are involved in the macroscopic interaction of light with matter [1-2].

4.1.1 Transparency

Reminding that light is scattered when it encounters an obstacle, the existence of transparent media such as glass, water, corneas, crystalline lenses, and air is not so simple to explain. Inside these kind of media, interactions between light and matter still occur, but it only leads to a more slowly light's travelling than in a vacuum. This slowing down is quantified as the refractive index n: the velocity of light in the medium amounts to $c' = c/n$, where c is the velocity of light in vacuum ($c \approx 300{,}000\ km/s$). An eye exhibits several portions of tissue that are more or less transparent, such as the cornea, crystalline lens, aqueous humor, and the vitreous body, as well as the inner layers of the retina. A medium is always transparent only to a certain part of the electromagnetic spectrum. For example, water is opaque to radiation in the infrared range, while the cornea blocks radiation in the ultraviolet range.

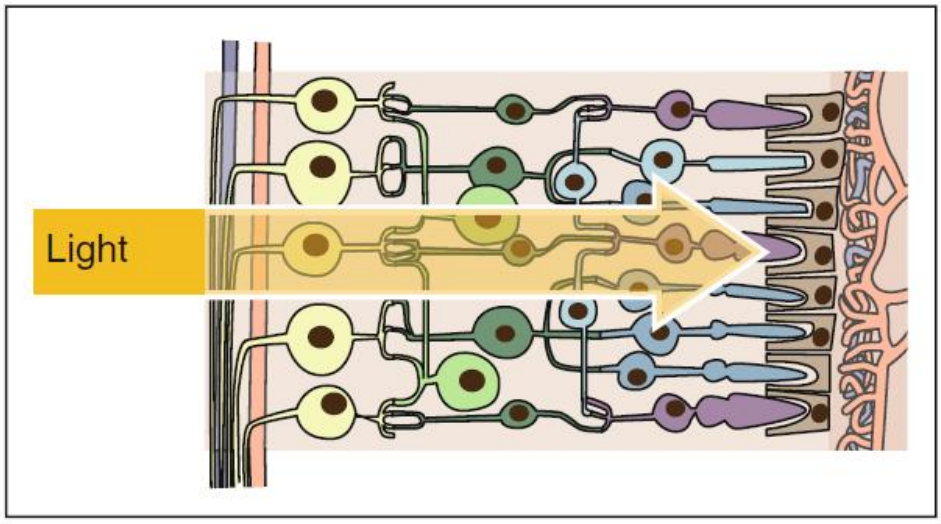

Figure 4.2 - Transparency of the retina [1].

The retina is transparent, so light can reach the cones and rods (the eyes elements that are responsible of colour vision) unimpeded (Fig. 4.2).

4.1.2 Refraction

If a beam of light meets a smooth interface between two transparent media that have different refractive indices, both reflection and refraction occur (Fig. 4.3).

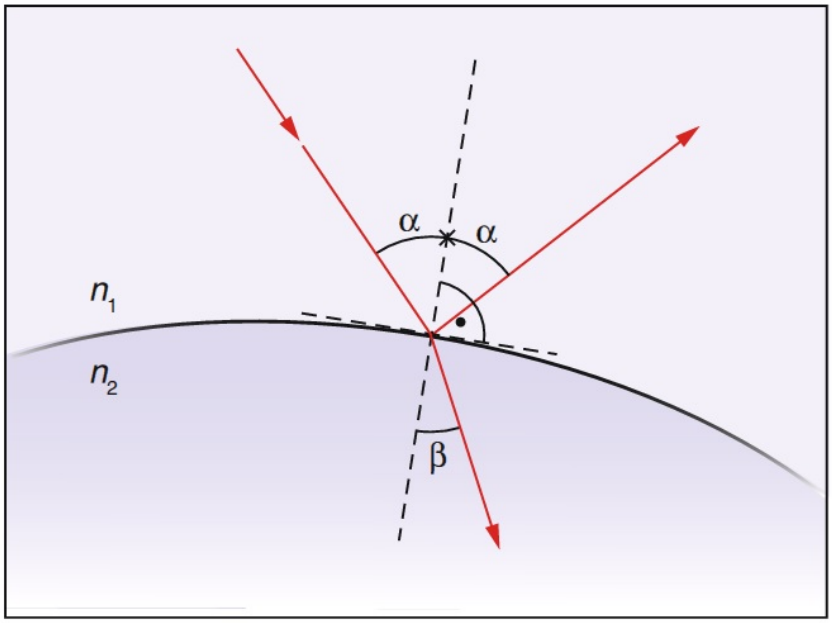

Figure 4.3 - Refraction at the interface of two media. The primary ray is partially reflected and partially refracted. α and β are the angles of the rays respect to the surface normal. The law of refraction determines the angle β when α and the refractive indices n_1 and n_2 are given: $sin\alpha \ / \ sin\beta \ = \ n_2/n_1$ [1].

The incident ray of light onto a surface, the refracted and reflected rays, and the surface normal all lie in the same plane (Fig. 4.3).

The reflection is symmetric respect to the surface normal, and the percentage of the light reflected increases with an increasing angle α. The refraction of light is the basis for the optical imaging through the cornea, crystalline lens, eyeglasses, and optical instruments. The amount of light refracted depends on the ratio of the refractive indices of the two media. The relationship between the two angles α and β is specified by the law of refraction:

$$sin\alpha \ / \ sin\beta \ = \ n_2/n_1 \tag{4.1}$$

Know as Snell or Descartes law.

Refraction is a consequence of the differing speeds of light in two media (Fig. 4.4).

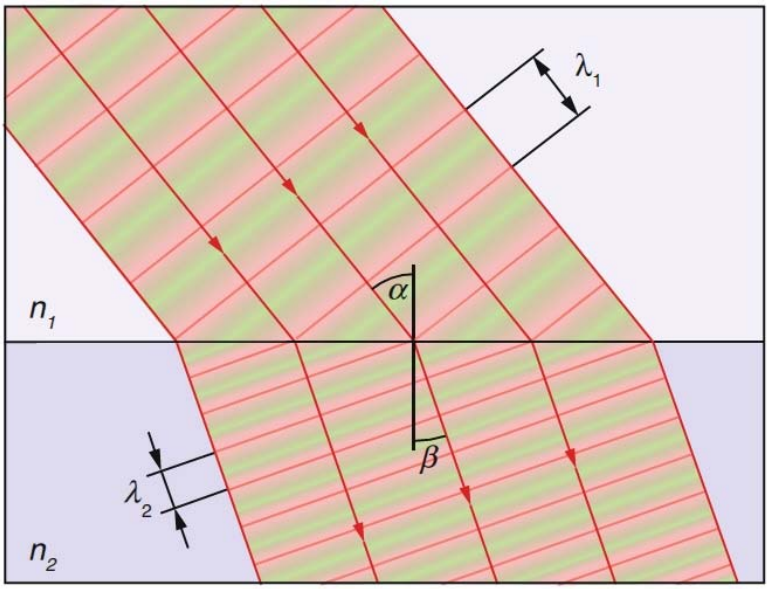

Figure 4.4 - Wave image of refraction. The differing light speeds in the two media give rise to differing wavelengths. The continuous transition of the phases at the interface is possible only with a change in direction. In a medium with an index of refraction n o, the wavelength is n times shorter than in a vacuum. $\lambda_1/\lambda_2 = n_2/n_1$ [1].

To understand this, it is possible to note that the frequency of the light vibrations remains the same in both media, but inside the medium with the slower light speed, the wavelength is smaller since the light moves one wavelength further during one period. Figure 4.4 shows that the continuous transition at the interface is possible only with a change in direction.

4.1.3 Dispersion

The refractive index of a transparent medium is slightly dependent on the wavelength and increases with shorter wavelengths. This gives rise to dispersion during refraction, i.e., to a breaking up of white light into various colours, as happened from prisms or crystals (Fig. 4.5).

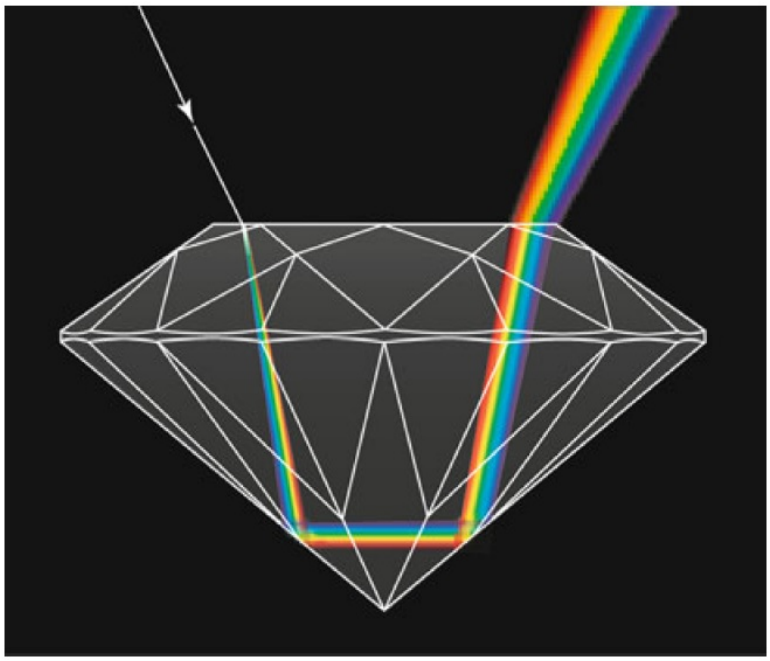

Figure 4.5 - Dispersion in a diamond. The refraction depends on the colour: blue light is more strongly refracted than red light (exaggerated in the figure) [1].

The colours of the rainbow are also based on the dispersion in water droplets. In imaging systems, the corresponding colour error is referred to as "chromatic aberration" which can be observed as coloured edges toward the periphery of the field of view of some binoculars.

Newton was interested in the chromatic aberration of the human eye. Its focal plane for blue light lies approximately 1 mm in front of that for red light (Fig. 4.6).

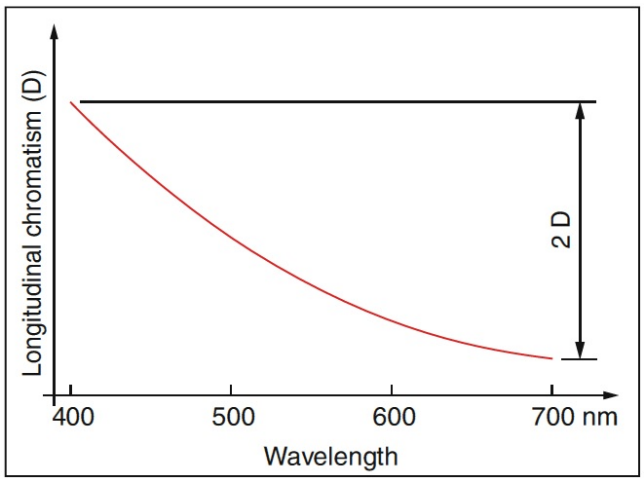

Figure 4.6 - The refractive power of the human eye depends on the colour of the light. The total refractive power of the eye amounts to ca. 58 D [1].

One reason could be that the innermost part of the central visual field is insensitive to blue since the blue-sensitive rods are completely absent in a circular area of approximately 20 min of arc.

4.1.4 Reflection

The phenomenon of reflection is seen, for example, when looking at a quiet surface of water. Reflection occurs at every smooth interface between media of differing optical density, i.e., other refractive indices (Fig. 4.3). Reflecting surfaces can be smooth or uneven. A smooth surface yields specular reflections such as in the mirrored objects; an uneven surface, such as a painted wall, leads to diffuse reflections.

The fraction of the light that is reflected depends on the angle of incidence, the ratio of the refractive indices of the two media, as well as from the state of polarization of the incident light, but it does not depend on the colour in most situations.

So-called total internal reflection occurs when a ray of light tries to exit an interface into a medium with a lower index of refraction and the angle of incidence with the surface normal exceeds a certain critical angle (Fig. 4.7). With total reflection, no light energy is lost. Light conducting glass fibres – having cores with higher and claddings with lower refractive indices – transmit signals with large bandwidths over large distances.

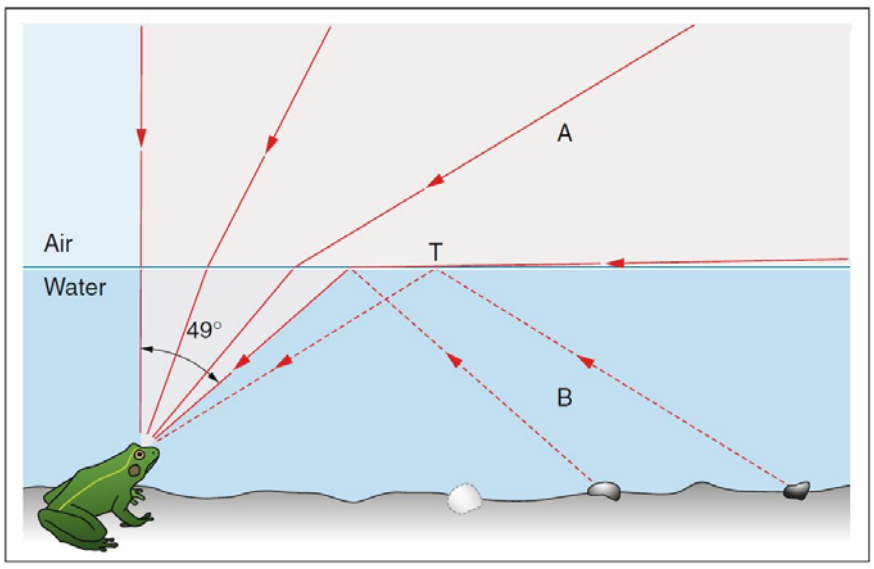

Figure 4.7 - Total reflection. In a part of its visual field, the frog sees a mirror image of the pond bottom (*B*) and, in another part, the outer world (*A*). For the transition from water into air (or vacuum) the critical angle is 49°. In accordance with the law of refraction, it corresponds to an angle of 90° in the optically thinner medium (air) [1].

Rough surfaces, such as a piece of paper, reflect light back in all directions. This also occurs when sunlight strikes the wall of a house or the green leaf of a plant. Thanks to the diffuse character of the reflection, we see the illuminated object from every angle.

The most obvious is the phenomenon of the colour of the reflecting surface. The wall of a house, being illuminated by the sun, appears white when its paint reflects all wavelengths of the incident light completely. The yellow colour of a sun flower arises through the absorption of blue: together, the remaining green and red produce the perception of yellow. If a surface partially absorbs all the spectral portions of the light uniformly (50 % of it, for example), it appears to be gray, that is, without any colour.

4.2 Reflectance

Focusing now the attention on the diffuse reflection that is the characteristic phenomenon of colour perception. The bidirectional reflectance distribution function (BRDF) of an opaque surface patch defines its reflectance by specifying what proportion of the light incident from each possible illumination direction is reflected in each possible observation or view direction [3]. Figure 4.8 shows a surface patch with normal **N** illuminated by a directional light source in direction **S** and observed by a viewer in direction **V**. In a three-dimensional world, two angles are necessary to uniquely specify the illumination direction **S** and two more to specify the view direction **V**.

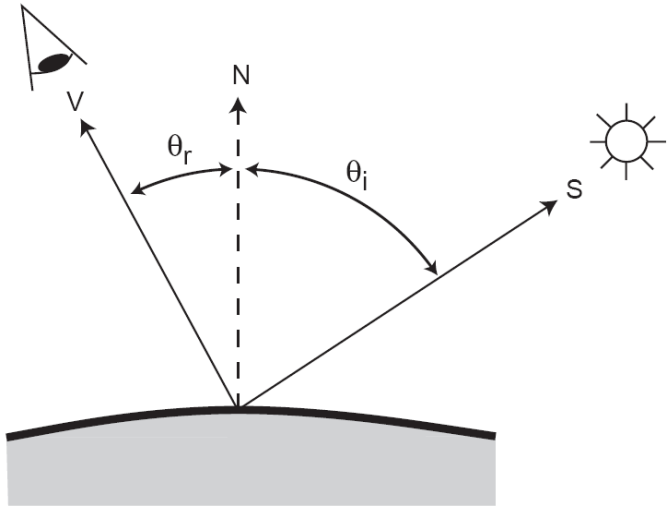

Figure 4.8 - A surface patch with normal N. The BRDF is a function of light source direction S and view direction V [3].

The BRDF is therefore a function of four continuous angular variables. Because surface radiance depends linearly on the amount of light incident from every direction, the BRDF of a surface patch determines its appearance under any illumination distribution. Reflectance also depends on the wavelength of the incident light. Because most materials reflect light of a given wavelength at the same wavelength, it is possible to describe the effect of colour on reflectance by writing the BRDF as a function of an additional variable representing wavelength. The expression of reflectance as a BRDF presupposes an opaque surface. Many real-world materials exhibit some degree of translucency, meaning that light incident at one point on the surface may be emitted at nearby points. One can capture their appearance properties with a bidirectional scattering-surface reflectance distribution function (BSSRDF), a generalization of the BRDF. The BSSRDF is a function of two positions on the surface as well as two directions in the three-dimensional world, so it depends on eight spatial variables. Two types of reflectance variation are commonplace. The first occurs at a boundary between two surfaces or between distinct materials within a surface. In these cases, reflectance changes help distinguish two or more different materials. The second involves regular variation of reflectance within a surface, associated with surface texture. In this case, the patterns of variation themselves are an important characteristic of the surface. Whether a texture results from fine-scale geometry or from actual reflectance variation, it will have a different appearance when viewed from different angles. A Bidirectional Texture Function (BTF) captures these properties by specifying the two-dimensional texture visible from each viewing angle for each lighting angle. One might model a BTF as a random field of BRDFs. The distinction between reflectance and texture is a matter of scale; as one views a surface from increasing distance, fine scale geometry variations will no longer be resolvable, but they will influence the measured surface BRDF.

4.2.1 Reflectance properties of materials

Maxwell's equations impose two constraints on the BRDF of a passive surface [3]. First, the BRDF must follow energy conservation or normalization; for any illumination, total reflected energy must be less than or equal to total incident energy. Second, the BRDF must satisfy the Helmholtz reciprocity principle, which guarantees symmetry between incident and reflected directions. Reciprocity requires that

$$f(\theta_i, \phi_i; \theta_r, \phi_r) = f(\theta_r, \phi_r; \theta_i, \phi_i) \tag{4.2}$$

Although some reflectance are much more common than others in the real world materials. Visual reflectance estimation is feasible partly because physical materials tend to produce certain types of BRDFs. This means that, the frequency distribution of surface BRDFs in the real world is not uniform. A great deal of research has focused on approximating common BRDFs by models with only a few free parameters. The applied physics literatures include models derived from the physics of light reflection as well as models designed empirically to fit experimental BRDF data.

These studies have focused on two general reflectance phenomena, diffuse and specular reflectance.

- Diffuse Reflectance is associated with matte surfaces such as plaster or uncoated paper. An ideal diffuse, or Lambertian, surface has equal radiance in all directions. Matte paint consisting of reflective patches suspended in a clear matrix approximates a Lambertian reflector, because light will emerge after multiple reflections in a more or less random direction. An ideal Lambertian reflector that emits a constant proportion ρ_d of the incident energy and absorbs the rest has a constant BRDF of the form

$$f(\theta_i, \phi_i; \theta_r, \phi_r) = \frac{\rho_d}{\pi} \tag{4.3}$$

  where $0 \leq \rho_d \leq 1$.

  Real diffuse reflectors deviate from this ideal behaviour, so the measured BRDF is not Lambertian. The BRDF models derived from these physical assumptions provide an accurate fit to measured BRDFs of natural surfaces such as plaster, chalk, and clay.

- Specular Reflectance is typified by a mirror. An ideal specular surface reflects all energy in an incident light ray such that the incident and reflected directions are bisected by the surface normal. Such a surface has a BRDF

$$f(\theta_i, \phi_i; \theta_r, \phi_r) = \frac{\delta(\cos\theta_i - \cos\theta_r)}{-\cos\theta_r}\,\delta(|\phi_r - \phi_i| - \pi) \tag{4.4}$$

  Specular surfaces such as metals also typically exhibit some fine-scale variation in surface geometry, indeed is the roughness causes the specular reflection of a point source to be distributed in a small region around the ideal mirrored direction.

Diffuse and specular reflectance differs fundamentally in two ways. First, specularities are typically visible over a narrow view angle, so that specular reflection tends to be sharper than diffuse reflection. Second, even a rough specular surface differs from a diffuse surface in the direction of dominant reflectance. A number of parameterized models of specular reflectance take into account the width of

the specular lobe. The earliest of these, is the Phong model [4-5], which uses one parameter to describe the strength of the specular reflectance and another to specify surface smoothness, which is inversely correlated to roughness and the width of the specular lobe. Ward proposed a variant of the Phong model that largely overcomes these problems [6-7]. The BRDF for the specular component of the Ward model takes the form

$$f(\theta_i, \phi_i; \theta_r, \phi_r) = \rho_s \frac{1}{\sqrt{\cos\theta_i \cos\theta_r}} \frac{\exp(-\tan^2\delta/\alpha^2)}{4\pi\alpha^2} \tag{4.5}$$

where δ is the angle between the surface normal and a vector bisecting the incident and reflected directions, the so-called "half-angle vector" (Figure 4.9). The specular component is spread out about the ideal specular direction in a Gaussian distribution with standard deviation α. The other free parameter, ρ_s, specifies the proportion of incident energy reflected by the specular component.

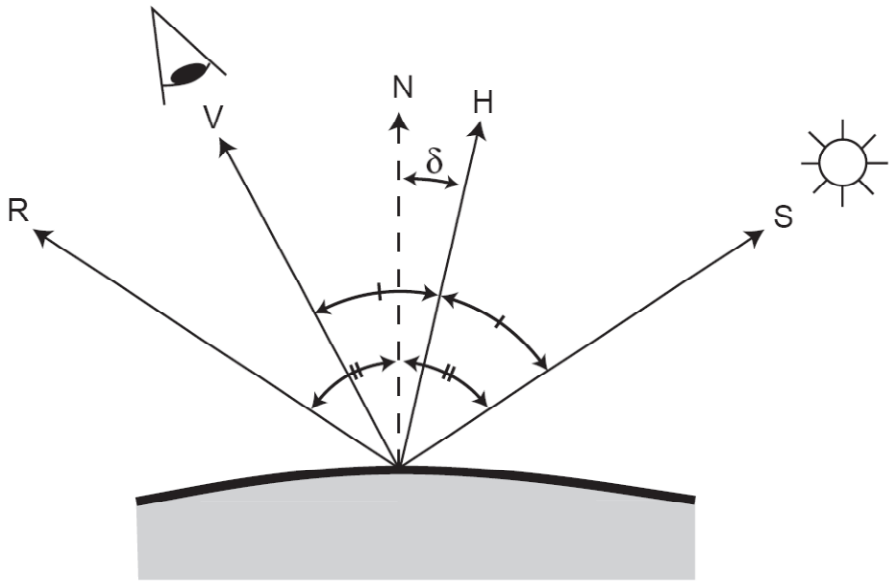

Figure 4.9 - Geometry used to define the specular component of the Ward model. **N** is the surface normal, **S** is the light source direction, and **V** is the view direction. The half-angle vector **H** bisects **S** and **V**. The direction of ideal specular reflection **R** is such that **N** bisects **R** and **S** [3].

Most surfaces reflect light by several physical mechanisms, including both specular and diffuse reflection. BRDFs are therefore typically modelled as a sum of a specular and a diffuse component. For example, the isotropic Ward model combines the specular component described by Equation (4.5) with the Lambertian component described by Equation (4.3):

$$f(\theta_i, \phi_i; \theta_r, \phi_r) = \frac{\rho_d}{\pi} + \rho_s \frac{1}{\sqrt{\cos\theta_i \cos\theta_r}} \frac{\exp(-\tan^2\delta/\alpha^2)}{4\pi\alpha^2} \quad (4.6)$$

The sum $\rho_d + \rho_s$ specifies the fraction of incident energy reflected by the surface, so normalization requires $\rho_d + \rho_s \leq 1$.

Many common materials have isotropic reflectance functions with no particular orientation [8].

4.3 Absorption

Scattering at an exterior surface can be modified by the absorption of a portion of the incident light. A black surface swallows up all incidents light. A piece of paper appears red when it absorbs the blue and green components of the light. If, for all colours, the same amount is absorbed, the surface appears gray. Absorption can also occur in the interior of a material and be also connected with light scattering [1-2].

Molecules that are intensively absorbing are called pigments. Through differing absorption spectra, brightness and colour contrasts arise. We distinguish between inorganic and organic pigments. Inorganic pigments are crystals, polycrystalline powder, aggregates, and agglomerates. They come in the form of oils, lacquers, etc. They were used in cave paintings as early as 30,000 years ago. Black and coloured pigments are also applied in so-called xerography. The Greek word "xeros" means "dry." In 1937, the printer Chester Carlson developed a printing process that does not require the use of liquid chemicals. Today, it is still the basic principle underlying laser printers and copy machines. The absorption of light by the retinal molecule in our retina is the physical basis for vision (Fig. 4.11).

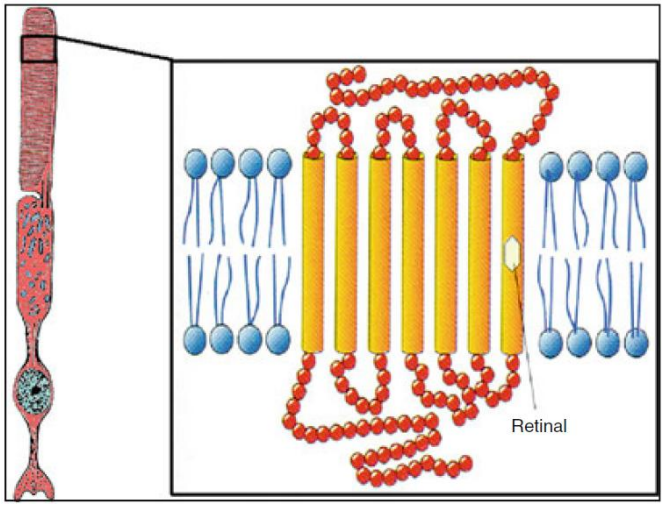

Figure 4.11 - Absorption of light by retinal. The same molecule (retinal) stands at the beginning of the cascade of processes leading from the arrival of a photon down to an electrical pulse in all three cones (red-, green-, and blue-sensitive) [1].

The retina is not completely transparent. Depending on the wavelength, light is more or less strongly absorbed in the differing layers. The absorption of light by water or pigments strongly depends on wavelength (Fig. 4.12).

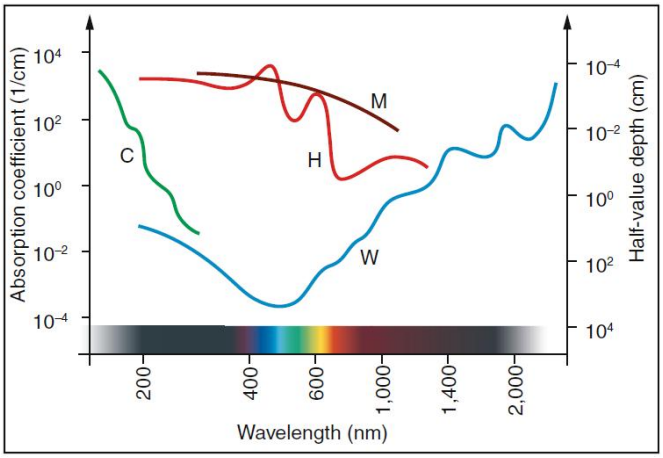

Figure 4.12 - Absorption coefficients of various materials. *W* water, *H* haemoglobin, *M* melanin, *C* collagen. ***Left ordinate***: in units of cm^{-1}. ***Right ordinate***: half is absorbed by the time it has travelled this far [1].

4.4 Overview to Colorimetry

The specifications of basic standards used in colorimetry are based on definitions of the Commission Internationale de l'Eclairage (CIE) by general consent in all countries [9]. The first major recommendations regarding colorimetric standards were made by the CIE in 1931. The original recommendations made in 1931 are reviewed from time to time by the CIE Colorimetry Committee and changes are made when considered necessary.

At the 6th Session of the CIE held at Geneva in 1924 it was decided to set up a Study Group on Colorimetry (CIE 1924). The measurement of colour had become an important factor in industry and scientific laboratories but there was not colour specification system that could be considered satisfactory for general practice. Later, it was agreed that efforts should be made to reach agreements on

- colorimetric nomenclature;
- a standard daylight for colorimetry;
- the "sensation curves" of the average human observer with normal colour vision.

At the 8th Session of the CIE held at Cambridge, England, in 1931, the first major recommendations were made which laid the basis for modern colorimetry (CIE 1931). There were a total of five recommendations. Recommendations 1, 4 and 5 established the CIE 1931 standard observer and a colorimetric coordinate system; recommendation 2 specified three standard sources (A, B and C) and recommendation 3 standardized the illuminating and viewing conditions for the measurement of reflective surfaces.

4.4.1 CIE standard observer

The CIE 1931 standard colorimetric observer was defined by two different but equivalent sets of colour-matching functions based on the photopic luminous efficiency function $V(\lambda)$ [9-10]. The first set of colour-matching functions, $\bar{r}(\lambda)$, $\bar{g}(\lambda)$, $\bar{b}(\lambda)$, was expressed in terms of spectral stimuli of wavelengths 700.0 nm (R), 546.1 nm (G), 435.8 nm (B) (Fig. 4.13). The equi-energy spectrum is a stimulus whose spectral concentration of power as a function of wavelength is constant.

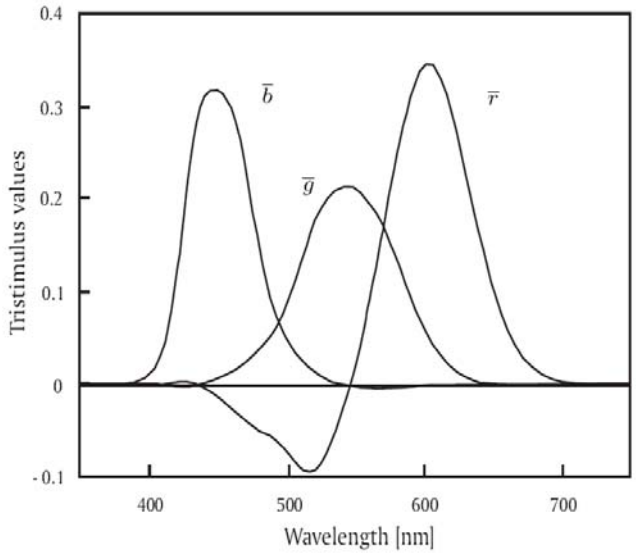

Figure 4.13 – Colour matching functions $\bar{r}$, $\bar{g}$ and $\bar{b}$ in terms of spectral stimuli of wavelengths 700.0 nm (*R*), 546.1 nm (*G*) and 435.8 nm (*B*), respectively [9].

For more convenient application in practical colorimetry , a second set of colour-matching functions, $\bar{x}(\lambda)$, $\bar{y}(\lambda)$, $\bar{z}(\lambda)$ (Fig. 4.14) was derivated from the first set, its was based on a proposal by Judd [11] in 1930 and involved a linear transformation. The coefficients of the transformation were chosen to avoid negative values of $\bar{x}(\lambda)$, $\bar{y}(\lambda)$, $\bar{z}(\lambda)$ and so that the luminance L_X, L_Y, L_Z of unit quantities of the stimuli were equal to 0, 1, 0 respectively, resulting in a set of colour matching functions in which $\bar{y}(\lambda)$ is

identical to $V(\lambda)$. The units of the new reference stimuli (X), (Y), (Z) were adjusted to make the chromaticity coordinates x, y, z also equal for the equi-energy spectrum.

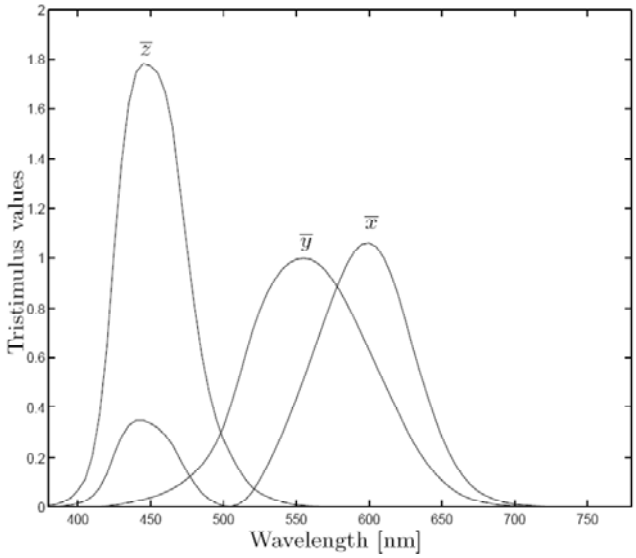

Figure 4.14 – Colour matching functions x, y and z [9].

The new colour-matching functions, $\bar{x}_{10}(\lambda)$, $\bar{y}_{10}(\lambda)$, $\bar{z}_{10}(\lambda)$, defining the supplementary standard colorimetric observer (CIE 1959) were officially adopted in 1964. They were derived from experimental data supplied by Stiles and Burch in 1959 and by Speranskaya in 1959 [12-13].

4.4.2 CIE coordinate system

One of the important problems the Colorimetric Committee has dealt with over several years concerns a coordinate system which would provide a three dimensional colour spacing that would be perceptually more uniform than the XYZ system. Many different proposals have been forwarded over the years. In the 14th Session of the CIE at Brussels in 1959 the committee considered a number of the systems. The MacAdam uniform chromaticity scale diagram of 1937 was adopted as a standard UCS diagram. The proposal was officially approved by the CIE in 1960, so the diagram is nowadays known as the CIE 1960 UCS diagram. At the 18th Session of the CIE in London in 1975 the Colorimetry Committee approved the adoption of two new colour spaces and associated colour difference formulae. These spaces are known as the CIE 1976 $L^*u^*v^*$ color space and the CIE 1976 $L^*a^*b^*$color space.

4.4.3 Illuminants for Colorimetry

Standard illuminants such as Illuminant A, B, C and D65 are recommended illuminants for colour calculations. Here "illuminant" refers to a specific spectral power distribution, not necessarily realized by a "source" which refers to a physical light emitter, such as a lamp, the sun and the sky. Illuminant A represents light from a full radiator at absolute temperature 2856 K according to The International Practical Temperature Scale, 1968. The relative spectral power distribution of illuminant A has been derived in accordance with Planck's radiation formula. Illuminant B was intended to represent direct sunlight with a correlated colour temperature of approximately 4900 K. Illuminant C was intended to represent average daylight with a correlated colour temperature of about 6800 K. In Fig. 4.15 standard illuminants A, B and C are shown. Illuminant D65 was intended to represent a phase of daylight with a correlated colour temperature of approximately 6500 K. The illuminant D65 is recommended for use whenever possible. Illuminants D50, D55 and D75 can still be used to realize a phase of daylight having correlated colour temperatures of approximately 5000 K, 5500 K, and 7500 K, respectively.

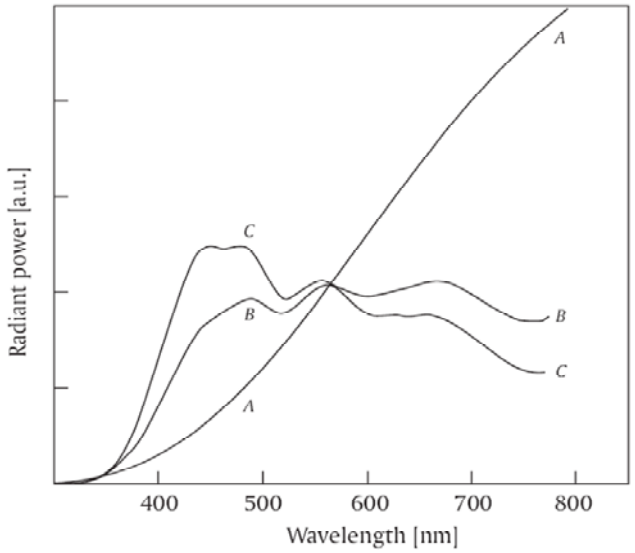

Figure 4.15 – Standard illuminants *A*, *B* and *C* [14].

In Fig. 4.16 examples of the standard daylight illuminants D55, D65 and D75 are shown.

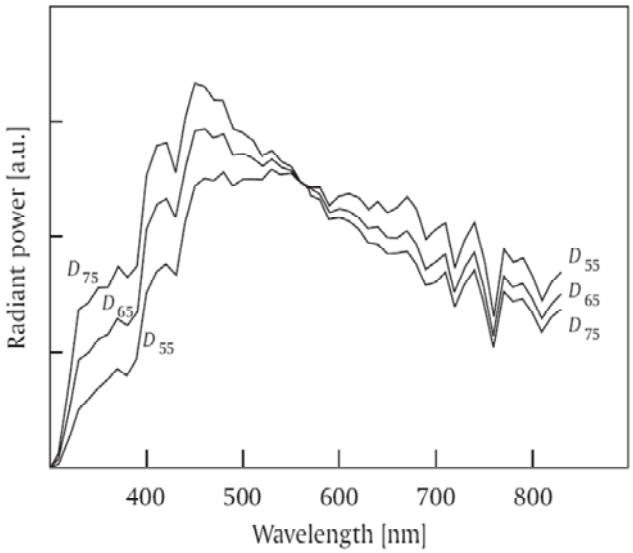

Figure 4.16 – Standard illuminants D55, D65 and D75 [14].

4.4.3.1 Sources representing illuminants

Standard illuminant A is to be realized by a gas-filled tungsten filament lamp operating at a correlated colour temperature of 2856 K. Illuminant B and C are to be realized using the source A, combined with a filter consisting of a layer of agreed solutions. At present, no artificial sources have been recommended to realize illuminant D65 or any other D illuminants of various correlated colour temperatures.

4.4.3.2 Illuminating and viewing conditions for a reflecting specimen

CIE recommends the use of one of the following illuminating and viewing conditions. Here reported also the relative symbols associated with each conditions:

- 45°/normal → $45/0$
- normal/45° → $0/45$
- diffuse/normal → $d/0$
- normal/diffuse → $0/d$.

In the $45/0$ geometry the sample is illuminated by one or more beams whose effective axes are at the angle of $45° \pm 2°$ from the normal to the sample surface. The viewing angle from the normal to the sample should be less than 10°.

In the $0/45$ geometry the illumination is in the direction normal to the sample, and the viewing angle is 45° from the normal. Now normal illumination is within 2°, and the angle between the axis and any ray should not exceed 8°. The same restriction should be observed in the viewing beam.
The illuminatig conditions $0/45$ and $45/0$ are shown in Fig. 4.17.

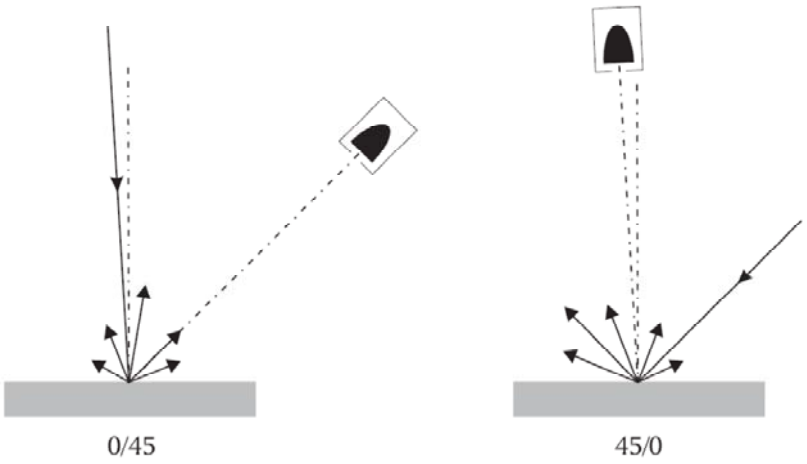

Figure 4.17 – Viewing geometries of $0/45$ and $45/0$ [9].

In the $0/d$ and $d/0$ conditions, specular reflection can be excluded or included by the use of a gloss trap; that represent SCE and SCI condition of measurements, respectively. In the $0/d$ condition, the sample should not be measured with a strictly normal axis of illumination if it is required to include the regular component of reflection. Note that only the $0/d$ geometry provides a spectral reflectance. The other conditions $d/0$, $0/45$ and $45/0$ gives a specific radiance factor.

4.4.4 Standard observer data

Due to the distribution of cones in the eye, the tristimulus values depend on the observer's field of view. To eliminate this variable, the CIE defined a colour-mapping function called the standard (colorimetric) observer, to represent an average human's chromatic response within a 2° arc inside the fovea. This angle was chosen starting from the assumption that the colour-sensitive cones resided within a 2° arc of the fovea. Thus the CIE 1931 Standard Observer function is also known as the *CIE 1931 2° Standard Observer*.

4.4.4.1 CIE 1931 standard colorimetric observer

Colorimetric specification of colour stimuli is based on the colour-matching functions $\bar{x}(\lambda)$, $\bar{y}(\lambda)$, $\bar{z}(\lambda)$, given in the CIE Standard on Colorimetric Observers. These colour matching functions are given in the Standard as values from 360 nm to 830 nm at 1 nm intervals with seven significant digits, and they define the CIE 1931 standard colorimetric observer. The values at 5 nm intervals over the range 380 nm to 780 nm are consistent with the Standard and are sufficient for most applications.

4.4.4.2 CIE 1964 supplementary standard colorimetric observer

Colorimetric specification of colour stimuli is based on the colour matching functions $\bar{x}_{10}(\lambda)$, $\bar{y}_{10}(\lambda)$, $\bar{z}_{10}(\lambda)$ given in the CIE Standard on Colorimetric Observers. These colour-matching functions are given in the Standard as values from 360 nm to 830 nm at 1 nm intervals, and they define the CIE 1964 standard colorimetric observer.

4.4.5 Calculation of tristimulus values and chromaticity coordinates

4.4.5.1 Calculation of tristimulus value

The CIE Standard on Colorimetric Observers recommends that the CIE tristimulus values of a colour stimulus be obtained by multiplying at each wavelength the value of the colour stimulus function $\phi_\lambda(\lambda)$ by that of each of the CIE color matching functions and integrating each set of products over the wavelength range corresponding to the entire visible spectrum 360 nm to 830 nm. The integration may be carried out by numerical summation at wavelength intervals, Δλ,

$$\begin{aligned} X &= k \sum_{\lambda} \phi_\lambda(\lambda)\, \bar{x}(\lambda)\, \Delta\lambda \\ Y &= k \sum_{\lambda} \phi_\lambda(\lambda)\, \bar{y}(\lambda)\, \Delta\lambda \\ Z &= k \sum_{\lambda} \phi_\lambda(\lambda)\, \bar{z}(\lambda)\, \Delta\lambda \end{aligned} \tag{4.7}$$

or

$$X_{10} = k \sum_{\lambda} \phi_\lambda(\lambda)\, \bar{x}_{10}(\lambda)\, \Delta\lambda \tag{4.8}$$

$$Y_{10} = k \sum_{\lambda} \phi_{\lambda}(\lambda)\, \bar{y}_{10}(\lambda)\, \Delta\lambda$$

$$Z_{10} = k \sum_{\lambda} \phi_{\lambda}(\lambda)\, \bar{z}_{10}(\lambda)\, \Delta\lambda$$

where X, Y, Z are tristimulus values, $\bar{x}(\lambda)$, $\bar{y}(\lambda)$, $\bar{z}(\lambda)$, are color-matching functions of a standard colorimetric observer, and k is a normalizing constant defined below. These equations may be written without or with the subscript 10 to correspond to the CIE 1931 or 1964 standard colorimetric system, respectively. For reflecting or transmitting object colours, the colour stimulus function, $\phi_{\lambda}(\lambda)$, is replaced by the relative colour stimulus function, $\phi(\lambda)$, evaluated as

$$\begin{aligned} \phi(\lambda) &= R(\lambda)S(\lambda) \\ \phi(\lambda) &= \tau(\lambda)S(\lambda) \end{aligned} \tag{4.9}$$

where $R(\lambda)$ is the spectral reflectance factor of the object colour, $\tau(\lambda)$ is the spectral transmittance of the object color, and $S(\lambda)$ is the relative spectral power distribution of the illuminant. In this case, the constants k and k_{10} are chosen so that $Y = 100$ for objects for which $R(\lambda)$, or $\tau(\lambda) = 1$ for all wavelengths and hence

$$\begin{aligned} k &= \frac{100}{\sum_{\lambda} S(\lambda)\bar{y}\,(\lambda)\Delta\lambda} \\ k_{10} &= \frac{100}{\sum_{\lambda} S(\lambda)\bar{y}_{10}\,(\lambda)\Delta\lambda} \end{aligned} \tag{4.10}$$

For self-luminous objects and illuminants the constants k and k_{10} are usually chosen on the grounds of convenience. However, if in the CIE 1931 standard colorimetric system the Y value is required to give the absolute value of photometric quantity the constant k must be equal to K_m, the maximum spectral luminous efficacy. This value is equal to 683 lumens per watt and $\phi_{\lambda}(\lambda)$ must be the spectral concentration of the radiometric quantity corresponding to the photometric quantity required.

4.4.5.2 Calculation of chromaticity coordinates

The chromaticity coordinates (x, y, z) should be calculated from the tristimulus values (X, Y, Z) as follows:

$$x = \frac{X}{X+Y+Z}$$
$$y = \frac{Y}{X+Y+Z} \qquad (4.11)$$
$$z = \frac{Z}{X+Y+Z}$$

Because of the relation x + y + z = 1, it is sufficient to quote x and y only. The chromaticity coordinates x_{10}, y_{10}, z_{10} are computed similarly from the tristimulus values X_{10}, Y_{10}, Z_{10}

Although any one of the three original tristimulus values could be used to pick off a point along the ray described by the chromaticity coordinates, typically the Y value is selected because it contains the luminance information. A chromaticity and luminance color specification (*x, y, Y*) can be transformed into tristimulus values *X, Y, Z* through the relations:

$$X = x\frac{Y}{y}$$
$$Y = Y$$
$$Z = (1-x-y)\frac{Y}{y}$$

The chromaticity diagram x, y CIE, for this colour space, is reported in Figure 3.35; in it, the achromatic colours are in the centre and the chromaticity increases toward the edges.

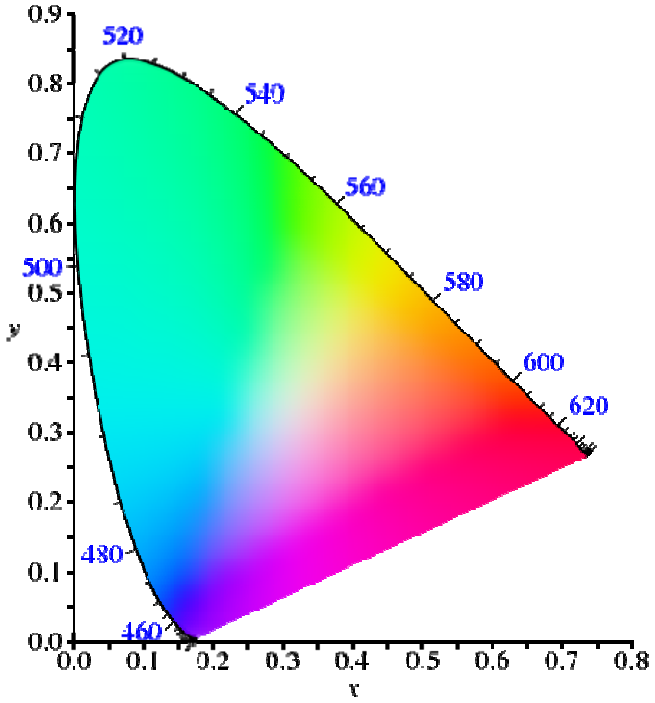

Figure 4.18 – Chromaticity diagram x, y 1931[http://en.wikipedia.org/wiki/CIE_1931_color_space].

4.4.6 Hue, saturation, and brightness in CIE XYZ space

A set of colour swatches from a paint store can be organized using the hue, saturation, and brightness vocabulary developed in an earlier section of the paper. This collection can subsequently be resolved to tristimulus values by using eq. 3.1, and can finally be plotted in CIE XYZ space [15].

There are certain correspondences that can be established between the hue, saturation, and brightness of these colour swatches and the position of their tristimulus values in the plotting space:

1. As predicted by the photometry experiments, each constant brightness spider has a constant Y value and therefore a constant luminance.

   However the spiders, which differ from one another by the same amount of brightness, are not equally spaced in CIE XYZ space. This means that although luminance can predict a brightness match it is not a direct measure of brightness magnitude.
2. The achromatic axis of the hue, saturation, and brightness system runs through the centres of the spiders and hence through the centre of the cone of realizable colour. The chromaticity coordinates for these neutral colours are close to the centre of the chromaticity diagram where $x = 1/3$ and $\mathrm{y} = 1/3$.
3. There is a correspondence between change in wavelength and change in hue. Sections of the chromaticity diagram can therefore be labelled by hue.
4. Saturation increases from a minimum at the centre of the chromaticity diagram to a maximum at the spectrum locus.

It must be emphasized that the above correspondence between CIE XYZ tristimulus values and the hue, saturation, and brightness notation system is not fixed. If, for example, the size or the background of the swatches is altered, the hue, saturation, and brightness specifications will change but the CIE XYZ tristimulus values will remain constant. The use of hue, saturation, and brightness to refer to locations in CIE XYZ space is therefore not recommended. However, since this practice is so common in the literature, it will be used occasionally in the remainder of this article.

4.4.7 Uniform colour spacing

The use of the xy chromaticity diagram of allows a visual assessment of the colour graphic that the tristimulus values don't give. However, this model is inadequate to represent the colour differences, in fact occurs that equal distances do not represent the same perceived colour differences. To overcome this problem different colour space were introduced.

4.4.7.1 The CIE 1976 uniform colour spaces

The use of the following colour spaces is recommended whenever a three-dimensional spacing perceptually more nearly uniform than that provided by the XYZ system is desired. Is a colour space adopted by CIE as a simple-to-compute transformation of the 1931 CIE XYZ color space, but which attempted perceptual uniformity.

CIE 1976 $L^*u^*v^*$ colour space or CIELUV colour space is defined by quantities L^*, u^*, v^*

$$L^* = 116\left(\frac{Y}{Y_n}\right)^{1/3} - 16 \quad \text{when } \left(\frac{Y}{Y_n}\right) > 0.008856 \tag{4.12}$$

$$u^* = 13L^*(u' - u'_n) \tag{4.13}$$

$$v^* = 13L^*(v' - v'_n) \tag{4.14}$$

where Y, u', v' describe the color stimulus considered and Y_n, u'_n, v'_n describe a specified white object colour stimulus. If Y/Y_n is less than 0.008856, the above equations are changed as follows

$$\left(\frac{Y}{Y_n}\right)^{1/3} \text{ is replaced by } 7.787\left(\frac{Y}{Y_n}\right) + \frac{16}{116}$$

The chromaticity diagram u', v' CIE, for this color space, is reported in Figure 4.19; in it, (u', v'), the chromaticity in CIELUV, is a pretty perceptionally uniform presentation of the chromaticity as (another than in CIE 1931) planar Euclidean shape. This presentation is a projective transformation of the CIE 1931 chromaticity diagram.

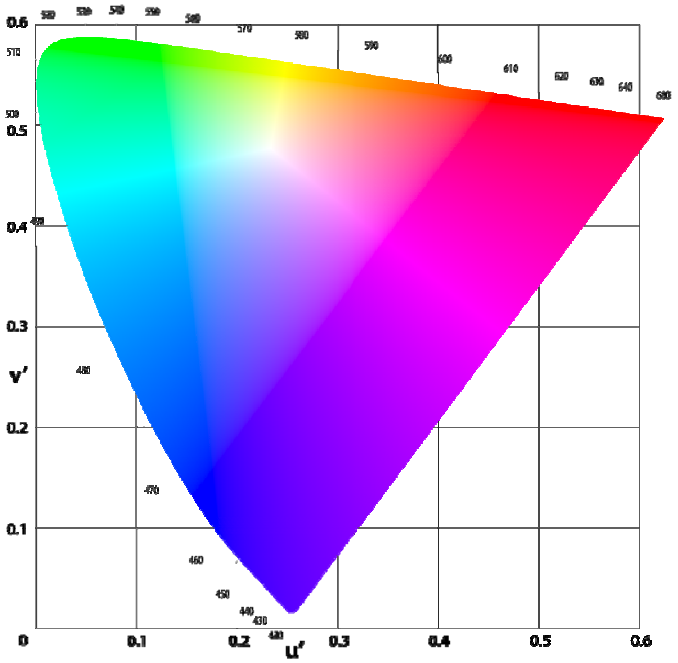

Figure 4.19 – (u',v') chromaticity diagram, also known as the CIE 1976 UCS (uniform chromaticity scale) diagram [http://en.wikipedia.org/wiki/CIELUV].

The CIE 1976 *L*a*b** color space or CIELAB color space is defined by quantities *L**, *a**, *b**

$$L^* = 116\left(\frac{Y}{Y_n}\right)^{1/3} - 16 \tag{4.15}$$

$$a^* = 500\left[\left(\frac{X}{X_n}\right)^{1/3} - \left(\frac{Y}{Y_n}\right)^{1/3}\right] \tag{4.16}$$

$$b^* = 200\left[\left(\frac{Y}{Y_n}\right)^{1/3} - \left(\frac{Z}{Z_n}\right)^{1/3}\right] \tag{4.17}$$

where X, Y, Z describe the color stimulus considered and X_n, Y_n, Z_n describe a specific white object colour stimulus. If X/X_n, Y/Y_n or Z/Z_n, is less than 0.008856, the above equations are changed as follows

$$\left(\frac{X}{X_n}\right)^{1/3} \text{ is replaced by } 7.787\left(\frac{X}{X_n}\right) + \frac{16}{116}$$

$$\left(\frac{Y}{Y_n}\right)^{1/3} \text{ is replaced by } 7.787\left(\frac{Y}{Y_n}\right) + \frac{16}{116}$$

$$\left(\frac{Z}{Z_n}\right)^{1/3} \text{ is replaced by } 7.787\left(\frac{Z}{Z_n}\right) + \frac{16}{116}$$

In the colour space L^*, a^*, b^* represented in fig.4.20, L^* indicates lightness, while a^* and b^* are the coordinates of chromaticity. The chromaticity diagram a^*, b^* CIE, for this color space, is reported in Figure 4.21; in it, (u', v'), the chromaticity in CIELUV, is a pretty perceptionally uniform presentation of the chromaticity as (another than in CIE 1931) planar Euclidean shape. This presentation is a projective transformation of the CIE 1931 chromaticity diagram.

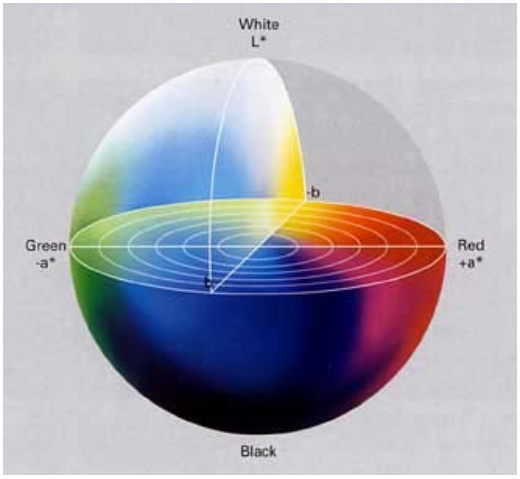

Figure 4.20 – Representation of the solid colour for the colour space L^*, a^*, b^*.

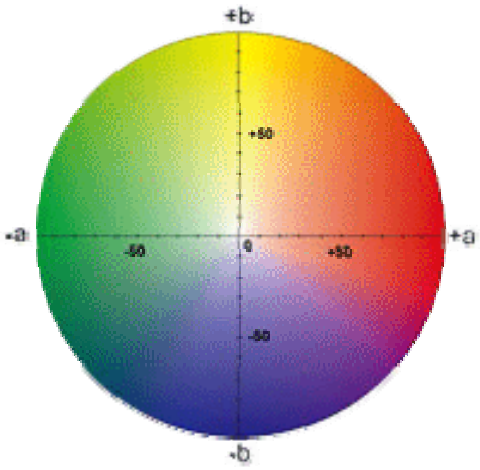

Figure 4.21 – Chromaticity diagram a^*, b^*

The differences ΔE^*_{uv} or ΔE^*_{ab} between two colour stimuli are calculated as the Euclidean distance between the points representing them in the space:

$$\Delta E^*_{uv} = \sqrt{(\Delta L^*)^2 + (\Delta u^*)^2 + (\Delta v^*)^2} \tag{4.18}$$

$$\Delta E^*_{ab} = \sqrt{(\Delta L^*)^2 + (\Delta a^*)^2 + (\Delta b^*)^2} \tag{4.19}$$

4.5 Experimental apparatus

The human eye can perceive colour differences as small as 0.5 CIELAB units and, thus, distinguish millions of colours. This 0.5 unit difference should be the goal for precise colour measurements. The best accuracy in colour measurement could be achieved by use of a spectrophotometer.

A spectrophotometer is a specific type of spectrometer, designed to measure light over the visible and near visible portion of the electromagnetic spectrum [16]. At its most basic level, a reflectance spectrophotometer consists of a diffuse light source to illuminate the object, a means of collecting the reflected and/or backscattered light from the surface, a spectral analyser and a means of measuring light intensity [17] (Figure 4.22). From this, the quantity of reflected light can be determined at specific wavelengths.

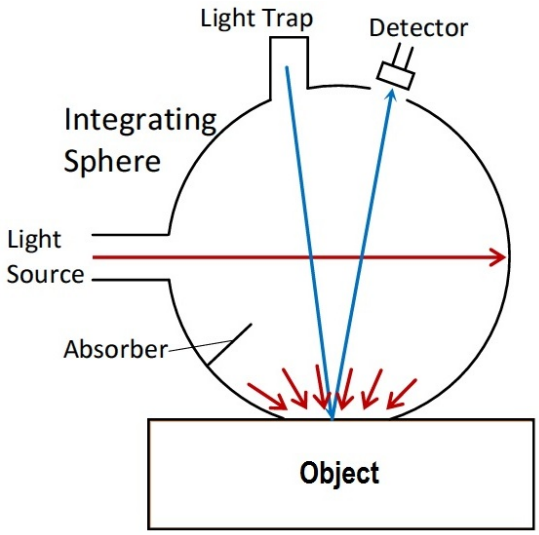

Figure 4.22 – Schematic diagram showing a basic spectrophotometer setup. The integrating sphere acts both as a means of producing a diffuse light source, and for collection of light from the patient surface [16].

The only geometry for measuring real spectral reflectance is normal/diffuse ($0/d$) geometry where the specimen is illuminated by a beam whose axis at an angle which does not exceed 10° from the normal to the specimen. The reflected flux should be collected by means of an integrating sphere. Regardless of how good an instrument one has, we need to point out that ultimately colour is a sensation produced in the human brain. It is evident that the information processing system of the human has learned to process, e.g. visual information, in an efficient way. The human eye is able to distinguish several million colours, and thus colour measuring instruments should accurately match the sensitivity of the eye to be able to detect small colour differences. The basic sensory system of the eye is known, but the operation of the process is an open question. The colour of any non fluorescent specimen can be matched with a mixture of red, green and blue primaries, because there are only three types of colour sensitive receptor on the retina. Human colour vision shows differences among people. Thus, some standard observers must be specified. The CIE 1931 standard observer is defined for a 2° field of view by two equivalent sets of colour matching functions. The first set is expressed in terms of spectral stimuli of wavelengths

700 nm (R), 546.1 nm (G), and 435.8 nm (B). The second set is a linear transformation of the first one and remains positive for all wavelengths. The CIE 1964 standard observer has been similarly defined for the 10° field of view. These sets are used throughout industry. As well as standard observers, standard illumination conditions must be defined as the form of tables of relative spectral power against wavelength. Illuminant A corresponds to the interior illumination by tungsten filament lamps, C represents average daylight with a correlated colour temperature of 6774 K, and the D sources aim to describe for other phases of daylight. For instance, the most widely used daylight standard is D65, which represents a source whose correlated colour temperature is 6504 K. There are a number of other illuminants which are used, too.

The spectrophometer used to carry out the measurements is CM 2600d by Konica-Minolta (figure 4.23) [18]. It is an instrument used for the spectral analysis that works making a comparison between two spectra, one of reference (such in the case of the surface of the test sample used for the reflected colour measure) and one real. This means that the only physical measures that this instrument is able to give us are only spectral reflectance factor (%), and the other data are calculated by that one, through software.

Figure 4.23 – CM 2600d spectrophotometer, Konica-Minolta.

Being a spectrophotometer, the range considered is the visible ones and the results returned are between 400nm and 700nm. The instrument suitable for colour measurements is characterized by four parts:

- A lighting system, which in the case of the spectrophotometer CM-2600d is a Xenon flash lamp.
- An optical apparatus to lightening the object and collect the diffuse light. The spectrophotometer CM-2600d uses the geometry in accordante with the standard CIE n°15, ISO 7724/I and returns simoultaneosly SCI and SCE measurements.

- An apparatus for the signal analysis, constituted by a spectrometer with grating and a photodiode array.
- An electronic apparatus that manage the measurements and elaborate all the data.

Here reported the entire single component that composes the CM-2600d spectrophotometer.

4.5.1 Integrating sphere

In diffuse reflectance, light is scattered in all directions from the sample. Provided that this scattered light can be collected onto an optical detector, the surface reflectance may be measured either at a given wavelength, or by performing a scan over a range of wavelengths. Such a wavelength scan can then be used to characterise colour. In specular reflectance, the light reflected from a sample has an angle of reflectance equal to the angle of incidence of the illuminating light. Specular reflectance is normally used for the measurement of samples whose surface reflects light but shows very little scatter. For example, the reflecting properties of a coated optical mirror may be measured using specular reflectance. In the past, mirror systems were used to measure diffuse reflectance, but nowadays accurate diffuse measurements are carried out by means of an integrating sphere.

An integrating sphere consists of a completely spherical chamber. The inner wall of the chamber is made of a material that provides the maximum possible reflectance over the entire visible wavelength range. Previously, barium oxide coatings were used but much improved results are now obtained by the use of the extremely reflective material, Spectralon. Sphere diameters are typically in the range of 50 mm to 300 mm diameter. Light is scattered in all directions from a sample within a half spherical space. This light is multiply reflected at the surface of the sphere and eventually reaches the optical detector for detection and measurement. Measurements of diffuse reflectance may be made either with the specular component included or excluded. The multiple reflection of the light at the inner surface of the integrating sphere demands the highest possible reflectivity of the inner surface of the sphere to minimise the attenuation of the light reaching the detector. For this reason the inner surface must be constructed from material of the highest reflectivity available. For accurate measurements, the surface area of the sphere that is used for the inlet, outlet and sample ports should not exceed 8% of the total surface area. In figure 4.24 reported the schema of an integrating sphere.

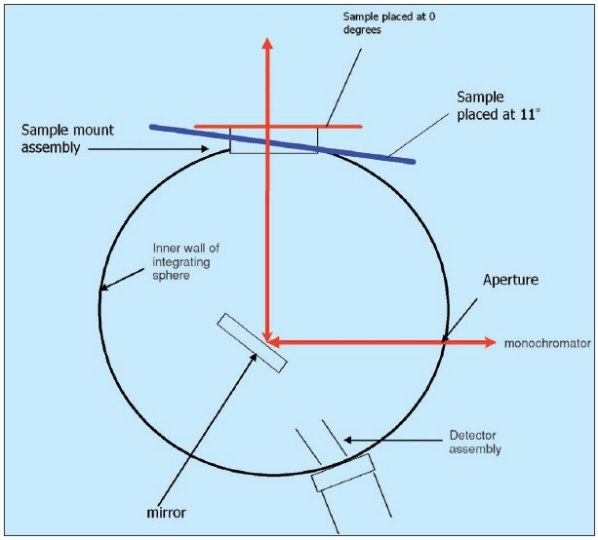

Figure 4.24 – A schematic view of the inside of an integrating sphere. Light of the selected wavelength enters the integrating sphere via the aperture and is reflected by the internal mirror on to the sample. All reflected light, no matter at which angle or in which plane is "collected"by the highly reflective internal surface of the sphere so that the total amount of light reflected by the sample can be measured by the detector. Changing of the angle at which the incoming light strikes the sample enables measurement of both diffuse and specular reflectance [19].

4.5.2 Grating

Most of the time gratings are used as the dispersive element in array spectrometers. They have the advantages of higher dispersion and lower production costs than prisms [20]. The basic grating equation is as follows:

$$\sin\theta_m = \sin\theta_i + m\frac{\lambda}{d}$$

with θ_i and θ_m angles of the incident as well as the diffracted wave directions to the normal of the grating surface, λ wavelength, d grating period and m order of diffraction (integer value, $m = 0, \pm1, \pm2, \ldots$). This equation is valid for reflexion gratings, whose grooves are perpendicular to the plane of incidence. Gratings in spectrometers are mostly used in reflectance mode.

The equation shows, that for $m \neq 0$ the radiation of different wavelengths is separated angularly. This effect is called dispersion. Furthermore, each wavelength is diffracted into different discrete angles according to the order m, causing an ambiguity. Spectrometers usually use the dispersed light of one order. Influences of other orders and the non-dispersive zero order has to be suppressed. Figure 4.25 shows the angular separation for monochromatic and polychromatic radiation, caused by a grating.

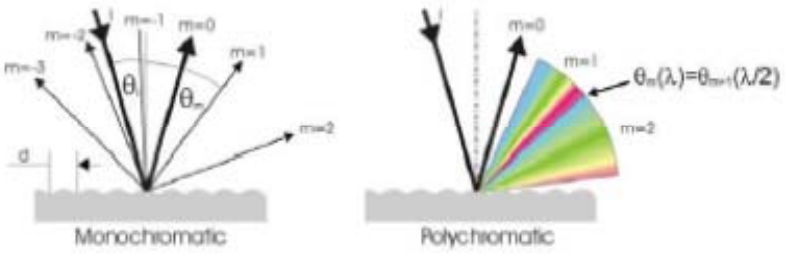

Figure 4.25 – Angular separation of mono and polychromatic radiation [20].

It demonstrates the overlap between the different orders - the diffraction angle for $m = 1$ in the red region coincidences with the corresponding angle of half of the wavelength for $m = 2$. The free spectral range (range without overlap) becomes smaller for higher diffraction orders.

As mentioned above, the order of diffraction can have negative or positive values. The common convention, also used here, calls the order positive, if the angle of diffraction exceeds the angle of incidence and lies on the opposite side of the grating normal.

The grating equation determines the angles of diffraction, but has nothing to do with the intensity distribution into the different orders. The fraction of light intensity diffracted in one order, related to the entire incident intensity is called diffraction efficiency of this order. The efficiency can be tuned by varying the shape and depths of the grooves. An increased efficiency is obtained by a saw tooth profile. The angle of the swots has to satisfy the condition of the regular reflexion law to reflect the incident beam into the angle of the chosen diffraction order. This is called blazing and the condition can be met exactly for one wavelength only, the blaze wavelength. It is practical to lay this wavelength in the region, where the other components of the system have low efficiency, e.g. the light source or the detector, to achieve a homogenisation of the system's performance.

The change of diffraction angle corresponding to a small change in wavelength is called angular dispersion of a grating. The following equation is obtained by differentiating the grating equation to the wavelength with fixed angle of incidence:

$$\frac{d\theta_m}{d\lambda} = \frac{m}{d \cdot \cos\theta_m}$$

The linear dispersion $dl/d\lambda$ is the product of the exit focal length f of the spectrometer and its angular dispersion:

$$\frac{dl}{d\lambda} = f \cdot \frac{d\theta_m}{d\lambda} = \frac{f \cdot m}{d \cdot \cos\theta_m}$$

It defines the extend of the spectrum on the detector array.

4.5.3 Photodiode Arrays

Photodiode arrays consist of several photodiodes arranged in a line. The light energy impinging on a diode generates a photocurrent, which is integrated by an integration circuitry associated with this pixel. During a sampling period the sampling capacitor connects to the output of the integrator through an analogue switch (Fig. 4.26) [20].

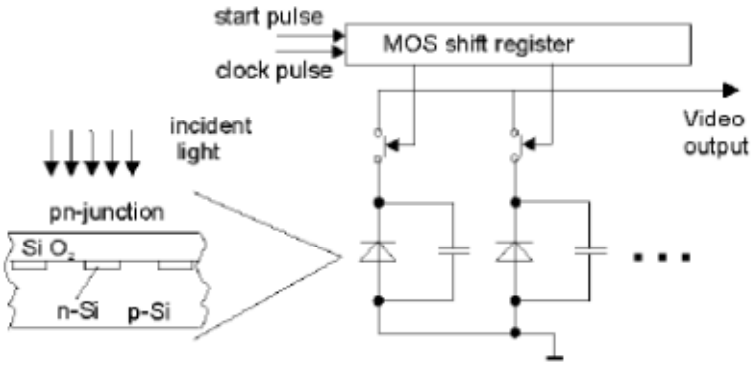

Figure 4.26 - Operation principle of photodiode arrays [20].

There exist two different types of photodiode arrays which differ by kind of their output signal. Current output arrays supply the recharge current of the depletion layer capacity as measuring signal. Therefore, an additional integrator is necessary. The relation between the peak value of this current and the integral is poor, so read out electronics based on the reading of the peak value are of lower quality. Especially with low saturation charge, it is difficult to measure the output correctly. A value of 1 pC equals about 10^7 electrons, with an electronic resolution of 16 bit one LSB is represented by only 1000 electrons.
Voltage output arrays have the integrator on board and deliver a photon flux proportional voltage for the measurement. This causes fewer problems with the read out electronics.

Bibliography

[1] Flammer J., Mozaffarieh M., Bebie H. "Basic Sciences in Ophthalmology", Springer, 2013, XV, 250 p., 441 illus., 396 illus. in color., Hardcover, ISBN: 978-3-642-32260-0 (Print) 978-3-642-32261-7 (Online).

[2] Brill, T.B. "Light:Its Interaction with Art and Antiquities", Hardcover, Springer, 1980, ISBN 10: 0306404168 / ISBN 13: 9780306404160

[3] Dror, R.O. "Surface Reflectance Recognition and real-world illumination statistics", Graduation thesys on "Doctor of Philosophy in Electrical Engineering and Computer Science at the Massachusetts Institute of Technology", 2002 Massachusetts Institute of Technology.

[4] Blinn, J.F. "Models of light reflection for computer synthesized pictures", Computer Graphics (SIGGRAPH), 11, 1977.

[5] Bui-Tuong Phong, "Illumination for computer generated pictures", Communications of the ACM, 18(6):311{317, 1975.

[6] Larson, G.W., Shakespeare, R. "Rendering with Radiance: The Art and Science of Lighting Visualization", Morgan Kaugmann, San Francisco, 1998.

[7] Ward, G.J. "Measuring and modeling anisotropic reflection", Computer Graphics (SIGGRAPH), 26(2): 265-272, 1992.

[8] Horn, B.K.P. "Robot Vision", MIT Press, Cambridge, MA, 1986.

[9] Hiltunen, J. "Accurate Color Measurement", University of Joensuu, Department of Physics, Väisälä Laboratory, Dissertation 30, 2002. - 88 p. ISBN 952-458-077-2.

[10] Oleari, C. "Misurare il Colore. Fisiologia della visione a colori - Fotometria - Colorimetria e norme internazionali", Hoepli; 2 edizione (1 ottobre 2008), 380 p., ISBN-10: 8820341263 - ISBN-13:978-8820341268.

[11] Judd, D.B. "Reduction of data on mixture on color stimuli," Bureau of Standards Journal of Research 4, 515–548 (1930).

[12] Stiles, W.S., Burch, J.M. "N. P. L. Colour-matching investigation: Final report," Optica Acta 6, 1–26 (1959).

[13] Speranskaya, N.I. "Determination of spectrum colour coordinates for twentyseven normal observers," Optics and Spectroscopy 7, 424–428 (1959).

[14] Wyszecki, G., Stiles, W.S. "Color Science: Concepts and Methods, Quantitative Data and Formulae", 2nd ed. (John Wiley & Sons, New York, 1982).

[15] Meyer, G.W. "Tutorial on color science", The Visual Computer (1986) 2:278-290, Springer-Verlag 1986.

[16] Lister, T. "Simulating the Colour of Port Wine Stain Skin", Thesis for the degree of Doctor of Philosophy, February 2013.

[17] Dawson, J.B, Barker, D.J, Ellis, D.J, *et al.* "A theoretical and experimental-study of lightabsorption and scattering by in-vivo skin". *Physics in Medicine and Biology,* 1980, 25(4): 695-709.

[18] CM-2600d Spectrophotometer: Portable Spectrophotometer|Optical Spectrophotometer Uses - Konica Minolta Measuring Instruments.

[19] Principles and applications of reflectance spectrophotometry, As published in LabPlus international - October 2006.

[20] Basics of Spectral Measurement - JETI Technische Instrumente GmbH 2005.

Chapter 5
Materials and methods

Most of the historical paints are mainly constituted by inorganic pigments, either pure or mixed, spread on the surfaces using different binding agents. The pigments[1] have always been part of the colour palette of the artists, thanks to their high colouring power, availability, stability and persistence over time. The use of some natural pigments, of mineral or organic origin, dates back to prehistoric times (red and yellow ochre, indigo etc.). Thereafter, the succession of different historical epochs has seen the advent of new pigments either in their pure form or in special mixtures by expanding the palette of the available colours.

In this chapter the pigments used are presented: the samples analyzed are mixtures realized using historical pigments, both in powder (pure or mixed) and using casein as painting medium.

5.1 Pigments

To realize this work, after an accurate study about the pigments used from prehistory to Modern Age, four of the most common pigments widely used for paint and/or polychrome surfaces were chosen: 4 for red, 4 for yellow, 4 for blue and 4 for white. They refer to the well-known Kremer's collection of artist's pigments [1].

Name, corresponding catalogue number, chemical composition and origin of each pigment are reported in Table 5.1.

[1] "Pigments are coloured, black, white or fluorescent particulate organic and inorganic solids which usually are insoluble in, and essentially physically and chemically unaffected by, the vehicle or substrate in which they are incorporated. They alter appearance by selective absorption and/or by scattering of light. Pigments are usually dispersed in vehicles or substrates for application, as for instance in inks, paints, plastics or other polymeric materials. Pigments retain a crystal or particulate structure throughout the coloration process. As a result of the physical and chemical characteristics of pigments, pigments and dyes differ in their application; when a dye is applied, it penetrates the substrate in a soluble form after which it may or may not become insoluble. When a pigment is used to colour or opacity a substrate, the finely divided insoluble solid remains throughout the coloration process." P. A. Lewis, Colorants: organic and inorganic pigments, in Azimuth, Volume 1 Color for Science, Art and technology, Edited by K. Nassau, Elsevier, Amsterdam, 1998, pp. 283-312.

Table 5.1. Survey of the analysed inorganic pigments and some of their characteristics.

Colour	Pigment	ID Kremer	Chemical formula	Origin
Red	***Cinnabar***	*10620*	HgS	Inorganic natural Mineral
	Sinopia	*11574*	$Fe_2O_3*nH_2O$	Inorganic natural Mineral
	Haematite	*48651*	$Fe_2O_3+ SiO_2+ Al_2O_3+CaO+MgO+K_2O+$	Inorganic natural Mineral
	Carmine	*42100*	$C_{22}H_2OO_{13}$	Organic natural lake
Yellow	***Lead-Tin Yellow***	*10100*	Pb_2SnO_4	Inorganic synthetic Mineral
	Ochre	*11572*	Fe_2O_3	Inorganic natural Mineral
	Raw Sienna	*17050*	$Fe_2O_3+Al_2O_3+SiO_2+SO_3+SO_3+Mn_2O_3$	Inorganic natural Mineral
	French Ochre	*40050*	Fe_2O_3	Inorganic natural Mineral
Blue	***Lapis Lazuli***	*10520*	$Na_2O*3Al*6SiO_2*2Na_2S$	Inorganic natural Mineral
	Artificial Ultramarine	*45000*	$Na_2O*3Al*6SiO_2*2Na_2S$	Inorganic synthetic Mineral
	Indigo	*36000*	$C_{16}H_{10}O_2N_2$	Organic natural dye
	Azurite	*10201*	$Cu_3(CO_3)_2(OH)_2$	Inorganic natural Mineral
White	***Bone white***	*58920*	$Ca_3(PO_4)_2$	Organic natural Mineral
	Zinc white	*46300*	ZnO	Inorganic synthetic Mineral
	Titanium white	*46200*	TiO_2	Inorganic synthetic Mineral
	Chalk white	*11415*	$CaCO_3$	Inorganic natural Mineral

Now are presented in detail the characteristic of each single pigment used, following the order showed in table 5.1 [2, 3].

5.1.1 Red Pigments

Cinnabar

Nomenclature: Vermilion; orange, Chinese, English, or scarlet Vermilion is used to designate different shades. The natural mineral was called cinnabar. In antiquity Vitruvius called the pigment minium. To differentiate between bright red varieties and those with a yellow tinge, the adjectives "light" and "deep" are sometimes used. (French: vermilion clair and foncé; German: Zinnober hell and dunkel.)

Appearance: Bright red, sometimes with a yellow tinge (rare in natural products) or with a slightly purple cast.

Group and origin: The natural mineral used formerly was found at Almadén, in Spain, and in Istria, in the form of bright red, soft, earthy lumps irregularly distributed in siliceous rock or as inconspicuous, longish violet-brown or deep crimson crystals, which only developed their typical vermilion colour during grinding. Since the time of Albertus Magnus (thirteenth century), the pigment has been made artificially from mercury and sulphur by various wet or dry methods, sometimes with the aid of potassium hydroxide of from mercury and sulphur compounds. It was not manufactured in specialized plants until 1785. The black ethiops mineral formed initially is changed into the bright red crystalline form by further treatment.

Chemical composition: Mercuric sulphide (HgS)

Texture: The decidedly soft powder feels somewhat greasy and is very easy to grind.

Permanence: Not reliably permanent in light, since many varieties have a tendency to blacken unpredictably. In paste and water-base techniques nearly all grades of powdered vermilion suffer from this to some extent, whereas the phenomenon is rarer in oil or resinous vehicles, probably because here the pigment particles are completely enclosed by the medium and are therefore protected from the direct influence of air and light. It is possibly also due to the influence of light refraction. It is still not certain whether the blackening is a reversal to the black modification of mercuric sulphide or whether other compounds are formed. August Eibner, then director of the experimental Institute for Painting Technique at Munich College of Technology, invented a non-scale in the laboratory. Large-scale manufacture according to his method was never successful. (See also Commercial grades).

Compatibility: Compatible with all pigments. Although there are occasional reports of blackening in mixtures whit white lead, the author attributes this in gouache painting to the formation of lead sulphide form atmospheric sulphur fumes and not to the action of free sulphur in the extremely stable vermilion.

Fastness to media: Compatible with all media.

Miscibility: Settles out in aqueous media and even in oil paint tubes because of its high specific gravity of 8.0.

Wetting: Sometimes difficult to mix with water.

Oil absorption: Up to twenty-five percent oil or more. Should be ground in linseed oil, with a small addition of boiled linseed oil and approximately two percent wax paste (one part beeswax, two parts turpentine) to prevent oil separation and thickening in the tube.

Stability of consistency: Lower than normal.

Tinting strength: Fairly good.

Hiding power: Very good.

Transparency: Not transparent.

Drying effect: None; may even have a retarding effect on drying.

Toxicity: Not poisonous, since mercuric sulphide is very insoluble. Even in technical literature one finds statements to the contrary, but these are now considered erroneous. Tubes of paint and watercolour cakes are no longer labelled as poisonous.

Commercial grades: Even without the epithet genuine, vermilion should always be pure mercuric sulphide. Mixtures with red lead, adulteration with barites, or topping with dyes are not permitted. Its high price and above-mentioned tendency to blacken are the reasons for the appearance on the market of vermilion imitations, more or less suitable for certain purposes (e.g., study and poster colours). In 1926 the author tested a range of artists' oil colours and found that the vermilion bleached out completely, leaving only the white substrate, when exposed to sunlight. There are now some extraordinarily light-fast substitutes, which are quite acceptable as long as they are clearly labelled and their contents exactly described. The various shades of vermilion are offered for sale from shade cards and by order numbers. Pure scarlet or brilliant scarlet, a mercuric iodide pigment, is of no interest to artists.

Tests: True vermilion burns with a bluish flame. Alcohol, benzene, or amyl acetate will extract coaltar dyes. Other adulterations and additions of red lead can only be positively identified by a chemist.

History: The pigment has been in use since antiquity and has been found in ancient China, Egypt, Assyria, Greece, Rome, Judea, and even in Mexico and Peru. According to Vitruvius, the Greek word kinnabari became the Latin cinnabris and was later changed to cinnabar. On Pompeian walls strikingly luminous and warm. However, after the excavations the walls were exposed to direct sunlight as never before, and soon the dreaded blackening began to appear in irregular patches (especially at the Villa dei Misteri near Pompeii). Yet on many walls in windowless rooms of the sometimes seem to refer to vermilion, at other times to red lead; it seems that the two names were often confused. There are also some ancient records of adulteration with burnt ochre or sinopia. In the Middle Ages vermilion was used to line early music staves and to decorate large initial letters. It has kept well on parchment in the old volumes protected from light and air. The sublimation process of production is said to have been known since the eight century. The artificial manufacturing method employed since 1687 was improved by Kirchhoff in 1779. With the inclusion of cadmium red among the artists' pigments in the first third of the twentieth century, vermilion has lost practical importance and is nowadays rarely by artists.

Application: In glue, casein, tempera, oil, lime (with limited light-fastness). In spite of its extremely slow drying, vermilion is now used only in oil.

Further remarks: The various wet and dry manufacturing processes are of no interest to artists. As a mercury compound with a characteristically high molecular weight, vermilion absorbs X-rays as strongly as white lead.

Red Earth Pigments

Nomenclature: Names often indicate the origin: Gulf red, Persian Gulf oxide, Spanish red oxide, Pozzuoli red, formerly also Indian and Venetian red (now used for artificial products), red ochre, red bole, natural red chalk, sinopis or sinopia of the ancients.

Appearance: These natural earths never occur in particularly bright red hues, but their fine, broken tints have always appealed to painters. Their shades very according to their origin and composition, and at any given location nature may produce strata or deposits of different colours, depending on the conditions prevailing during they formation.

Group and origin: Natural mineral pigments, obtained from pits or quarries; levigated, ground, and wind-sifted (forced through a fabric screen by a stream of air). Some grades are washed out of iron ores and then levigated. Sinopia was mined from caves and tunnels.

Chemical composition: Varieties rich in clay and silica (Pozzuoli red and red bole) contain up to approximately twenty percent FE2O3; Persian and Spanish products may contain up to ninety-five percent ferric oxide.

Texture: Pozzuoli red occurs in soft, earthly lumps, rich in clay, and is reduced relatively easily to homogeneous, soft powder. Persian Gulf oxides are harder, almost rocklike, and sometimes violet in colour. Spain produces several varieties of high-quality red iron ores, one of which is so soft that it is the time of the old masters. Natural occurrences generally vary in hardness. Good Armenian bole is especially soft and smooth, while German kind is rather hard and sandy. Red iron oxides often occur near active or extinct volcanoes.

Permanence: Perfectly high-fast and weatherproof – the most permanent of all pigments.

Compatibility: Compatible with all pigments.

Fastness to media: Can be safely used in all media and techniques, even in cement.

Miscibility: Good with varieties containing clay. The heavier, coarsest varieties settle out to such a degree, especially in aqueous media, that they are sometimes difficult to stir up.

Wetting: Generally good, but some varieties rich in clay wet less readily in water.

Vehicle absorption: varies greatly; from thirty to sixty percentage in oil. High-quality grades need to be carefully bound in casein, glue, and tempera with ample amounts of vehicle. The colour of iron oxides will vary according to the composition of a natural or synthetic emulsion. Red-chalk drawings darken considerably when fixed. Glazes on murals need mere traces of vehicle.

Stability of consistency: normal with all varieties.

Tinting strength: depending on the clay content; very great with pure varieties rich in iron oxide. In Pompeii, inscriptions painted on walls with this pigment merely suspended in water have diffused into stone and mortar to such an extended that to this day they have not been washed out by rain.

Hiding power: very good. Varieties containing much clay cover less well in oil.

Transparency: can be used for glazing in spite of its opacity, owing to its high tinting strength.

Drying effect: the high content of iron oxide has a drying effect on oil.

Toxicity: not poisonous.

Commercial grades: the various products are offered for sale by names describing their origin or by samples painted on shade cards with glue or methyl cellulose. Since the quality of natural products varies, colour manufactures are often forced to combine several shipments of raw materials so that the hues of the shade card can be matched.

Tests: usually tested by laying down samples only. Adulterations are rare.

History: different shades of red iron oxides have been known since prehistoric times. They can be found in rock and cave paintings. The ancient painters collected lumps of coloured earth. In antiquity, deposits in Egypt, and on the island of Lemnos and Malta, were used. Modern analytical methods can sometimes prove the provenance of red-earth pigments. The ancient sinopia deserves a special mention. Pliny (Book XXXV, chapter 31) mentions three types of sinopys pontica – light, middle and dark. The three varieties were used extensively. The light shades are yellowish, like slightly burnt ochre, while some of the dark shades had a violet hue. The earths from Sinope are among the most powerful red pigments known. Even when used a glazes, their tinting strength is remarkable. During the trecento and quattrocento, it was common practice in Italy to paint the design for a mural on the rough plaster with various shades of sinopia. This preparatory drawing for fresco, which was often very detailed, is still called sinopia. Many of these have been skilfully uncovered during fresco transfers. Unfortunately, artillery fire during World War II is also responsible for uncovering some of them in the Campo Santo in Pisa.

Application: in glue, casein, tempera, oil, lime, cement, silicate. Oxides of iron may be used in all techniques, but only soft varieties in pastel. Armenian bole has always been considered the softest variety and the richest in clay; hence it is especially suitable as a base for gilding that is meant to be burnished. For centuries the most common use for iron-oxide pigments has been in house painting on wood or plaster, and in colouring cement and graffito mortar. For painting exterior walls the pigment was strongly diluted with quicklime. Even primitive tribesmen have always delighted in using the red earths, sometimes in the most surprising ways.

Further remarks: the high cost of processing and transportation are leading to the gradual disappearance from the market of the natural red-earth pigments. Terra di Treviso, a beautiful pigment from north-eastern Italy, is practically unknown to artists today. With many natural products only the names are left, which are now used as designations for certain shades irrespective of origin. The red quarries of Pozzuoli in the Gulf of Naples have been exhausted since 1935. Only pozzuolana, dull-red earth containing much silica, is still mined and used as natural cement. Doerner's opinion that Pozzuoli red, because of its cementlike effect, is unsuitable for fresco has not been borne out. On the contrary, it was found to harden graffito plaster. Numerous artificial iron oxides have now replaced the natural products. Grades composed mainly of iron oxide absorb X-rays fairly strongly and may therefore look deceptive in radiographs.

Carmine

Nomenclature: Carmine, crimson. The lake pigment is called carmine, crimson, or Florentine lake. (French: carmin, lacque carmine; German: Karmin, Karminlack.).

Appearance: A clear, cool red with a bluish tinge. Lately the colour has been matched by a few modern synthetic dyes. The word crimson is sometimes used as a descriptive term.

Group and origin: Natural organic animal dye, usually struck on substrata for oil colours. Female cochineal insects (Coccus cacti) bred on one of the cereus cacti in Central America and the Canary Islands are dried and form the raw material. Black cochineal (as opposed to the red variety) yields the highest quality dye. This apparently contradictory name describes the blackish-gray appearance of heat-dried insect bodies.

Chemical composition: The colouring principle is carmine acid, an oxyanthraquinone dye. It is extracted from the insects and precipitated on alumina with aluminium acetate.

Texture: Very fine, light, voluminous powder.

Permanence: Unfortunately not very light-fast and not alkali-proof. There are now more permanent substitutes.

Compatibility: Compatible with all other pigments, but it is normally only mixed with blue pigments.

Fastness to media: Impermanent in lime and silicate but may be used in alkaline casein emulsions.

Miscibility: Good.

Wetting: Poor; requires wetting agents.

Oil absorption: Sixty to eight percent oil, but without practical significance, since the pigment is unsuitable for artists' use.

Stability of consistency: Of no practical importance.

Tinting strength: Very high with pure varieties.

Hiding power: Poor.

Transparency: Typical glazing pigment.

Toxicity: Not poisonous; used as cosmetic colour.

Commercial grades: Although the pigment cannot be recommended for artists' use, nacarat carmine, which is the only suitable variety, is sometimes used. Java cochineal and Guatemala cochineal are unsuitable ad pigments. Pigment described as light –fast is probably some high-quality coal-tar product like "permanent carmine FBB extra", a mono-azo dye of the naphthol-AS series made by Farbwerke Hoechst AG. This contains no acid groups, is alkali-proof, and has a light-fastness of 7 to 8.

Test: Should be tested only by qualified chemists.

History: In antiquity kermes or "grain", obtained from a different insect, was used as dye and lake (kermes lake, grain lake). The little globular animals lived on oaks in Southern Europe and were mistaken for vegetable berries; hence the name grain. During the Middle Ages Venetian scarlet was made from this dye. In the sixteenth century kermes was replaced by cochineal, which had been known since the conquest of Mexico. In spite of its decided impermanence, it is still popular with the less-knowledgeable artist, mainly in watercolour.

Application: Most commonly as watercolour. Experts avoid it in oil.

Further remarks: The cool, bluish-red tint of carmine is undoubtedly superior to the colour of even the best madder, but professional artists should not be tempted to use this pigment, which is far too impermanent. It has yet to be proven whether permanent coal-tar pigments meet the requirements of artists' materials. The outlook seems favourable. Carmine cannot be seen on radiographs.

5.1.2 Yellow Pigments

Lead-tin yellow

Nomenclature: The name of this mineral pigment means "little yellow" by giallulinum a diminutive of giallus (yellow), also known as giallorino.

Appearance: An opaque yellow with good covering power.

Group and origin: It's a Lead-Tin oxide, discovered in the 13th and used until 18th Century, but most common from 15th to 17th centuries.

Chemical composition: There are two type of lead tin yellow, type I and type II. Type I is lead-tin oxide (Pb_2SnO4) and is most frequently found on old paintings. Type II is a second variety of lead-tin oxide that may contain free tin oxide and additional silicon ($PbSnO_3$, $PbSn_{(1-x)}Si_xO_3$, or $Pb_2Sb_2O_7$).

Texture: Very fine, light, powder.

Permanence: Lead-tin yellow is not affected by light and is stable under normal atmosphere.

Compatibility: On paintings, lead-tin yellow (type I) has been found mixed with lead white, vermilion, yellow lakes, ochre's, verdigris, indigo and azurite.

Fastness to media: it is soluble in nitric acid. Is used in fresco technique and oil. Not recommended for temperature and encausto.

Miscibility: is altered and blackened by sulphur-based compounds

Oil absorption: Lead-tin yellow a small amount of oil (16 g oil per 100 g of pigment). It is a fast dryer in oil paint and forms an excellent film.

Stability of consistency: good stability to light and moisture, black in contact with atmosphere sulphides

Toxicity: Lead-tin yellow contains lead and is poisonous. Utmost care should be used in handling the dry powder pigment to avoid inhaling the dust.

History: The giallorino yellow pigment, well-known in medieval epoch in Italy; was discovered in the 13th and used until 18th century. Lead-tin yellow frequently occurs in European painting before the 18th century. The earliest recipes for a yellow pigment from lead and tin was found in the Bolognese manuscript from the first half of the fifteenth century. Old Italian manuscripts make reference to a

pigment of pale yellow colour called *giallo lino* or *giallorino* while northern manuscripts use the term massicot (which now designates yellow lead oxide) to describe a pigment prepared from lead and tin. Only during 17th century lead tin yellows gradually evolved to lead antimonate yellows. The presence of lead makes the giallorino a toxic pigment and not longer used.

Ochre and Yellow Earth colours

Nomenclature: Ochre; other names according to shade or origin (distinguished by letters in France) (French: *ocre jaune*, *ocre d'or*, *ocre brun*; German: *Gelb Ocker*, *lichter Ocker*, *Goldocker*, *Dunkelocketr*). The distinctions between yellow, light, brown, gold ochre, or Roman ochre are rather arbitrary (see *Commercial grades*).

Appearance: There is a great variety of shades ranging from a pale, broken yellow to brown.

Group and origin: Ochre's are natural earth pigments with little variation in composition (see *Commercial grades).* They occur all over the world as soft rock or hard earths and are retrieved predominantly by open-cast mining. The natural product is refined by levigation, grinding, and sifting.

Chemical composition: Weathering products of iron-bearing rocks or minerals. Hydrous iron oxides produce the coloration. Among the secondary components are clay (aluminium silicates) and calcium compounds. Ochre's mixed with chrome yellow (to improve drying) are of no interest to artists. One has to choose between pigment rich in clay and varieties rich in chalk, according to the technique to be employed. Ochre collected as a sediment of iron minerals from pit seepage are now of little practical importance in Germany (see also Iron Oxides).

Texture: Soft or coarse, sometimes even gritty, powder. They are never "cut" with extenders. Toning or topping with other pigments of coal-tar dyes makes them unsuitable for artists use.

Permanence: Absolutely light-fast and weatherproof, unless they contain undesirable pigment additions or dyes.

Compatibility: Compatible with all pigments.

Fastness to media: Remains unchanged in all media. (Only ochre containing manganese is prone to darken in oil.).

Miscibility: Good.

Wetting: Normal.

Oil absorption: Grades containing little clay need approximately fifty percent, those containing much clay more than sixty percent linseed oil.

Stability of consistency: Fairly normal; varies slightly according to kind and origin of the raw material.

Tinting strength: Varies considerably according to content of hydrous iron oxide. French ochre are regarded as having the greatest tinting strength.

Hiding power: Depends on the composition. Ochre containing clay has the greatest opacity.

Transparency: Ochre with a high content of calcium carbonate are moderately transparent in than layers. For glazing, *terra di Siena* is preferred.

Drying effects: No catalytic action in drying oils. Ochre that contains clay, and therefore need more oil, dries more slowly than those containing chalk.

Toxicity: Not poisonous.

Commercial grades: French powder pigments are marked with capital letters according to their properties. Generally, ochre is distinguished by their shade, origin, or suitability for certain techniques or media. Artist's – colour manufactured blend the commercial pigments to obtain standard shades because natural products are very rarely of even quality and colour, and artists invariably demand that their tube colours match the respective firm's shade card. This means that the most valuable, strongly coloured grades are not sold as they were at the time of the old masters. Instead they are dissipated to adjust to the shades of ordinary raw products. (The author once recommended the use of unusually strong, golden-yellow ochre that only occurred naturally in isolated "pockets"; yet even experienced painters rejected materials, falsely suspecting it of having been "toned").

Tests: Alcohol, benzene, or amyl acetate should not extract any colour unless the material has been topped with coal-tar days. Only an experienced chemist can determinate the proportions of iron oxide, clay, chalk or silicate. He can also test for lead or additions of chrome yellow, neither of which are permissible for artists' natural ochre.

History: Ochre is among the oldest pigments known to man. They can be found in prehistoric cave paintings and, in great variety, in all techniques throughout the entire history of art. Only artificial ochre is of recent origin.

Application: May be used in pastel, casein, tempera, oil (linseed oil), lime cement, silicate. Pure, unadulterated ochre are the most reliable pigments available for any technique. They are also the cheapest. There is an understandable difference between pigments for ordinary house paint and specially selected pleasing shades that are prepared with greater care and always wind-sifted. This is a process in which the finely ground powder is whirled by a propeller against wire screens of increasing fineness, and finally, it is made to pass through a silk screen. On the other hand, to colour cement pr mortar for graffito, coarser and even gritty grades are preferred, because their larger particles resemble the mortar aggregate in size and this ends to reduce cracking.

Further remarks: Since it has been possible to manufacture hydrous iron oxide chemically in a great variety of concentrations, we are less dependent on natural occurrences selected for their shades. As a consequence of industrialization, the beautiful, soft, high-quality ochre once collected from the mine seepage at Goslar in the Hartz Mountains can no longer compete with the growing production of artificial iron oxide. The once highly valued material is now discarded, because transport and production costs have made its use uneconomical. On radiograph thinly layered ochre can hardly be seen because of the low absorption of the main component, aluminium oxide.

5.1.3 Blue Pigments

Lapis lazuli

Nomenclature: Lapis lazuli, azuro oltramontio (French: bleu d'autor; German: Lapislazuli, Larunstein).

Appearance: The colour of the mineral s difficult to describe.

Group and origin: Natural mineral pigment, originally available only as a finely crushed stone; later a refining process was developed. It is found as the mineral lazurite, mainly around Lake Baikal, in Afghanistan, and in Tibet, but also in Spain and Chile. In its natural state lazurite may vary considerably from extremely hard, believable plates of semiprecious stone to calcareous rock in which silica, more or less closely packed in interspersed with blue fragments of various sizes, sometimes as small as 1/16 inch. Inclusions of pyrites in golden veins or specks are frequent.

Chemical Composition: The composition and origin of this mineral are even now not clearly understood. It is thought to have following approximate formula (Na ….

Texture: Semiprecious stone of handiness 4, crudely broken and sorted; crushed and ground as finely as possible.

Permanence: Almost perfectly light-fast, alkali-proof, waterproof.

Compatibility: its compatibility with other pigments is unimportant, since it has never been common practice to mix this precious material with other pigments.

Fastness to media: Can be used in all media, but was mainly used as pigment for mural painting as tempera emulsions. It also occur in glair (egg-white) or in gums, but not until later does it appear in resin-oil glazes, and then only as purified ultramarine.

Miscibility: Unimportant, does not occur in mixtures;

Wetting: Normal.

Tinting strength: Low

Hiding power: Moderate to good.

Transparency: The powered mineral has a moderate transparency (see Ultramarine Blue, Natural).

Toxicity: Not poisonous

Commercial grades: Nowadays only available as fragments of semiprecious stone.

Tests: Microscopically and by chemical analysis only by a colour chemist.

History: The earliest finds connected with were found in a Sumerian mosaic dating from the third millennium B, C. Other examples were found in the treasury of Ramses II (1290-123 B.C). Lapis lazuli was mentioned by Greeks and Romans in early antiquity. The Greek name for it was kyanos: the Romans called it *caeruleum scythicon*. These and other names were, however, used for several blue pigments, and even Raehlmann confuses them at times, Painy's mention of pyrites inclusions, once erroneously thought to be gold, proves that he was speaking of genuine lapis lazuli, but its use as a pigment is first reliably recorded by Marco Polo in 1271. The material was imported from mines in Afghanistan. At the beginning of the fourteenth century we find a reference to azurinum ultraumatinum (blue from beyond sea), which may mean the Indian Ocean. Others interpret it as Caspian Sea or Black Sea. Particularly were found more recently at Lake Baikal, in the USSR. The pigment that was imported via Persia and Mediterranean was probably an already purified blue prepared from lapis lazuli, as

mentioned in recipes dating from 1271. About 1390 Cennini gives very detailed instructions about the process (see Ultramarine Blue, Natural). From the beginning of the sixteenth century on, crude, simply crushed lapis lazuli disappears from paintings, and one finds, instead the highly refused product that was eventually replaced by factory made artificial ultramarine in 1834. In his investigation, A.M. de Wild recorded natural ultramarine on paintings between 1438 and 1810.

Application: In glue and gum media, tempera, and lime. Only the refined ultramarine blue obtained from lapis lazuli was also used in glair and later on in oil and resin glazes.

Further remarks: The various blue pigments of antiquity and the middle Ages are not always clearly distinguished, and in later period's azurite are often confused with ultramarine. Even today, the difference between the primitively prepared mineral lapis lazuli and the laboriously refined high quality natural ultramarine is often overlooked.

Artificial Ultramarine

Nomenclature: Ultramarine blue, ultramarine, French ultramarine, French blue, Gmelin's blue, new blue, permanent blue, royal blue; also Academy blue, lime blue, sky blue (the last named are mixtures of eat varieties), (French: *uotremer*; German: *Ultramarinblau*)

Appearance: The colour resembles genuine ultramarine but is made wide range of shades from greenish to deep blue and includes reddish varieties.

Group and origin: Artificial mineral pigment made by calcinations of sulphur, sodium carbonate, and kaolin by the so-called soda process or of kaolin, quartz, and sodium sulphate by the sulphate process. The manufacturing process is quite complicated and is covered by numerous patents. The process is still carried out with crucibles in pot kilns. Experiments with other types of kilns have proved unsuccessful.

Chemical composition: Sodium aluminium silicate-polysulfide. The exact formula has not been determined but can be represented by $(Na_8\ Al_6\ Si_6\ O_{24}\ S_4)n$. It should not contain free sulphur.

Texture: Fine, soft powder varying greatly in shade (see above). The dark varieties are slightly coarser, the pale shades considerably finer in texture.

Permanence: All shades are absolutely light-fast and alkali-proof. Nevertheless, not all varieties are suitable for fresco painting or for work in cement. In the past some products were likely to cause efflorescence.

Up to now, the weatherproof deep-blue ultramarine JC 832 (now Z 2786) from Vereinigte Ultramarinfabriken AG, Marienbeg, has proved most successful in fresco. Most ultramarines are affected by acids. This can show itself with acid preservatives in glue or tempera, but even acid city air can bleach delicate ultramarine passages in exterior paintings. Greenish varieties are more permanent than deep-blue shades. (According to Erich Tanke, *Pigmente* (edited by Hanks Kittel), there are now some special acid-proof varieties).

Compatibility: Being a sulphur compound, ultramarine blue should not be combined with copper and lead pigments like the copper-arsenate emerald green. Theoretically, it is incompatible with white lead, but in practice no discoloration due to lead sulphide formation ever occurs with well-washed white lead.

Fastness to media: Ultramarine is alkali-fast and therefore fast to all media. However, in lime, cement, and silicate techniques on exteriors, only special grades should be used.

Miscibility: Good.

Wetting: Good. Even so, many varieties are treated with wetting agents or glycerine by the manufacturer to improve their brilliance, which in turns improves their wetting properties still further.

Oil absorption: Thirty to fifty percent poppy oil and two percent wax paste.

Stability of consistency: Very poor in oil. When oil is added to sparingly, ultramarine will form a puttylike mass and may even start to burn in the roller mill. The colour tends to become dull and lose its brilliance. Addition of a little concentrated soft-resin solution (e.g., resin AW 2) improves the brilliance and transparency, but the consistency may rapidly be reduced to a point where the paint runs. This break in consistency is reached quite suddenly. For this reason, a little beeswax dissolved 1:2 in turpentine is usually added. Ultramarine is the most difficult pigment to grind by hand.

Tinting strength: Unadulterated grades, the only ultramarine pigments used by artists, have a high timing strength.

Hiding power: In aqueous techniques, adequate; in some tempera media, moderate; low in oil, since ultramarine is a typical glazing pigment. It is most opaque in lime.

Transparency: Unadulterated artificial ultramarine is one of the best glazing pigments available. (See Ultramarine Blue, Natural and Lapis Lazuli).

Drying effect: No catalytic effect.

Toxicity: Not poisonous and, according to Haug, does not cause silicosis.

Commercial grades: Ultramarine pigments are sometimes sold by colour manufactures that do not produce the colour themselves. This is because in Germany the manufacture of this material with its particularly complex production problems has largely been taken by Vereinigte Ultramarinfabriken AG (formerly Leverkus, Zeltner and Consorten) of Marienberg near Bensheim, Hessia. Various grades are sold by numbers and letters, which indicate their type. Artists'-colour manufactures use terms light and deep to distinguish between shades, light ultramarine being of a cooler nuance, while the dark pigment has a reddish tinge. The difference is thus not merely one of saturation, as with cobalt blue.
The decorating trade uses a large number of cut grades in many shades. Violet hues are obtained by final treatment with acids. These are sometimes called red ultramarine, although a more appropriate name would be ultramarine violet. Green varieties sold as ultramarine green are obtained by replacing sodium carbonate with sodium sulphate and calcinate at a temperature of 900°C. Green varieties are also formed in the course of ordinary manufacture.

Tests: The pigment can be recognized even by laymen by the hydrogen-sulphide odour it develops when treated with dilute hydrochloric acid. Organic compounds used for adulteration leave a gray ash on heating. Only a chemist can detect extenders like gypsum, etc.

History: Attempts to discover its composition have been made since 1795. In France a prize offered for the manufacture of synthetic ultramarine was awarded to B. Guimet in 1824; production by this method on a commercial scale was begun in 1826. Quite independently, G.G. Gmelin of Tübingen and F. A. Köttig of Meissen discovered their respective processes in 1828, and Köttig produced the pigment from 1829 onward. Commercial production by Leverkus at Wermelskirchen did not start until 1834, and by Leykauf and Heyne of Nuremberg not until 1838. This rapidly reduced to a minimum the manufacture of natural ultramarine, and only in England was manufacture on an insignificant scale continued into the twentieth century. As mentioned above, in Germany the manufacture of ultramarine pigments has been in the hands of the Vereingte Ultramarinfabriken AG since 1894.

Application: In glue, casein, tempera (avoid acid preservatives), oil (usually with wax additions); only special grades in lime and cement.

Further remarks: Ultramarine is one of the pigments whose appearance depends to a marked degree on the binding medium, which affects not only the saturation (by virtue of its light refraction) but sometimes even the hue. The principal difference between the delicate, pastel like surface effect and

influence of the media. It is one of the peculiarities of deep ultramarine shades cannot be reproduced exactly by even the most efficient colour films, or by three – or four – colour reproduction processes. Special pigments must be employed to reproduce the shade. Graphic designers who want their work reproduced in correct colours should preferably avoid ultramarine and limit themselves to range of colours specially chosen for them.

Indigo

Nomenclature: Indigo, intense blue, wood (French: *Indigo*; German: *Indigo*).

Appearance: Deep violet-blue. Neither natural nor synthetic indigo has been pleasant shade of Monastral blue or Prussian blue. The colour varies considerably.

Group and origin: (A) Natural vegetable pigment; (B) Synthetic organic pigment. (A) The natural pigment is obtained from the Indian *Indigofera tinctoria,* the Chinese *Polygonum tinctorium*, or, in southern Europe, from wood (*Isactis tinctoria*). The leaves of these plants are soaked in warm or cold water until they ferment, and the extract is oxidized air to indigo then washed, boiled and dried. (B) The synthetic pigment is made by various methods from phenyl-glycine or produced as thionindigo.

Chemical composition: (A) The plant leaves contain indicant, which forms indoxyl by hydrolysis or fermentation and is in turn oxidized to indigotin. (B) Synthetic organic compound of the same constitution. (Formulas of organic compounds are not given in this list).

Texture: (A) Irregularly angular Jumps of ½ to 1 inch diameter that yield a blackish – blue powder when ground. (B) Soft, deep blue, lustrous powder.

Permanence: Artificial thioindigo is slightly faster to light than all natural grades, but neither performs adequately enough to be used in art. To be sure, they are neither insoluble in water or alcohol, but neither acid nor alkali-proof.

Compatibility: Compatible with all pigments.

Fastness to media: fast to oil but not alkali-proof.

Miscibility: Normal, but occasionally Boats on top of water-base mixtures.

Wetting: Difficult with finely ground pigment.

Oil absorption: Normal.

Stability of consistency: Normal.

Tinting strength: Fairly moderate.

Hiding power: Good.

Transparency: Moderate.

Toxicity: Not poisonous.

Commercial grades: (A) Bengal indigo is considered the best grade. (B) As a rule, thioindigo is not identified as such.

Tests: Natural indigo varieties burn and leave a pale ash. Exact analysis should be carried out by a chemist.

History: Natural indigo has been known since antiquity and is mentioned by Diascordes, Vitruvious, and Pliny. Rsehlmann writes of a trace of indigo found in paint pots in a Roman tomb near Herne-SL-Hubert, Belgium. Wood was cultivated in France and Germany as early as the ninth century. At the beginning of the sixteenth century East Indian indigo was imported to Europe. The cultivation of indigo in British India declined rapidly during the first decade of the twentieth century. Although A. von Bayer had discovered the process for synthesizing the dye as early as 1880, the artificial product did not begin to compete with the natural material until after 1897.

Application: Only in watercolour. In the early part of the twentieth century it was also used in oil, but it is becoming rare. Unsuitable for all other techniques, except tempera.

Further remarks: The most important application of indigo has always been as reducible vat dyestuff. When artificial indigo appeared on the market, the natural vegetable colour, being less attractive and not always of even quality, was quickly superseded. This led to an upheaval of the dyestuff market, at first in England and later throughout the world.

Azurite

Nomenclature: Azurite, mountain blue, copper blue; the artificial pigment is called blue bice or blue verditer (French: *blue Paul Vèronèse, cendre*; German: *Azurit, Bergblau*.)

Appearance: A cool, pale blue, comparable to cerulean.

Group and origin: (A) Natural mineral pigment resulting from the weathering of copper-sulphide minerals. It is found in Hungary, Czechoslovakia, the Tyrol, southern France, and in very modest amounts even in the Black Forest in Germany. It occurs mostly in red sandstone and has always been a rare and therefore relatively expensive pigment. (B) Artificial mineral pigment prepared form copper-chloride solution with slaked lime, calcium hypochlorite, ammonium chloride, and copper sulphate.

Chemical composition: Basis copper carbonates ($2CuCO_8 – Cu(OH_4)$)

Texture: (A) Blue mineral of hardness 3.5 to 4, crushed and ground in a rather laborious process. Some raw material must be carefully sorted to remove impurities. The saturation of the colour is reduced by decreasing the particle size of the pigment. (B) Light blue, sometimes slightly greyish, rough powder pigment.

Permanence: Good-light fastness. Turns slightly green in oil, possibly due to the formation of copper oblate; in egg-yolk it turns greenish-gray; blackened by hydrogen sulphide. (A) The natural pigment is not permanent in lime. (B) The artificial product is said to be alkali-proof (this has not been tested by the author, since the pigment has lost its practical significance).
The author's collection contains several pieces of blue azurite that have, even in their natural state, changed to the chemically related green malachite in some sports. Such changes to malachite can also be observed in Signorelli's frescoes in the Cathedral of Orvieto, where azurite layers applied in secco technique on fresco under painting now show large green patches, sometimes erroneously interpreted as clouds. Similar changes can be observed on Giotto's painting in the Arena Chapel at Padua. The change is caused by prolonged exposure to dampness and small amounts of carbon dioxide.

Compatibility: Limited compatibility, as is characteristic of all copper compounds and therefore used only on its own or in mixtures whit white.

Fastness to media: Not fast to oil. (A) Natural azurite not permanent in lime (see above).

Miscibility: Without practical significance.

Wetting: Good.

Oil absorption: Not used in oil.

Tinting strength: Low.

Hiding power: Adequate.

Transparency: Moderate.

Drying effect: Without practical significance.

Toxicity: Poisonous, since it is a copper compound.

Commercial grades: (A) Azurite is no longer available commercially, except as a collector's item from mineral dealers. (B) Artificial blue verditer is almost impossible to obtain, since it is now commonly replaced by imitations.

Tests: Blackened by hydrogen sulphide. When examined microscopically the pigment is sometimes confused with lapis lazuli. Exact analysis should therefore be carried out by a qualified chemist.

History: (A) Reports that the pigment was used an antiquity may be the erroneous result of inaccurate methods of investigation. The existence in the fifteenth century of natural azurite (called *azurro della magna* by Cennino Cennini) has been established beyond doubt. In his table of analyzed pigments from paintings A. M. de Wild recorded it between 1490 and 1660. It is rarely encountered after the discovery of cobalt blue (1777); its role as a characteristic pigment is therefore limited. (B) The artificial blue verditer was made from eighteenth century on. In modern watercolour boxes mountain blue and blue verditer are usually only names given imitations.

Application: (A) In glue, casein, tempera (not in pure egg-yolk); on old frescoes it was added in secco techniques. (B) In glue, casein, tempera, lime. Neither variety can be used in oil. Even oil varnishes cause blackish discolorations.

Further remarks: Azurite now has only historic significance, but it is of importance to conservation. Even in the middle Ages it was frequently confused with lapis lazuli and smalt.

5.1.4 White Pigments

Bone white

Nomenclature: Bone Ash

Appearance: is a greyish white, slightly gritty powder

Group and origin: Bone calcined in the presence of oxygen until all organic matter has been burned away. Mostly tribasic phosphate with traces of calcium carbonate and other salts.

Chemical composition: $Ca_3(PO_4)_2$

Texture: powder coating

Compatibility: chemically inert and free of organic matter

Miscibility: In painting grounds, it makes a durable surface while adding some tooth especially for egg and casein tempera, distemper, encaustic and oil painting. Use in chalk and gesso grounds to increase absorbency and add texture. Bone ash is used in Cennino's recipe for silverpoint grounds.

Wetting: excellent non-wetting properties

Oil absorption: Add to oil colours and mediums to create textural and bodying qualities to oil paint without affecting the colour. Bone ash has little colour in drying oil, so it can be added to oil paint without affecting the colour temperature.

Stability of consistency: high thermal stability, so it maintains its form in extremely high temperatures.

Tests: Put half of the required water together with all the bone ash powder in a container. Add enough water to get a good mixing action. Continue mixing until lump free and uniform consistency is obtained. Do not vortex the mixture in order to avoid air entrainment. Add the remaining water as required by the formula or recipe.

History: Bone ash is made from selected bones properly leached, ground, chemically treated, calcined by a special procedure and milled to a small particle size. Our bone ash is obtained by roasting degelatinized bone up to a temperature of approximately 1100° C. Afterwards, the bone ash is cooled and ground to a fine particle size so that a minimum of 95% will pass through a 325-mesh (U.S. Standard) sieve. The excellent properties of bone ash are attributed to the internal structure of the small, individual particles. The original cellular structure of the bone is preserved, thus giving the material a high resistance to heat transfer (natural thermal insulator). Bone ash is primarily tri-calcium phosphate or a form of calcium hydroxyapatite

Zinc white

Nomenclature: Zinc white, zinc oxide, Chinese white, permanent white (French: *blanc de zinc; German: Zinkweiss).*

Appearance: Artist's zinc white should be pure white. Pigment dyed blue to make it appear white should be refused. The appearance of high-quality zinc white powder is somewhat lighter than the lightest Munsell value V-9.18.

Group and origin: Artificial mineral pigment made by burning metallic zinc vapour, other, so-called direct, methods are of no interest here.

Chemical composition: Pure zinc oxide (ZnO).

Texture: A soft, snow-white powder available in various degree of fineness under names like where seal (ef, *Commercial grades).* All grades can be ground without difficulty; sometimes mixing with a palette knife will be sufficient.

Permanence: Very light-fast. Causes no yellowing in oil. Its colour is not affected by hydrogen sulphide; therefore it does not darken in air. Affected by acid media but may also be difficult to use in slightly alkaline casein medium, where it tends to set or flocculate. Zinc white may become brittle in oils and emulsions. In most air the soft zinc-oxide powder changes to a gritty, granular, and sometimes lumpy material, and becomes difficult if not impossible to use. It has changed to crystalline basic zinc carbonate dioxide. Artists should not accept such material, which can only be restored by recalcination.

Compatibility: Compatible with all pigments. Occasional cases of bleaching cannot be attributed to the quality or characteristic of the zinc white concerned.

Fastness to media: May be used in all binding media except waterglass, lime-casein, or alkaline casein medium. With oil it forms zinc soaps to a limited extent.

Miscibility: Excellent.

Oil absorption: Needs seventeen to twenty-five percent oil; poppy oil is used to reduce yellowing, although this retards drying.

Stability of consistency: At first decidedly good, but deteriorates after approximately twelve hours, even in poppy or sunflower oil. Sizable amounts of powder pigment will then have to be added to regain the original consistency. Additions of wax are not necessary.

Tinting strength: With white pigments, this is called reducing power. All grades of zinc white have good reducing power but are surpassed by pure titanium dioxide in this respect.

Hiding power: Appreciably lower than white lead or titanium white but nevertheless adequate even in old painting, where its pliancy gives it an advantage over white lead.

Transparency: Although it may sound paradoxical to use a white pigment for glazing. In practice it is sometimes quite important. Delicate scumbies of white are used for modeling in painting. In special cases white pigments of low hiding power are used to give colours certain turbidity.

Drying effect: Extremely slight, but for this very reason zinc white is preferred to other whites by portrait painters because it allows them to paint wet-in-wet for longer periods with oil colours.

Toxicity: Contrary to some opinions, not poisonous when applied externality. Zinc white paste is even used as a medical ointment.

Commercial grades: During the burning of zinc vapour, zinc oxide of various particle sizes is produced and caught in successively arranged containers. The coarsest powder falls into the first container, while the hot-air current carriers the finest particles on to the last container. The finished product falls thought funnels directly into barrels, which were once marked with seals of different colours. Thus, event today the coarsest zinc white is called Red Seal, white medium qualities are called Green Seal, and the finest grades White Seal. Red Seal is only used for lucid paints and for preparation of grounds. The finest powder, White Seal, is so light and voluminous that sometimes artists prefer the cheaper Green Seal for painting, even for technical reasons (e.g. less danger of shrinkage cracks). The lower qualities, graded as Blue and Yellow Seal, contain a higher proportion of lead and other impurities and are unsuitable for artists‘use.

Tests: As a simple identification, to distinguish it from other white pigments, the material should be heated. All grades of zinc white will turn pale yellow but will become white again on cooling. Tests for lead or extenders should be carried out by a qualified chemist. In ultraviolet light zinc white fluoresces pale yellow green. (This is of importance during the examination of painting).

History: The manufacture of zinc white was only possible after the production of pure, metalliz zinc by Henkel in 1721. Champion in 1758, and Ruberg in Upper Silesia in 1880. However, as early as 1782 Courtois of Djion is reputed to have replaced white lead with zinc whit. According to Wagner zinc white was first produced on a large scale in 1835; according to Trillich in 1884 by Leclairein Paris. The indirect process was adopted by the zinc mining company Rochatz & Co. at Eppinghofen in the Ruhr shortly after 1850. In 1865 Wilhelm Grillo of Oberhauses started producing zinc white in 1870. The

Union of German Zinc White Manufactures was founded in 1926, followed by the Zinc White Research Society in 1943.

Application: Zinc White can be used in all techniques. For a time it was used in pastels instead of the poisonous white lead, which blackens in air, or instead of chalk, which darkness when fixed. Nowadays it is also used instead of white lead in watercolour and gouache, but rarely in casein. It is not commons in fresco techniques-not even in stucco-lustre, where lime alone is hardly sufficient (see Titanium White). Its most important application is in oil painting. Its hiding power is increased considerably by adding titanium dioxide so that is equal to flake white. A mixture of zinc white and flake white in equal parts is used by painters as mixed white, a paint in which the properties of the two pigments complement each other.

Further remarks: At the end of the impressionist era in the twenties, the question of which white pigment was preferable was the subject of some heated discussion. At that time titanium white was not yet available to artists and it was the practice to have both flake white and zinc white on the palette occasionally side by side, because of their different handling and hiding properties. In spite of its lower molecular weight, zinc white appears on radiographs just as clearly as lead white, partly because, having been used only in recent times; it is frequently found in thick, clearly absorbing layers.

Titanium white

Nomenclature: Titanium white, titanium dioxide, "Titanom" (French: *blanc titanu;* German: *Titanweilss*).

Appearance: High-quality grades and pure titanium oxide reflect 93.2 percent of all incidents light (Ostwald). After magnesium dioxide and *blanc fixe* used as colorimetric standards, titanium white is the pigment with the highest reflectivity of light, it is this the most brilliant of the white pigments.

Group and origin: Artificial mineral pigment; titanium dioxide is extracted from ilmenite, a black titanium oce, in eight separate stages and made into different types of titanium white.

Chemical composition: Titanium dioxide (TiO_2) occurs in two crystalline forms

Texture: According to type, the powder may feel soft or have a slight tooth. Lighter than white lead; heavier than zinc white:

Permanence: The new grades are neutral (pH 7) and are extraordinarily permanent. Certain brands of titanium white are no longer prone to yellowing or chalking and resist weathering excellently-

Compatibility: Compatible with all pigments; the new grades are compatible even with all coal-tar pigments.

Fastness to media: Can be used in all media.

Miscibility: Mixes well with all pigments, whether in a dry or wet state. Grades containing barium sulphate show a tendency to settle out in dilute watery suspensions.

Wetting: Good.

Oil absorption: Relatively low-depending on the type; fifteen to twenty percent poppy or sunflower oil.

Stability of consistency: Normal.

Tinting strength (reducing power): Good.

Hiding power: Pure titanium oxide greatly surpasses the obscuring power of all other white pigments. Admixture of other white pigments or extenders, necessary for certain techniques, because only a relatively slight reduction of hiding power in practice.

Transparency:-

Drying effect: Titanium dioxide has no drying action on oils::the technical reason for the admixtures is to improve drying.

Toxicity: Not poisonous.

Commercial grades: Titanium dioxide manufacturers do not as a rule list all the necessary admixtures with the designations of their pigments. These may include zinc oxide, barium sulphate, or calcium carbonate single or combinated in varying proportions, depending on the type of pigment desired. This does not mean that the composition of the products is necessarily kept secret. Generally, the crystals structure (anatase or rutile) and percentage of titanium oxide contained in the pigment is given in the trade designation. Consumers should state the purpose for which the material is to be used, in order to obtain the most suitable type. The following internationally known grades, made by the Titanium pigment corporation of New York, are of interest to artists:

Titanox A-168-Mo: ninety-seven percent TiO2 (anatase structure); modified to prevent yellowing; weatherproof.

Titanox A-WD: ninety-eight percent TiO2 (anatase structure); especially suited to aqueous techniques; easily dispersible.

Titanox RA: ninety-seven percent TiO2 (rutile structure); has less yellowing effect on media.

Titanox RC: titanium white with thirty percent tiO2 (rutile structure); seventy percentCaSO4, specially suited for outdoor use.

TitanoxRC-HT: titanium white with thirty percent TiO2 (rutile structure); seventy percent CaSO4; causes no yellowing; suitable for interior techniques.

Titanox RA-AC(=The German Kronos-Titandioxid RN47): 90.5 percent TiO2,stabilized against the influence of light and weather; a slightly warmer white because of its rutile structure; easily made into a paste or ground in medium; never chalks, even outdoors.

Titanox RA-AC increases the opacity of all other white pigments in oil and emulsions and in mural techniques. The artist can choose the other white components himself, according to the technique being employed. Even the hiding power of slaked lime (calcium hydroxide) can be improved with it, a fact that is most important in the stucco-lustre technique. A German pigment comparable to the American Titanox RC-HT would be Kronos-Titanweiss E 30, made by TItangesellschaft m.b.H., Leverkusen. Another of their products, Kronoa-Titanweiss R 25, which contains twenty-five percent of specially stabilized rutile titanium dioxide, is used mainly in oil, but also in lime and cement mortar for outdoor work.

Tests: Qualitative and quantitative analyses can only be made by qualified chemists.

History: The element titanium, which occurs in many places in the world, was discovered in 1789. In 1791 an English parson in Cornnwall found black, magnetic sand that is said to have contained about fifty percent of the white metallic oxide unknown before that date. Rose produced the first pure titanium dioxide in 1821. In 1870 Overton of Louisville succeeded in producing the first titanium pigment from rutile. In 1916 the Norwegian Titan Co. A/S, built a large plant at Fredrikstad, near huge ilmenite deposits. The German Titangesellschaft m.b.H. at Leverkusen has been producing Kronos titanium-dioxide pigments since 1928. These have been received with worldwide acclaim and have been accepted, with good reason, by manufactures of artists' colours

Application (see Commercial grades): There is a suitable grade available for every technique, from glue paint to fresco, whether indoors or out.

Further remarks: In spite of our fast-paced times artists were very slow to accept this pigment, which had been in production since 1870. This initial reluctance was justified, since there were some drawbacks that could only gradually be considerably reduced or completely eliminated through the development of special pigment types. Reliably stabilized types of titanium dioxide and titanium white have come into existence only in recent years. This advance has been invaluable for the technique of painting.

Chalk white

Nomenclature: The name "Chalk" comes from Latin *calx* = *lime*, limestone; from Greek *khalix* = *pebble*

Appearance: White pigment

Group and origin: Chalk is a rock derived from marine ooze and largely composed of fossil remains of unicellular algae. Mineral: calcite.

Chemical composition: calcium carbonate $CaCO_3$.

Texture: Very finely powdered

Compatibility: Chalk is unaffected by alkalis.

Fastness to media: Linseed oil, Alkyd, Acrylic, Watercolor, Gouache, Tempera, Pastel, Chalk.

Miscibility: dissolves in acids with effervescence (the carbonic acid escape).

Oil absorption: Oil colours which contain chalk are converted into quicklime. Oil colours which contain chalk "set" quickly in the tubes.

Stability of consistency: It is stable under ordinary conditions.

Hiding power: limited hiding power.

Toxicity: Chalk is not poisonous and has little covering power.

Application: In unvarnished tempera chalk may be used as an addition to white. It is also used in the manufacture of pastels and in putty for restoration purposes.

Further remarks: When heated it remains white. Impure sorts discolour; for example, when they contain iron, they turn red. When strongly heated, chalk is converted into quicklime. The whiter it is, the greater its value; therefore French chalk are not useful in grounds; they develop ugly dark spots when touched by oil. Very finely powdered chalk must be thoroughly soaked in very fine material. Gray chalks are not useful in grounds; they develop ugly dark spots when touched by oil. Very finely powdered chalk must

be thoroughly soaked in water, because sometimes it takes water poorly and then causes very fine air bubbles in a ground.

5.2 Sample preparation

The pigments shows previously, which initially were in the form of grains of variable size, were reduced to fine powder particle size by means of agate mortars (Fig. 5.1) and sieved (Fig. 5.2) selecting the granulometry (Fig. 5.3).

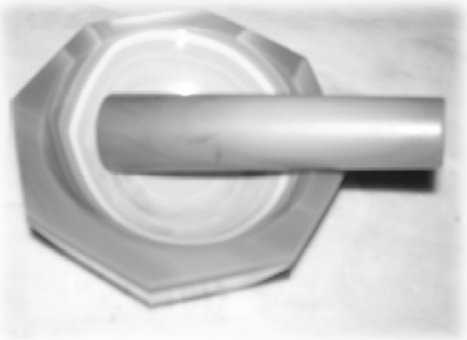

Figure 5.1 – agate mortar used to crush the pigments.

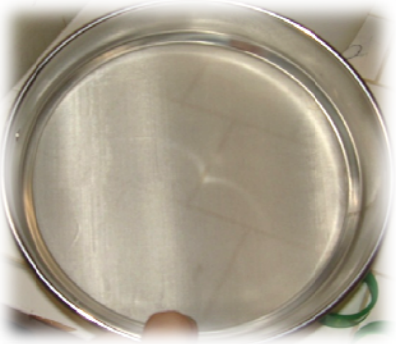

Figure 5.2 – sieve used to select granulometry to use for our purpose.

The granulometry selected for each pigment were separated into 4 groups:

1. Used to realize the tablets of pure pigments
2. Used to realize the pictorial layer (with casein)
3. Used to realize the tablets of binary mixtures
4. Used to realize the pictorial layer (with casein) of binary mixtures

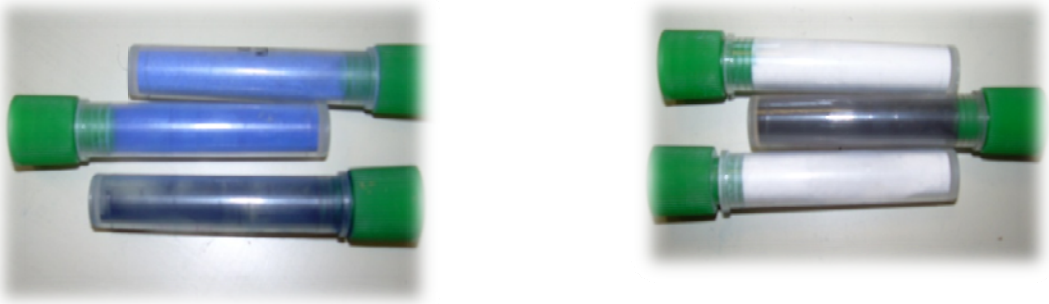

Figure 5.3 – powder pigment after sieving.

In order to perform all the characterization measurements on pure and mixed pigments, all the analysed samples were pigment powders compressed by a 1.8 Tons pressure into tablets of 1.2 cm diameter and 0.2 cm thick (Fig 5.3) and pictorial layer with casein spread on canvas that has a preparation layer of gypsum and glue (Fig 5.4).

Figure 5.3 – tablets of powder pigments realized at the *Laboratorio di Fisica e Tecnologie Relative – UniNetLab – Dipartimento di Fisica e Chimica Università di Palermo.*

Figure 5.4 – pictorial layer on canvas realized at the *PH3DRA Laboratories –Dipartimento di Fisica e Astronomia - Università di Catania.*

As said before, the pigments were used also to realize binary mixtures in order to obtain quantitative information on each ones of the two components.

The theory used for realize the binary mixtures, has follow two different hypotheses:

1) Variation of saturation → it was an usual practique to mix the pigment of different hues with white pigments to obtain different level of saturation of pigments to be used for realizes a pictorial layer.
2) Realization of secondary hue, starting from mixing Red+Yellow+Blu, as described by Itten Theory.

Table 5.2 show the schema used to realize the mixtures: they were obtained by mixing two pigments (namely *X* and *Y*) and varying, in 10% weight step, the percentages of the component pigments.

Table 5.2 – schema to realize binary mixtures

	Pigment Y								
Pigment X	10%	20%	30%	40%	50%	60%	70%	80%	90%
10%									**M1**
20%								**M2**	
30%							**M3**		
40%						**M4**			
50%					**M5**				
60%				**M6**					
70%			**M7**						
80%		**M8**							
90%	**M9**								

5.3 Characterization and quantitative methods

In order to obtain a compositional, elemental and spectrophotometric characterization of all the samples, XRF, micro-Raman and Colorimetric techniques were used.

A portable XRF system, namely the ArtTAX 400 spectrometer from Bruker AXS (Fig. 5.5), was used to acquire XRF spectra. It is equipped with a Mo (K_α = 17.5 keV) low-power excitation tube (with a 100 μm thick beryllium window), enclosed by a safety radiation shield.

Figure 5.5 – ArtTAX 400 portable XRF spectrometer from Bruker AXS available at *Laboratorio di Tecniche Fisiche per lo Studio e la Caratterizzazione dei Beni Culturali.*

A filter disk system, put before the X-ray beam placed between the X-ray tube and the sample, can be used in order to attenuate the Bremsstrahlung radiation and to reduce the diffracted component of the X-ray beam. A pinhole system in the X-ray source provides a collimated beam on the sample making the instrument suitable to perform spatially resolved multi-elemental analysis on three-dimensional structures. The detector is an XFlash 1001 (a Peltier cooled silicon drift detector) with high speed, low noise electronics, and a FWHM energy resolution < 145 eV at the Mn K_α energy (5.9 keV) with an active area of 5 mm^2 and an 8 μm beryllium window. The detection head contains the detector and the X-ray tube, fixed on a movable tripod allowing independent vertical and horizontal movement, and its power supply. The mobile XRF moving head includes also a micro camera to visualise the positioning of the incident beam on the sample. Helium flux system, reducing the photoelectric absorption of the sample characteristic X-rays by the air molecules, allows the detection of light elements. In particular, this XRF equipment allows the detection of chemical elements with atomic number Z > 11 (i.e. Na).

The geometry between primary beam, sample, and detector is fixed at 0°/40° relative to the perpendicular of the sample surface. Measurement setup was as follows: tube voltage 25 and 40 kV; current 1300 and 700 μA; acquisition time 300 sec; no filter disk between the X-ray tube and the sample; He flow rate 1.6 $Lmin^{-1}$, lateral resolution 0.65 mm.

Raman micro-spectroscopy was undertaken using an instrumental apparatus equipped with a micro sampling system which uses the microscope objective to focus the laser beam on the sample and to collect the scattered light. This configuration allows to analyse very small portions of sample, reaching spatial resolution values of the order of few microns.

The spectra obtained by 785nm laser source were acquired at PH3DRA Laboratories (University of Catania – Physics and Astronomy Department), through an Olympus BX40 confocal microscope, either with 50× objective lenses. Interferences, caused by the fluorescence background, were minimised by the use of the near-infrared laser. The Raman scattered light is collected by a TRIAX 320 spectrometer (Fig. 5.6) from Horiba Jobin-Yvon characterized from 1800 grooves mm^{-1} dispersive grating and a spectral resolution of 3 cm^{-1}. The dispersed spectrum is sent to a charge-coupled device detector (CCD: 1024×128), and then processed, amplified and digitalised by the CCD control unit (Symphony).

The Raman measurements were obtained on samples of pure and mixed pigments using the 50× objective lens. All measurements were acquired in the spectral range 200–1600 cm^{-1} with collection times varying in the range from 2 to 100 seconds and accumulation from 2 to 10 scans to provide a suitable signal-to-noise ratio (SNR) enhancement. Spectra were calibrated in intensity through the

acquisition and subsequent processing of the standard NIST SRM2241 spectrum (NIST-Standard Reference Material) related to the laser intensity of 785 nm.

Figure 5.6 – Raman Spectrometer TRIAX 320 from Horiba Jobin-Yvon available at PH3DRA Laboratories.

The spectra obtained by 458, 488 and 514 nm laser source were acquired at LADIR Laboratory (*Laboratoire de Dynamique Interaction et Réactivité, UMR7075 – Université Pierre et Marie Curie - Paris)* with a dispersive spectrometer HR800 Jobin-Yvon Horiba (Fig. 5.7) characterised by a focal distance of 800 mm.

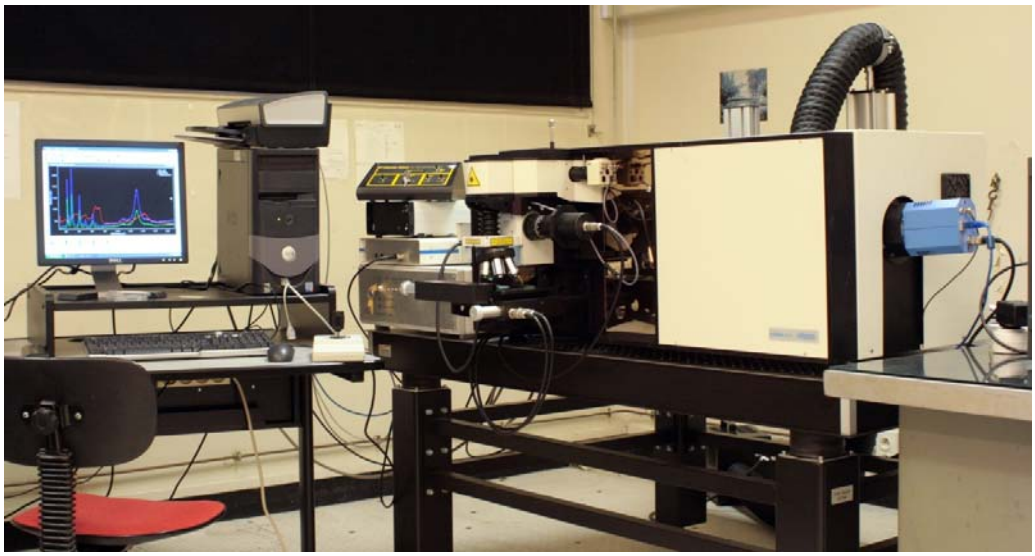

Figure 5.7 – Raman Spectrometer HR800 Jobin-Yvon Horiba available at LADIR Laboratory.

For our experiments we use a 600 lines/mm grating (allowing the recording in one acquisition of the whole spectral range of our interest) and the 458/488/514 nm radiation of an air cooled ionised Argon Laser (Coherent I-90C-6). Detection is performed through a Peltier cooled CCD detector.

For 458 / 488 nm laser sources, Rayleigh filtering is achieved thanks to Edge filters; for 514 nm ones, low frequency spectra recording (until ~10 cm^{-1}) is achieved thanks to a Rayleigh filtering using ultra narrow band Notch BragGrate Filters.

The spectrometer is coupled to an Olympus microscope and observation and analysis is performed using Olympus objectives of 100×. Laser power at the sample is modulated in order to respect sample integrity and avoid thermal transformations. For our samples power is generally adjusted between 100-110 μW at the sample with a 100× objective.

Colour measurements were obtained with a portable spectrophotometer Konica-Minolta CM2600D instrument (Fig. 5.8), equipped with an integrating sphere in the geometry d/8° after the usual procedures for black (CM-A32) and white (CM-A145.) adjustment, selecting an area of 11 mm diameter. The data acquired were relative to the standard observer 10° and D65 illuminator.

Figure 5.8 – CM 2600d spectrophotometer, Konica-Minolta.

5.3.1 Quantitative method by XRF

This experimental approach allows to calculate the weight percentage of the single component, on an unknown (for the analyst) mixture, composed by two known pigment, by inverse prediction on the calibration curve. In order to build fitting and calibration curves, net area values for selected peaks of pigments characteristic elements have been plotted vs. pigment concentration (weight %) [4].

It is well known that, the quantitative XRF analysis is based on the fundamental requirement of microscopic homogeneity of sample composition through the probed thickness. Such homogeneity

must hold on distances much smaller than the average length travelled by characteristic X-rays. The XRF signal strongly depends on the weight fraction of the elements constituting the samples. This means that the densities of samples obtained by mixing pigments with different relative densities, affect the XRF signal which will be then strongly dependent on the relative percentage of the two pigments in the mixing. This circumstance will be less important in mixtures composed by pigments characterised by comparable densities.

XRF data for the different mixtures have been analysed in detail in order to get insights on the mixture density dependence. In particular, it was defined the maximum value I_{max} of XRF intensity which can obtained from a chemical element in a hypothetical mixture $(X + Y)$, having the density of the measured mixture and the molar fraction x of the element (A) taken into account in the pure pigment. For example, in the case of a general A element, I_{max} can be then calculated as follows:

$$I_{A(max)} = \frac{I_{A(X+Y)} \cdot x_{A(Y)}}{x_{A(X+Y)}} \tag{5.1}$$

Thus, the I_{max} behaviour can be considered as an indicator of how the variation of the mixture density affects the XRF response of a particular chemical element. In other words: if there is no correlation between density and XRF response, I_{max} should remain independent of density, i.e. keep a constant value.

Experimental data have been fitted by the following double exponential decay curve:

$$y(x) = y_0 + A_1 \exp(-\frac{x - x_0}{t_1}) + A_2 \exp(-\frac{x - x_0}{t_2}) \tag{5.2}$$

Plotting the $I_{A(max)}$ value *vs.* weight percentage of the mixture, for the characteristic element of each component in the mixture, it is possible to obtain quantitative information on the pigments used.

5.3.2 Quantitative method by Raman spectroscopy

In the analytical Raman spectroscopy is an important question the need to adopt a procedure for correcting the relative intensity of the spectra. This often resulted in a serious spectral distortion of the relative peak intensity, which prevented the transfer of calibration and damage the spectral coupling in

library routines research, especially for the measurements with different excitation wavelengths. To overcome the various difficulties then discussed, standard luminescent are used.

5.3.2.1 Standard Reference Materials

The SRM (standard reference materials) are a methodology that simplifies the calibration of the Raman instrumental function. This method provides a correction curve that generates spectra corrected in terms of the Raman relative intensity.

With this procedure it is possible to determine the instrumental response function by measuring the luminescence of the SRM. In theory, any standard selected for a specific wavelength Raman, will have a unique profile of luminescence emission, which depends on the composition of the glass and by the wavelength of the laser.

The calibration standard used for this thesis is a standard-based instruments using excitation at 785nm, the laser wavelength used.

The known spectrum of the standard luminescent is represented, as we will see, with a polynomial trend, which is used in a rapidly computational procedure, from which the curve of intensity correction is obtained; it is the NIST SRM2241 standard.

The SMRS 2241 is composed of a matrix of sodium, chromium-treated borosilicate glass. Each unit of this SRM includes a glass sheet of approximately 10.7 mm in width, 30.4 mm in length, and 2 mm thick. One of the surfaces is finished for the optical efficiency, the other is subjected to grinding process, i.e. is rendered uniformly rough.

This will have the effect of reducing the penetration depth of the focused laser, so the luminescence spectrum of the glass will be read essentially from the upper surface of the glass sheet.

To obtain correct intensity of Raman spectra, a preliminary measurement of the luminescence spectrum of the SRM 2241 through a Raman apparatus is required, and then the mathematical treatment of this spectrum and that of the observed sample (in our case the pigment or mixture) must be analysed.

The spectral range of the certification is $\Delta\bar{\upsilon} = 200\ cm^{-1} \div 3350\ cm^{-1}$.

The elements of certified relative spectral intensity SRM 2241 $I_{SRM}(\Delta\bar{\upsilon})$ are calculated according to Equation 5.3:

$$I_{SRM}(\Delta\bar{\upsilon}) = A_0 + A_1 \bullet (\Delta)^1 + A_2 \bullet (\Delta)^2 + A_3 \bullet (\Delta)^3 + A_4 \bullet (\Delta)^4 + A_5 \bullet (\Delta)^5 \quad (5.3)$$

where $(\Delta\bar{\upsilon})$ is the Raman shift (cm^{-1}) and A_n are the coefficients listed in Table 5.3

The certified values of the polynomial coefficients data in table are considered for the use at temperatures between 20 °C and 25 °C.

Table 5.3 – polynomial coefficient value for SRM2241 [5].

Polynomial Coefficient	Certified Value Polynomial Coefficient (*) 20 °C to 25 °C
A_0	1.3535E-01
A_1	2.1658E-04
A_2	0
A_3	1.8936E-10
A_4	-9.837E-14
A_5	1.2414E-17

In Figure 5.9, is shown the trend of the fifth order certified polynomial which describes the SRM 2241 correct intensity luminescence spectrum, represented graphically for the Raman interval 250-3350 cm^{-1}. Along with this curve, are shown the confidence associated curves of 95%.

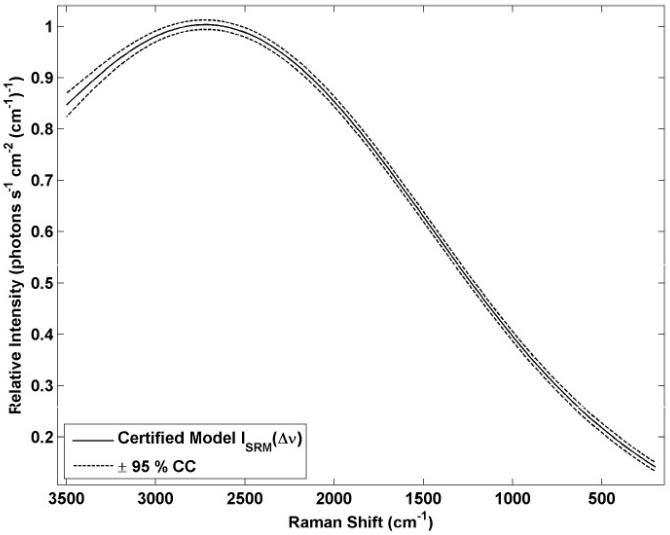

Figure 5.9 - SRM theoretical luminescence spectrum [5].

The elements of the correction curve, $I_{CORR}\ (\Delta\bar{\upsilon})$, defined by Equation 5.4, are obtained from $I_{SRM}\ (\Delta\bar{\upsilon})$ and from the elements of the glass luminescence experimental spectrum, $S_{SRM}\ (\Delta\bar{\upsilon})$, following that equation:

$$I_{CORR}\ (\Delta\bar{\upsilon}) = I_{SRM}\ (\Delta\bar{\upsilon})/S_{SRM}\ (\Delta\bar{\upsilon}) \tag{5.4}$$

The ratio between $I_{SRM}(\Delta\bar{\upsilon})$ and the measured spectrum of the sample $S_{SRM}(\Delta\bar{\upsilon})$, made point by point, implement the correction of any intensity instrumental artefacts present in the measured spectrum.
The elements of the Raman spectrum of adjusted intensity, $S_{CORR}(\Delta\bar{\upsilon})$, are derived by multiplication of the elements of the sample's measured Raman spectrum, $S_{MEAS}(\Delta\bar{\upsilon})$, for the elements of the correction curve:

$$S_{CORR}(\Delta\bar{\upsilon}) = S_{MEAS}(\Delta\bar{\upsilon}) \bullet I_{CORR}(\Delta\bar{\upsilon}) \tag{5.5}$$

Using that equation all the experimental spectra, both for pure and mixed pigments, are been corrected in intensity.

5.3.2.2 Quantitative Method

Raman spectroscopy provides useful information for detecting and identifying constituent materials in artworks; but in most cases it is not possible to obtain spectra of single pigments. When mixed pigments do not behave as expected, problems of identification arise.
It was found that, compared with the theoretical results, some Raman peaks of one pigment were not detected in most of the Raman spectra mixtures In this work, we present the theory that when the reflection coefficient of one component is larger than the other, a contribution to the spectra of mixture may occur. The Raman spectrum of a mixture is not qualitatively proportional to the weighted sum of the Raman spectra of the pigments taken individually. Depending on the mixture, and the respective concentrations of individual pigments in the mixture, it happens that some peaks of specific pigments are not recognized. This effect is mainly due to the molecular contribution of each pigment that composes the mixture, and secondly by the energy quantity effect when the radiation interacts with the system of mixed pigments. This nonlinear behaviour can be further attributed also to the specific properties of each pigment; one hypothesis is that the difference in pigment densities disturbs the addition of the spectra of single components in a mixture. This evidence will be clearer in the next chapter where all the spectra related to the characterization measurement will be presented.
For that reason the quantitative analysis by means of Raman spectroscopy was not completely obtained due to inability to identify the peaks Raman of each components of the mixture for all the percentages realized.

5.3.3 Quantitative method by Colorimetric analysis

The pigments behaviour in the visible region was studied in order to associate to chromatic variations, the Spectral Reflectance Factor curves (SRF%) of the mixtures and to obtain quantitative information of pigments in mixtures. Then, the first derivatives of the reflectance spectra [6] of the binary mixtures were considered. In this case, is possible to distinguish, for each spectrum, the formation of two different peaks, each one due to the presents of the single pigment in mixture.

In order to find a law that allow to effectuate a quantitative analysis, the peak value (positive) of the first derivate of SRF% for each Itten binary mixtures were used.

It is possible to see in each spectrum the presents of two peaks, called V_x and V_y.

So, for each weight percentage, the ratio $R_{mixture} = V_x/V_y$ was calculated and the different vales obtained for each weight percentage were plotted *vs* mixtures concentration.

Experimental data have been fitted by the following exponential decay curve:

$$y(x) = y_0 + A_1 \exp(-\frac{x}{t_1}) \tag{5.6}$$

All the spectra and the quantitative analysis behaviour are show in the next chapter.

Bibliography

[1] http://www.kremer-pigmente.com/

[2] Wehlte, K. "The materials and techniques of painting", ISBN 0-9712176-0-2.

[3] Doerner, M. "The materials of the artist and their use in painting", ISBN 0-15-657716-X.

[4] Fontana, D., Alberghina, M.F., Barraco, R., Basile, S., Tranchina, L., Brai, M., Gueli, A., Troja, S.O. "Historical pigments characterisation by quantitative X-ray fluorescence", Journal of Cultural Heritage (2013), http://dx.doi.org/10.1016/j.culher.2013.07.001.

[5] National Institute of Standards & Technology Certificate Standard Reference Material 2241 Relative Intensity Correction Standard for Raman Spectroscopy: 785 nm Excitation

[6] Bacci, M., Casini, A., Cucci, C., Picollo, M., Radicati, B., Vervat, M. "Non-invasive spectroscopic measurements on the Il ritratto della figliastra by Giovanni Fattori: identification of pigments and colourimetric analysis", Journal of Cultural Heritage 4 (2003) 329–336.

Chapter 6
Experimental results

The characterization of the materials constituting a work of art is the main issue for obtaining fundamental information necessary in planning an appropriate conservation procedure in the Cultural Heritage field. The knowledge of the chemical composition of the works of art, indeed, offers an insight on the realization techniques used by the artists, on the presence of forgeries and retouches, on the degradation processes affecting the Cultural Heritage and on the compatibility of the materials to be used for the conservation. In this context, the identification and chemical characterization of pigments also play a relevant role, in order to answer technical and historical questions and to track the original appearance of the works of art. The pigments have always been part of the colour palette of the artists, thanks to their high colouring power, availability, stability and persistence over time. The different historical epochs have seen the introduction of new pigments either in their pure form or in special mixtures so expanding the palette of the available colours. The study of the pigment features has been topic of many papers focused on pigment identification, characterization and dating. The knowledge of the exact amount of different constituents of the paint, as well as of the mixing and pictorial techniques, is crucial for a careful program of conservation of polychrome works. Moreover, since the availability of these pigments has been changing through the centuries, their identification and chemical characterization is useful for authentication purposes through relative dating because the identification of one pigment respect to another one can be used as a terminus *post quem* or *ante quem* the artwork was realized. Starting from that assumption, the different pigments described in the previous chapter were characterized form elemental, compositional and spectrophotometric point of view. In particular, XRF, Raman and spectrophotometric measurements were carried out to characterize the pigments (used to prepare binary mixtures) both in powder and layered with casein, and to realize fitting curves in order to obtain quantitative information on the prepared mixtures.

6.1 Characterization of "*pure*" pigments

The first steps of our investigation regards the XRF, Raman and spectrophotometric analyses executed (accomplished) to characterize the pigments (used to prepare binary mixtures) both in powder and

layered with casein in order to evaluate the differences with a particular real case. The instrumentations used for these measurements are just described in the Chap 5.

6.1.1 Elemental characterization: XRF measurements

The XRF measurements have been taken with the portable device [1-3] set with the following instrumental parameters: 25kV – 1300 μA – 300 sec; 40 kV – 700 μA – 300 sec.

The XRF spectra are acquired on 16 powder and layered samples of pure pigments, for each samples 3 measurement point were acquired and the spectra here showed are the average of these measurements.

In the first experimental step, an XRF analysis was carried out. The spectra obtained for each sample pigments are shown below. The spectra (Fig. 6.1 a - d) are presented grouped by hue, from red to white.

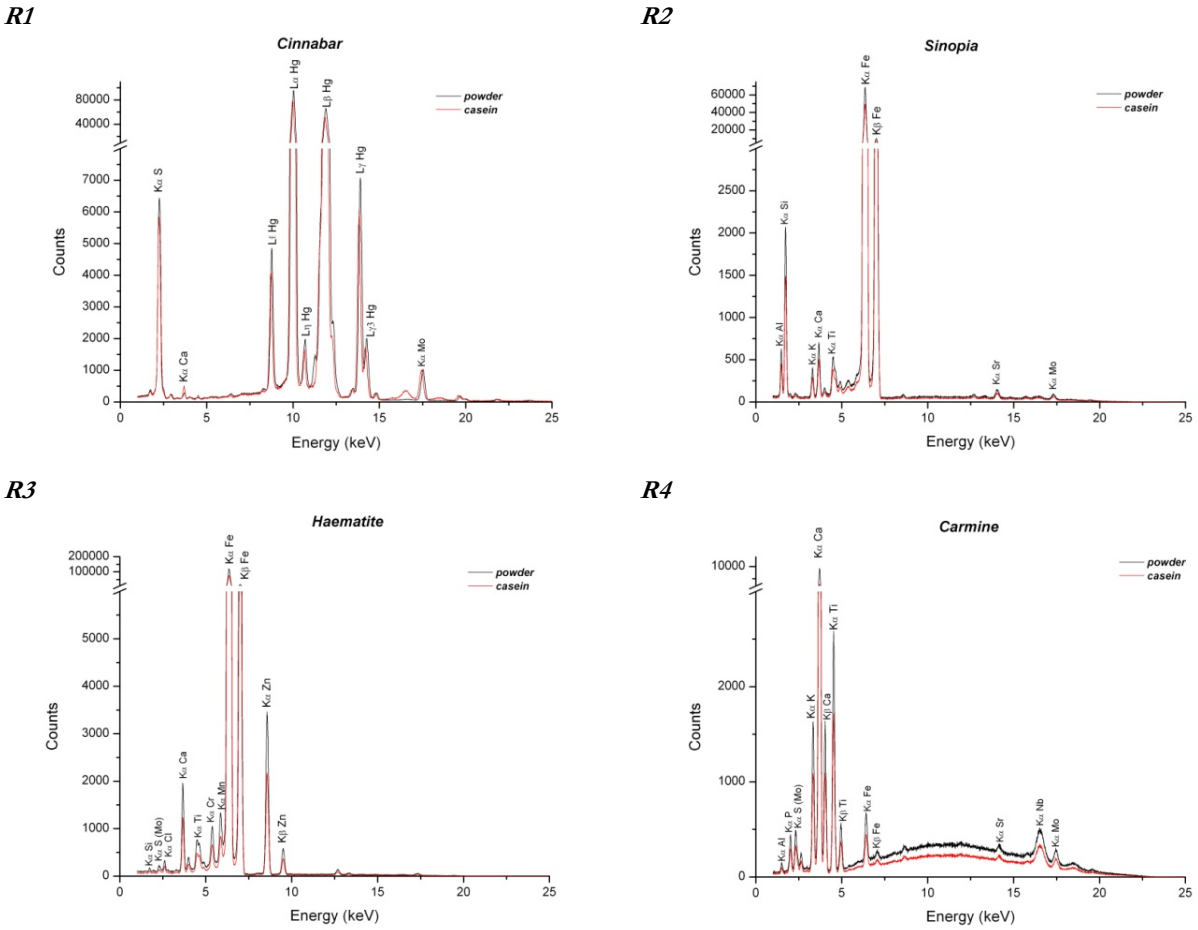

Figure 6.1 a: XRF spectra of ***red*** pigments, both in powder and layered with casein. All the characteristic lines of the elements constituent the pigment samples are reported and labelled.

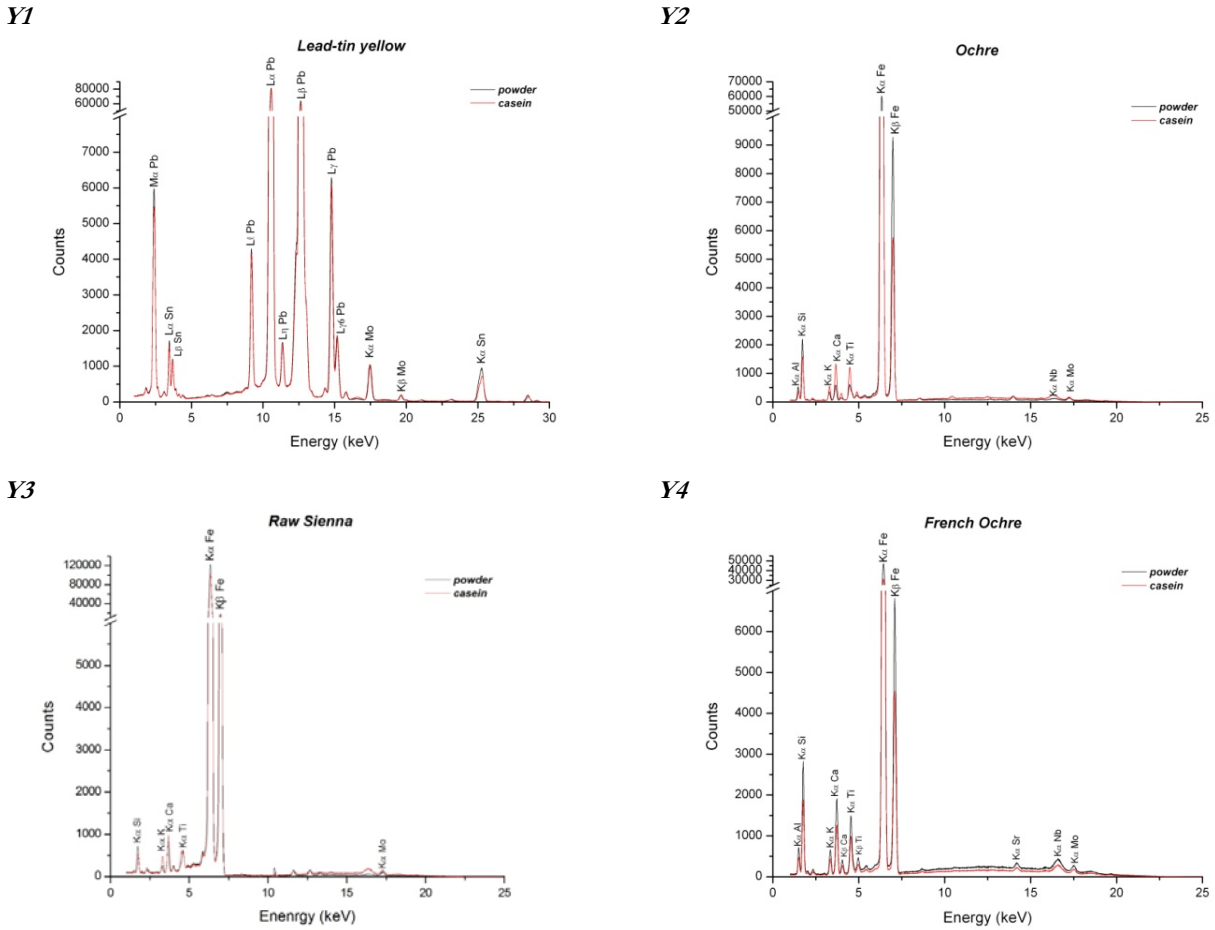

Figure 6.1 b: XRF spectra of ***yellow*** pigments, both in powder and layered with casein. All the characteristic lines of the elements constituent the pigment samples are reported and labelled.

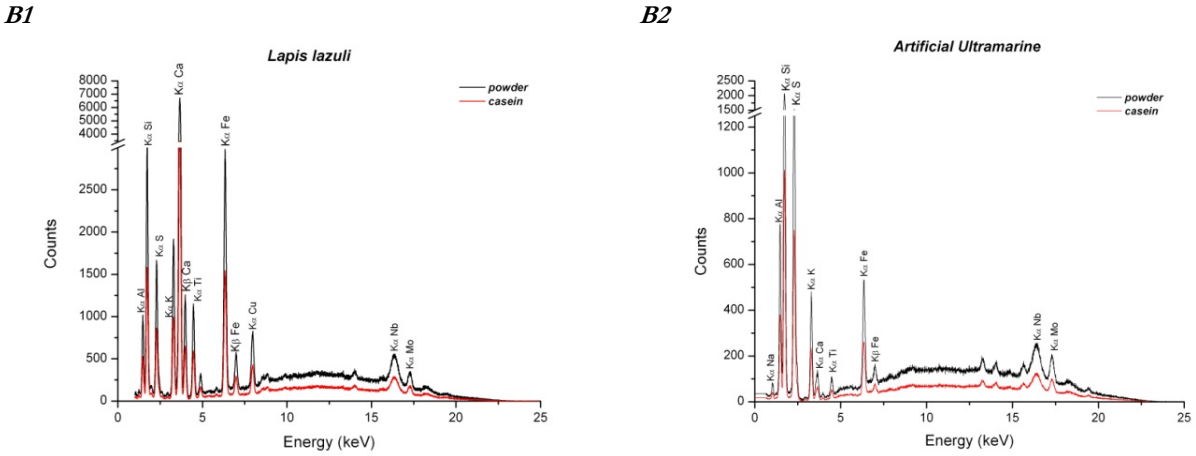

B3

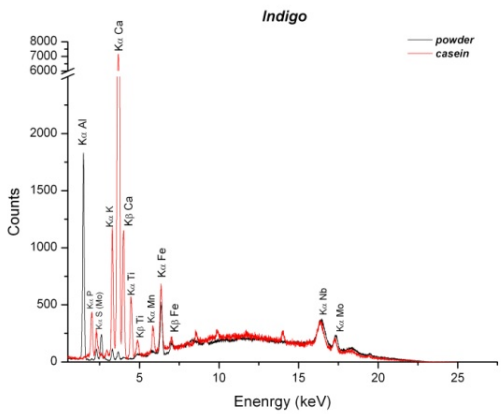

B4

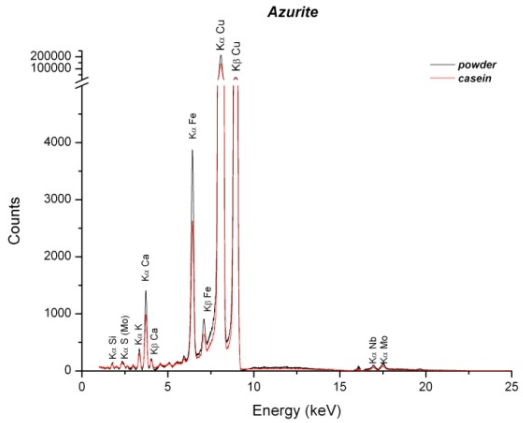

Figure 6.1 c: XRF spectra of ***blue*** pigments, both in powder and layered with casein. All the characteristic lines of the elements constituent the pigment samples are reported and labelled.

W1

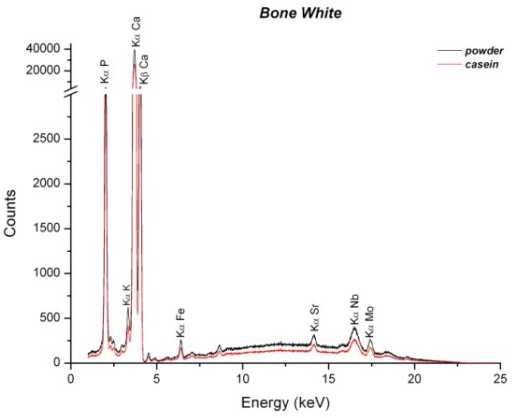

W2

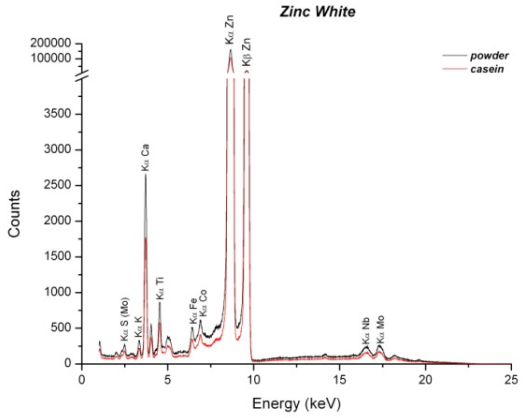

W3

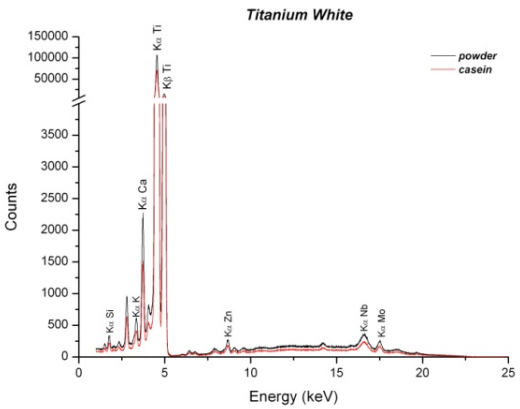

W4

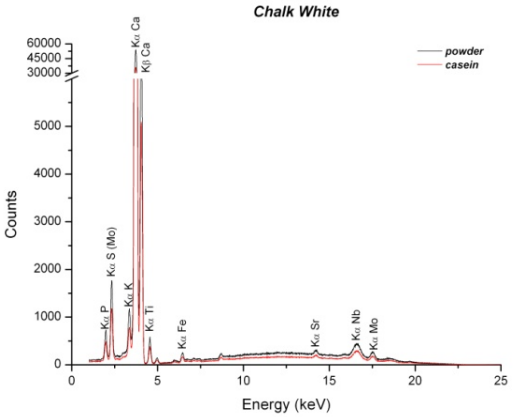

Figure 6.1 d: spectra of ***white*** pigments, both in powder and layered with casein. For each spectra are reported the entire characteristic lines of the elements that compose the pigment samples.

For a more compact and complete visualization of the XRF results, Table 6.1 lists all the elements detected in the samples, allowing a better identification of the pure pigments.

Hue	*Sample*	*Chemical composition Kremer*	*Na*	*Al*	*Si*	*P*	*S*	*Cl*	*K*	*Ca*	*Ti*	*Cr*	*Mn*	*Fe*	*Co*	*Ni*	*Cu*	*Zn*	*Sr*	*Sn*	*Hg*	*Pb*
RED	Cinnabar	**HgS**					•			•											•	
	Sinopia	**$Fe_2O_3*nH_2O$**		•	•				•	•	•			•					•			
	Haematite	**Fe_2O_3+ SiO_2+ Al_2O_3+CaO+MgO+ K_2O+**			•		•	•		•	•	•	•	•				•				
	Carmine	**$C_{22}H_2OO_{13}$**		•		•	•		•	•	•			•					•			
YELLOW	Lead-tin yellow	**Pb_2SnO_4**																		•		•
	Ochre	**Fe_2O_3**		•	•				•	•	•			•								
	Raw Sienna	**Fe_2O_3+Al_2O_3+SiO_2+ SO_3+SO_3+Mn_2O_3**			•				•	•	•			•								
	French Ochre	**Fe_2O_3**		•	•				•	•	•			•					•			
BLUE	Lapis lazuli	**Na_2O*3Al*6SiO_2*2N a$_2$S**		•	•		•		•	•	•			•			•		•			
	Artificial Ultramarine	**Na_2O*3Al*6SiO_2*2N a$_2$S**	•	•	•		•		•	•	•			•					•			
	Indigo	**$C_{16}H_{10}O_2N_2$**		•			•		•	•			•	•								
	Azurite	**2$CuCO_3$*Cu$(OH)_2$**			•		•		•	•				•			•					
WHITE	Bone White	**$Ca_3(PO_4)_2$+$CaCO_3$**				•			•	•	•			•					•			
	Zinc White	**ZnO**					•		•	•	•			•	•			•				
	Titanium White	**TiO_2**			•				•	•	•							•				
	Chalk White	**$CaCO_3$**				•	•		•	•	•			•					•			
NOISE	Canvas					x	x			x	x			X					x			

Table 6.1 – list of all the elements individuated by XRF measurements, for each historical pigment.

All the elements listed in the previous table are referred to the tablets of powder pigments. In the XRF spectra of pigments with casein it is possible to observe an influence due to the medium used and to canvas support. This involves two effects:

1) a variation of the densitometric matrix which produces a slight variation of the intensity ratios of the lines within the same sample;
2) the presence, in some cases, of other elements due to the support. The indigo is the more evident case (Fig. 6.1 d – B3); as the material is an organic compound ($C_{16}H_{10}O_2N_2$) it minimizes the effects of absorption of the matrix of X-rays coming from the support.

Except in the case of the white pigments, mainly constituted from calcium, the set of elements that characterize the canvas support cannot be considered as reference elements.

As it is possible to see in all the acquired spectra, there is a relevant difference between the chemical composition declared by Kremer and the set of elements experimentally identified. The most relevant case is represented by lapis lazuli (Fig 6.1 d –B1): the spectra show, beside the characteristic chemical elements, also some impurities maybe due to both the mineralogical origin and/or the production procedures (note declared by Kremer).

6.1.2 Compositional characterization: Micro-Raman measurements

In the second experimental step, after the elemental characterization by XRF analysis, the compositional characterization was carried out through Micro-Raman spectroscopy. The spectra of each sample pigments, obtained with about 100 mW of laser power and with accumulation between 2-10, are shown in Fig. 6.2 (a - e); also in this case, the spectra are presented grouped by hue, from red to white.

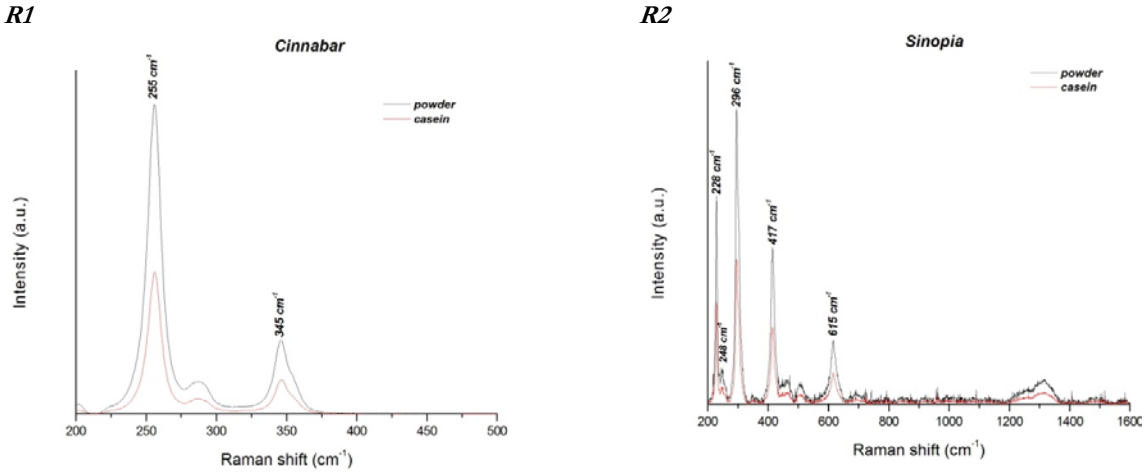

R3

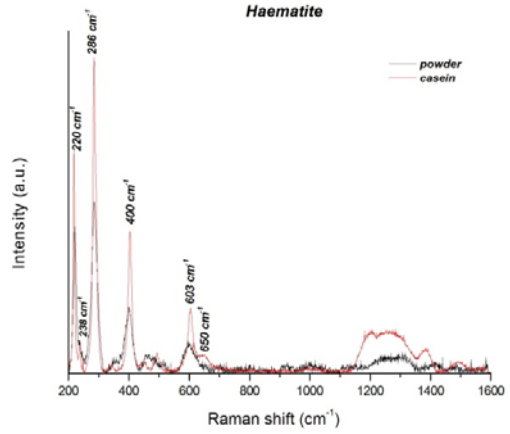

R4

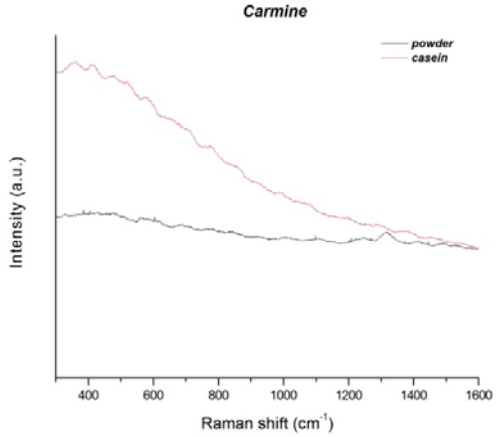

Figure 6.2 a: spectra of ***red*** pigments, both in powder and layered with casein. For each spectra are reported the characteristic Raman peaks (cm^{-1}).

The spectrum of Cinnabar shows the presence of the α-mercury (II) sulphide [4]. The Raman spectra obtained on Sinopia and Haematite pigment samples, allow to identify in each spectrum the presence of the mineral haematite (α-Fe_2O_3 with main band at ~ 220 and 240 cm^{-1}); only in the Haematite spectrum are also presents the bands of kaolin $\{(Al)_4[Si_4O_{10}](OH)_8\}$, an clayish mineral presents in the natural pigment (bands at ~ 610-660 cm^{-1}), not present in the pure ferric oxide such as in Sinopia [5]. The Carmine indeed doesn't presents main bands that can lead to an unambiguous identification.

Y1

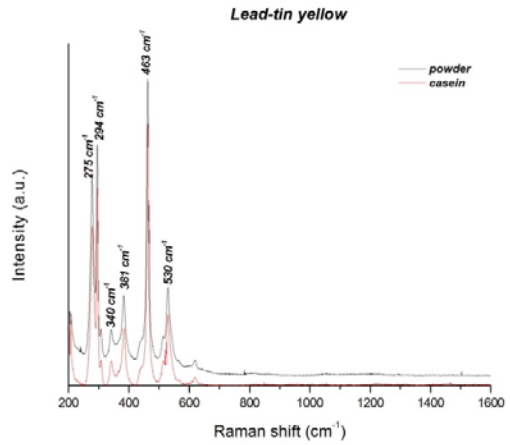

Y2

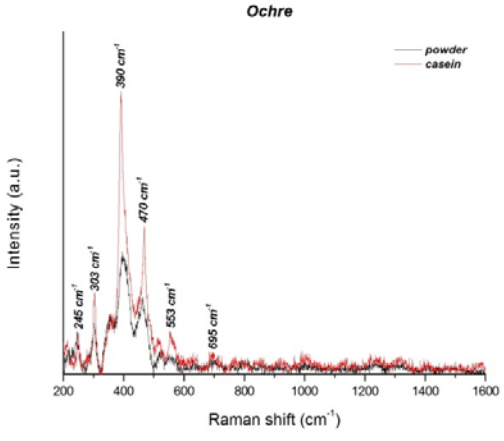

Y3

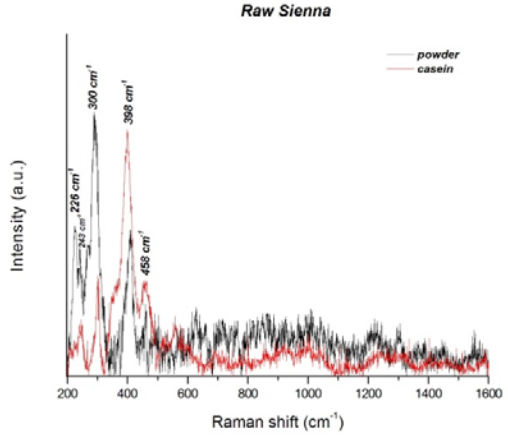

Y4

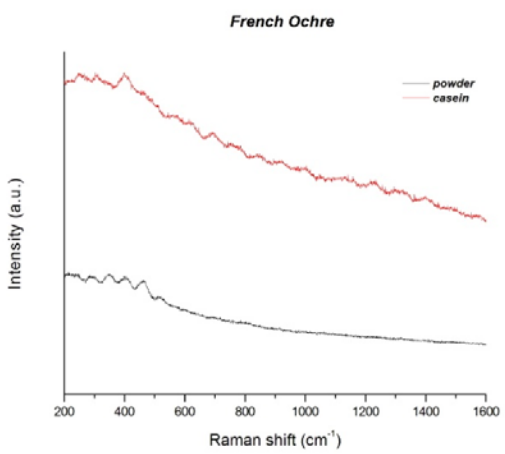

Figure 6.2 b: spectra of ***yellow*** pigments, both in powder and layered with casein. For each spectra are reported the characteristic Raman peaks (cm^{-1}).

The Raman spectra of yellow pigments show respectively: the main band of lead-tin oxide for Y1; the presence of goethite (α-FeO.OH) for Y2 (band at ~ 393 cm^{-1}); Y3 presents the main band of the iron oxides (Fe_2O_3). Only for the French Ochre is not possible to identify Raman peaks because of the high fluorescence of the pigment [4, 5].

B1

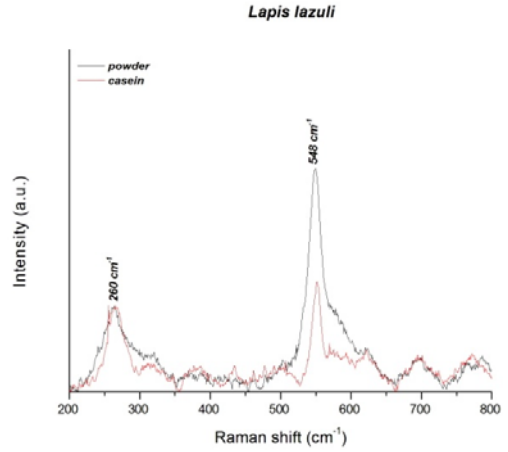

B2

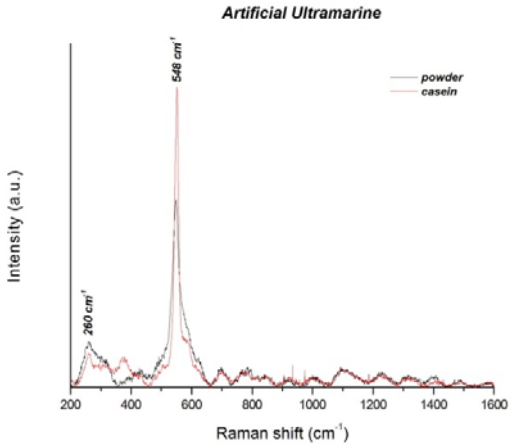

B3 ***B4***

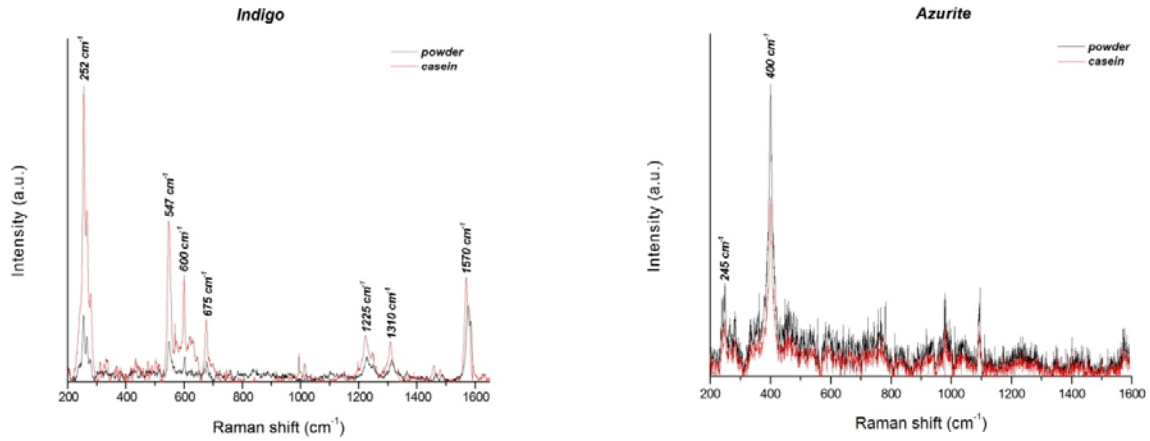

Figure 6.2 c: spectra of ***blue*** pigments, both in powder and layered with casein. For each spectra are reported the characteristic Raman peaks (cm^{-1}).

For the blue pigments, Lapis lazuli (natural) and Ultramarine Blue (synthetic) show the peak of lazurite (~ 548 cm^{-1}) [4,6]; the Indigo sample present the stretching vibration of C=C, C=O and N-H groups (~ 1573 cm^{-1}) and band attributed to N-H rocking vibration is observed at about 1224 cm^{-1}[7]. In the Azurite spectra are reported the bands assigned to the O-Cu-OH bending modes (~ 240 cm^{-1}) and to Cu-O stretching modes (~ 400 cm^{-1}) [8].

W1 ***W2***

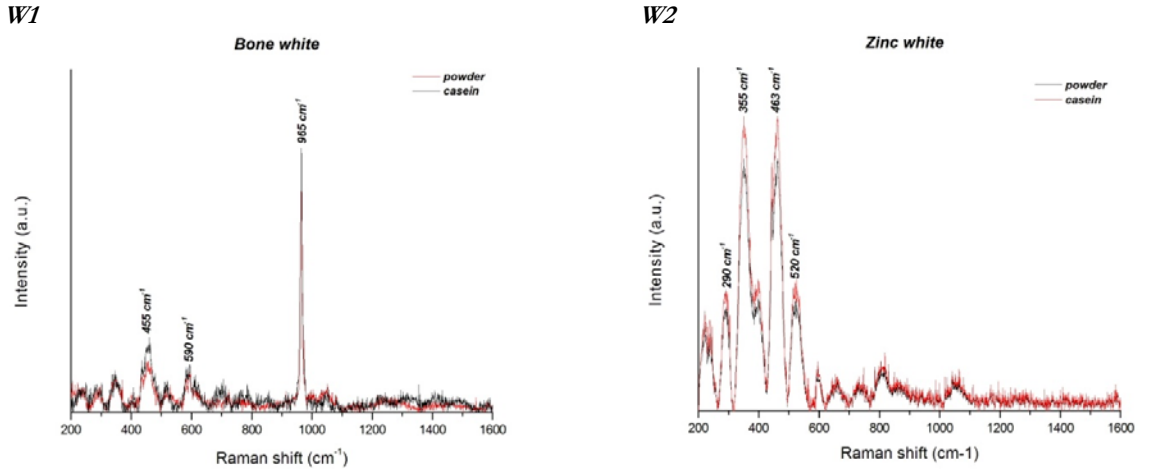

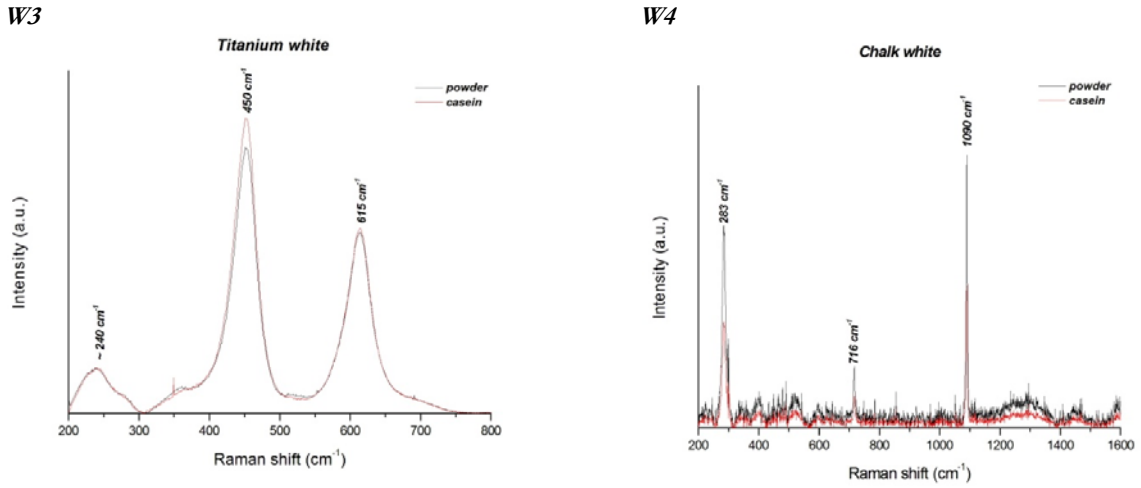

Figure 6.2 d: spectra of ***white*** pigments, both in powder and layered with casein. For each spectra are reported the characteristic Raman peaks (cm^{-1}).

The white pigments here reported presents the following mineral composition: W1 hydroxyapatite (~ 960 cm^{-1}); W2 zinc oxide (~ 440 cm^{-1}); W3 is composed by rutile, the most common crystalline modification of titanium dioxide (~ 230-440-610 cm^{-1}) and W4 is the composed by calcite because present the main band at ~ 1090 cm^{-1}[4]. One disadvantage of NIR-Raman spectroscopy is that the υ^4 factor works greatly against it, requiring longer scans (2-10) and higher laser powers than for visible excitation. Moreover, compounds containing either iron or copper which have electronic absorption bands in the near-infrared region, may fluoresce on this excitation radiation, and therefore may not be identifiable by Raman spectroscopy [4].

The database and library of pigments present in literature [9-12] often used visible excitation wavelength to record Raman spectra of pigments. By the comparison with the reference spectra in literature, it is possible to observe that some of the pigments analysed with our instrumental apparatus were not identified because of their fluorescence in NIR-Raman spectroscopy; other pigments show the Raman bands characteristic of their composition but most of them presents slight shift in position.

In order to obtain a better characterization of each pigments and to evaluate the shift present on bands wavenumber position, all the pigments were analyzed also with a different instrumental apparatus, available at LADIR (*LAboratoire de Dynamique, Interactions et Reactivite* - UMR 7075 CNRS et UPMC - Université Pierre et Marie Curie - Paris 6), with three different visible laser sources. Here reported all the spectra acquired (Fig. 6.3) obtained with about 100-110 mW of laser power and with accumulation between 1-3.

R1

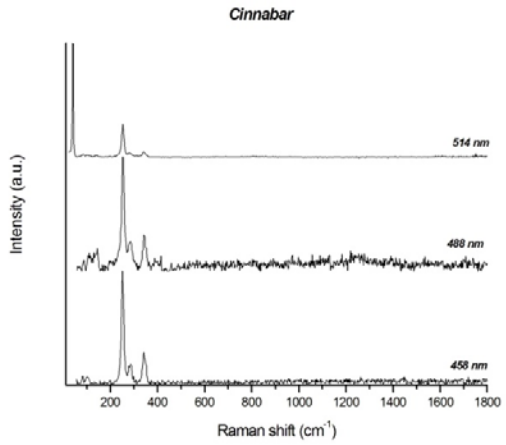

R2

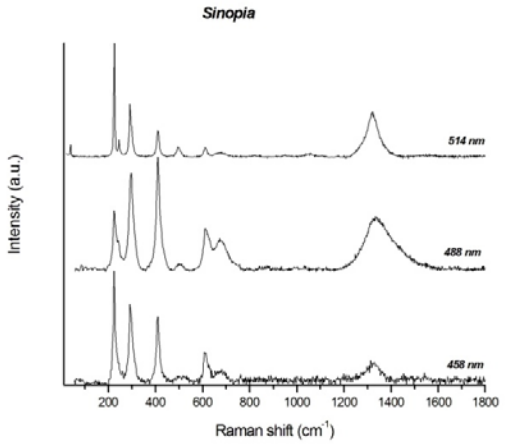

R3

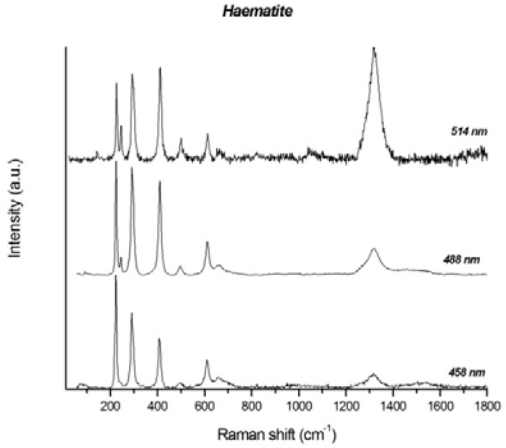

R4

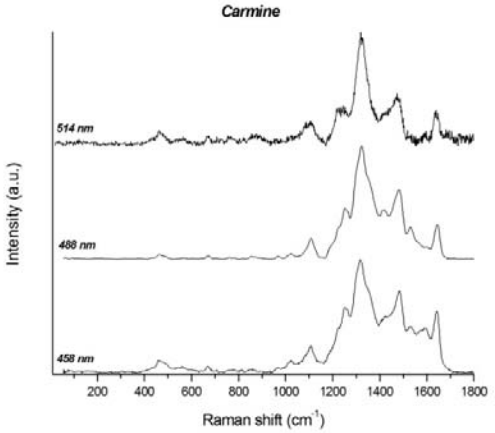

Figure 6.3 a: spectra of ***red*** pigments layered with casein, acquired with three different laser sources.

Y1

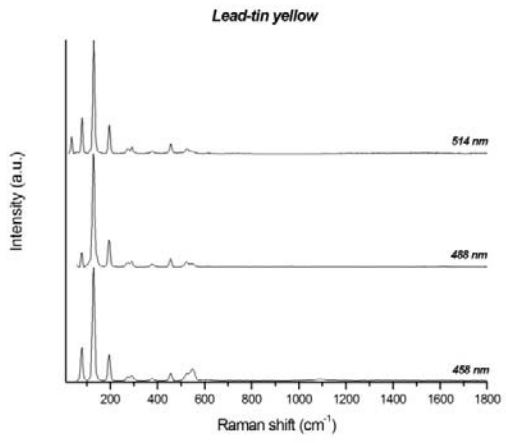

Y2

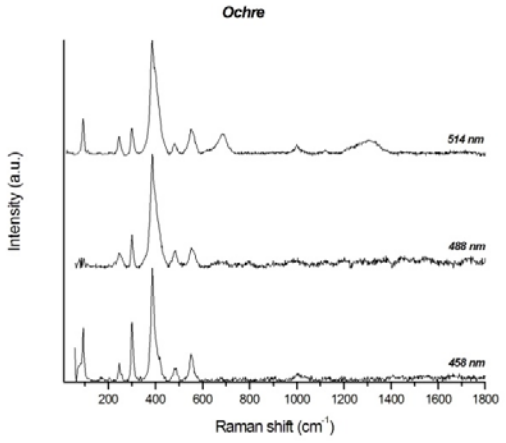

Y3

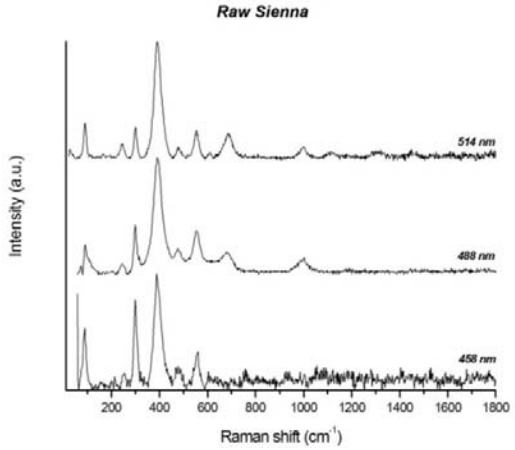

Y4

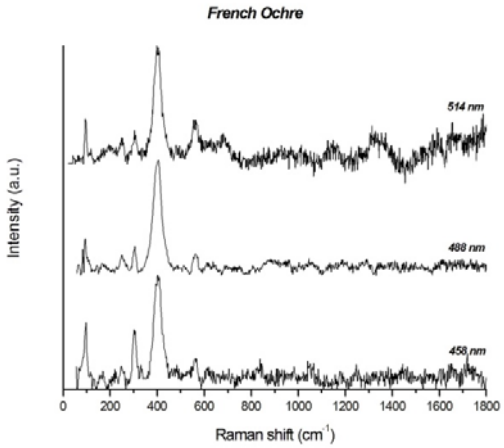

Figure 6.3 b: spectra of ***yellow*** pigments layered with casein, acquired with three different laser sources.

B1

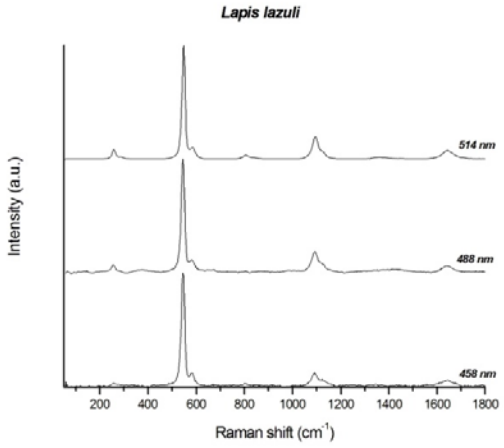

B2

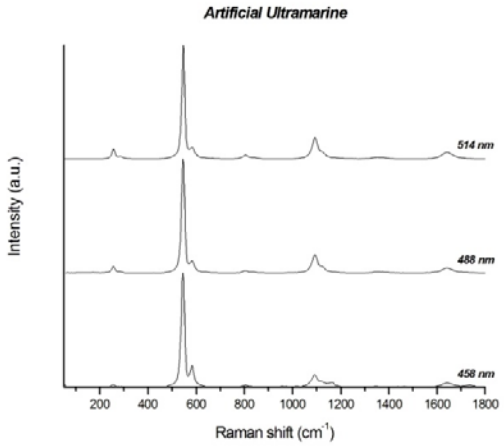

B3

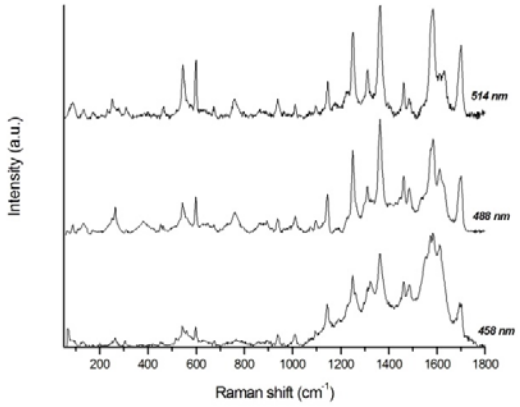

B4

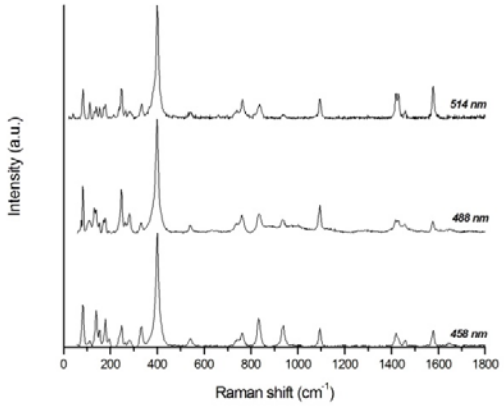

Figure 6.3 c: spectra of ***blue*** pigments layered with casein, acquired with three different laser sources.

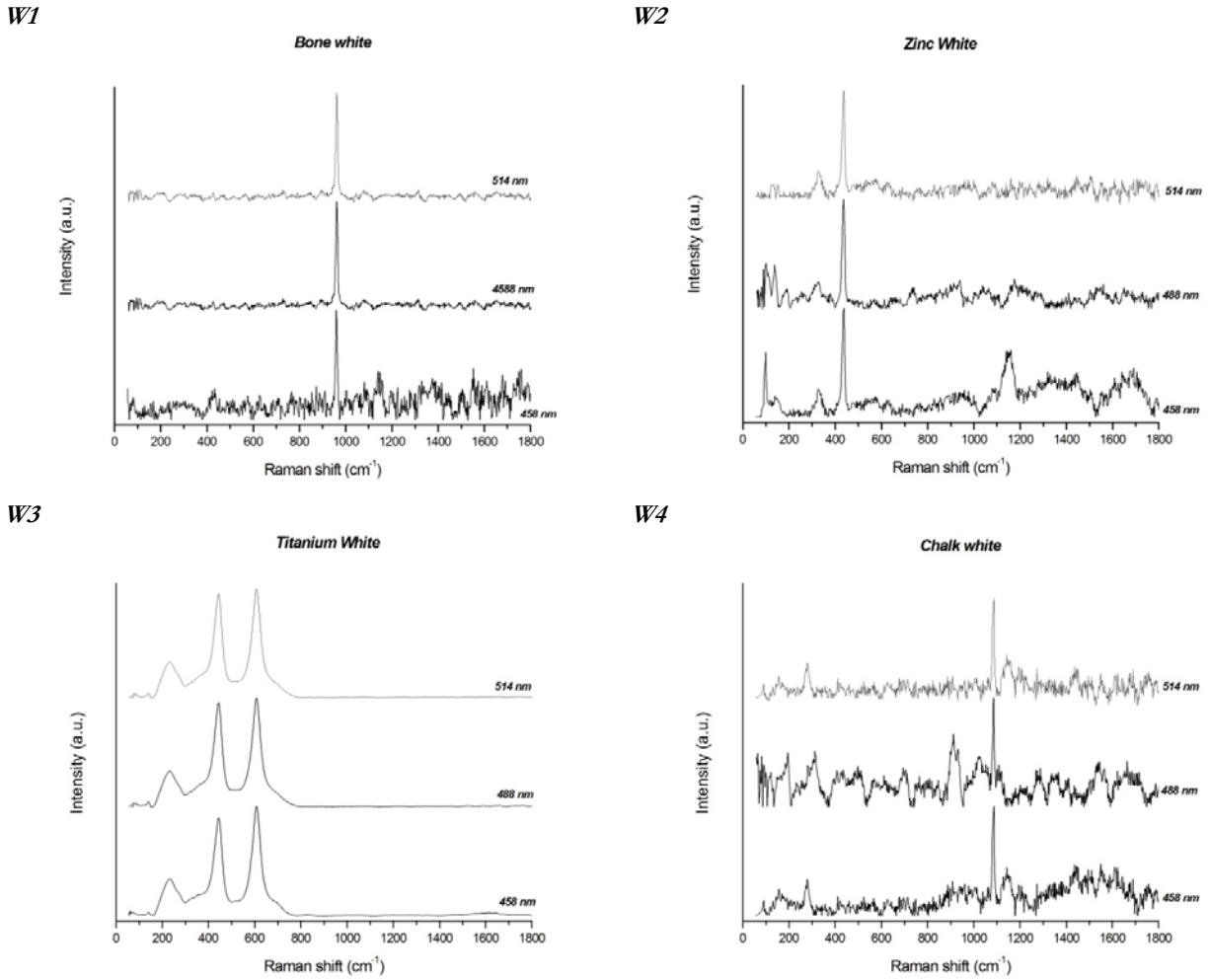

Figure 6.3 d: spectra of ***white*** pigments layered with casein, acquired with three different laser sources.

For different laser sources, Table 6.2 presents a summary report of all the picks identified for the pigments spread with casein, acquired with different laser sources.

Table 6.2 – identification of Raman peaks for each excitation wavelength used.

Hue	***Sample***	***Chemical composition Kremer***	***458 nm***	***488 nm***	***514 nm***	***785 nm***
RED	Cinnabar	**HgS**	251, 285, 343	252, 285, 344	40, 252, 342	255, 345
	Sinopia	**Fe_2O_3*nH_2O**	224, 294, 409, 615, 1323	224, 240, 296, 411, 503, 615, 674, 1343	40, 225, 244, 290, 409, 496, 610, 1321	228, 248, 296, 417, 615
	Haematite	**Fe_2O_3+ SiO_2+ Al_2O_3+CaO+MgO+K_2O+**	229, 291, 408, 611, 1313	224, 244, 293, 409, 497, 611, 659, 1316	144, 225, 245, 295, 411, 500, 612, 1320	220, 286, 400, 603
	Carmine	**$C_{22}H_2OO_{13}$**	470, 1100, 1243, 1317, 1475, 1598, 1643	1106, 1240, 1324, 1425, 1479, 1536, 1643	1233, 1322, 1466, 1637	
YELLOW	Lead-tin yellow	**Pb_2SnO_4**	127, 194, 273, 290, 377, 456, 524, 548, 1097	127, 194, 273, 290, 377, 455, 523, 547	34, 79, 129, 195, 274, 291, 378, 457, 527	275, 294, 340, 381, 463, 530

	Ochre	**Fe_2O_3**	92, 246, 300, 387, 483, 552	248, 300, 390, 482, 555	92, 245, 300, 392, 481, 553, 683, 1000, 1299	303, 390, 470
	Natural Sienna Earth	**Fe_2O_3+Al_2O_3+SiO_2+SO_3+ SO_3+Mn_2O_3**	299, 391, 557	245, 299, 392, 479, 554, 683	89, 244, 299, 392, 480, 553, 686, 998	300, 398, 458
	French Ochre	**Fe_2O_3**	302, 403	303, 401, 561	94, 246, 302, 402	
BLUE	Lapis lazuli	**Na_2O*3Al*6SiO_2*2Na_2S**	545, 586, 1094, 1151, 1647	256, 545, 584, 801, 1094, 1640	258, 288, 547, 586, 808, 1096, 1366, 1645	260, 548, 1293
	Artificial Ultramarine	**Na_2O*3Al*6SiO_2*2Na_2S**	544, 583, 1093, 1156, 1645	256, 545, 584, 803, 1094, 1642	257, 287, 546, 585, 807, 1094, 1170, 1357, 1643	260, 548
	Indigo	**$C_{16}H_{10}O_2N_2$**	263, 305, 543, 557, 597, 939, 1009, 1144, 1250, 1320, 1364, 1484, 1575, 1617, 1696	262, 543, 598, 763, 939, 1011, 1097, 1144, 1224, 1250, 1294, 1311, 1363, 1461, 1485, 1576, 1585, 1617, 1670	34, 85, 132, 172, 253, 312, 464, 546, 598, 674, 761, 939, 1011, 1094, 1146, 1249, 1310, 1363, 1461, 1484, 1580, 1621, 1697	252, 547, 600, 675, 1225, 1310
	Azurite	**2$CuCO_3$*Cu$(OH)_2$**	109, 138, 153, 177, 194, 245, 280, 331, 399, 540, 740, 762, 833, 936, 1094, 1421, 1458, 1577	82, 108, 134, 152, 172, 246, 280, 330, 398, 540, 739, 762, 834, 936, 1093, 1416, 1427, 1457, 1576	82, 111, 131, 139, 153, 175, 236, 247, 282, 332, 400, 541, 737, 763, 836, 1095, 1419, 1429, 1458, 1577	245, 400
WHITE	Bone White	**$Ca_3(PO_4)_2$+$CaCO_3$**	959	961	960	455, 590, 965
	Zinc White	**ZnO**	97, 435	137, 435	435	290, 355, 463, 520
	Titanium White	**TiO_2**	239, 441, 607	227, 441, 607	230, 441, 607	240, 450, 615
	Chalk White	**$CaCO_3$**	279, 1084	1086		283, 716, 1090

By the comparison among the detected picks, it seems clear a better identification of those more characteristics, allowing a more accurate characterization of our samples. However the main bands of each pigment were unequivocally identified also with NIR laser.

6.1.3 Spectrophotometric characterization: Colorimetric measurements

After the complete compositional characterization, the spectrophotometric characterization plays an important role in this work because an accurate evaluation of the colour behaviour in our samples allows to obtain information useful for applicative purposes.

The spectra obtained for each sample pigments are shown in Fig. 6.3 (a - e); also in this case, they are presented according the previous modality.

R1

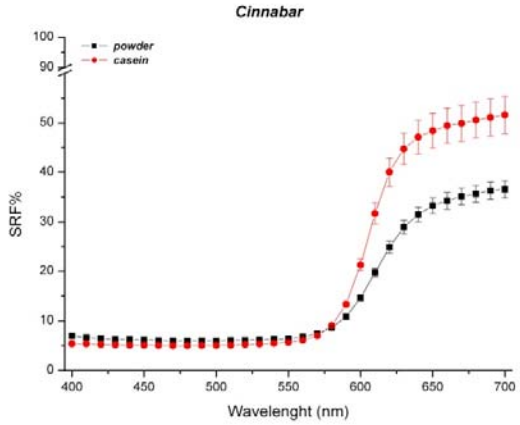

R2

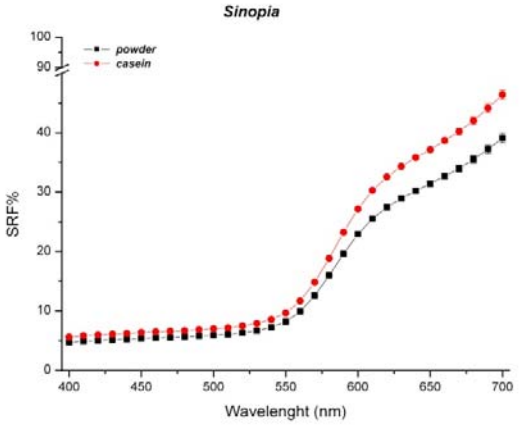

R3

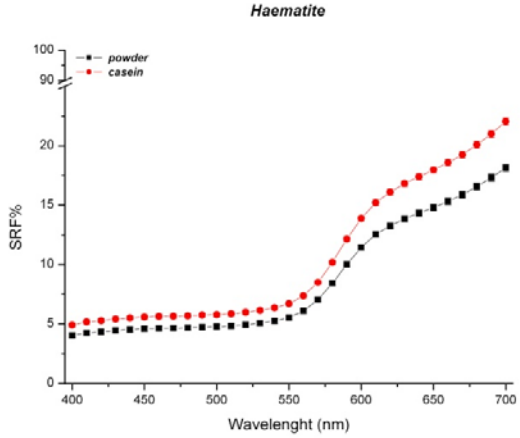

R4

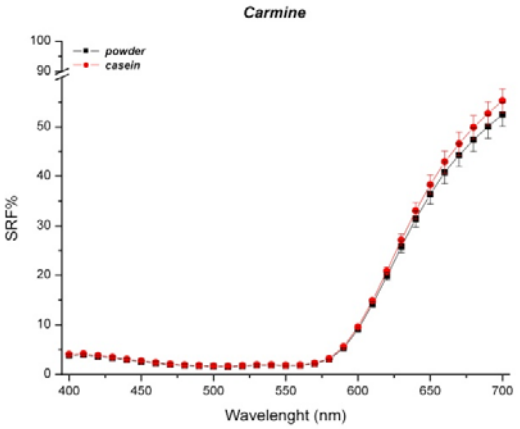

Figure 6.4 a: spectra of ***red*** pigment both in powder and layered with casein, acquired with in contact spectrophotometer.

Y1

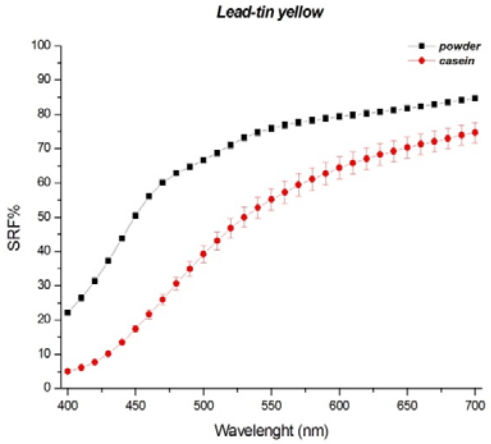

Y2

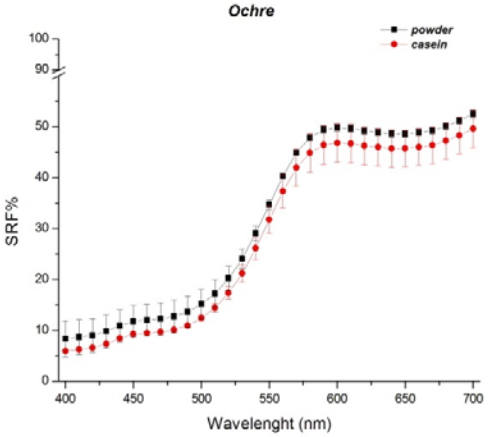

Y3

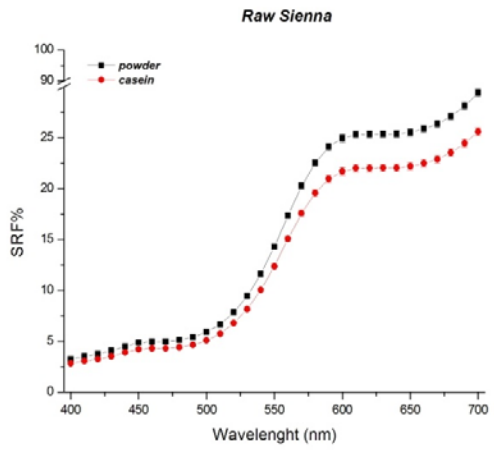

Y4

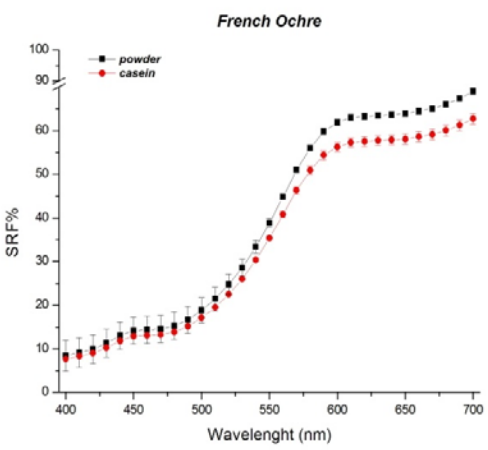

Figure 6.4 b: spectra of ***yellow*** pigment both in powder and layered with casein, acquired with in contact spectrophotometer.

B1

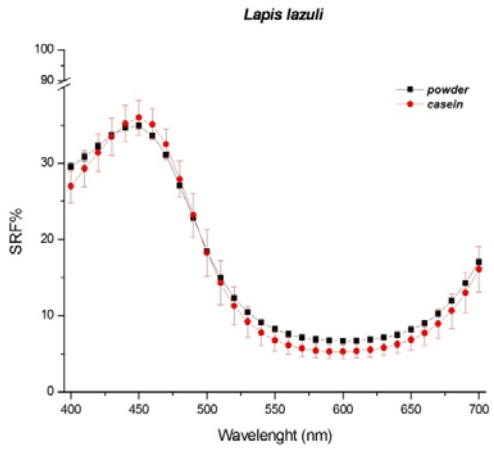

B2

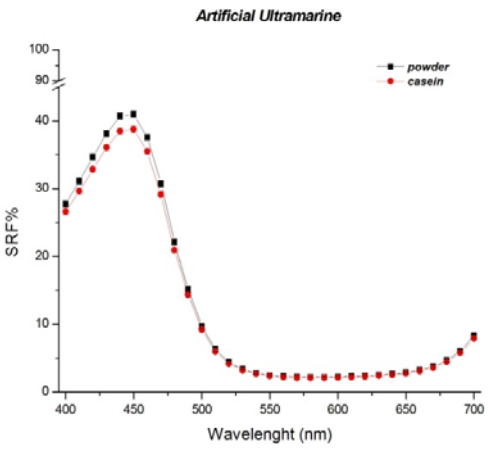

B3

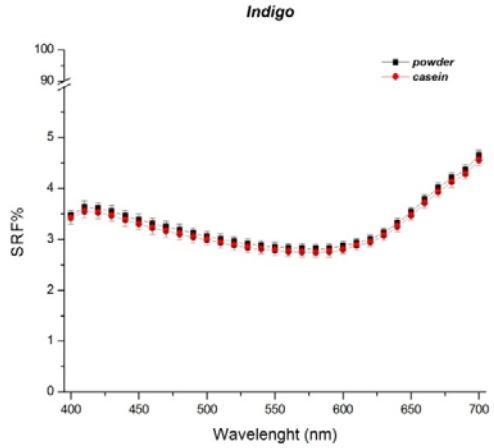

B4

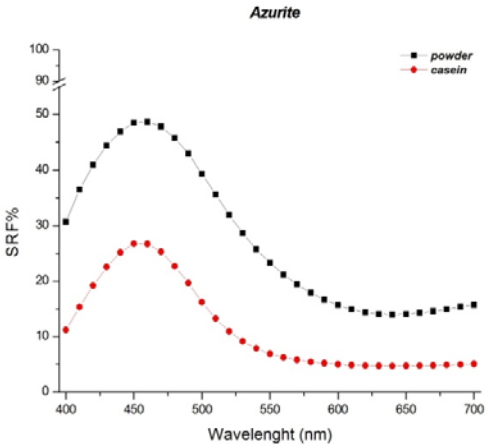

Figure 6.4 c: spectra of ***blue pigment*** both in powder and layered with casein, acquired with in contact spectrophotometer.

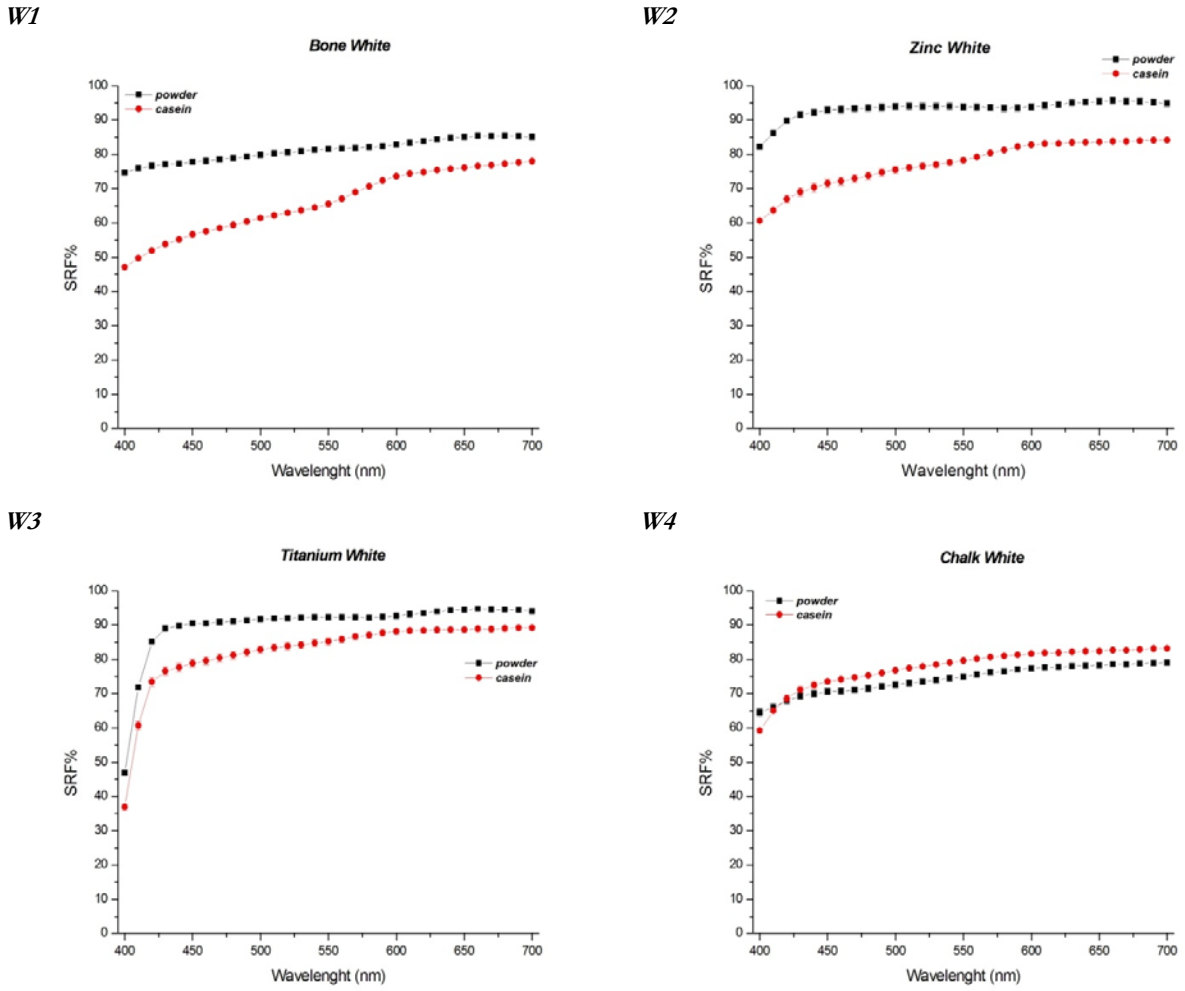

Figure 6.4 d: spectra of ***white pigment*** both in powder and layered with casein, acquired with in contact spectrophotometer.

It is well known that the use of first derivative of the reflectance spectra is useful to better identify the different hues of pigments, also in the mixtures case, as those analysed in the next paragraph. Then, the first derivative curves of the pigments reflectance spectra [13] were considered (Fig. 6.5 a - d). In this case, is possible to associate a peak for each inflection point present in the SRF% spectrum.

R1

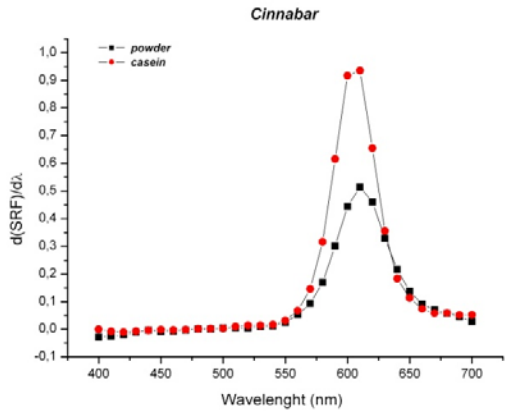

R2

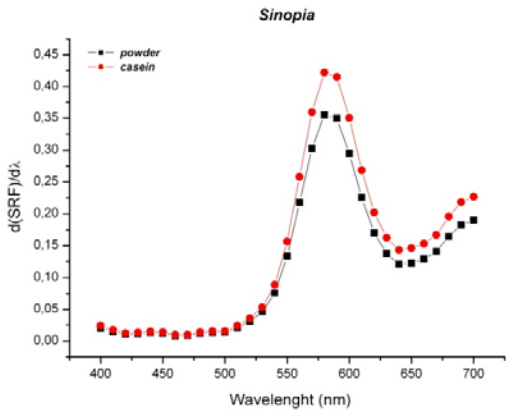

R3

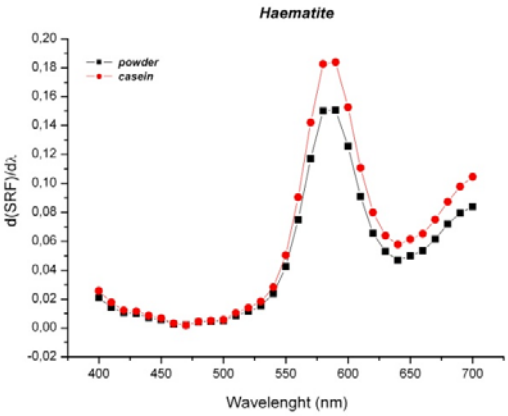

R4

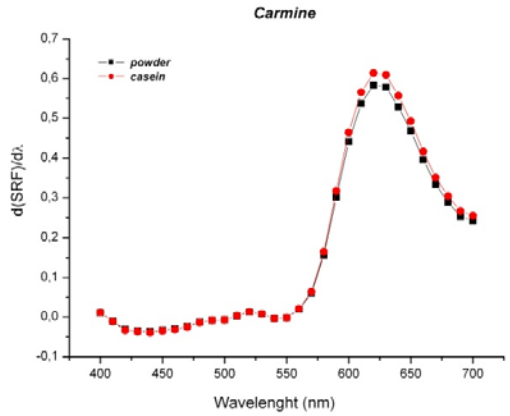

Figure 6.5 a: first derivative spectra of ***red*** pigment both in powder and layered with casein, acquired with in contact spectrophotometer.

Y1

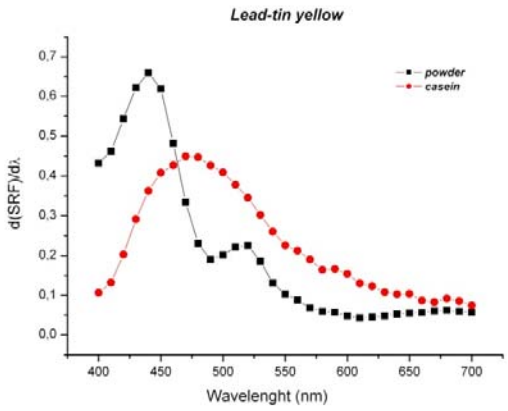

Y2

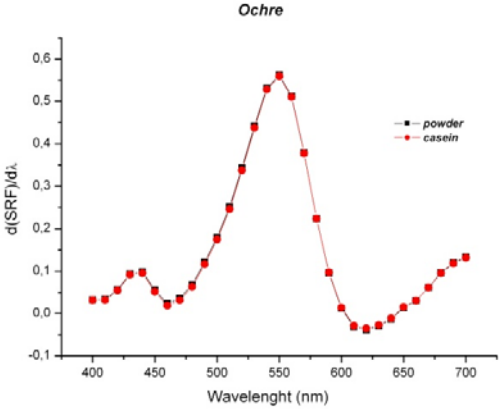

Y3

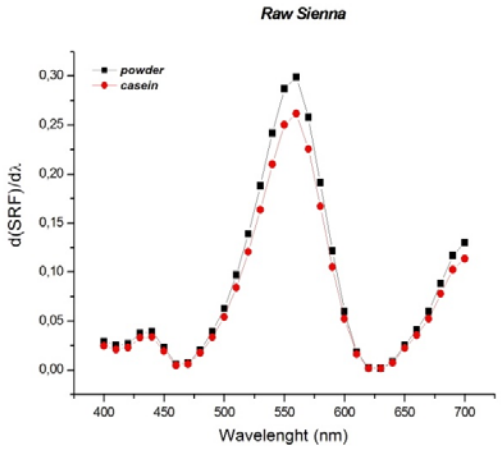

Y4

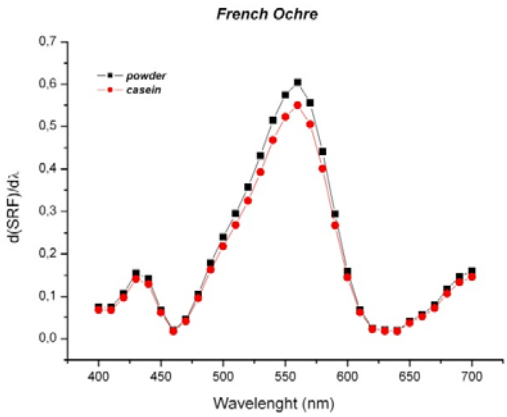

Figure 6.5 b: first derivative spectra of ***yellow*** pigment both in powder and layered with casein, acquired with in contact spectrophotometer.

B1

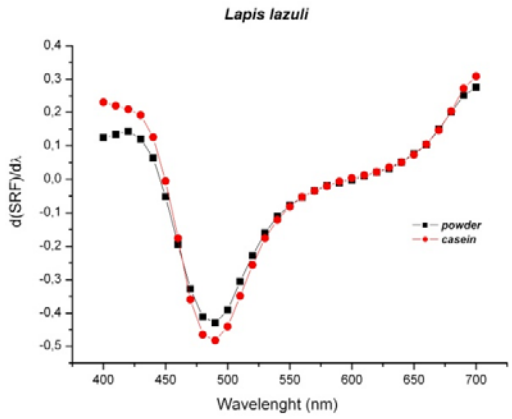

B2

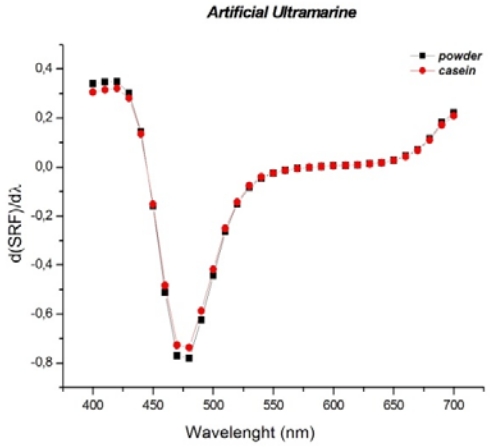

B3

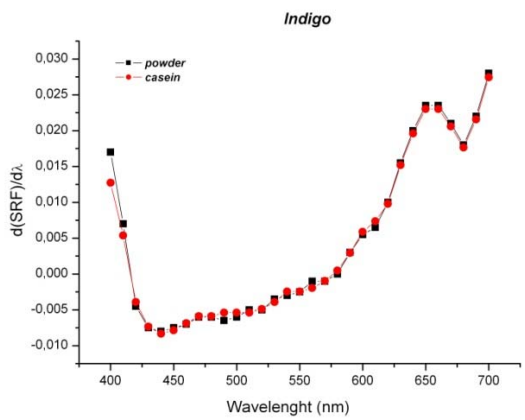

B4

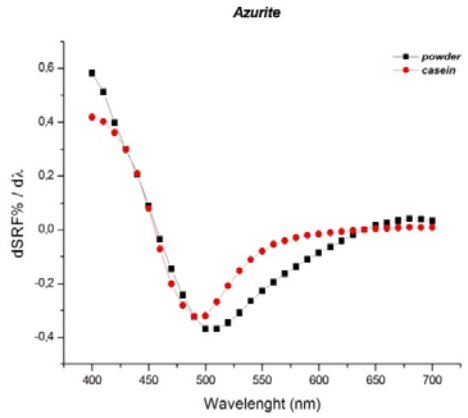

Figure 6.5 c: first derivative spectra of ***blue*** pigment both in powder and layered with casein, acquired with in contact spectrophotometer.

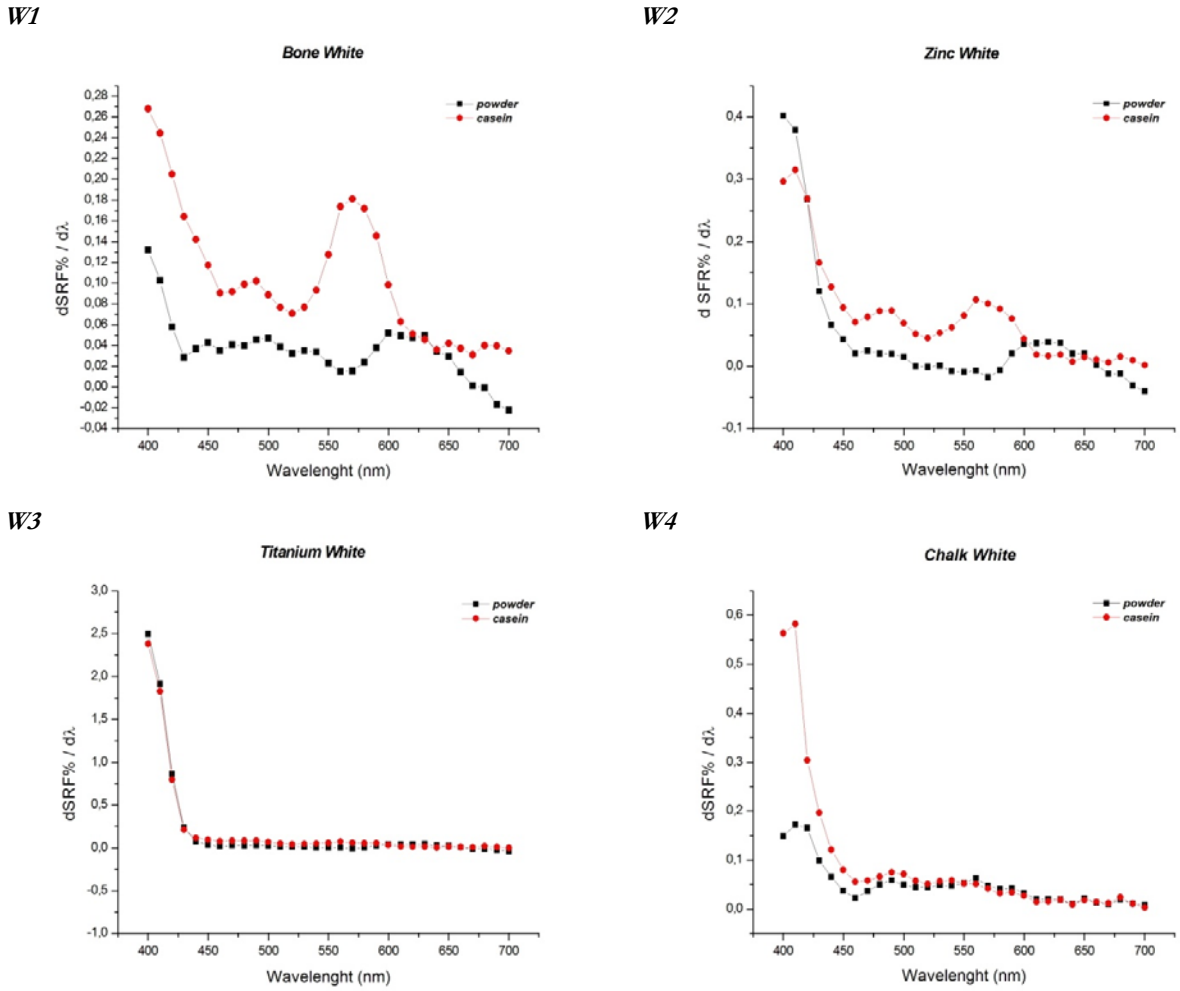

Figure 6.5 d: first derivative spectra of ***white*** pigment both in powder and layered with casein, acquired with in contact spectrophotometer.

First derivative curves calculated from the reflectance spectra of the reference pigments allow to better study the spectral behaviour of the pigments in the different region of visible range. In each case, the identification of a maximum or mininum peak in the SRF% derivate spectra allow to better recognize the different hue. Table 6.3 lists the wavelength of the first derivative curve peak for each pigment, both in powder and mixed with casein.

Table 6.3 – identification of maximum/minimum peaks of first derivative curve.

Hue	***Sample***	***Powder***	***Casein***
RED	Cinnabar	610 nm	
	Sinopia	580 nm	
	Haematite	590 nm	
	Carmine	620 nm	
YELLOW	Lead tin yellow	440 nm/520 nm	470 nm

	Ochre	440 nm/550 nm	
	Raw Sienna	440 nm/ 500 nm	
	French Ochre	430 nm/ 560 nm	
BLUE	Lapis	490 nm	
	Ultramarine	480 nm	
	Indigo	660 nm	
	Azurite	510 nm	490 nm
WHITE	Bone white	430 nm	490 nm / 570 nm
	Zinc white	400 nm	410 nm / 490 nm / 570 nm
	Titanium white	410 nm	
	Chalk white	410 nm / 490 nm	

Focusing the attention on chromatic pigments, only for first derivative curve of Lead-tin yellow (Fig. 6.5 b – Y1) the spectra present a different behaviour between the powder pigment and than one mixed with casein. This is probably due to the slight chromatic component of the medium, which tends to yellow; this component causes a shift and enlargement of the dSRF% maximum making indistinguishable the two peaks of powder pigment (440 – 520 m).

For what concerns the white pigments, i.e. the bone and zinc white, they present the first derivative curve of the sample spread with casein, completely different from those in powder. For both pigments, are presents the same maximum peaks (490 nm / 570 nm) maybe related, also in this case, to the influence of the medium (casein).

6.2 Elemental, compositional and spectrophotometric characterization for mixture

As explained previously (chapter 1 and 5), the schema used to realize the binary mixtures was applied following two different hypotheses:

1) Variation of saturation of the 3 different hues, mixing one chromatic pigment with an achromatic (white).
2) Realization of secondary hue, starting from mixing Red+Yellow+Blu, as described by Itten Theory.

In order to make the binary mixtures, one pigment for each hue was chosen; among the different hue, in particular for red, yellow, blue and white hue, cinnabar, lead-tin yellow, lapis lazuli and chalk white

were selected, respectively. These last are four of the most used pigment by the artist's from Prehistory to Modern Age.

6.2.1 Binary mixtures: Hue + White

The mixtures were organized following the schema here reported (see Tables 6.4 a - c): each hue (R1 – Y1 – B1) were mixed with white sample (W4), varying their weight percentage, with steps of 10%.

Mixture		*R1 - Cinnabar*								
		10%	20%	30%	40%	50%	60%	70%	80%	90%
W4 – Chalk white	10%									***R90+W10***
	20%								***R80+W20***	
	30%							***R70+W30***		
	40%						***R60+W40***			
	50%					***R50+W50***				
	60%				***R40+W60***					
	70%			***R30+W70***						
	80%		***R20+W80***							
	90%	***R10+W90***								

Table 6.4 a – schema used to realize the binary mixture Cinnabar+Chalk White.

Mixture		*Y1 – Lead-tin yellow*								
		10%	20%	30%	40%	50%	60%	70%	80%	90%
W4 – Chalk white	10%									***Y90+W10***
	20%								***Y80+W20***	
	30%							***Y70+W30***		
	40%						***Y60+W40***			
	50%					***Y50+W50***				
	60%				***Y40+W60***					
	70%			***Y30+W70***						
	80%		***Y20+W80***							
	90%	***Y10+W90***								

Table 6.4 b – schema used to realize the binary mixture Lead-tin yellow+Chalk White.

Mixture		*B1 – Lapis lazuli*								
		10%	20%	30%	40%	50%	60%	70%	80%	90%
W4 – Chalk white	10%									***B90+W10***
	20%								***B80+W20***	
	30%							***B70+W30***		
	40%						***B60+W40***			
	50%					***B50+W50***				
	60%				***B40+W60***					
	70%			***B30+W70***						
	80%		***B20+W80***							
	90%	***B10+W90***								

Table 6.4 c – schema used to realize the binary mixture Lapis lazuli+Chalk White.

Figure 6.6 shows these pigment samples layered with casein on a cannas support.

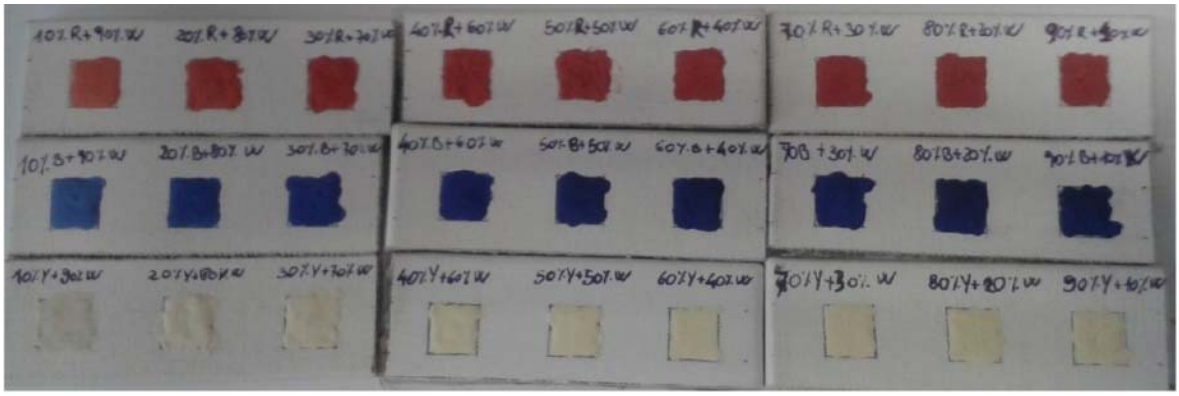

Figure 6.6 – pigment samples layered with casein of **the** Binary mixtures Hue + White.

6.2.1.1 XRF characterization

The XRF spectra plotted in Figs. 6.7 a – f, regarding the investigated mixtures, are the average of the 3 measurements acquired for each weight percentage of each binary mixture.

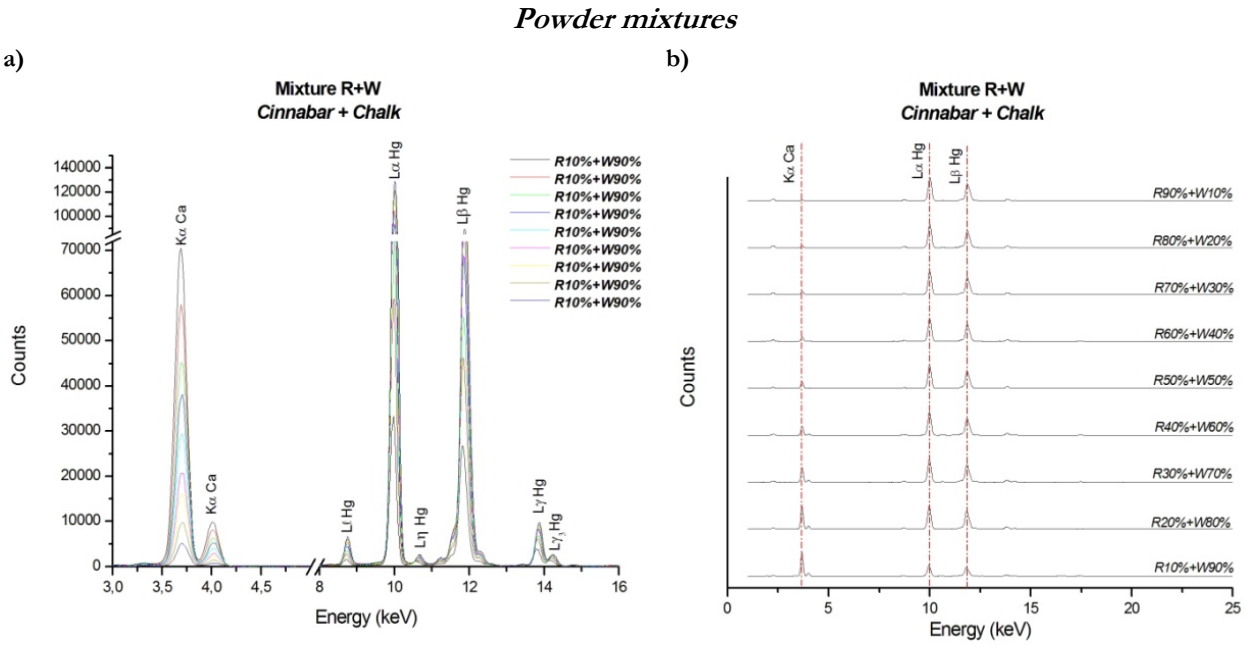

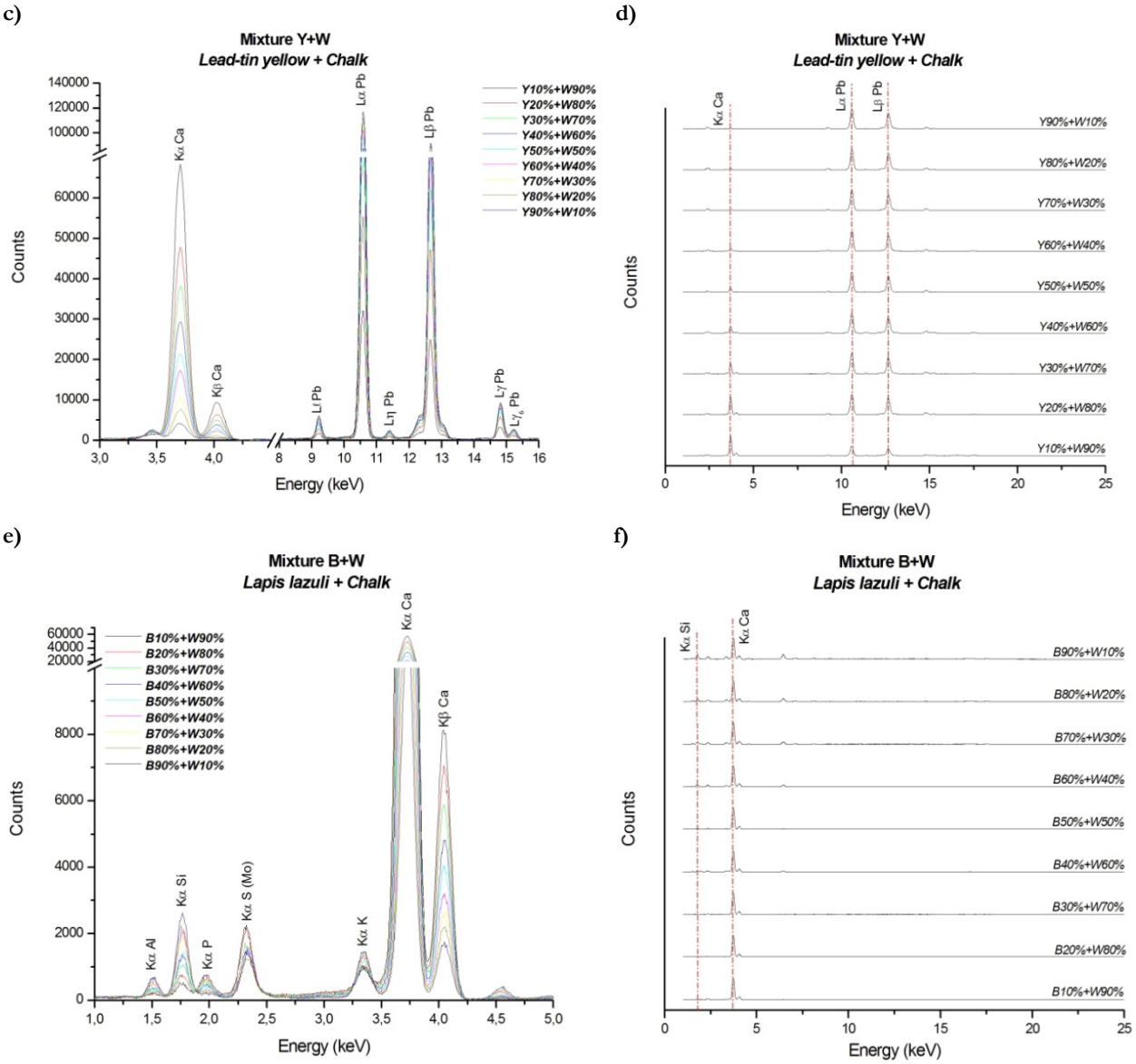

Figure 6.7 – XRF spectra of in powder binary mixtures. All the characteristic lines of the elements constituent the mixture are reported and labelled.

The element characterizing each pigment are present also in the binary mixtures (Fig. 6.7 a, c, e) and for all the weight percentage analysed (Fig. 6.7 b, d, f).

Casein mixtures

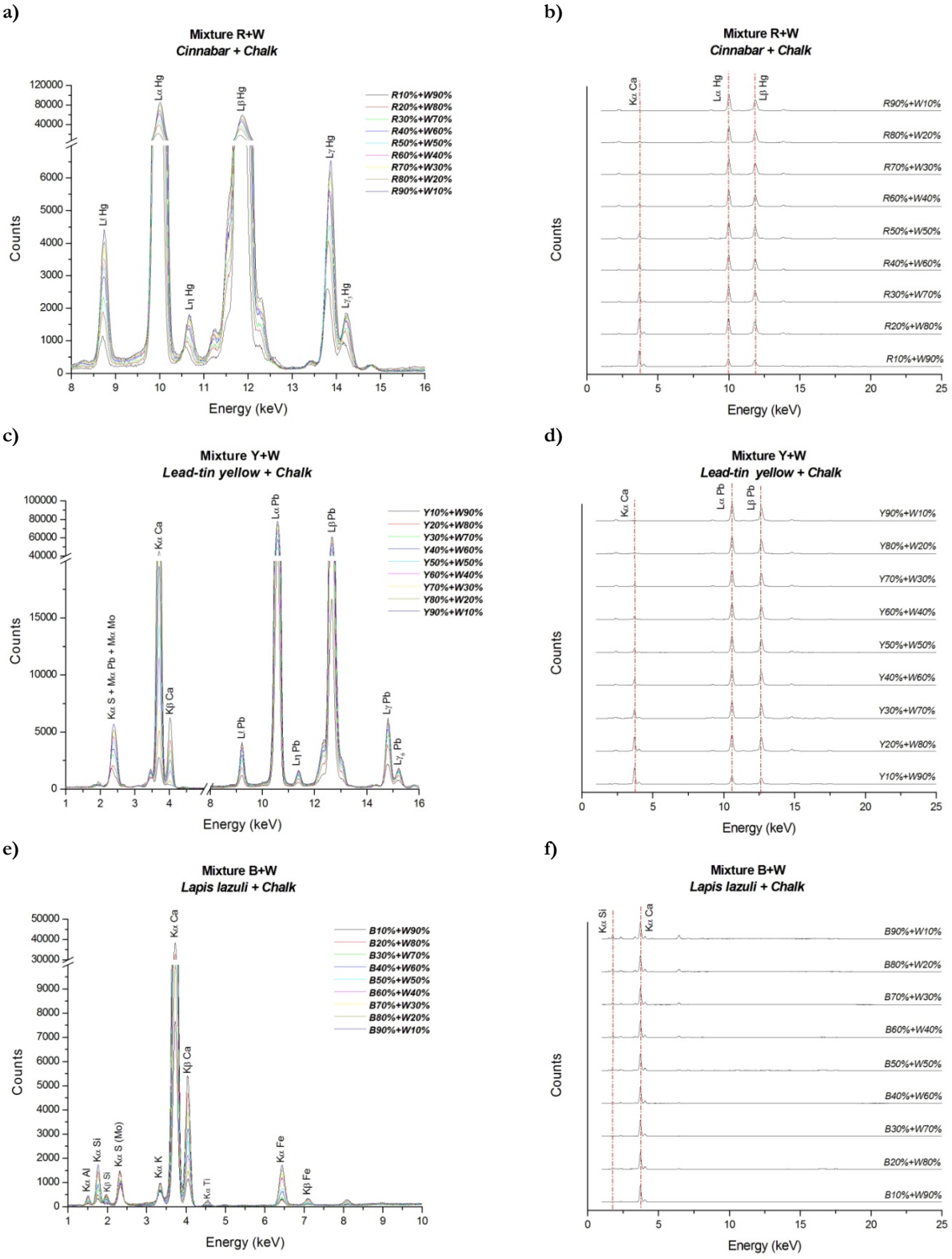

Figure 6.8 – XRF spectra of binary mixture layered with casein. All the characteristic lines of the elements constituent the mixture are reported and labelled.

The characteristic element of each pigment are present also in the binary mixtures layered with casein (Fig. 6.8 a, c, e) and for all the weight percentage analysed (Fig. 6.8 b, d, f).

The intensity of the characteristic lines varies with the pigment concentration within the mixture; this evidence will be used for the evaluation through quantitative analysis of the amount of each pigment that composes the mixtures.

With reference to Table 6.1 and to the pigments chemical composition, Table 6.5 reports the elements characterizing the pigment, detectable also in each mixture: R+W_Cinnabar+Chalk White, Y+W_Lead-tin yellow+Chalk White and B+W_Lapis lazuli+Chalk White.

Mixture	Cinnabar	Lead-tin yellow		Lapis lazuli		Chalk white
	Hg	Pb	Sn	Si	Al	Ca
R+W	•					•
Y+W		•	•			•
B+W				•		•

Table 6.5 – elements identified in each weight percentage, which will be used for the quantitative analysis.

6.2.1.2 Micro-Raman characterization

Following the same procedure used for the characterization of pure pigments, after the XRF elemental characterization, the compositional characterization of binary mixture was carried out through Micro-Raman spectroscopy. The spectra obtained for each mixture are shown in Fig. 6.9 (a - f); also in this case, the spectra are presented firstly in powder, after spread with casein.

Powder mixtures

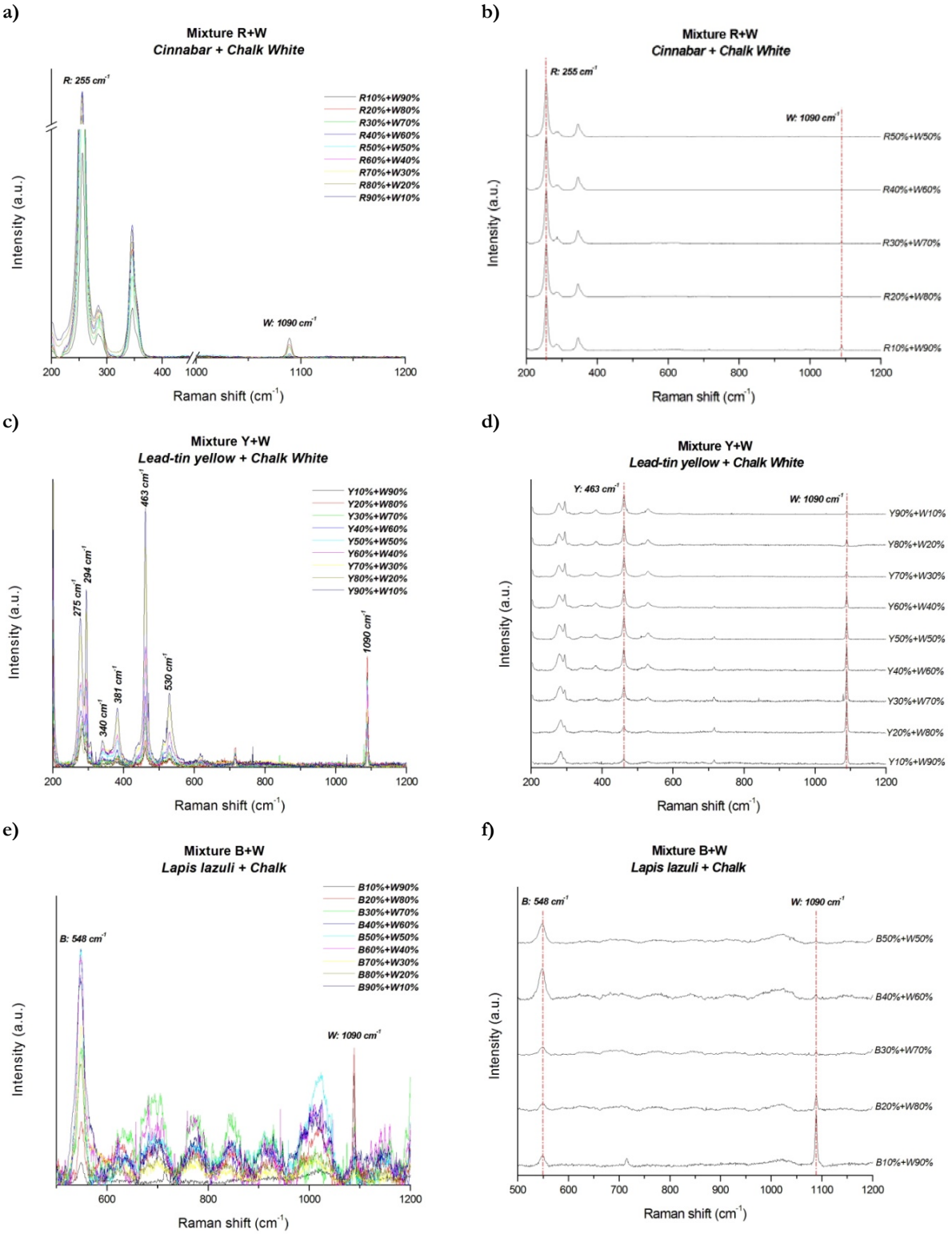

Figure 6.9 - spectra of in powder binary mixtures. For each spectra are reported the main characteristic bands of the pigments that compose mixtures.

The Raman peaks of each pigment are present in the binary mixtures (Fig. 6.9 a, c, e) but in this case the bands are not detectable for all the investigated weight percentage (Fig. 6.9 b, d, f). For weight percentage up to 50% the detection of the Raman bands is not possible for all the analyzed mixtures.
Only for mixture Y+W (Lead-tin yellow+Chalk White) the main band of calcite (1090 cm^{-1}) is present for all the mixed weight percentage.

Casein mixtures

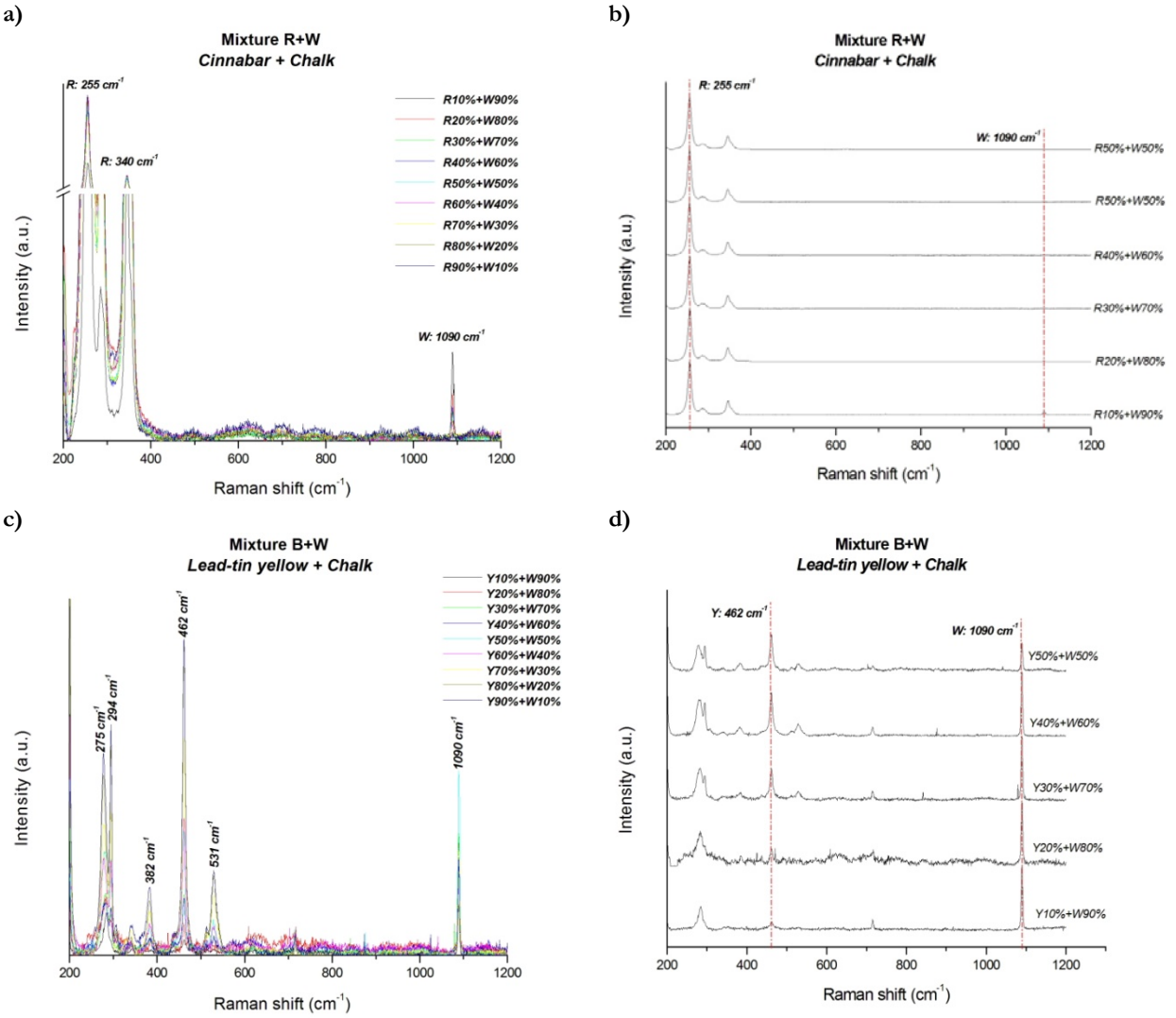

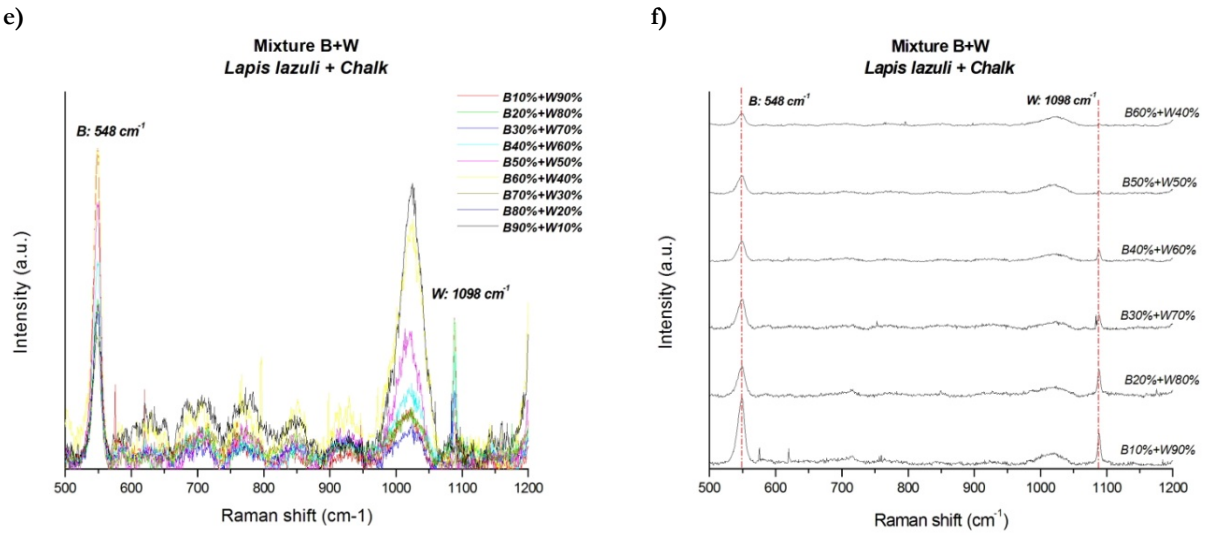

Figure 6.10 - spectra of binary mixture layered with casein. For each spectra are reported the main characteristic bands of the pigments that compose mixtures.

The Raman peaks of each pigment are present in the binary mixtures layered with casein (Fig. 6.10 a, c, e) and also in this case the bands are not detectable for all the weight percentage analysed (Fig. 6.10 b, d, f).

By adding in the mixture a third element (casein) also for Y+W (Lead-tin yellow+Chalk White) the main band of calcite (1090 cm^{-1}) is not detectable for % lower than 50%, as reported in Table 6.6 (a – b – c).

Mixture	Weight (%)	POWDER		CASEIN	
		Cinnabar	Chalk white	Cinnabar	Chalk white
		255 cm^{-1}	1090 cm^{-1}	255 cm^{-1}	1090 cm^{-1}
R+W	***10%+90%***	•	•	•	•
	20%+80%	•	•	•	•
	30%+70%	•	•	•	•
	40%+60%	•	•	•	•
	50%+50%	•	•	•	•
	60%+40%	•		•	
	70%+30%	•		•	
	80%+20%	•		•	
	90%+10%	•		•	

Table 6.6 a – Raman bands identified in each weight percentage, which will be used for the quantitative analysis.

Mixture	Weight (%)	POWDER		CASEIN	
		Lead-tin yellow	Chalk white	Lead-tin yellow	Chalk white
		462 cm^{-1}	1090 cm^{-1}	462 cm^{-1}	1090 cm^{-1}
Y+W	*10%+90%*	•	•	•	•
	20%+80%	•	•	•	•
	30%+70%	•	•	•	•
	40%+60%	•	•	•	•
	50%+50%	•	•	•	•
	60%+40%	•	•	•	
	70%+30%	•	•	•	
	80%+20%	•	•	•	
	90%+10%	•	•	•	

Table 6.6 b – Raman bands identified in each weight percentage, which will be used for the quantitative analysis.

Mixture	Weight (%)	POWDER		CASEIN	
		Lapis lazuli	Chalk white	Lapis lazuli	Chalk white
		548 cm^{-1}	1090 cm^{-1}	548 cm^{-1}	1090 cm^{-1}
Y+W	*10%+90%*	•	•	•	•
	20%+80%	•	•	•	•
	30%+70%	•	•	•	•
	40%+60%	•	•	•	•
	50%+50%	•	•	•	•
	60%+40%	•	•	•	
	70%+30%	•	•	•	
	80%+20%	•	•	•	
	90%+10%	•	•	•	

Table 6.6 c – Raman bands identified in each weight percentage, which will be used for the quantitative analysis.

6.2.1.3 Spectrophotometric characterization

In this case the curve of spectral reflectance factor (SRF%) of the binary mixtures were acquired and the first derivative curves were calculated in order to associate the maximum and/or minimum peak of the curve to each hue that compose the mixture; this information will be used to obtain quantitative information on the mixtures.

The saturation level caused by the addition of gradually higher weight percentages of white pigment was also evaluated in order to obtain chromatic information.

To this point it is important to focus the work' aim: obtain quantitative information on mixtures of pigments used by the ancient artist; for this reason it is crucial to associate also to characterization and

quantitative measurements, the study of chromatic behaviour of the mixtures realized in order to recreate sample as much as possible compatible to the real mixtures created by artists.

The spectra, both SRF% and dSRF%, obtained for each samples are shown in Fig. 6.11 (a – f) for powder mixtures and in Fig. 6.12 (a – f) for casein ones.

Powder mixtures

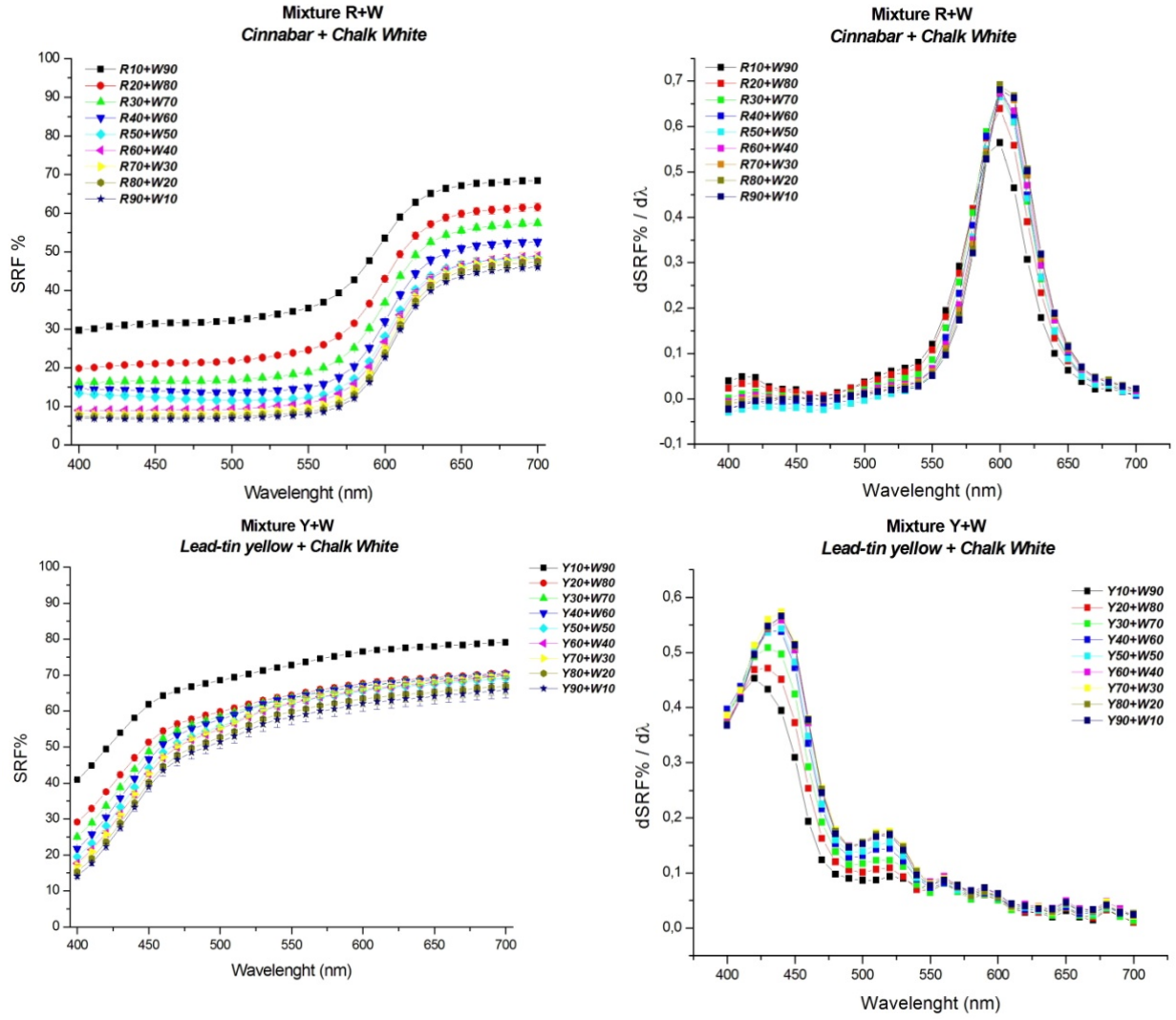

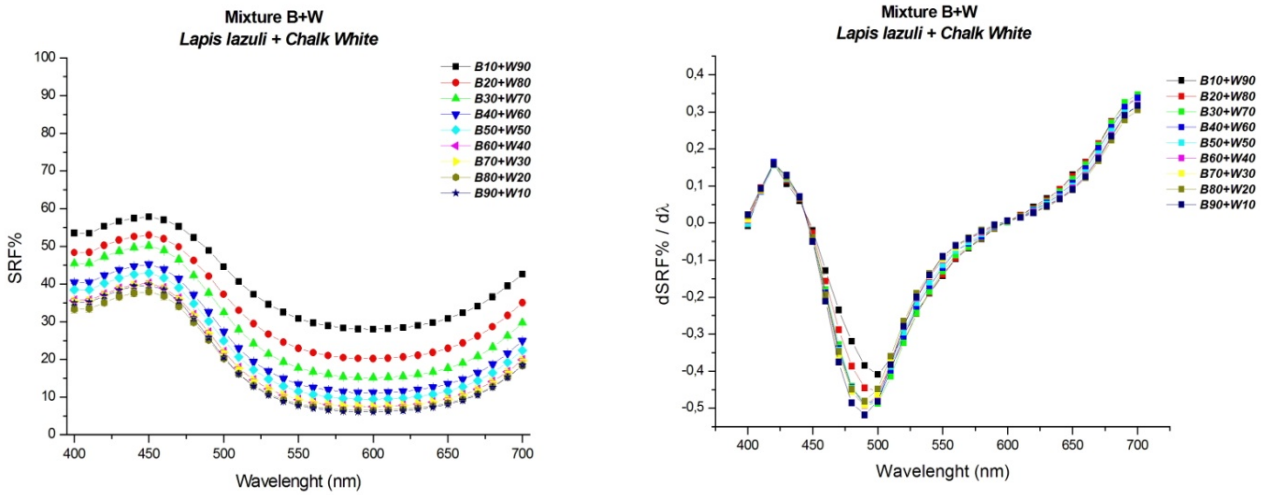

Figure 6.11 - spectra of powder binary mixture. For each weight percentage the SRF% and the first derivative curves are reported.

Casein mixtures

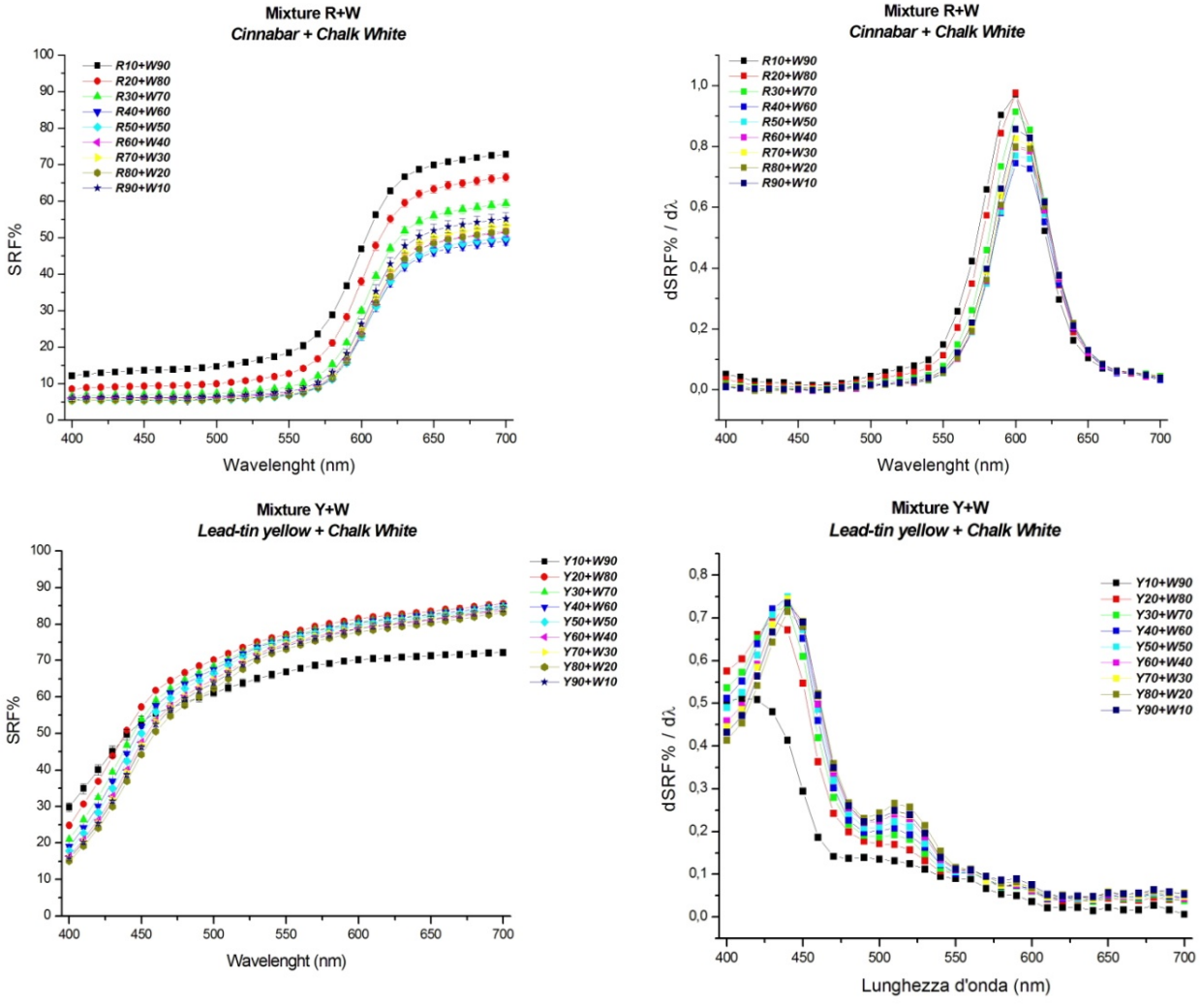

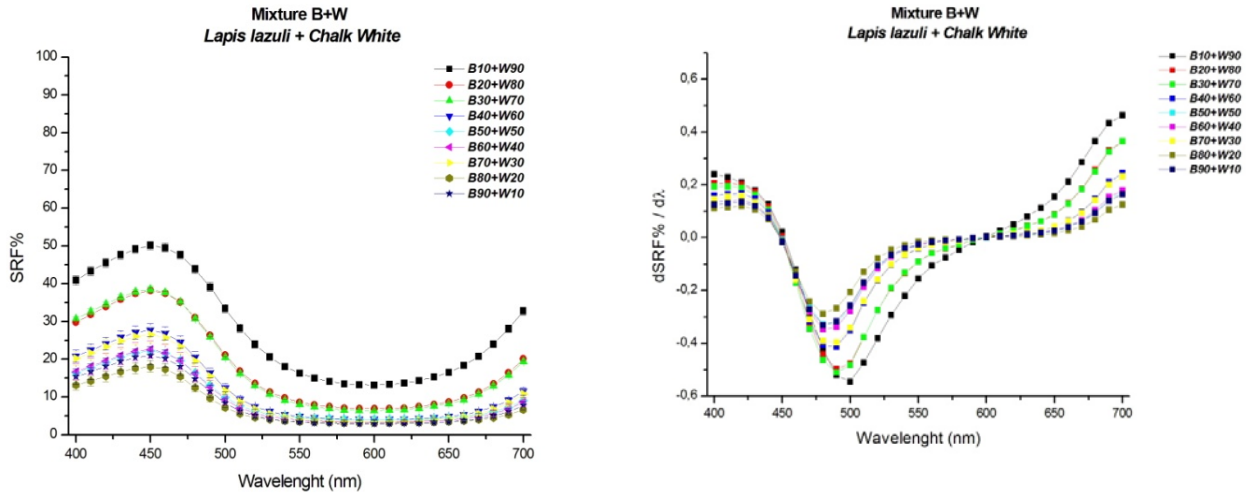

Figure 6.12 – spectra of binary mixture layered with casein. For each weight percentage the SRF% and the first derivative curves are reported.

The spectral behaviour, for both the typology of binary mixtures, show the same trend and the first derivative curves don't allow to obtain information to each hue that compose the mixtures, such explained before for pure pigments: indeed the chalk white don't show a maximum or minimum that allow to characterize the pigment.

6.2.2 Binary mixtures: Itten's Theory

In order to recreate the secondary hue prepared by the ancient artists following the Itten Theory, explained in the chapter 1, three pure pigments were chosen. The mixtures were organized following the schema here reported:

- Primary Colour → Red – Yellow – Blue
- Secondary Colour → Orange = Red + Yellow
  → Violet = Red + Blue
  → Green = Blue + Yellow

Figure 6.13 – *Farbkreis* by Johannes Itten (1961).

One pigment for each primary hue (R1 – Y1 – B1) were mixed together, varying their weight percentage, with steps of 10%. Tables 6.7 a – c show the percentage used for each Itten mixture.

Mixture		***R - Cinnabar***								
		10%	20%	30%	40%	50%	60%	70%	80%	90%
Y – Lead-tin yellow	10%									***R90+Y10***
	20%								***R80+Y20***	
	30%							***R70+Y30***		
	40%						***R60+Y40***			
	50%					***R50+Y50***				
	60%				***R40+Y60***					
	70%			***R30+Y70***						
	80%		***R20+Y80***							
	90%	***R10+Y90***								

Table 6.7 a – schema used to realize Orange's Itten mixtures: Cinnabar + Lead-tin Yellow.

Mixture		***R - Cinnabar***								
		10%	20%	30%	40%	50%	60%	70%	80%	90%
B – Lapis lazuli	10%									***R90+B10***
	20%								***R80+B20***	
	30%							***R70+B30***		
	40%						***R60+B40***			
	50%					***R50+B50***				
	60%				***R40+B60***					
	70%			***R30+B70***						
	80%		***R20+B80***							
	90%	***R10+B90***								

Table 6.7 b – schema used to realize Purple's Itten mixtures: Cinnabar + Lapis lazuli.

Mixture		***B – Lapis lazuli***								
		10%	20%	30%	40%	50%	60%	70%	80%	90%
Y – Lead-tin yellow	10%									***B90+Y10***
	20%								***B80+Y20***	
	30%							***B70+Y30***		
	40%						***B60+Y40***			
	50%					***B50+Y50***				
	60%				***B40+Y60***					
	70%			***B30+Y70***						
	80%		***B20+Y80***							
	90%	***B10+Y90***								

Table 6.7 c – schema used to realize Green's Itten mixtures: Lapis lazuli + Lead-tin yellow.

Here show the tablets of Itten mixtures realized.

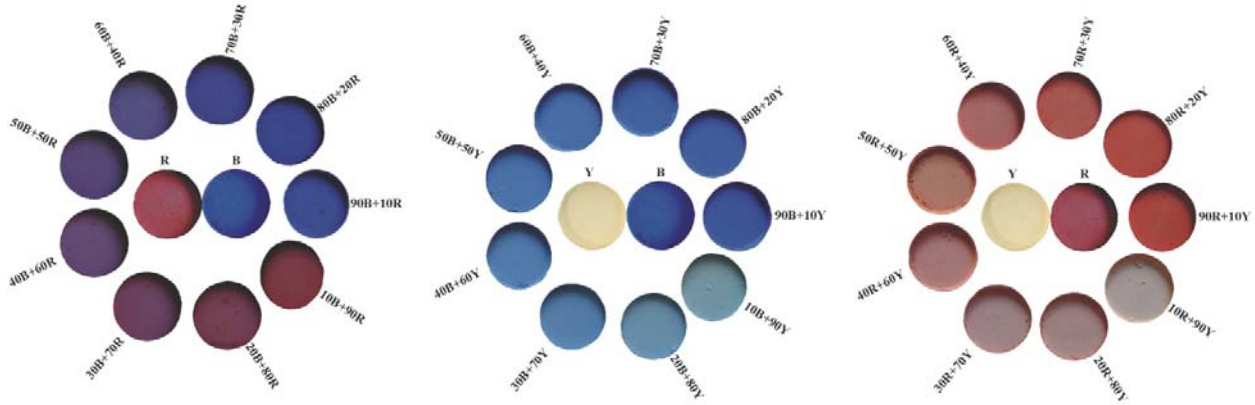

Mixture R+B
Cinnabar + Lapis lazuli

Mixture B+Y
Lapis lazuli + lead-tin yellow

Mixture R+Y
Cinnabar + Lead-tin yellow

Figure 6.14 – tablets of powder Itten mixtures realized.

6.2.2.1 XRF characterization

The XRF analysis carried out on these samples are shown in the Figs. 6.15 a – f as average of the 3 measurment points analized.

Powder mixtures ***Casein mixtures***

a) **b)**

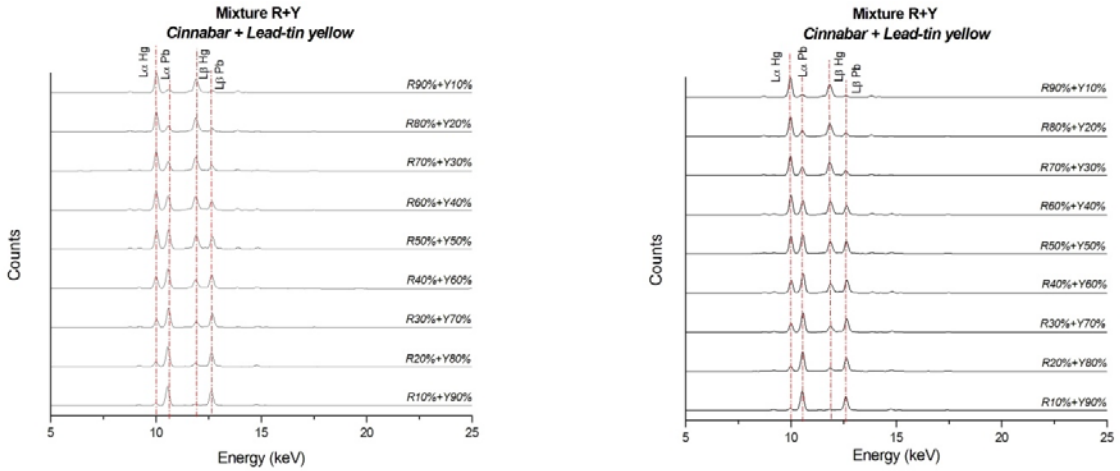

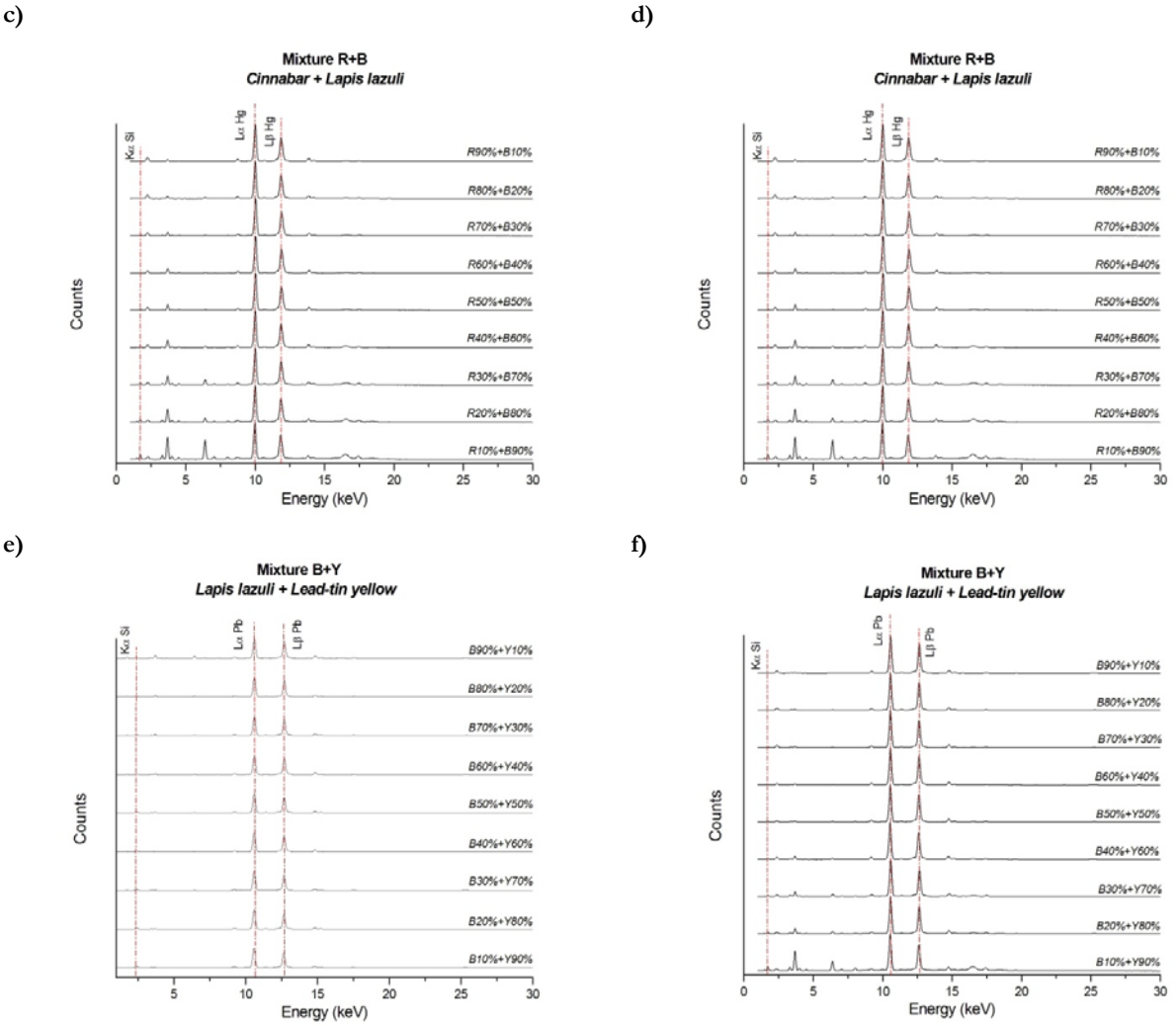

Figure 6.15 – XRF spectra both for podwer and casein Itten mixtures.

The characteristic elements of each pigment are present also for all the weight percentage analysed of Itten mixtures (Fig. 6.15).

As in the previous case, the intensity of the characteristic lines varies with the pigment concentration within the mixture; this evidence is important for the quantitative analysis of the amount of each pigment that composes the mixtures.

Table 6.8 is the analogous of the Table 6.1. It reports the elements that characterize the pigment, also identifiable in each mixture:

- *Orange's Itten* - R+Y_Cinnabar + Lead-tin yellow
- *Purple's Itten* - R+B_Cinnabar + Lapis lazuli
- *Green's Itten* - B+Y_Lapis lazuli + Lead-tin yellow

Mixture	Cinnabar	Lead-tin yellow		Lapis lazuli	
	Hg	Pb	Sn	Si	Al
R+Y	•	•	•		
R+B	•			•	•
B+Y		•	•	•	•

Table 6.8 – elements identified in each weight percentage, which will be used for the quantitative analysis.

6.2.2.2 Micro-Raman characterization

The compositional characterization of Itten mixture was carried out through Micro-Raman spectroscopy. The spectra obtained for each mixture are shown in Fig. 6.16 (a – f) both in powder and spread with casein.

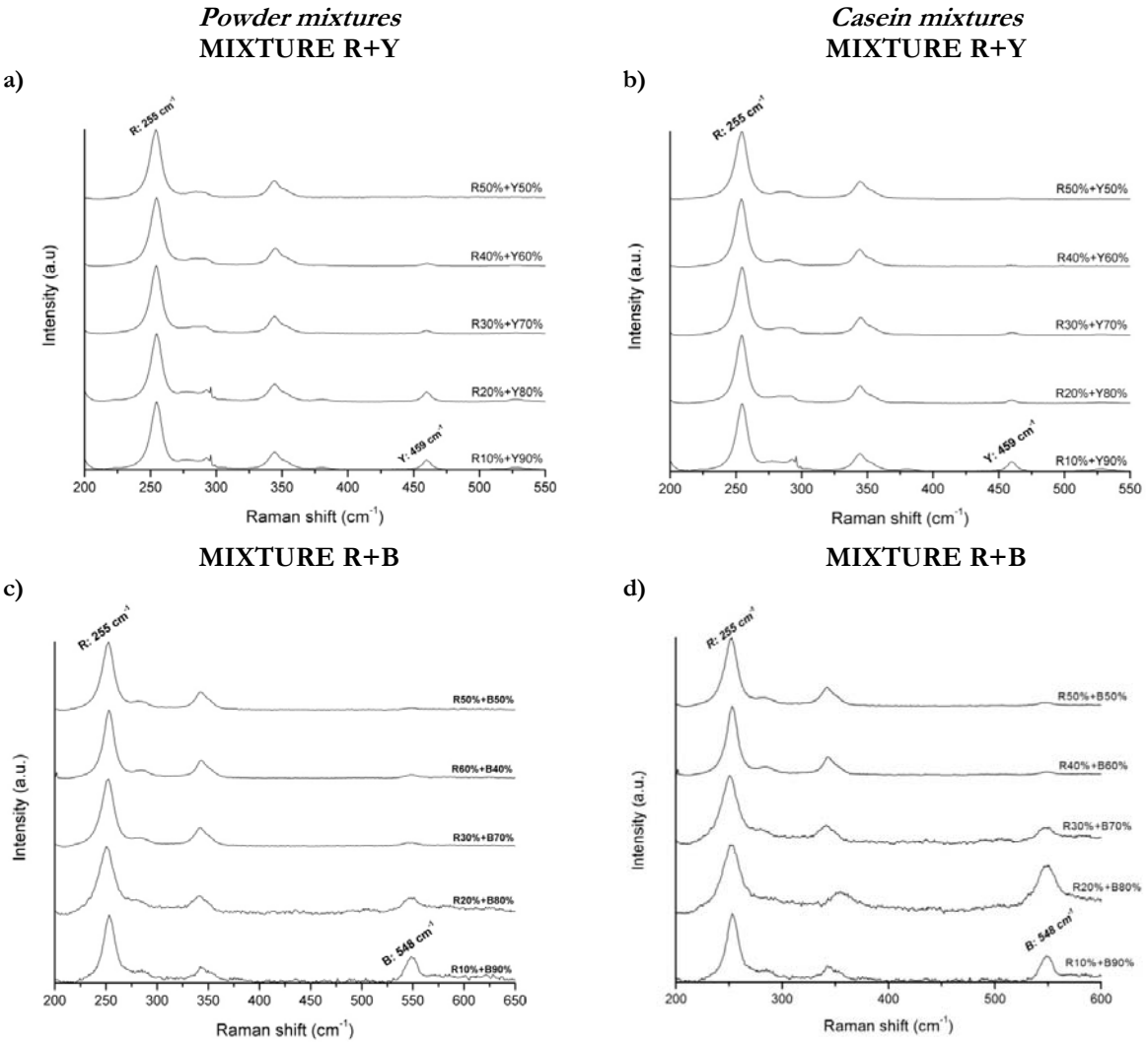

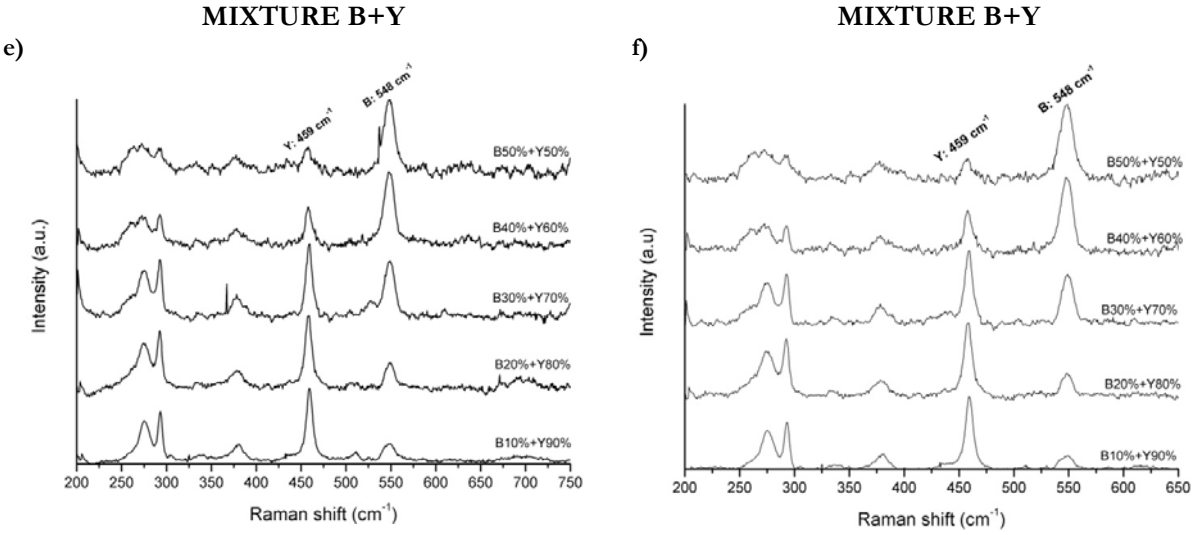

Figure 6.16 – Raman spectra of mixtures, both for powder (left) and with casein (right). Fig.6.13: a-b) R+Y (cinnabar + lead-tin yellow), c-d) R+B (cinnabar + lapis lazuli), e-f) B+Y (lapis lazuli + lead-tin yellow).

The Raman peaks of each pigment are present in the Itten mixtures but in this case the bands are not detectable for all the weight percentage. As explained for binary mixtures with chalk white, for weight percentage up to 50% the detection of the Raman bands is not possible for all the mixtures.

That kind of behaviour is evident for each mixtures, in particular: for the Orange's Itten mixture increasing the amount of cinnabar the characteristic bands of lead-tin yellow are not detectable; this happened because the weak lead-tin yellow Raman bands need an higher stimulation time (~ 30 sec) to be detected; indeed the high Raman response of cinnabar, also with very low time (~ 5 sec) of stimulation, cover completely the weak lead-tin yellow bands. If higher times of stimulation are used, the intensity of 255 cm^{-1} band of cinnabar causes CCD saturation, invalidating the identification of the pigments in mixture.

The same consideration can be given for the Purple and Green's Itten mixtures: in the purple ones the cinnabar (~ 5 sec) cover completely the weak signal of lapis lazuli (~ 100 sec), that is also covered by lead-tin yellow (~ 30 sec) in the green mixtures.

6.2.2.3 Spectrophotometric characterization

With the aims described before, also in this case the spectral reflectance factor (SRF%) and the first derivative curves of mixtures are shown. In particular, the spectra of SRF% are shown in Fig. 6.17 (a – f) and of dSRF% ones in Fig. 6.18 (a – f).

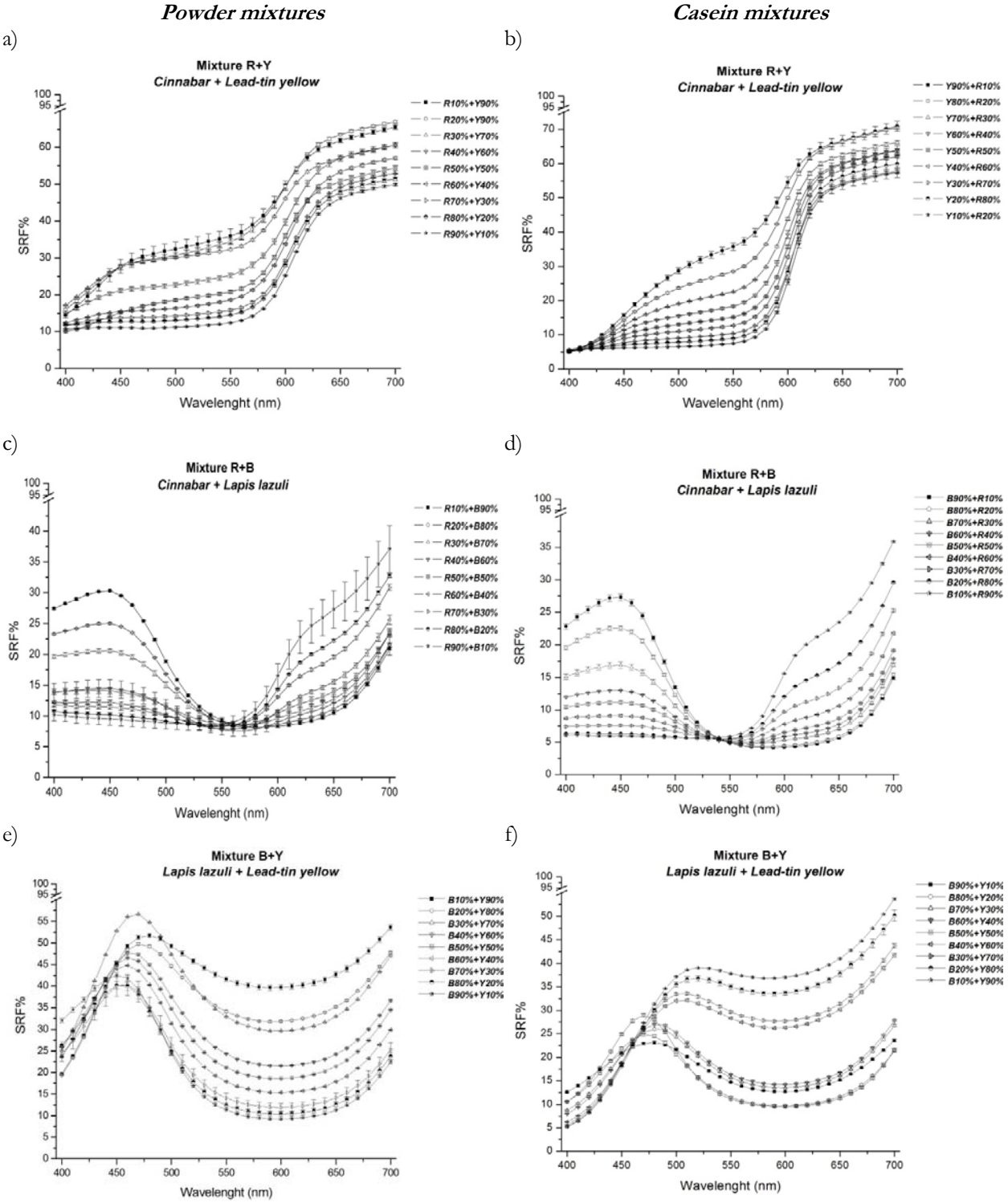

Figure 6.17 – Reflectance spectra of mixtures, both for powder (left) and with casein (right). Fig.6.14: a-b) R+Y (cinnabar + lead-tin yellow), c-d) R+B (cinnabar + lapis lazuli), e-f) B+Y (lapis lazuli + lead-tin yellow).

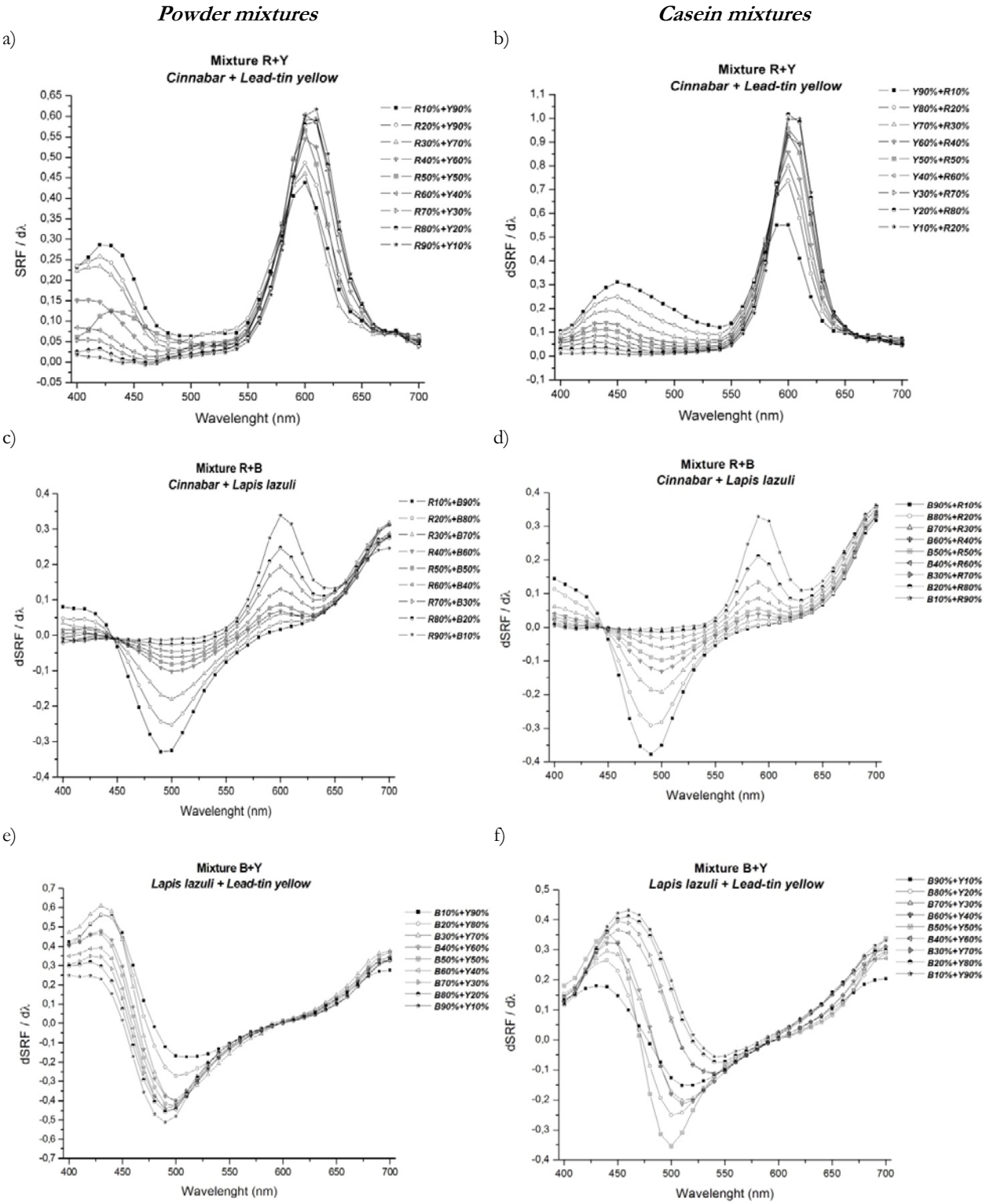

Figure 6.18 – first derivative curve of Itten binary mixtures, both in powder and spread with casein. Fig. 6.15: a-b) R+Y (cinnabar + lead-tin yellow), c-d) R+B (cinnabar + lapis lazuli), e-f) B+Y (lapis lazuli + lead-tin yellow).

Contrary to what was described for the mixtures with chalk white, in this case in the first derivative curves of Itten mixtures are present maximum and/or minimum peaks that allow to identify the

different hue involved in the mixture. So in this case, the first derivative curves will be used for the quantitative analysis.

6.3 XRF quantitive method

X-ray fluorescence data from historical pigments, both pure and mixed, will be presented, in order to obtain quantitative information on the samples and to extract calibration curves to the aim of evaluating the pigment concentration in unknown mixtures.

The analysis of the XRF spectra obtained for each weight percentage was carried out following the procedure explained in the paragraph 5.3.1.

In order to build fitting and calibration curves, to be used to obtain by inverse prediction the concentration of the two pigments composing the mixture, net area values for selected peaks of pigments characteristic elements have been plotted *vs.* pigment concentration (weight %).

Only chemical elements directly related to the presence of the three main pigments, and having statistically significant peak counts, have been used for fitting.

These elements are: Hg for cinnabar, Si for lapis lazuli, Pb and Sn for lead-tin yellow, Ca for chalk white.

As said in the previous chapter, the densities of samples obtained by mixing pigments with different relative densities, affect the XRF signal which will be then strongly dependent on the relative percentage of the two pigments in the mixing. This circumstance will be less important in mixtures composed by pigments characterised by comparable densities.

The densities of cinnabar, lead-tin yellow, lapis lazuli and chalk white are 8.1, 6.6, 2.4 and 2.93 g cm^{-3}, respectively.

Here reported the calibration curve obtained for Itten binary mixtures.

The density $D_{I,J}$ of each mixture has been calculated from the densities D_I and D_J and mass percentages p_I and p_J of the pure pigments according to the following equation [14].

$$D_{I,J} = \frac{p_I + p_J}{\frac{p_I}{D_I} + \frac{p_J}{D_J}} \tag{6.1.}$$

Further tests have been carried out in order to check and validate the procedure, performing inverse predictions on fitting or calibration curves.

As show in the spectra presented in section 6.2.2.1, all the characteristic elements peaks of primary pigments are present in the spectra with peak areas proportional to their relative concentration.
So, starting from that assumption, net peak area of the characteristic elements of the pigments were plotted *vs.* weight percentage of the pigment in the mixture (Fig. 6.19).

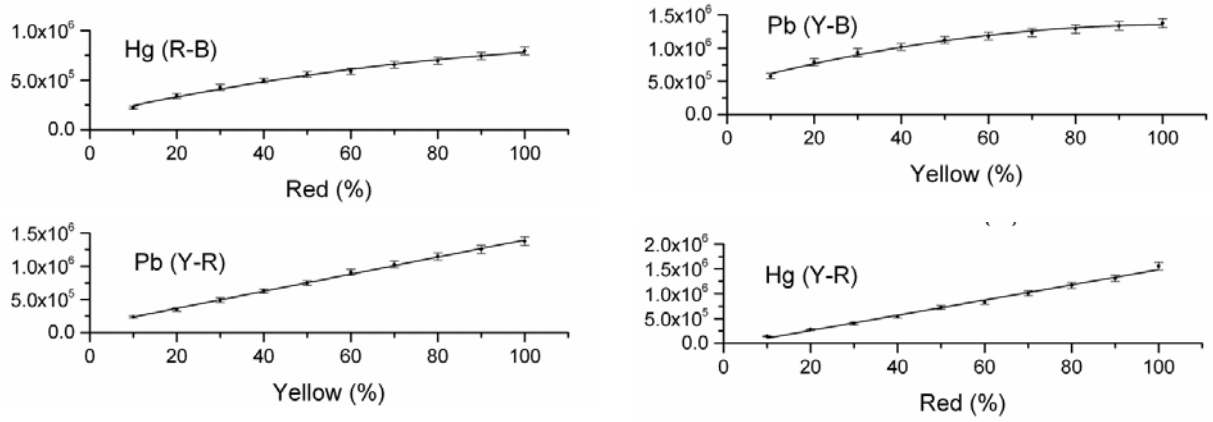

Figure 6.19 - Experimental net peak areas *vs.* pigment weight fraction and fitting curves. Error bars are also shown. From top to bottom: Hg in R-B *vs.* R%; Pb in Y-B *vs.* Y%; Pb in Y-R *vs.* Y%; Hg in Y-R *vs.* R%. See Table 6.9 for numerical details.

In these figures, net areas for Hg L_α line in the R-B mixture vs. R% concentration, and Pb L_α line in the Y-B mixture *vs.* Y% concentration have been fitted by a second order polynomial equation. This non-linearity, with a decreasing slope of the curve, can be explained by the fact that the density of the sample will strongly increase with the heavy pigment (R or Y) percentage. The opposite behaviour, with an increasing slope, would be obviously obtained by plotting the XRF signal *vs.* the light pigment concentration (e.g. Si K_α peak area *vs.* B percentage in the Y-B mixture, see Table 6.9). In the case of Y-R mixtures, the two pigments have comparable densities; the peak intensity will not be affected by density of the mixtures, so leading to a linear behaviour in calibration curves ($R^2 > 0.999$).

Mixture (element)	***Model (R^2)***	***Reference value (%)***	***Calculated value (%)***
R-B (Hg)	Quadratic (0.992)	R 75	R 75.7
B-Y (Pb)	Quadratic (0.989)	Y 85	Y 83.9
B-Y (Si)	Quadratic (0.998)	B 15	B 18.4
R-Y (Pb)	Linear (0.998)	Y 25	Y 24.3 (21.0−27.6)
R-Y (Hg)	Linear (0.994)	R 75	R 73.3 (67.5−79.1)
R-Y (Sn)	Linear (0.997)	Y 25	Y 24.8 (20.4−29.1)

Table 6.9 - Numerical results for fitting of peak net areas vs. pigment concentrations. The second column lists the model along with the R^2 values. The last two columns list the expected weight percentages of pigments in the test binary mixtures (reference values %) along with the values obtained by inverse prediction. In the case of a linear regression model, the concentration and their ≅ 95% confidence ranges are also shown.

XRF data for the different mixtures have been analysed in detail in order to get insights on the mixture density dependence. The densities values of the three pure pigments are: 8.1 g cm $^{-3}$ for cinnabar, 6.6 g cm $^{-3}$ for lead-tin yellow and 2.75 g cm $^{-3}$ for lapis lazuli. Only the last one, the lapis lazuli, has a density value higher than one declared by Kremer. Indeed, the XRD analysis (Fig. 6.20 a-c) carried out in order to better characterize the chemical composition and the mineralogical phases of the three pure pigments shows that the red, yellow and white pigment presents only the mineralogical phases declared by Kremer (cinnabar, lead-tin oxide and calcite respectively), on the contrary, the lapis lazuli matrix appear more complex, characterized by the presence of various mineralogical phases: lazurite, muscovite, diopside, calcite and pyrite with weight percentage of 40, 31, 17, 8 and 4% respectively; hence the density value of this pigment was calculated by eq. (6.1), using the weight % of the different minerals present.

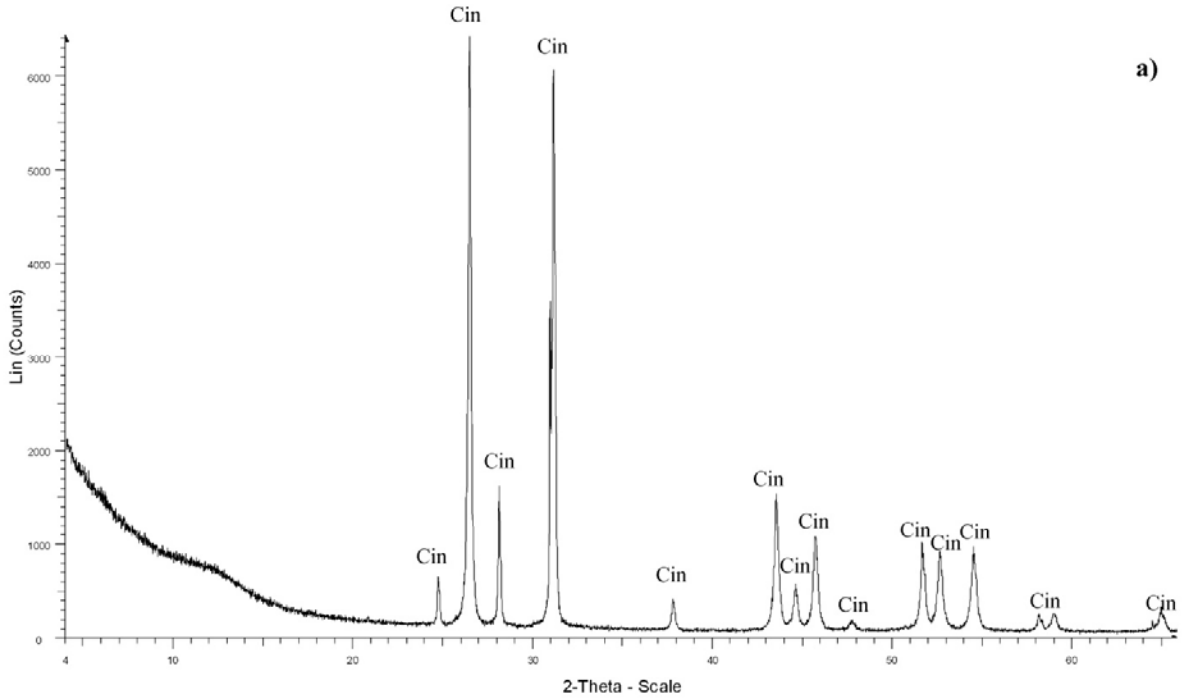

Figure 6.20 a - Fig. 3. XRD spectra: (a) cinnabar; (b) lapis lazuli and (c) lead-tin yellow. Mineralogical phases are reported: Cin: cinnabar; LTO: lead-tin oxide; La: lazurite; Mu: muscovite; Di: diopside; Ca: calcite; Py: pyrite.

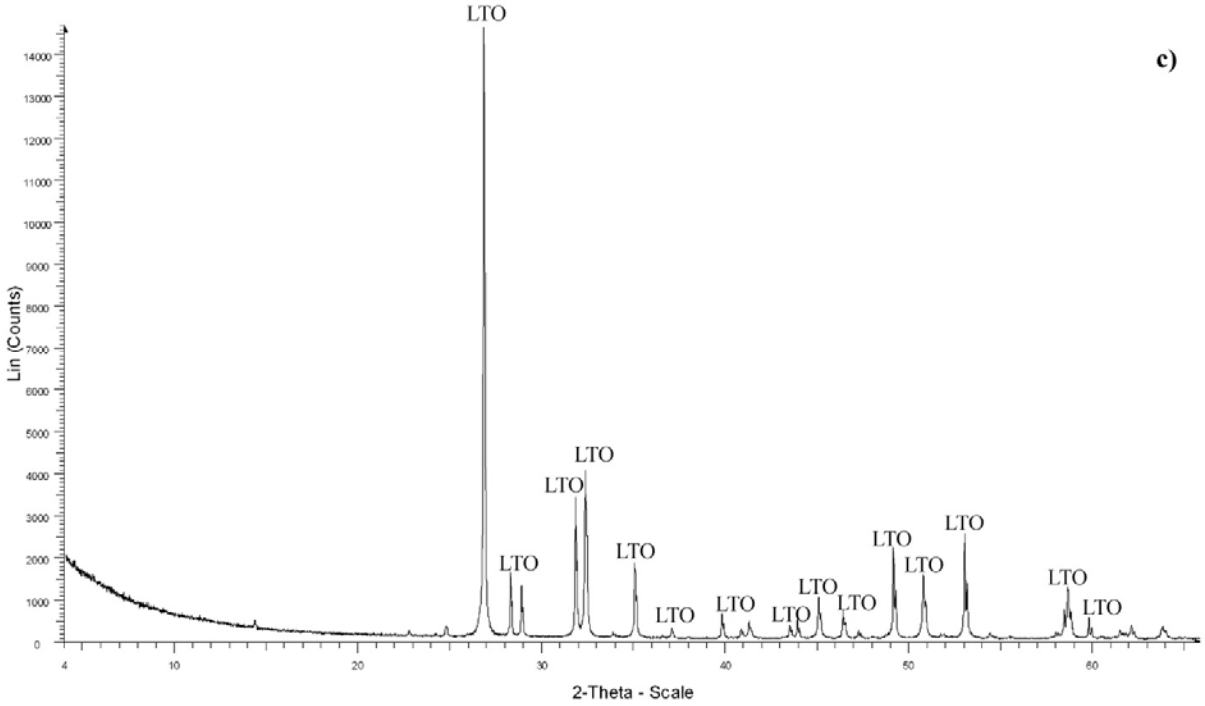

Figure 6.20 b - Fig. 3. XRD spectra: (a) cinnabar; (b) lapis lazuli and (c) lead-tin yellow. Mineralogical phases are reported: Cin: cinnabar; LTO: lead-tin oxide; La: lazurite; Mu: muscovite; Di: diopside; Ca: calcite; Py: pyrite.

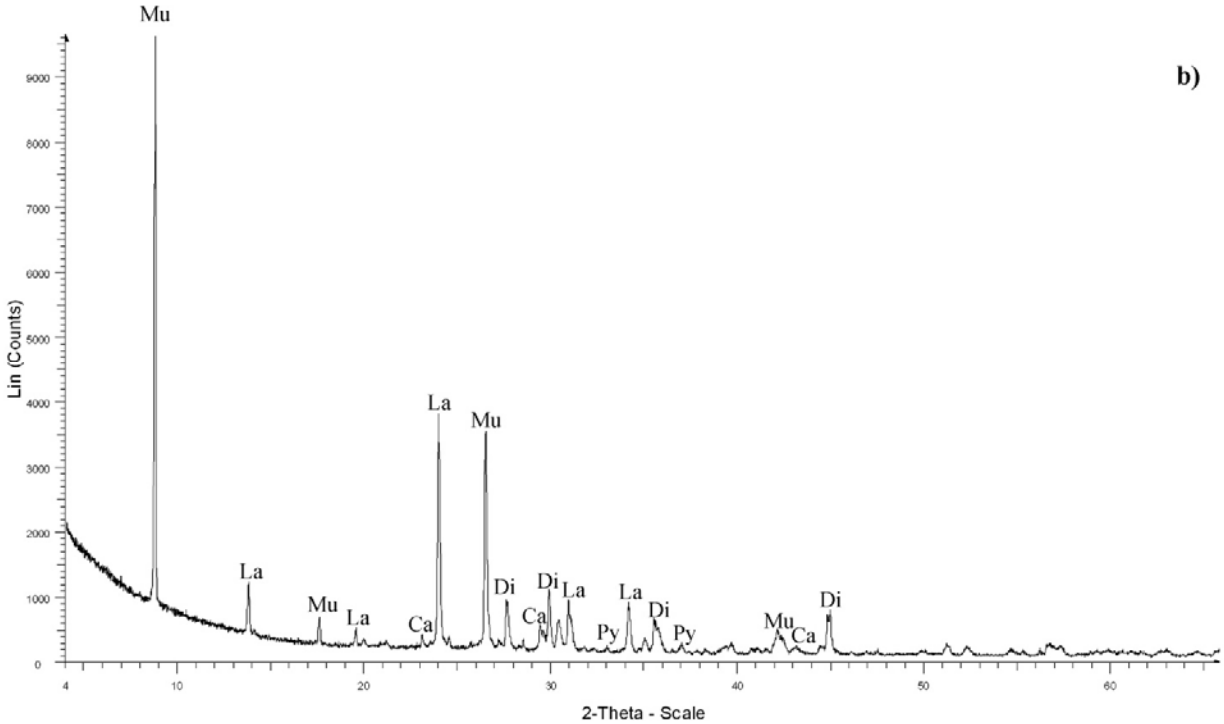

Figure 6.20 c - Fig. 3. XRD spectra: (a) cinnabar; (b) lapis lazuli and (c) lead-tin yellow. Mineralogical phases are reported: Cin: cinnabar; LTO: lead-tin oxide; La: lazurite; Mu: muscovite; Di: diopside; Ca: calcite; Py: pyrite.

In particular, we define the maximum value I_{max} following the equation (5.1). The behaviour of I_{max} *vs.* density along with fitting curves, for the considered chemical elements characterizing the investigated mixtures, is shown in Figs. 6.21 and 6.22.

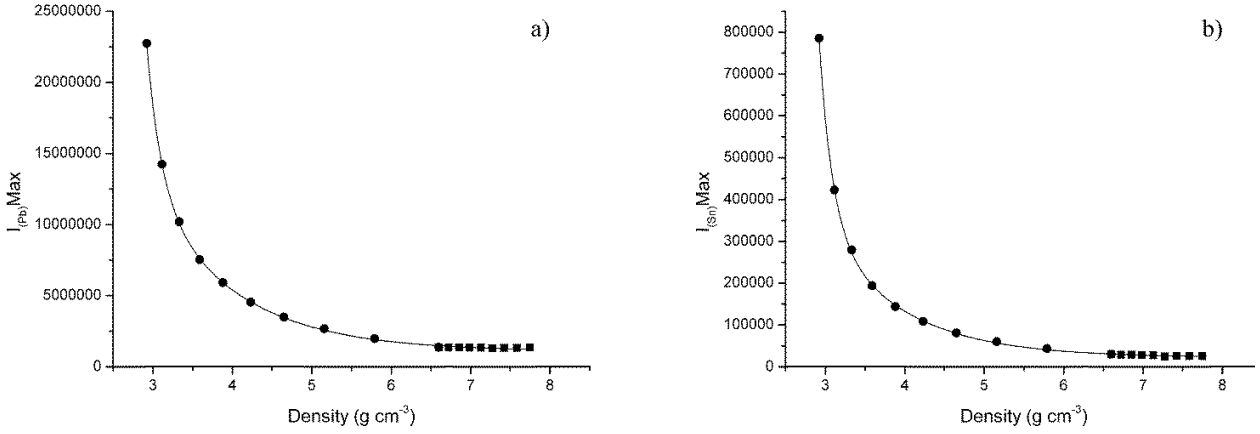

Figure 6.21 - I_{max} values and fitting curves according eq. (5.2) in the density range of the Y-B and Y-R mixtures, i.e. from 2.58 g cm^{-3} in the 10% Y–90% B mixture up to 7.92 g cm^{-3} in the 10% Y–90% R mixture, for: (a) Pb, fitting curve with R^2 = 0.999 and (b) Sn, fitting curve with R^2 = 0.999.

In particular, Fig. 6.21 a and b report the I_{max} values in the density range of the Y-B and Y-R mixtures (from 2.92 g cm^{-3} for the 10% Y–90% B up to 7.92 g cm^{-3} for the 10% Y–90% R) for Pb and Sn, respectively. It is worth pointing out that, since all XRF measurements of mixtures containing lead-tin yellow have been acquired with the same experimental parameters all I_{max} values are plotted in the same graph. Both plots show a steeply decreasing of I_{max} as mixture density increases up to the value of 6.60 g cm^{-3}, then a plateau region, corresponding to the density values of Y-R mixtures, is reached. On the basis of the above considerations, the achievement of constant I_{max} values is to be understood as equivalent to a non-dependence of the XRF signal on the matrix density. This evidence proves the linear calibration curves obtained for Pb and Sn in the Y-R mixtures.

Similar considerations can be made on the behaviour of I_{max} for Hg in R-B and R-Y mixtures, shown in Fig. 6.22 a and b, respectively.

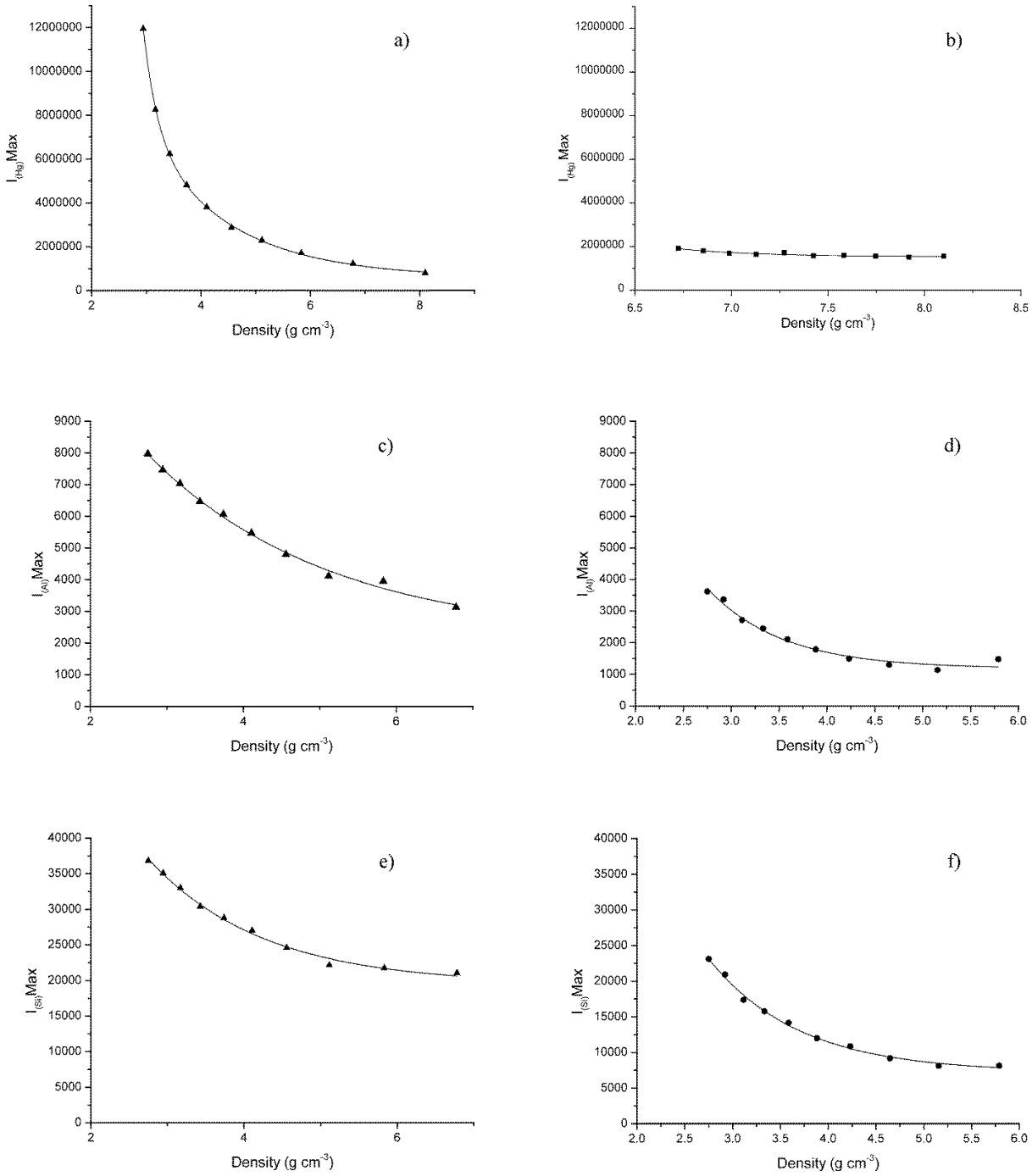

Figure 6.22 - I_{max} values and fitting curves according eq. (5.2) for: Hg **(a)** in R-B mixtures, fitting curve with R^2 = 0.999; **(b)** in R-Y mixtures, fitting curve with R^2 = 0.999; Al **(c)** in B-R mixtures, fitting curve with R^2 = 0.993 and **(d)** in B-Y mixtures, fitting curve with R^2 = 0.993; Si **(e)** in B-R mixtures, fitting curve with R^2 = 0.994 and **(f)** in B-Y mixtures, fitting curve with R^2 = 0.995. Measurement parameters used for the XRF acquisitions: 25 kV and 1300 μA for (a), (c) and (e) spectra; 40 kV and 700 μA for (b), (d) and (f) spectra.

Despite the different measurement parameters used for the XRF acquisitions (Panel 6.22 a: 25 kV and 1300 μA; Panel 6.22 b: 40 kV and 700 μA), it is possible to find a similar behaviour with a plateau

region in the 6.60–8.20 g cm^{-3} density range. Unfortunately, due to the low efficiency of our instrumental apparatus in the detection of the light elements (such as Al and Si) components of the blue pigment, I_{max} data obtained for these two elements can only be evaluated by a qualitative point of view. However, also in this case, a dependence of I_{max} on density appears to be more noticeable in the density range of 2.40–4.50 g cm^{-3} (Fig. 6.20, panels' c, d, e and f). This means that XRF measurements of both B-Y and B-R mixtures are affected by density changes, and all elements constituting these mixtures, as expected, cannot show a linear calibration curve.

In order to validate both the measurement and the fitting procedures, concentration values have been calculated via inverse prediction for some *ad hoc* prepared mixtures (see Table 6.9). In the case of linear fitting, the ≅ 95% confidence ranges for concentrations, calculated by inverse prediction, are also reported for Pb, Hg and Sn in the R-Y mixtures. The concentration values obtained from the fitting curves are in good agreement with the expected ones, confirming the reliability of measurements and statistical procedures. The evaluation of the behaviour of I_{max} *vs.* the mixture density suggests that, only for the linear calibration curves, it is possible to use the fitting obtained for Hg, Pb and Sn in order to gather quantitative data of these elements in matrices of density comparable to the one of the mixtures here investigated. The outcomes highlight the different behaviour of the calibration curves with respect to the different densities of the pigments constituting the binary mixtures. Indeed, only mixtures of pigments with comparable density exhibit a linear behaviour for the net peak areas *vs.* the weight fraction. In mixtures of pigments with different densities, the slope of the net calibration curve decreases with the weight fraction of the heavy pigment, due to the increasing of the sample density.

The procedure developed for the powder mixtures was also carried out for mixtures spread with casein, obtaining the following calibration curves (Figs. 6.23 – 6.26).

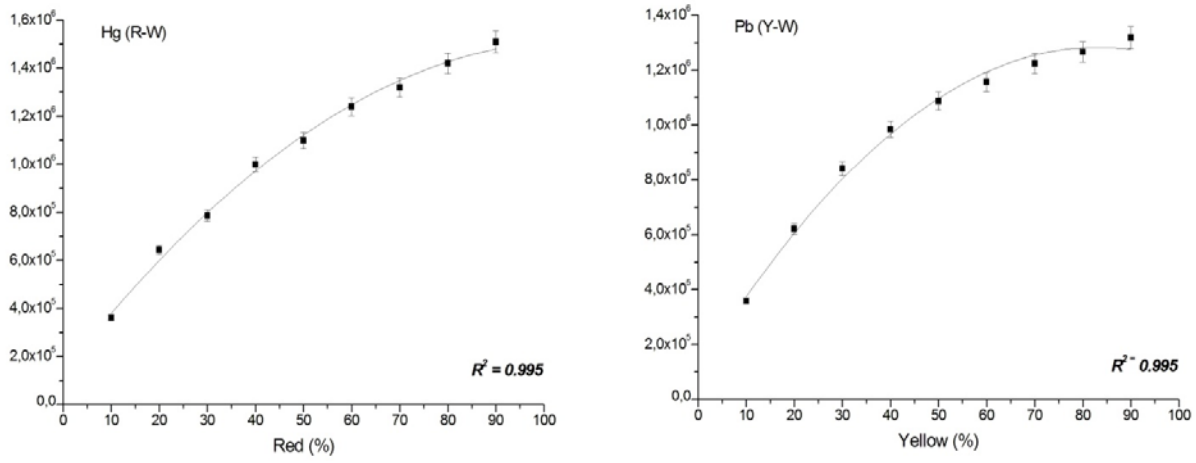

Figure 6.23 - Experimental net peak areas *vs.* pigment weight fraction and fitting curves. Error bars are also shown. From left to right: Hg in R-W *vs.* R%; Pb in Y-W *vs.* Y%. The R^2 values for each fitting curve are reported in the graphs.

Also in this case, net areas for Hg L_α line in the R-W mixture vs. R% concentration, and Pb L_α line in the Y-W mixture *vs.* Y% concentration have been fitted by a second order polynomial equation, showing the same behaviour of powder mixtures due to the density different between the two pigments (Y heavy *vs.* W light).

In the following figures are reported the calibration curves and the behaviour of I_{max} *vs.* density, for the considered chemical elements characterizing the investigated mixtures layered with casein, both for White and Itten mixtures.

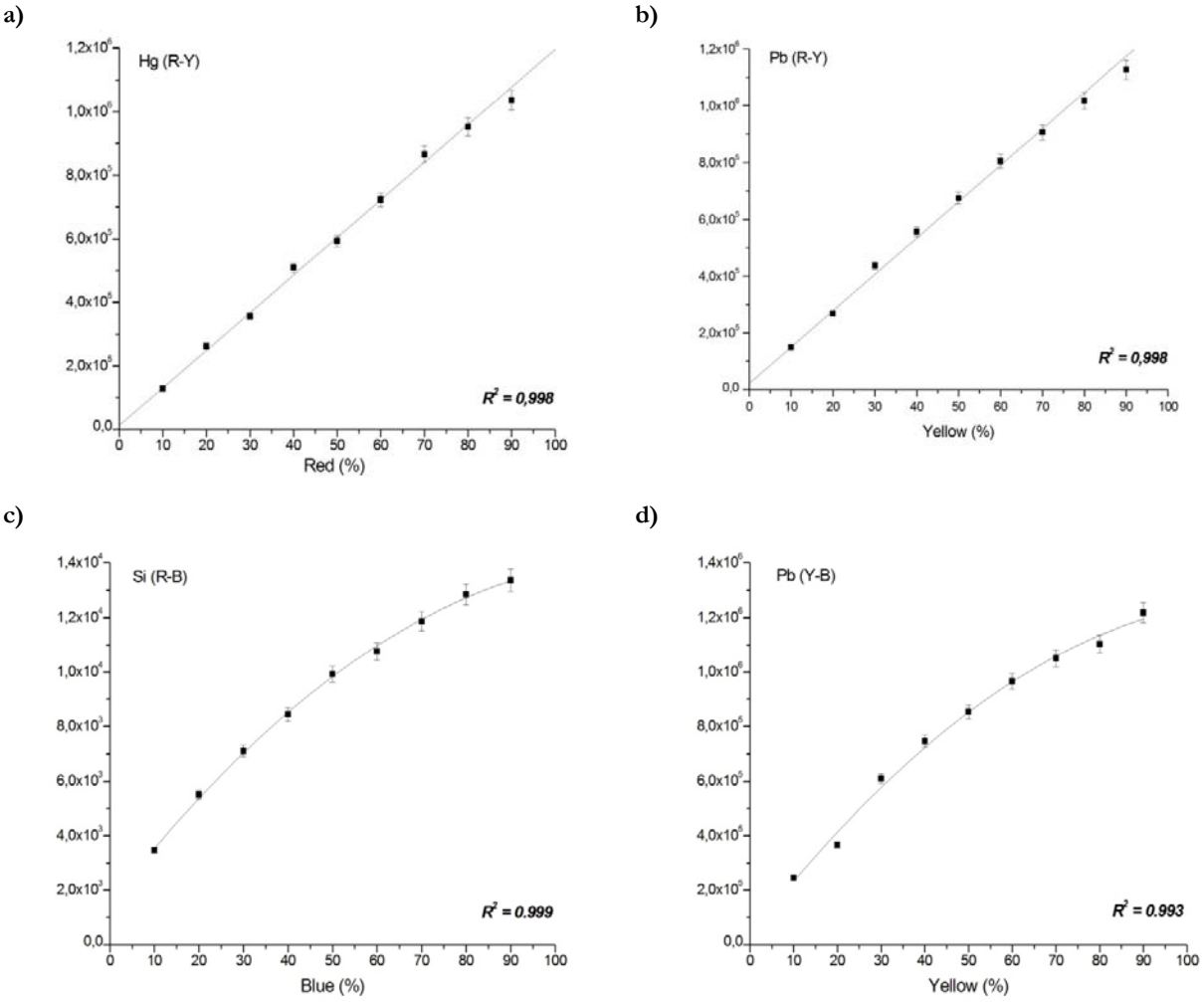

Figure 6.24 - Experimental net peak areas *vs.* pigment weight fraction and fitting curves. Error bars are also shown. From left to right: Hg in R-Y *vs.* R%; Pb in R-Y *vs.* Y%. The R^2 values for each fitting curve are reported in the graphs.

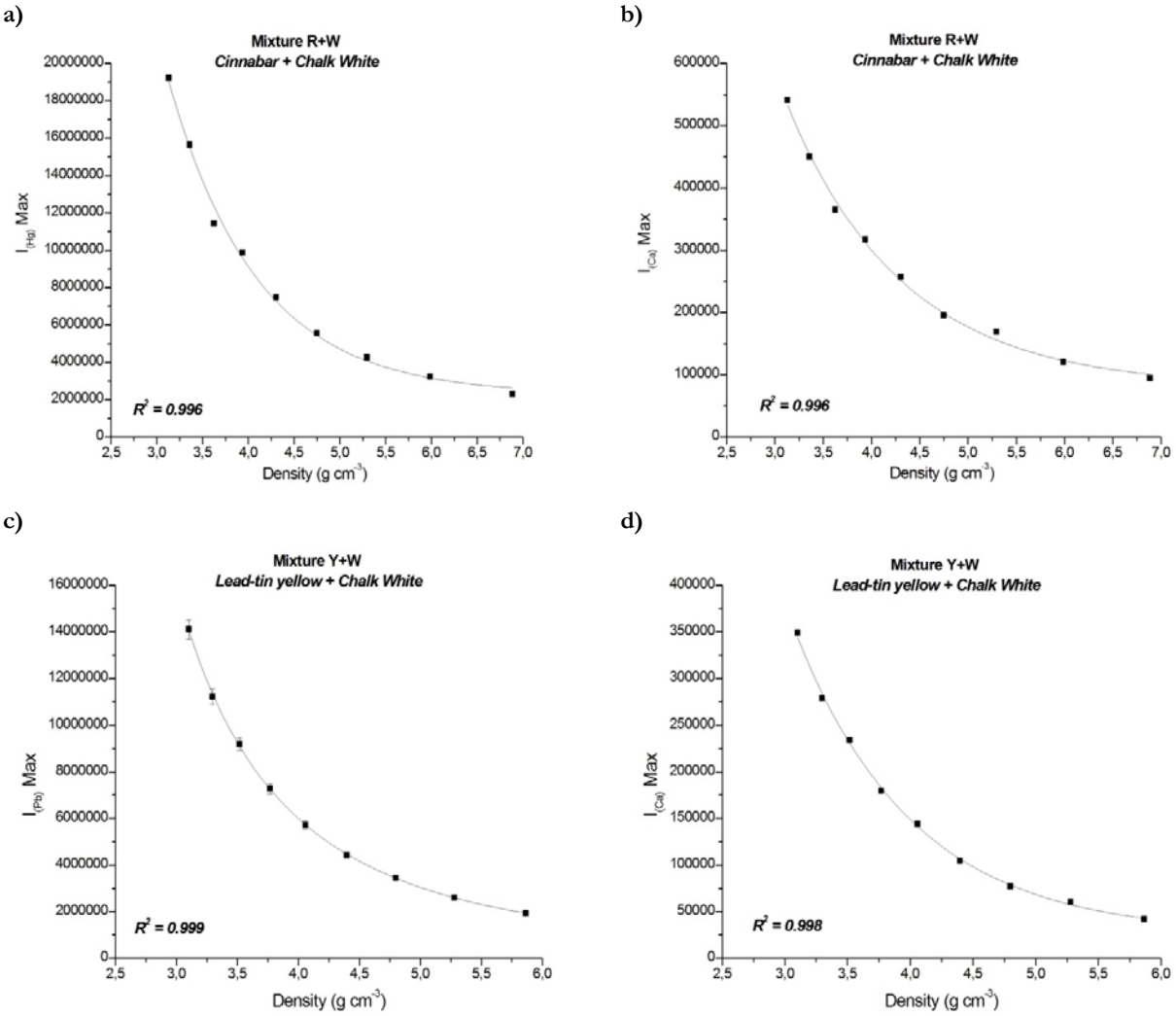

Figure 6.25 - I_{max} values and fitting curves according eq. (5.2) for: R+W (Hg and Ca); Y+W (Pb and Ca). The R^2 values for each fitting curve are reported in the graphs.

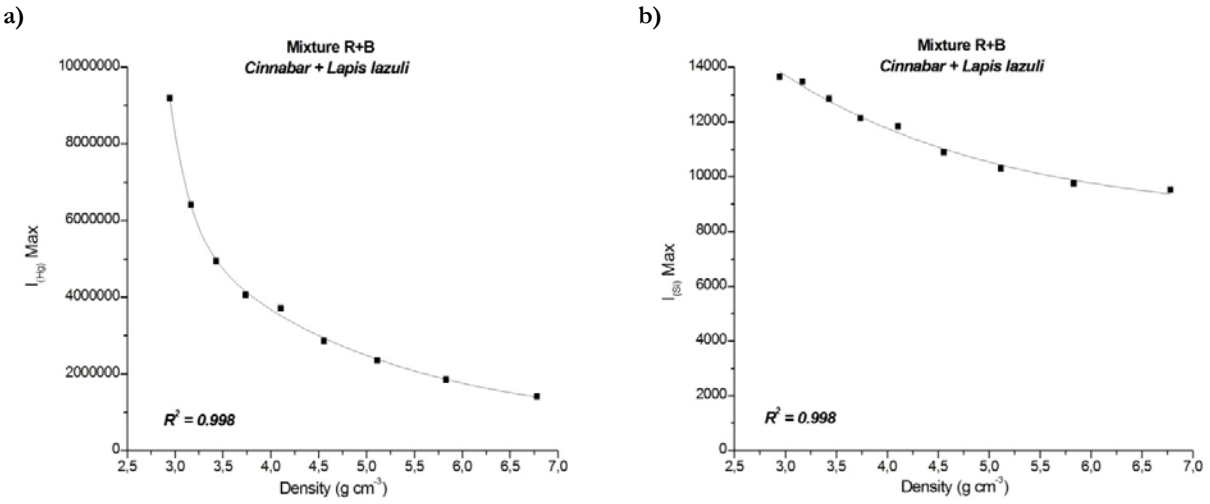

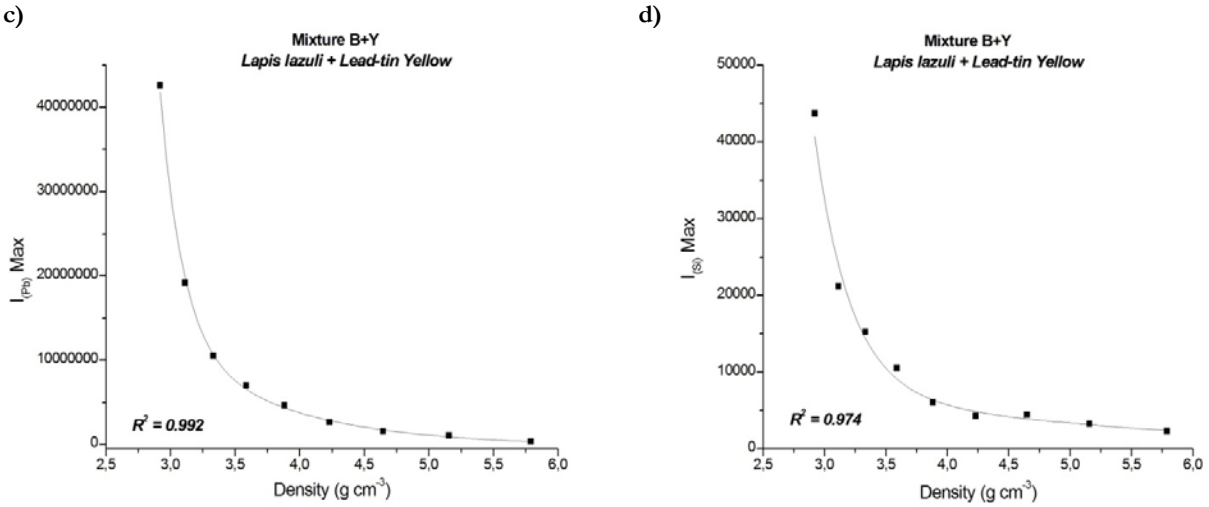

Figure 6.26 - I_{max} values and fitting curves according eq. (5.2) for: R+B (Hg and Si); B+Y (Si and Pb). The R^2 values for each fitting curve are reported in the graphs.

However, also in this case, XRF measurements of both R+B and B+Y mixtures are affected by density changes, and all elements constituting these mixtures, as expected, cannot show a linear calibration curve.

6.4 RAMAN quantitive method

As said before, the Raman spectrum of a mixture is not qualitatively proportional to the weighted sum of the Raman spectra of the pigments taken individually; indeed, depending on the mixture concentration and number of molecule of each pigment [15], it happens that some peaks of specific pigments are not recognized.

As it is possible to see in the characterization measurements related to the binary mixtures (section 6.2.2.2), the characteristic bands of the two pigments constituting the mixtures are not detectable for each weight percentage; after fraction of 50%+50% the main band of pigment with lower weight percentage was not identified.

This evidence strongly affects the possibility to obtain quantitative information for all the made weight fraction. In figures 6.27 – 6.28 are reported the fitting curves obtained for each binary mixture.

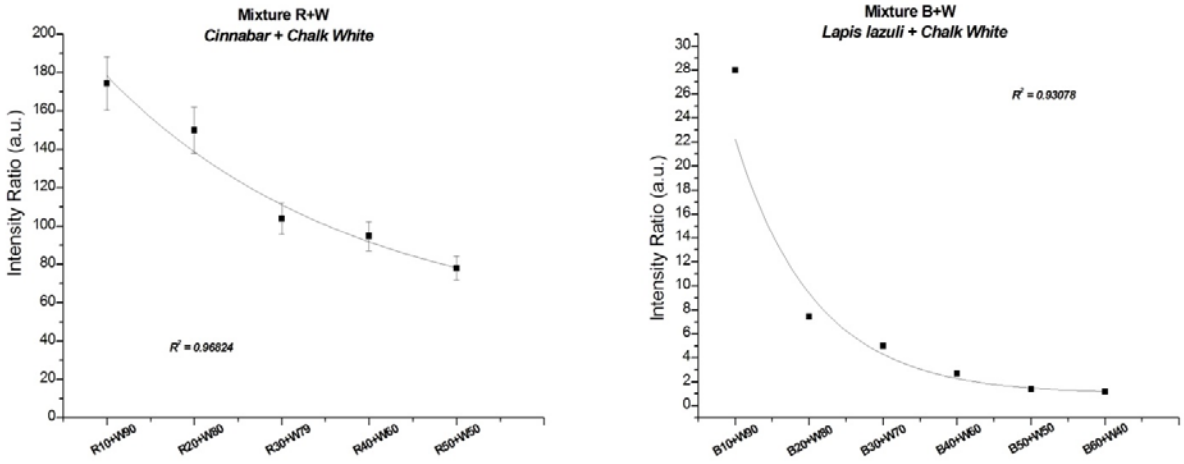

Figure 6.27 – Fitting curve obtained for Binary mixture: R+W and B+W.

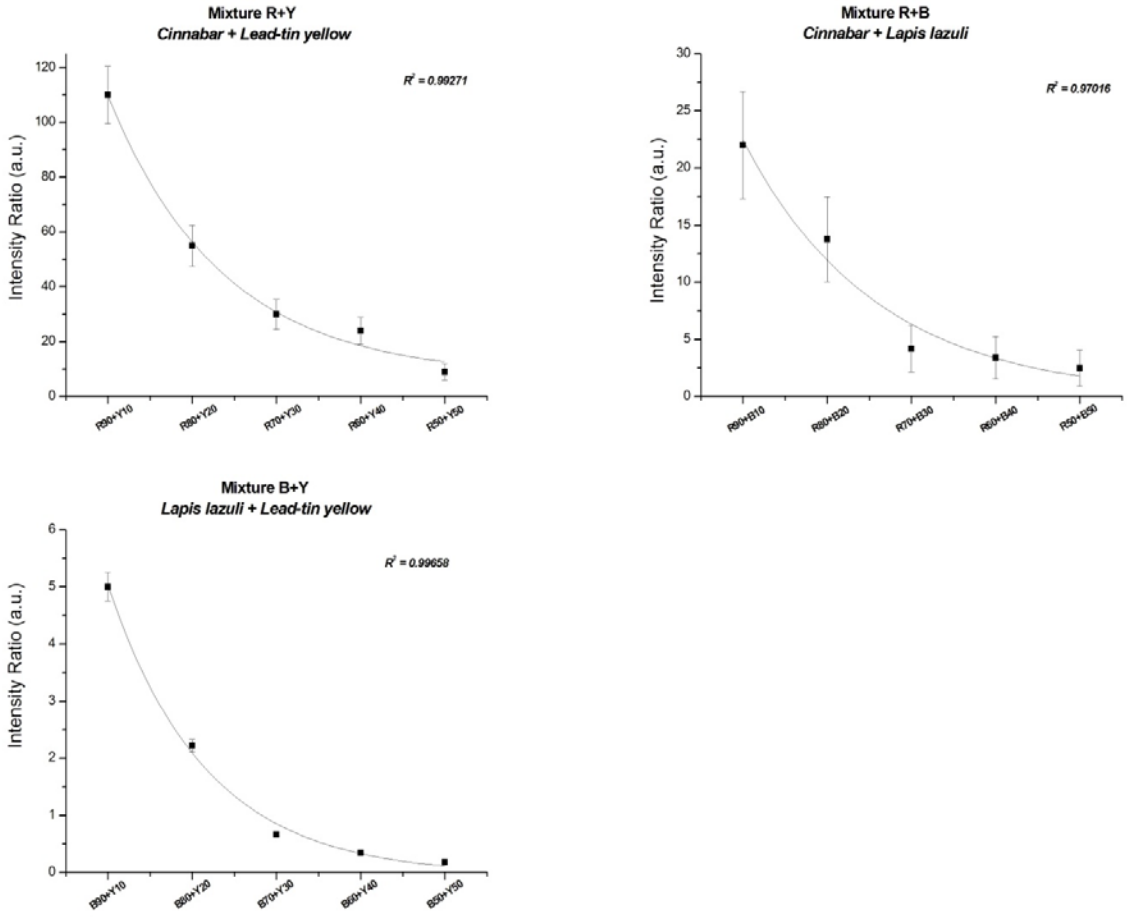

Figure 6.28 – Fitting curve obtained for Itten mixtures: R+Y, R+B and B+Y-

The fitting curves by means of Raman spectroscopy show an exponential behaviour but the inability to detect the main band of pigments for all the weight percentage don't allow to use this kind of technique

to obtain quantitative information's. Further study will be carrying out in order to understand the role of density and quantity of moles for each percentage.

6.5 Spectrophotometric quantitive method

In the case of spectrophotometric measurements, in order to find a law, that allows to effectuate a quantitative analysis, the peak value (positive) of the first derivate of SRF% for each binary mixtures were used.

So, for each weight percentage, the ratio

$$R_{mixture} = V_x / V_y \tag{6.2}$$

was calculated and the different vales obtained for each weight percentage were plotted *vs.* mixtures concentration (Fig. 6.29).

a)

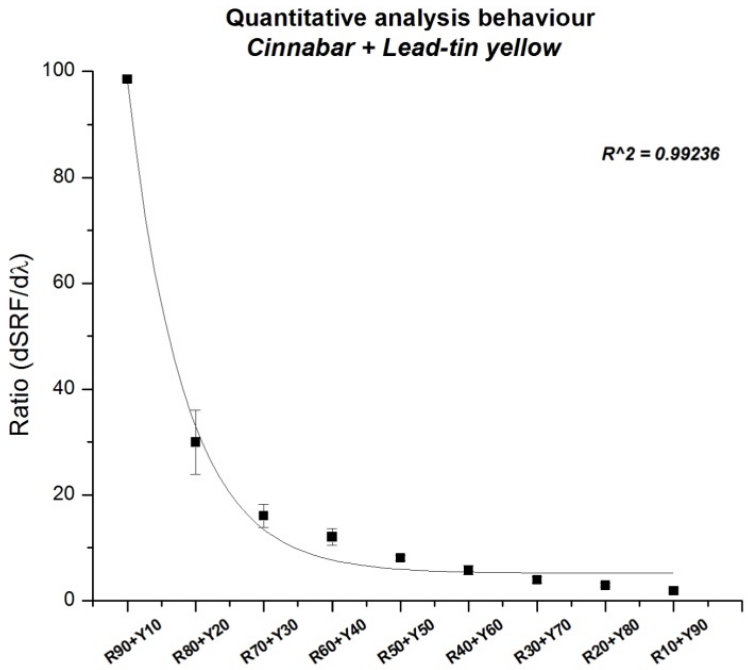

b)

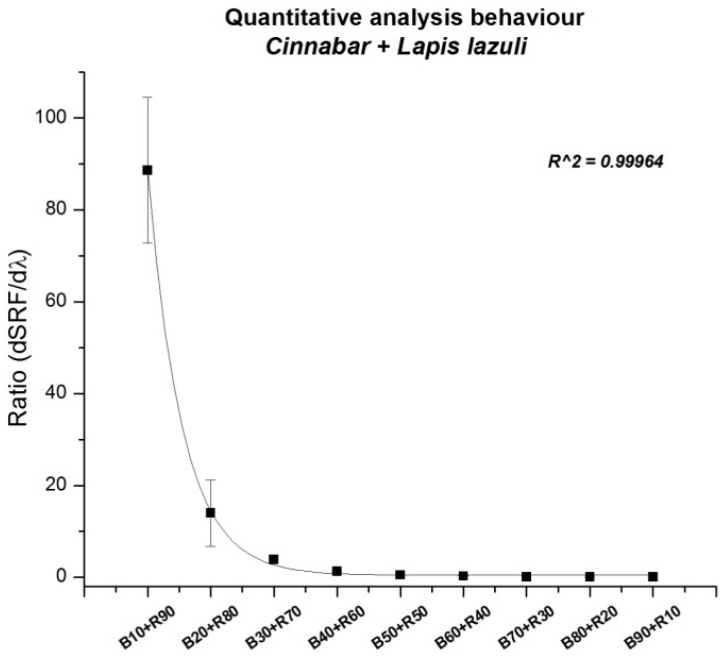

c)

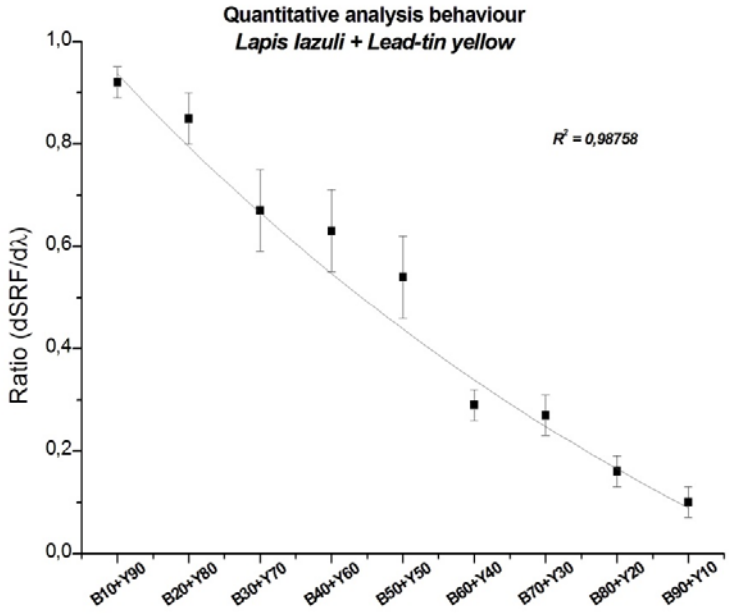

Figure 6.29 – quantitative calibration curves obtained for each mixture. **a)** R+Y (cinnabar + lead-tin yellow), **b)** R+B (cinnabar + lapis lazuli), **c)** B+Y (lapis lazuli + lead-tin yellow).

In this case only for the Itten mixtures the quantitative analysis was obtained. For mixtures with white pigment problems arise: the white pigment doesn't present maximum and/or minimum peaks (Fig. 6.5

d) in the first derivate curve of SRF%, so it was not possible to study the quantitative behaviour of that mixtures.

A possible solution to solve this problem would be to study the white pigments behaviour with spectrophotometers that investigate the near-UV region, where these pigments have different and well distinguishable spectral behaviour [13].

Also with this technique, to validate the method developed, specimens with unknown (for the analyst) concentration were prepared. Using the calibration curves previously showed the weight percentage of the single component of the unknown mixtures, composed by two known pigment, and by inverse prediction on the calibration curve were calculated, as reported in Table 6.10.

Mixture	***Model (R^2)***	***Measured Weight***		***Calculated Weight***	
		Pigment	***%***	***Pigment***	***%***
R+Y_Itten Orange	Exponential (0.992)	Cinnabar	75	Lead-tin yellow	**77.4 ± 5.1**
		Lead-tin yellow	25	Lead-tin yellow	**22.6 ± 1.5**
R+B_ Itten Purple	Exponential (0.999)	Cinnabar	75	Cinnabar	**73 ± 6.4**
		Lapis lazuli	25	Lapis lazuli	**27 ± 2.4**
B+Y_ Itten Green	Exponential (0.987)	Lead-tin yellow	85	Lead-tin yellow	**84.5 ± 7.2**
		Lapis lazuli	15	Lapis lazuli	**15.5 ± 1.3**

Table 6.10 - Numerical results for fitting of first derivative peak ratio vs. pigment concentrations. The second column lists the model along with the R^2 values. The last two columns list the expected weight percentages of pigments in the test binary mixtures (reference values %) along with the values obtained by inverse prediction.

Bibliography

[1] Križnar, A., Muñoz, V., de la Paz, F., Respaldiza, M.A., Vega, M. "Portable XRF study of pigments applied in Juan Hispalense's 15th century panel painting", X-Ray Spectrom.40 (2011) 96-100.

[2] Ferrero, J.L., Roldàn, C., Juanes, D., Rollano, E., Morera, C. "Analysis of pigment from Spanish works of art using a portable EDXRF spectrometer", X-Ray Spectrom.31 (2002) 441-447.

[3] Van Der Snickt, G., De Nolf, W., Vekemans, B., Janssens, K. "μ-XRF/ μ -RS vs. SR μ -XRD for pigment identification in illuminated manuscripts", Applied Physics A 92 (2008) 59-68.

[4] Burgio, L., Clark, R.J.H. "Libraryof FT-Raman spectra of pigments, minerals, pigment media and varnishes, and supplement to existing library of Raman spectra of pigments with visible excitation", Spectrochimica Acta Part A 57 (2001) 1491–1521.

[5] http://www.ciam.unibo.it/laureescientifiche/corsi-laboratorio/chimica-e-beni-culturali/lezione 4 terre.pdf

[6] Colomban, P. "Lapis lazuli as unexpected blue pigment in Iranian Lâjvardina ceramics", J. Raman Spectrosc. 34 (2003) 420-423.

[7] Menezes, R.C. "Raman Spectroscopy - A fast and reliable tool to detect secondary fungal metabolites", Institute of Microbiology, Friedrich Schiller University, Jena, Germany and Institute of Photonic Technology Jena e.V., Germany.

[8] Frost, R.L., Martens, W.N., Rintoul, L., Mahmutagic, E., Kloprogge, J.T. "Raman spectroscopic study of azurite and malachite at 298 and 77 K", Journal of Raman Spectroscopy, 33(4) (2002) pp. 252-259.

[9] Bell, I.M., Clark, R.J.H., Gibbs, P.J. "Raman spectroscopic library of natural and synthetic pigments (pre- ≈ 1850 A.D.)", Spectrochim. Acta, Part A 53 (1997) 2159-2179.

[10] Vandenabeele, P., Moens, L., Edwards, H.G.M., Dams, R. "Raman spectroscopic database of azo pigments and application to modern art studies", J. Raman Spectrosc. 31 (2000) 509-517.

[11] Burrafato, G., Calabrese, M., Cosentino, A., Gueli, A.M., Troja, S.O., Zuccarello, A. "ColoRaman project: Raman and fluorescence spectroscopy of oil, tempera and fresco paint pigments", J. Raman Spectrosc. 35 (2004) 879–886.

[12] Bell, I.M., Clark, R.J.H., Gibbs, P.J. "Raman spectroscopic library of natural and synthetic pigments (pre- ≈ 1850 AD)", Spectrochim. Acta, Part A 53 (1997) 2159-2179.

[13] Bacci, M., Casini, A., Cucci, C., Picollo, M., Radicati, B., Vervat, M. "Non-invasive spectroscopic measurements on the Il ritratto della figliastra by Giovanni Fattori: identification of pigments and colourimetric analysis", Journal of Cultural Heritage 4 (2003) 329–336.

[14] Fontana, D., Alberghina, M.F., Barraco, R., Basile, S., Tranchina, L., Brai, M., Gueli, A., Troja, S.O. "Historical pigments characterisation by quantitative X-ray fluorescence", Journal of Cultural Heritage (2013), http://dx.doi.org/10.1016/j.culher.2013.07.001.

[15] Breitman, M., Ruiz-Moreno, S., Pérez-Pueyo, R. "Study of Raman spectra of pigment mixtures", Journal of Cultural Heritage 4 (2003) 314s–316s.

Discussion and Conclusions

The knowledge of the exact amount of different constituents of the paint, as well as of the mixing and pictorial techniques, is crucial for a careful program of conservation of polychrome works. Moreover, since the availability of these pigments has been changing through the centuries, their identification and chemical characterisation is useful to acquire or deepen information about the artist and his/her work.
In the course of the research, presented in this thesis, was explored the potential offered by an integrated analytical approach in order to compare and make complementary the results of the different diagnostic methodologies conducted for archaeometric and/or conservative purposes during the study of works of art, both for the compositional and physical-optical characteristics analysis on surfaces of interest.
The results obtained are focused on the integration of diagnostic methodologies applied for the characterization (elemental, compositional and colorimetric) of laboratory specimens that simulate pictorial layers reproducing pigments mixtures used by ancient artists
The measurements carried out on the laboratory specimens can be grouped in different steps that have characterized the development of methodological approach followed during the research activities: i) characterization of pure pigments, ii) characterization of Binary mixtures and iii) quantitative analysis.

The first step of analysis was focused on the characterization of the historical pigments chosen. By means of XRF, Raman and Colorimetric point of view in order to obtain a complete characterization of the specimens.
For the analysis of the chemical composition, great attention has been paid to the comparison of results provided by the physical techniques XRF and Raman Spectroscopy.
The elemental and compositional information given by, XRF and Raman measurements, respectively, has allowed to unequivocally characterize the pigments, by detecting a relevant difference between the chemical composition declared by Kremer and the set of elements experimentally identified. So compositional characterization through Micro-Raman spectroscopy was also compared with elemental ones.
It was possible to observe that the pigments show their characteristic Raman bands according to the reference spectra in literature. Moreover, some of the pigments analysed with the TRIAX 320 Horiba Jobin-Yvon instrumental apparatus were not identified because of their fluorescence in NIR range;

other pigments presents slight shift in position. In order to obtain a better characterization of each pigments and to evaluate the shift present on bands wavenumber position, all the pigments were also analyzed with a different instrumental apparatus, available at LADIR (*LAboratoire de Dynamique, Interactions et Reactivite* - UMR 7075 CNRS et UPMC - Université Pierre et Marie Curie - Paris 6), with three different visible laser sources: 458, 488 and 514 nm. By the comparison among the detected picks, it seems clear a better identification of those more characteristics, allowing a more accurate characterization of our samples.

After the complete chemical characterization, the spectrophotometric analyses have played an important role because an accurate evaluation of the colour behaviour in our samples has allowed to obtain information useful for applicative purposes.

In this context, the SRF% of pure pigments was recorded and the first derivative curve was calculated; both useful to better identify the different hues.

Thanks to the complementary information by the 3 diagnostic methodologies was possible to obtain an exhaustive characterization of the pure pigments analysed.

Found the fingerprints characterizing each pure pigment, the binary mixtures made, following the "recipes" of ancient artist, were also characterized with the three diagnostic methods in order to verify if each experimental apparatus was able to detect each single component in the mixtures.

For each type of binary mixtures, the fingerprints of pigments have been detected and in particular:

- for XRF spectra, the intensity of the characteristic lines varies with the pigment concentration within the mixture; this evidence has been used for the evaluation through quantitative analysis of the amount of each pigment that composes the mixtures;
- for Raman spectra, the main bands of each pigment are present in the mixtures but in this case not detectable for all the weight percentage. Indeed, for weight percentage up to 50% the detection of the Raman bands is not possible for all the mixtures.

  This kind of behaviour evidenced for each mixtures happens because to detect the Raman bands of different pigments, different stimulation time are required. However, some pigments present a high Raman response, such as cinnabar, also with very low stimulation time, covering completely the weaker bands of the other compounds. If higher times of stimulation are used, the more intense band causes CCD saturation, invalidating the identification of the pigments in mixture;
- for Spectrophotometric analysis, the spectral behaviour of first derivative curves of binary mixtures shows the presence of maximum/minimum peaks of the hue constituting the Itten

mixtures. For the mixtures with white, it was not possible to identify the peaks of white pigment making difficult the recognition of the two different hues.

Final goal of this experimental approach was to calculate the weight percentage of the single component, on an unknown (for the analyst) mixture, composed by two known pigment, by inverse prediction on the calibration curve.

It is focused on the elemental quantitative characterization of three binary mixtures obtained by varying the weight fractions of the constituting pigments. In particular, the study has concerned, after an appropriate characterization of the pure samples, the analysis of binary mixtures by means of X-ray fluorescence, Raman Spectroscopy and Spectrophotometric investigations.

XRF net peak areas for the characteristic elements have been used to build calibration curves in order to perform inverse prediction of concentration. The outcomes highlight the different behaviour of the calibration curves with respect to the different densities of the pigments constituting the binary mixtures. Indeed, only mixtures of pigments with comparable density exhibit a linear behaviour for the net peak areas *vs.* the weight fraction. In mixtures of pigments with different densities, the slope of the net calibration curve decreases with the weight fraction of the heavy pigment, due to the increasing of the sample density.

These findings, associated with those from others non-invasive methodologies, can be considered particularly useful for the recognition of weight percentage of pigments constituent an unknown painting mixture.

Starting from that assumption, the information obtained were integrated with that one's by Raman and spectrophotometric analyses.

The fingerprint of different pigments, acquired with Raman spectroscopy, appears in each weight percentage of binary mixtures but only up to percentage of 50%+50%. For this reasons, with Raman spectroscopy is not possible to indentify a quantitative behaviour necessary for building calibration curves. The $R_{mixture}$, calculated for each weight percentage by first derivative spectrophotometric curves, have been used to build calibration curves aimed to perform inverse prediction of concentration. The outcomes highlight a comparable behaviour of the calibration curves with respect to the different hue of pigments used; all the calibration curves are obtained.

The results so collected make possible to evaluate the reliability of the integration of the three techniques to acquired useful information both for chemical and chromatic characterization of mixtures and for quantitative analysis by XRF and spectrophotometric measurements.

Our analytical approach integrating non invasive/destructive techniques can be considered a practical tool of analysis for the study and characterization of painting and/or polychrome artworks on conservations and restoration programs.

It worth to point out that this study still requires deeping and enlargement of both the pigment samples and mixtures, and the analytical techniques to be used.

Then, work in progress is to study the quantitative analytical response of measurements performed on more complex matrix and to evaluate the influences of the binding agents used for the realization of the pictorial materials.

Acknowledgments

I want to dedicate the last page of this thesis to all those people who have made possible its realization and who have supported me during its writing.

First of all I wish to thank my tutors, Prof.ssa M. Brai for the opportunity that she gives me to work in her group at *Laboratorio di Tecniche Fisiche per lo Studio e la Caratterizzazione dei Beni Culturali* (University of Palermo – Physics and Chemistry Department) with a team of professional and wonderful people; and Prof. S.O. Troja of PH3DRA Laboratories (University of Catania – Physics and Astronomy Department) for believing strongly in this research project.

I also want to thank them for being my guide and mentor during this 3 years and for the time they spend answering my questions.

Secondly, I want to thank Prof. L. Bellot-Gurlet for the time that he spent with me during my 3 months in Paris: thanks to him I had the opportunity to work within a wonderful research group and to know and learn in detail the secrets of Raman Spectroscopy... merci à toi et à tout le merveilleuses personnes du LADIR.

Now I want to thank all the people who helped me and supported me during my PhD...my travel buddy!

Thanks to my Palermo's family: "mommy" Dr. Francesca Alberghina and "daddy" Dr. Salvatore Schiavone for welcoming me into their lives and making me feel a part of their family...I love you so much! A special thanks to Francesca for being present in every moment ... both good or bad... thank you from heart of hearts.

Thanks to my "avatar" Dr. Rosita Barraco for the personal and professional support in all the steps of my research activity.

Thanks to Dr. Luigi Tranchina for his "chemical contribution" in each data processing and for being a perfect tour guide of Palermo.

A special thanks to Dr. Giusepe Stella...good and great longtime friend, who supported and help me all the time, for every problem that occurred during my path. To him I owe much of the critical sense and the desire for knowledge that I have developed over the years. This thesis is also your...thank you so much "boss".

Last but not least, I want to thank my family who always gave me the courage to go ahead: thanks to my mother for pushing me to improve myself, thanks to my father for teaching me to always walk with

heads held high, thanks to my brother, Simone, for teaching me to make me a good laugh even in the worst moments and thanks to Fabrizio for being an important part of my life.

HEARTFELT THANKS TO ALL OF YOU!!!